Electronic and
Electrical
Engineering.

Adaptive Techniques for Estimation and Online Monitoring of Battery Energy Storage Devices

by

Shahab Nejad

A thesis submitted in partial fulfilment of the requirements for the degree of

DOCTOR OF PHILOSOPHY

© May 2017

to my beloved family

Abstract

The battery management system (BMS) plays a defining role in the safety and proper operation of any battery energy storage system (BESS). Without significant advances in the *state-of-the-art* of BMS algorithms, the future uptake of high power/energy density battery chemistries by consumers in safety-critical applications, is not feasible. Therefore, this thesis aims to provide a coherent body of work on the enhancement of the most important tasks performed by a modern BMS, that is, the estimation and monitoring of various battery states, e.g. state-of-charge (SOC), state-of-health (SOH) and state-of-power (SOP).

The Kalman Filter is an elegant set of robust equations that is often utilised by designers in modern BMS, to estimate the battery states and parameters in real time. A nonlinear version of the KF technique, namely the Extended Kalman Filter (EKF) is applied throughout this thesis to estimate the battery's states including SOC, as well as the battery's impedance parameters. To this end, a suitable model structure for online battery modelling and identification is selected through a comparative study of the most popular electrical equivalent-circuit battery models for real-time applications. Then, a novel improvement to the EKF-based battery parameters identification technique is made through a deterministic initialisation of the battery model parameters through a broadband system identification technique, namely the pseudorandom binary sequences (PRBS). In addition, a novel decentralised framework for the enhancement of the EKF-based SOC estimation for those lithium-ion batteries with an inherently flat open-circuit voltage (OCV) response is formulated. By combining these techniques, it is possible to develop a more reliable battery states monitoring system, which can achieve estimation errors of less than 1%. Finally, the proposed BMS algorithms in this thesis are embedded on a low-cost microprocessor hardware platform to demonstrated the usefulness of the developed EKF-based battery states estimator in a practical setting. This a significant achievement when compared to those costly BMS development platforms, such as those based on FPGAs (field-programmable gate arrays).

List of Publications

Parts of the work presented in this thesis have been enclosed in the following internationally-respected publications.

Journal publication

1. **S. Nejad**, D. T. Gladwin, and D. A. Stone, "A systematic review of lumped-parameter equivalent circuit models for real-time estimation of lithium-ion battery states," *J. Power Sources*, vol. 316, 2016.

Conference Proceedings

1. **S. Nejad**, D. T. Gladwin, and D. A. Stone, "Sensitivity of lumped parameter battery models to constituent parallel-RC element parameterisation error," in *Industrial Electronics Society, IECON 2014 - 40th Annual Conference of the IEEE*, 2014

2. **S. Nejad**, D. T. Gladwin, and D. A. Stone, "Enhanced state-of-charge estimation for lithium-ion iron phosphate cells with flat open-circuit voltage curves," in *Industrial Electronics Society, IECON 2015 - 41st Annual Conference of the IEEE*, 2015

3. **S. Nejad**, D. T. Gladwin, and D. A. Stone, "A microcontroller-based state-of-health estimator for lithium-ion batteries," in *Power Electronics, Machines and Drives (PEMD 2014), 7th IET International Conference on*, 2014

4. **S. Nejad**, D. T. Gladwin, and D. A. Stone, "A Hybrid Battery Parameter Identification Concept For Lithium-ion Energy Storage Applications," in *Industrial Electronics Society, IECON 2016 – 42nd Annual Conference of the IEEE*, 2016

5. **S. Nejad**, D. T. Gladwin, and D. A. Stone, "On-Chip Implementation of Extended Kalman Filter For Adaptive Battery States Monitoring Applications," in *Industrial Electronics Society, IECON 2016 – 42nd Annual Conference of the IEEE*, 2016

Manuscripts in preparation

6. **S. Nejad**, D. T. Gladwin, and D. A. Stone, "Dual Extended Kalman Filter Initialisation Using PRBS Excitation for Adaptive Battery Parameters Identification," *IEEE Transactions on Industrial Electronics*

7. **S. Nejad**, D. T. Gladwin, and D. A. Stone, "Enhanced Battery State-of-Charge Estimation Through a Decengtralised Adaptive Extended Kalman Filter Framework," *IEEE Transactions on Industrial Electronics*

Acknowledgment

With the sincerest gratitude in my heart, I would like to thank my academic supervisor and mentor, Dan Gladwin, and my co-supervisor, Dave Stone, for their support and encouragement throughout the course of my PhD degree.

I would like to thank my family for their everlasting moral support and encouragement, without whom, this journey would have not been possible. Also, a cheering thanks to my nephews, who always fill my moments with happiness. I would also like to thank all my friends, who created a positive environment for me to complete my PhD studies in.

I wish to give my special thanks to other academic members at The University of Sheffield who have blessed me with their technical and moral support throughout my research. Also, a big thank you goes to all my colleagues in the former ME01 who have been a pleasure to work with during the past four years.

Contents

Nomenclature

AC	Alternating current
Ah	Amp-hour
AKF	Adaptive Kalman Filter
AEKF	Adaptive Extended Kalman Filter
ANN	Artificial neural network
ArtHiUFL	Artemis Highway Free Urban
AGM	Absorbent glass mat
BESS	Battery energy storage system
BES	Battery energy storage
BMS	Battery management system
C	Current rate
CC	Constant current
CCCV	Constant-current constant-voltage
CDKF	Central-difference Kalman Filter
CESS	Composite energy storage systems
DAQ	Data acquisition
DC	Direct current
DEKF	Dual Extended Kalman Filter
DVA	Differential voltage analysis
EIS	Electrochemical impedance spectroscopy
EKF	Extended Kalman Filter
EMF	Electromotive force
EOL	End-of-life
EV	Electric vehicle
e-UAV	Electric unmanned-aerial vehicles
F	Faraday's constant
HEV	Hybrid electric vehicle
HPPC	Hybrid-Pulse-Power-Characterisation
I	Current
IC	Incremental capacity
ICA	Incremental capacity analysis
ICE	Internal combustion engine

KF	Kalman Filter
LCO	Lithium cobalt oxide
LFP	Lithium-ion iron phosphate
LTO	Lithium-titanate
NaS	Sodium-sulphur
NEDC	New European Drive Cycle
NCA	Lithium nickel cobalt aluminium oxide
NiCd	Nickel cadmium
NiMH	Nickel metal-hydride
NMC	Lithium-ion nickel manganese cobalt oxide
OCV	Open-circuit voltage
PDE	Partial differential equations
PHEV	Plug-in hybrid electric vehicle
PNGV	Partnership for New Generation Vehicles
R	Gas constant
RC	Resistor-capacitor
RLS	Recursive least-squares
RLMS	Recursive least-mean-squares
RMS	Root-mean-square
RMSE	Root-mean-square error
RUL	Remaining useful life
SEI	Solid electrolyte interface
SOA	Safe operating area
SOC	State-of-Charge
SOF	State-of-Function
SOH	State-of-Health
SOP	State-of-Power
SPKF	Sigma-point Kalman Filter
SVM	Space vector machine
UKF	Unscented Kalman Filter
UPF	Unscented-particle filter
T	Temperature in Kelvin
Δt	Sampling period
U	Voltage amplitude

V	Voltage
VRLA	Valve-regulated lead-acid
W	Watt
Wh	Watt-hour
WRLS	Weighted recursive least-squares
Z	Complex impedance
$\|Z\|$	Magnitude of impedance
Z′	Real part of complex impedance
Z″	Imaginary part of complex impedance
ZEBRA	Zeolite Battery Research Africa Project

List of Figures

List of Tables

Chapter 1

Introduction

This Chapter introduces the work carried out in this thesis and explains the motivation for the conducted research. It provides the reader with an overview of the current issues and challenges facing battery energy storage systems, and how the future uptake of next-generation batteries, especially of lithium-ion chemistry, in safety-critical applications will depend on the enhancements made in the battery management system algorithms. Finally, an outline for the structure of the thesis is provided and the relevance/novelty of each chapter is stated.

1.1 Motivation

In today's technology-driven society, secondary (or rechargeable) batteries power a large number of applications, ranging from low-power (milli to tens of Watts) portable electronic devices to high-power (kilo Watts) electric/hybrid-electric vehicles (EV/HEV) and the recently-emerged super-power (mega Watts) grid-tie battery energy storage systems (BESS). A necessity to all these applications is a management system, which, in simple terms, serves as the brain of the battery, monitoring/controlling every aspect of the operation.

The battery management system (BMS) plays a significant role in ensuring a safe operating envelope, whilst maximising the battery's energy and/or power delivery

capabilities and improving its overall service lifetime. Fig. 1.1 shows a fire-damaged lithium-ion battery pack out of a Boeing 787 Dreamliner, whose failure is thought to be strongly linked to a defective BMS which led to a thermal runaway event in some of the constituent cells. From this photograph, it can be seen that a reliable BMS is of utmost importance when it comes to safety-critical battery applications, especially in avionic systems, where a battery failure of the aforementioned nature can directly put the passenger's lives at risk. This is also true for those battery-powered portable electronic devices, where the consumer's convenience and safety is the number one priority for battery system designers. Other benefits offered by a robust BMS is the prolongation of the battery's service lifetime, by operating the battery under favourable conditions and avoiding operation beyond the battery's manufacturer's recommended limits.

Fig. 1.1 Example of a failed lithium-ion battery in a Boeing 787 Dreamliner [1]

The BMS is responsible for a number of hardware and software operations that keep the battery under a safe condition at all times. At the heart of the BMS lies a battery monitoring system, which is conventionally required to perform the following tasks.

- Bus voltage and current measurement;

- String and cell voltage measurement

- Charging control;

- Over- and under-voltage safety control;

- High current protection; and

- Digital communication to/from the BMS.

Nowadays, due to the innovations in battery technologies, such as the lithium-ion batteries who can provide a superior energy and power density, the modern battery monitoring systems need to be able to carry out a number of advanced functionalities; some of which are listed below [2].

- Active/passive cell equalisation;

- Online battery parameter identification;

- Online estimation of various battery states, such as state-of-charge (SOC); state-of-health (SOH), state-of-power (SOP) and state-of-function (SOF);

- Prediction of remaining useful life (RUL);

- On-board diagnosis and prognosis.

Recognising these requirements imposed on modern battery monitoring systems, a trending desire has been set out by researchers from both worlds of academia and industry to develop advanced algorithms for the estimation of SOC, SOH, SOP and SOF in real time. In addition to meeting the technical necessities for realisation of modern BMS architectures, there is also a societal need to earn the consumer's trust on the safety aspect of new battery technologies (e.g. lithium titanate battery), in order to increase the future uptake of such energy storage devices in a wider range of safety-critical applications, e.g. in EV/HEVs [3] and all-electric commercial aircraft [4]. Therefore, this thesis aims to expand upon the current state of the art of advanced BMS algorithms, by preparing a novel body of work on adaptive battery states estimation techniques, with a view to later implement the developed algorithms on a low-cost microprocessor of the kind typically employed in BMS applications.

1.2 Thesis Contributions

This thesis offers five research chapters on online battery modelling and identification techniques which lead to the development of a low-cost microprocessor-based battery states monitoring system. The novel techniques presented in this thesis have been published in one journal and five conference proceedings, with another two journal papers in preparation. Below is a summary of the contributions offered by this thesis, together with a list of the relevant publications produced for each novel chapter.

1. **Development of a cycle-based battery SOH and RUL estimation technique as implemented on a low-cost microprocessor-based power cycler**

   It is important to have an understanding of the SOH degradation pattern in a battery in order to be able to predict its RUL, which is a defining parameter in determining the battery's end-of-service lifetime. Thus, in Chapter 3, a cycle-based SOH and RUL estimation technique is developed and implemented on a low-cost self-designed battery power cycler to verify its performance. The techniques presented in Chapter 3 are highly beneficial to those battery-powered systems which cannot afford to go offline due to failures stemming from aged cells.

2. **Experimental evaluation of most popular battery models as presented in literature with a proposal for a suitable model structure for online battery SOC and parameters estimation**

   Modern BMSs employ equivalent-circuit model representation of the battery under operation to allow for the accurate estimation of SOC, SOP, SOH and other battery parameters which are vital to proper management of the battery's power and energy delivery capabilities. Thus, in Chapter 4, the performance of a number of battery models are experimentally reviewed in terms of modelling accuracy and applicability to online SOC and SOP estimation. A resistor-capacitor (RC) network model is put forward which is

capable of producing a superior model representation of the battery, when compared to other battery model structures presented in literature. Due to its high modelling accuracy and relatively low complexity, the proposed RC model structure is highly beneficial for BMS operations on low-cost microprocessor platforms.

3. **Identification of a minimum order-number for an *RC* equivalent-circuit battery model, with a sensitivity analysis of the model output response to erroneous model parameters**

The proposed RC model structure in Chapter 4 can produce a very accurate representation of the battery device under operation. However, there exists a trade-off between desired accuracy and model complexity which needs to be identified. To this end, Chapter 5 presents a frequency-domain analysis on RC battery models of up to fifth order. It is determined that a model order of a second is the optimal choice for modelling lithium-ion batteries. Moreover, in Chapter 5, a sensitivity analysis of the candidate second-order battery model is undertaken. The results show that RC battery model is most sensitive to those resistive-element parameters, which can affect the quality of the battery state estimates. This sets the requirement for an accurate online battery identification technique to reduce the battery modelling errors.

4. **Development of a novel hybrid battery identification technique based on pseudorandom binary sequences (PRBS) to improve the performance of standard Extended Kalman Filter (EKF) for online battery SOP estimation**

Persistence of excitation is a fundamental requirement for almost all the online battery parameter identification techniques. In real battery systems, this condition might not be satisfied at all times, resulting in a non-convergent set of battery parameters and thus unreliable battery state estimates. In Chapter 6, a novel battery parameter identification technique is proposed to overcome this issue. The proposed technique is based on a deterministic initialisation of an Extended Kalman Filter (EKF) – typically employed in online BMS estimation

problems – using pseudo random binary sequences (PRBS). When applied to any battery energy storage system (BESS), the technique guarantees a convergent set of battery impedance parameters which ultimately improves the quality of online battery SOP and SOH estimation.

5. **Improvement to EKF-based battery SOC estimation for lithium-ion batteries with flat OCV curves and deployment on a low-cost microprocessor unit for online battery states monitoring**

The SOC plays a defining role in proper energy/power management of any battery system. For most battery chemistries, a pre-determined relationship between the battery's open-circuit voltage (OCV) and its SOC can be used to achieve a sufficient estimate for SOC in real time. However, for those lithium-ion batteries with a fairly flat OCV-SOC relationship curve, it becomes extremely difficult to keep a robust tracking of SOC within the flat OCV region, resulting in a divergent SOC estimate; thus, the reliability of the BMS will be undermined. To overcome this technical challenge, in Chapter 7, an adaptive EKF system identification technique is proposed to enhance the OCV-based SOC estimation of lithium-ion batteries, especially those suffering from a flat OCV-SOC curve. Finally, Chapter 7 combines together the outcomes of every chapter presented in this thesis, in order to realise an online battery states monitoring system. A microprocessor implementation of the designed battery states monitoring system is also offered, which compared to its counterparts in literature, benefits from a simple and low-cost design, without the necessity for costly FPGAs (field-programmable gate array). This is a significant step forward to realisation of a smart-cell BMS architecture for next-generation battery energy storage systems.

1.3 Thesis Organisation

This thesis is organised into several chapters, each contributing a part to the overall objective of the thesis. A list of publications corresponding to each chapter is made available in the beginning of the thesis. The chapters in this thesis are structured in

a linear format, where each chapter provides an expansion and improvement on the previous. A brief description of each chapter is provide below.

Chapter 1 introduces the thesis and discusses the motivations behind the research work conducted herein. To enable the reader to form an appreciation for the contributions of each chapter, a breakdown of the thesis structure is provided.

Chapter 2 reviews the *state-of-the-art* of battery energy storage systems as a whole, covering battery electrochemistry basics and the most commonly used battery technologies in electrical energy storage applications. The reader is also provided with a background of BMS algorithms that are responsible for carrying out advanced tasks, such as battery impedance and states estimation, while the battery system is operating online. Various battery modelling and identification techniques are discussed, with a view to later develop an adaptive battery state monitoring system, which can robustly adapt to variations in the battery's operating conditions such as temperature and ageing. Finally, the setup and procedures for experimental control and verification of the proposed battery estimation techniques in this thesis is explained in this chapter.

Chapter 3 discusses the importance of SOH estimation and being able to predict the battery's remaining-useful life (RUL) in order to avoid undesirable battery failures. A novel bidirectional microprocessor-based battery power cycler, for the purpose of cycle-based SOH characterisation. Also in this Chapter, a method for the online estimation of SOH for the lithium-ion iron phosphate (LFP) cells is proposed, which is implemented on the AVR microprocessor (μP) unit that is used in the design of the battery power cycler. In order to predict the cell's RUL, an empirical model is also developed in chapter, whose coefficients are calculated based on the first 3-4% of SOH degradation.

Chapter 4 reports on the significance of battery modelling and identification in online BMS problems. it is discussed that for online estimation and monitoring of various battery states, appropriate battery models must be employed. To this end, an experimental study on most commonly used battery models in both motive and stationary battery storage applications is undertaken in this chapter. Ten battery

model structures including, the combined model, Rint model, two different hysteresis models, Randles model, a modified Randles model, and two resistor-capacitor (*RC*) network models with and without hysteresis included are studied. The performance of each model structure is examined under various operating conditions, with respect to terminal voltage, SOC and SOP estimation accuracy, with a view to identify a suitable model structure for adoption in the work presented in this thesis.

Chapter 5 determines the minimum order-number required for an equivalent-circuit battery model to sufficiently describe the dynamic behaviour of a battery under operation, without being too complex in structure. A frequency-domain analysis on the complex impedance data gathered for two variations of lithium-ion cell chemistry is carried out. Then, a sensitivity analysis on the selected second-order model structure is carried out with respect to parameterisation error, in an effort to gain a better understanding of the impact of erroneous or static model parameters on the quality of the model-based battery state estimates such as SOC and SOP.

Chapter 6 presents a novel hybrid battery identification technique which can be applied to any BESS to adaptively identify the impedance parameters of the battery in real time. The proposed technique is based on pseudorandom binary sequences (PRBS) excitation of the battery whilst in open-circuit mode, in order to provide the aforementioned EKF estimator with a correct set of initial conditions on the battery parameters. The result is a deterministic battery identification system, a virtue that is lacking in pure EKF-based battery parameter estimators. The hybrid identification technique is capable of producing accurate battery model parameters, even under varying operating conditions.

Chapter 7 reports on a decentralised adaptive EKF framework for the enhancement of the battery SOC estimation. The proposed technique differs to the standard EKF estimator in a sense that, the SOC state filter's process and measurement noise covariance are estimated in real time, accounting for the large modelling uncertainties that are introduced into the filter's output by the largely nonlinear

function that describes the OCV-SOC relationship in the model. In addition, a dynamic technique for the online estimation of SOH is proposed in this chapter, which is more practical for motive and stationary battery applications that are operated with a transient current demand. Finally, the battery identification and state estimation techniques proposed throughout this thesis are all brought together and implemented on an ARM Cotex-M0 μP unit, to give realisation to a low-cost adaptive battery states monitoring system.

Finally, **Chapter 8** draws a number of conclusions and summarises the contributions that this thesis work has made to the *state-of-the-art* of battery management systems. The scope for the future work which can expand on this thesis is set out.

Chapter 2

Background and *State-of-the-Art* Review of Battery Management Systems

Battery devices are becoming the favourite choice for electrical energy storage and supply in a wide range of motive and stationary power applications. Without significant improvements in battery technologies and battery management systems, the future uptake of these electrochemical energy storage devices will remain a challenge. Therefore, this Chapter initially aims to provide a review of the state of the art in battery energy storage systems (BMS), comparing various battery chemistries and their applications. Thereafter, a comprehensive review of the state-of-the-art of BMS algorithms reported in literature is undertaken. This is to provide the reader with an appreciation for the contributions of this thesis. Finally, the hardware setup and procedures adopted for training and experimental verification purposes are discussed.

2.1 Battery Energy Storage

This section provides a comprehensive survey of the following aspects of battery energy storage (BES); a brief history on electrochemical cells; common definitions and terminologies used in BES systems; battery electrochemistry basics; and a literature survey of the current battery technologies, their pros and cons, and typical applications. It will be shown that, lithium-ion batteries are the right candidate for many power applications, where high energy and power densities are necessitated.

2.1.1 History

The emergent of first battery dates back to 250 BC during the Persian Empire period in Baghdad, where earthen containers have been found serving as galvanic cells. These containers consisted of cells formed of iron and copper electrodes, flooded with an organic acidic solution. Each cell was capable of supplying a current of 250 mA at a voltage of 250 mV for about 200 hours. The primary use of these primitive electrochemical cells was to gild silver.

Luigi Galvani and Alessandro Volta are two physicists of Italian decent, whose names are closely associated with the development of batteries and the related science of electrochemistry. In 1791, Galvani performed an experiment on dead frogs suspended from an iron hook. In that experiment, Galvani realised that the frog's legs contracted when struck by different metal materials such as copper. Volta attributed these muscle contractions of the dead frog's legs to the electric current flowing between the two metals connected in series.

To prove his point, in 1800, Volta built and patented a voltaic 'pile' or the first battery in modern times. This structure consisted of alternating plates of silver and zinc interleaved with brine-soaked papers. As a result, Volta discovered the law of electrochemical series, which states that the electromotive force (EMF) of a galvanic cell consisting of a pair of metal electrodes separated by an electrolyte is the difference between the two electrodes' potentials. Later on, in 1834, Michael Faraday derived the laws of electrochemistry based on Volta's findings, which established a connection between the chemical and electrical forms of energy.

On the basis of Volta's work, other scientists also developed electrochemical batteries of various designs. However, a recurring issue associated with all of these batteries was gas formation at the electrodes. The released gas was part of an irreversible reaction, whose energy could not be recovered, thus, limiting the battery's available capacity. In 1866, a French scientist named Leclanché found the most successful solution to this problem. He invented and patented the Leclanché cell [5], [6] in which he used an electrolyte solution of ammonium chloride, a positive electrode of manganese dioxide mixed with carbon for better conductivity,

and a negative electrode of zinc. This cell structure revolved around a graphite plate serving as a current collector. The Leclanché achieved an EMF of 1.4V per cell, which saw extensive usage in telegraphy, signalling, electric bells and similar applications of intermittent current demands. On the basis of the Leclanché cell's electrochemistry, the modern primary zinc-carbon or zinc-manganese dioxide ($ZnMnO_2$) batteries emerged, which still dominate the worldwide market of non-rechargeable batteries [5].

Later in the 19th century, Gaston Planté constructed batteries as a sandwich of thin lead layers, separated by sheets of coarse cloth in a cylindrical container filled with diluted sulphuric acid [5], [6]. The thin layers were connected as two separate electrodes with a voltage difference applied between them, which charged the cell. By alternating this charge process with a subsequent discharge step, Planté eventually managed to form a positive electrode that consisted of lead-dioxide and a negative of finely distributed lead.

In order to prevent the breakdown of the lead plates, Planté later used thicker plates. This resulted in heavier and bulkier batteries, which were used mainly for stationary BES applications. Nowadays, the so-called lead-acid batteries are still widely used in many applications, including automotive and grid-tie energy storage. To solve for the sulphate accumulation problem in traditional lead-acid batteries, advanced lead-carbon batteries have been recently developed [7]–[9].

Waldemar Jungner in Sweden and Thomas Edison in the USA formed the foundations of the nickel cadmium (NiCd) and nickel iron alkaline storage battery industry between 1895 and 1905 [5]. The NiCd batteries are still used today in applications where high power density is favoured to high energy density. In late 1980's, while the existing battery chemistries were continuously being improved, new technologies also kept appearing. The commercial uptake of nickel-metal hydride (NiMH) in 1990 and lithium-ion batteries in 1991 revolutionised the portable consumer products by allowing for smaller and yet higher energy density solutions.

Apart from the continuous need for higher energy and power densities for portable BES applications, such as in electric vehicles (EV) and hybrid electric vehicles (HEV), environmental concerns regarding hazardous materials such as cadmium has led to a boost in the development and manufacturing of NiMH and lithium-ion batteries. In the next section, some of the most commonly used terminologies in BES industry are discussed.

2.1.2 Battery Terminologies

Various terminologies are used in literature to describe different characteristics of BES systems. Those terms relevant to this thesis are provided in this section, which will later help derive and develop useful equations for testing and validation of the proposed battery monitoring algorithms.

2.1.2.1 Cell, Module and Pack

The term battery is often associated with one or more secondary cell(s) connected in a series and/or parallel configuration in order to provide the desired voltage and ampere-hour rating. A 'string' usually consists of a number of series or parallel connected cells. A 'string' of cells connected physically and electrically together is called a 'module', whereas a number of modules connected electrically and operated as single unit, is called a 'battery pack'.

2.1.2.2 Capacity

Battery capacity can be defined using two terms. Ampere-hour (Ah) capacity is the total amount of releasable charge stored in a battery under some predefined conditions. It is not unusual to use Watt-hour (Wh) instead of Ah to define a battery's capacity. The rated Wh capacity is mathematically defined as,

$$\text{Rated Wh Capacity} = \text{Rated Ah Capacity} \times \text{Rated Nominal Voltage.} \quad (2.1)$$

2.1.2.3 C-rate

C-rate is an arbitrary metric used to define the current rate, at which the battery will take approximately one hour to fully discharge under standard conditions. For example, a rated 3.3 Ah cell will take a current of 3.3 A to fully discharge in one hour.

2.1.2.4 Specific Energy and Power

Also known as the gravimetric energy density, specific energy is used to quantify the amount of energy a battery can store per unit mass. It is expressed in Wh/kg as,

$$\text{Specific Energy} = \text{Rated Wh Capacity} / \text{Battery Mass.} \qquad (2.2)$$

Similarly, specific power represents the battery's peak-power per unit mass, expressed in W/kg as,

$$\text{Specific Power} = \text{Rated Peak Power} / \text{Battery Mass.} \qquad (2.3)$$

2.1.2.5 Energy and Power Density

Also referred to as volumetric energy density, energy density is the nominal battery energy stored in a given space per unit volume. This is expressed in Wh/l as,

$$\text{Energy Density} = \text{Rated Wh Capacity} / \text{Battery Volume.} \qquad (2.4)$$

Specific power is the term given to the peak-power per unit volume of a battery, expressed in W/l as,

$$\text{Power Density} = \text{Rated Peak Power} / \text{Battery Volume.} \qquad (2.5)$$

2.1.2.6 Safe Operating Envelope

The battery's operation is usually constrained to a range of voltage, current and temperature limits. These limits are provided by the battery manufacturer and must not be violated at any time.

2.1.2.7 State-of-Charge (SOC)

SOC is defined as the remaining quantity of releasable charge in a battery with respect to the maximum available capacity. SOC is influenced by C-rate, temperature and the age of the battery.

2.1.2.8 State-of-Health (SOH)

There are two distinct definitions for SOH in literature relating it to either a power or energy fade. The source/sink power capability of a battery largely depends on its internal resistance. As the resistance grows with ageing, the battery's instantaneous available power fades away. Moreover, as the battery ages, it loses some of its ampere-hour capacity, leading to an energy fade.

2.1.2.9 State-of-Power (SOP)

SOP is a measure of the amount of electrical power that a battery can deliver under specified operating conditions. Factors such as, instantaneous current demand, operating temperature, SOC, and SOH directly affect the maximum power capability of a battery.

2.1.2.10 State-of-Function (SOF)

Various definitions of SOF have been reported in literature, which all relate to the battery's power capabilities. In other words, SOF is a digital yes/no parameter indicating whether the battery is capable of sourcing/sinking the applied power to carry out a particular function.

2.1.3 Electrochemistry Basics

In simple words, a battery is a device capable of storing electrical energy in the form of chemical energy and converting it back to electrical energy when needed. The smallest constituent component of a battery is called the cell. As illustrated in Fig. 2.1, a cell consists of a negative electrode (anode) and a positive electrode (cathode) both immersed in an ion-conducting medium called the electrolyte. The chemical energy is stored in the electroactive species of the two electrodes inside the cell.
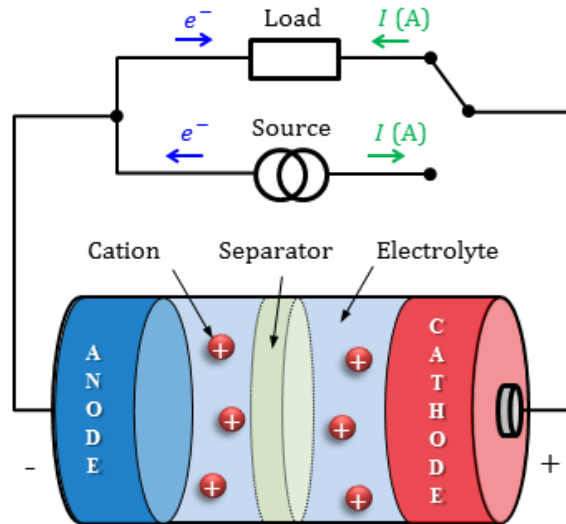
Fig. 2.1 Representation of the internal structure of an electrochemical cell

2.1.3.1 *Electrochemical reactions*

The energy conversion or the charging and discharging of a cell is realised through a cyclic reduction-oxidation (redox) or charge-transfer reactions [10]–[12]. These reactions involve the exchange of electrons between the active species inside the electrodes through an external circuit to the battery. These reactions occur at the boundary region between the electrodes' surfaces and the electrolyte. During the charge process, the cathode active material is oxidised releasing electrons to the external circuit, whilst the anode active material is reduced extracting electrons away from the external circuit. The transfer of the positively charged ions (cations) from the cathode to the anode through the selective membrane of a separator (i.e. no electron flow through the electrolyte) permits the chemical storage of electrical energy. Under a discharge regime, the aforementioned reactions are reversed.

2.1.3.2 *Nernst's equation*

The energy released from the movement of ions in an electrochemical system, gives rise to a potential difference. The battery is said to be in a state of equilibrium when no external load is connected at its terminals and the reaction rates of the interaction of the positive and the negative electrode and the electrolyte are the same. The Nernst's equation defines the relationship between the chemical energy released in a battery and its electric potential. The equilibrium potential (E_{eq}) of

each electrode can be obtained using the Nernst's equation [10]–[12] expressed for the positive and negative electrodes in equations (2.6) and (2.7), respectively.

$$E_+^{eq} = E_+^o + \frac{RT}{nF} \ln \frac{(a_+^{ox})^B}{(a_+^{red})^A} \qquad (2.6)$$

$$E_-^{eq} = E_-^o + \frac{RT}{nF} \ln \frac{(a_-^{ox})^C}{(a_-^{red})^D} \qquad (2.7)$$

where E_i^o is the standard redox potential of electrode i in volts, $R = 8.314\ \text{J/mol. K}$ is the gas constant, T is the temperature in degrees Kelvin, n denotes the number of electrons involved in the charge-transfer reactions, $F = 96485\ \text{C/mol}$ is the Faraday's constant and a_i relates to the activity of species of electrode i.

The activity a_i has a linear relationship with its concentration, c_i in mol/m^3, and its molar amount, m_i, which can be given as,

$$a_i = \gamma . c_i = \frac{\gamma m_i}{V_i}. \qquad (2.8)$$

In equation (2.8), γ is the dimensionless activity coefficient, often assumed to be unity and V_i is the volume in which the species of electrode i resides. Considering equations (2.6)–(2.8), the final equilibrium potential of the complete cell can be obtained and given as,

$$E_{cell}^{eq} = E_+^{eq} - E_-^{eq} = E_+^o - E_-^o + \frac{RT}{nF} \ln \left[\frac{(a_+^{ox})^B (a_-^{red})^D}{(a_+^{red})^A (a_-^{ox})^C} \right] \qquad (2.9)$$

where E_{cell}^{eq} may also refers to the cell's electromotive force (EMF). According to (2.9), the value of the cells EMF is dependent on the ratio of the activities of the oxidised and reduced species in the positive and negative electrodes.

2.1.3.3 Gibbs free energy

In a thermodynamic system, the Gibbs free energy provides a measure of the quantity of useful or reversible work that the system could provide at a constant temperature and pressure. In an electrochemical cell, the change in Gibbs free energy, denoted as ΔG^{o}, can be used to determine the thermodynamic potential that allows for an electric current to be delivered/accepted by the cell under a discharge/charge process. This parameter in joules per mole (J/mol) is usually expressed as [10], [12]

$$\Delta G^{\mathrm{o}} = -nF(E_{+}^{\mathrm{o}} - E_{-}^{\mathrm{o}}) = -nFE_{\mathrm{cell}}^{\mathrm{o}}. \tag{2.10}$$

where $E_{\mathrm{cell}}^{\mathrm{o}}$ is the cell's standard electrochemical potential. Conventionally, a positive $E_{\mathrm{cell}}^{\mathrm{o}}$ implies a spontaneous (i.e. galvanic) process and a negative $E_{\mathrm{cell}}^{\mathrm{o}}$ means that the process is nonspontaneous (i.e. electrolytic). Depending on the applied convention, equation (2.10) may also be found in the form of $\Delta G^{\mathrm{o}} = +nFE_{\mathrm{cell}}^{\mathrm{o}}$. The reason behind the conflicting use of signs in literature is that ΔG^{o} depends on whether the reaction is an oxidation or a reduction [12].

2.1.3.4 Electrode overpotential

An oxidation reaction results in a current, I^{ox}, which corresponds to a flow of electrons out of an electrode and conversely a reduction reaction results in a current, I^{red}, which corresponds to an electron flow into an electrode. In an equilibrium state, these two currents are of the same magnitude, but in opposite direction, resulting in a zero net current flow. However, in a non-equilibrium state, the magnitude of one current becomes larger than the other. Thus, the cell's actual terminal voltage will no longer be equal to $E_{\mathrm{cell}}^{\mathrm{eq}}$ in equation (2.9), giving rise to a charge-transfer overpotential [5], [11], [12].

The charge-transfer overpotential (η^{ct}) is caused by the polarisation effect, which occurs at the boundary region between the electrode and electrolyte interface during operation. This parameter is derived as the difference between the actual cell potential $E_{\mathrm{cell}}^{\mathrm{act}}$ and that at equilibrium $E_{\mathrm{cell}}^{\mathrm{eq}}$ as [5],

$$\eta^{\text{ct}} = E^{\text{act}}_{\text{cell}} - E^{\text{eq}}_{\text{cell}} \tag{2.11}$$

The overpotential η^{ct} is comprised of two parts; a kinetic overpotential (η^{k}) and a mass-transport phenomenon that results in a diffusion overpotential (η^{d}). In order to describe the relationship between these overpotential components and the applied current, the Butler-Volmer equation [5] is employed.

$$\left.\begin{aligned} \eta^{ct} &= \eta^{\text{k}} + \eta^{\text{d}} \\ \eta^{\text{k}} &= \frac{RT}{\alpha nF}\ln(I) - \frac{RT}{\alpha nF}\ln(I^{\text{o}}) \\ \eta^{\text{d}} &= \frac{RT}{nF}\ln\left(\frac{c^{\delta}}{c^{b}}\right) \end{aligned}\right\} \tag{2.12}$$

where $I = I^{\text{ox}} - I^{\text{red}}$ is the net reaction current, I^{o} is the exchange current for the charge-transfer reaction between the electrodes, and α is a dimensionless transfer coefficient between 0 and 1. A coefficient of $\alpha = 0.5$ implies that the electrode has a symmetrical charge-transfer characteristic for both charge and discharge processes, which is not true for most electrochemical cells.

As the magnitude of η^{ct} increases, the value of I in (2.11) will be dominated by either I^{ox} or I^{red}. In this case, the charge-transfer current will be limited by the dominating electrode. Therefore, by assuming a dominant current direction (i.e. $I = I^{\text{ox}}$ or $I = I^{\text{red}}$), the Tafel relation as described in [13] can be used to simplify the Butler-Volmer equation given in (2.25) as,

$$\eta = \frac{RT}{\alpha nF}\ln\left(\frac{I}{I_0}\right). \tag{2.13}$$

Although simple, equation (2.13) assumes that the values of α and I_0 are constant throughout operation, which results in large modelling errors. Moreover, an electrochemical cell under a dynamic operation may experience other overpotential phenomena, which will require a more detailed analysis to understand.

2.1.4 Battery Technologies and Applications

The environmental concerns over the emissions of greenhouse gases, together with the volatile and ever-increasing prices of fossil fuels have led to the large-scale adoption of battery devices in the transport and utility sectors. These motives, together with the recent advances in electrochemistry science and manufacturing techniques have resulted in numerous battery technologies, each having their own specific performance capabilities. In this section, a performance review of the current battery technologies used in BES systems and their applications is provided.

2.1.4.1 Lead-acid batteries

Table 2.1 General performance profile for lead-based batteries [5], [14]

Specification	VRLA
Nominal cell voltage:	Nominal: 2.1 V
Specific Power:	75–300 W.kg^{-1}
Specific Energy:	30–50 Wh.kg^{-1}
Energy Density:	50–80 Wh.l^{-1}
Peak currents:	Charge: 1C
	Discharge: 8C
Operating temperatures:	Charge: -40–50°C
	Discharge: -40–60°C
Abuse tolerance:	High
Self-discharge per day:	0.1–0.3%
Cycle life (to 80% capacity):	500–1000

The most common types of valve-regulated lead-acid (VRLA) batteries are gel and absorbent glass mat (AGM). In gel batteries, the electrolyte is turned from liquid to a paste-like solid using a silica-based gel. On the other hand, the AGM batteries are constructed by replacing the ceramic or plastic stud that separates the cells in a stack with a glass fibre mat, which is soaked in the electrolyte. Due to the absorbent properties of the mat glass separator, water loss is significantly reduced, eliminating the need for periodic refiling of AGM batteries. Table 2.1 provides a summary of the performance capabilities for AGM and gel VRLA batteries [14].

The more recently developed lead-carbon VRLA batteries [15] offer several advantages over the conventional lead-acid batteries. Essentially, by adding a carbon plate to the negative electrode, the battery is converted into a quasi-asymmetric supercapacitor. As a result, these batteries can provide a higher energy density than AGM and gel batteries, combined with a high specific power capability, which has been a challenge for a long time [16].

Although larger and heavier than other portable battery technologies, VRLA batteries are low-cost and have a high tolerance for abuse, in terms of capability to operate at high currents and/or low temperatures for short time intervals. These properties make them an ideal candidate for those large-scale energy storage applications where weight and plant size are not restricted. Other applications of VRLA batteries include back-up power supplies in hospitals, airports and telecom towers. Owing to their significantly enhanced cycle life and dynamic charge acceptance, the lead-carbon VRLA batteries have become an enabling technology for the new micro-hybrid start-stop technology in modern ICE vehicles [17].

2.1.4.2 Nickel-based batteries

Table 2.2 Comparison of different nickel-based battery technologies [5], [18]

Specification	NiCd	NiMH
Nominal cell voltage:	1.2 V	1.2 V
Specific Power:	150–300 W.kg^{-1}	250–1,000 W.kg^{-1}
Specific Energy:	40–60 Wh.kg^{-1}	50–80 Wh.kg^{-1}
Energy Density:	50–150 Wh.l^{-1}	190–230 Wh.l^{-1}
Peak currents:	Charge: 4C	Charge: 4C
	Discharge: <10C	Discharge: <10C
Operating temperatures:	Charge: 0–40°C	Charge: 0–40°C
	Discharge: -20–70°C	Discharge: -20–65°C
Abuse tolerance:	Moderate	Low
Self-discharge per day:	0.2–0.6%	0.6–1%
Cycle life (to 80% capacity):	500–1,000	1,000+

The emergence of modern sealed nickel-cadmium (NiCd) batteries in the late 40's entailed several advantages for portable energy storage applications. These batteries consisted of a cadmium negative electrode and a nickel oxide-hydroxide positive electrode, submerged in an alkaline electrolyte [19]. NiCd batteries offered an excellent low-temperature performance, which made them a key player in the early days of aircraft system electrification [19]. Nowadays, NiCd batteries are used for applications where performance reliability under harsh conditions is a necessity. However, due to environmental concerns over cadmium and the appearance of new technologies, a decline in the future uptake of NiCd batteries is inevitable.

The nickel metal-hydride (NiMH) battery is similar in structure to the NiCd battery, except for the replacement of the negative electrode with a metal hydride alloy [20]. With their emergence, the NiMH batteries provided an attractive and practical solution for the electric powertrain of early EV and plug-in HEV (PHEV) designs (e.g. Toyota Prius). However, due to several drawbacks such as low specific energies and high self-discharge rates, NiMH batteries will no longer serve in next-generation EV/HEVs. Table 2.2 presents the performance profile of NiCd and NiMH batteries for comparison.

2.1.4.3 Sodium-based or thermal batteries

Table 2.3 Comparison of different sodium-based battery technologies [18], [21]

Specification	NaS	ZEBRA
Nominal cell voltage:	2.1 V	2.58 V
Specific Power:	150–230 W.kg^{-1}	150–200 W.kg^{-1}
Specific Energy:	150–240 Wh.kg^{-1}	100–120 Wh.kg^{-1}
Energy Density:	150–250 Wh.l^{-1}	150–180 Wh.l^{-1}
Peak currents:	Charge: <1C	Charge: <1C
	Discharge: <1C	Discharge: <1C
Operating temperatures:	300°C~350°C	245°C~350°C
Abuse tolerance:	Moderate	Moderate
Self-discharge per day:	~20%	~15%
Cycle life (to 80% capacity):	2,500	2,500+

Sodium-based batteries are high temperature battery technologies that use molten salts as the electrolyte, which remains solid and inactive at ambient temperatures. However, when exposed to high temperatures of 300–350°C, an ionic and thus electrical conductivity occurs, sourcing electrical energy to an external circuit [21]. There are two main classes of sodium-based batteries. In the early 80's, the sodium-sulphur (NaS) battery emerged as a solution for many large-scale on/off-grid energy storage applications.

Later on, the sodium-nickel-chloride battery was developed by the Zeolite Battery Research Africa Project (ZEBRA) to replace NaS batteries [22]. The solid-state nature of the materials used in the positive electrode makes ZEBRA batteries less prone to corrosion effects [21]. Moreover, the lower operating temperatures required for ZEBRA batteries means that they are safer and more cost-effective than NaS batteries. These improvements make ZEBRA batteries a more practical solution for large-scale grid energy storage problems [23]. Other applications of ZEBRA batteries include traction of heavy EV/HEVs (e.g. Iveco EcoDaily all-electric vans) and railway systems. Table 2.3 provides a summary of the performance capabilities for the aforementioned sodium-based rechargeable battery technologies.

2.1.4.4   *Flow batteries*

In a flow battery, the electrolyte that contains the dissolved electroactive materials flows through an electrochemical cell, where the conversion of chemical energy into electrical energy takes place. Generally, the electrolyte is stored in tanks and is pumped through the cell(s) of the main reactor unit [16]. Flow batteries benefit from a faster charging time that is achieved by quick refilling of the electrolyte liquid in the storage tanks [16].

There are two main types of flow batteries. The redox flow battery is a reversible fuel cell with active species dissolved in the electrolyte [24]. In flow batteries, energy is mostly related to the volume of the electrolyte or the tank size [25] and power is related to the electrode area or the reactor area [26]. In contrast to redox flow batteries, hybrid flow batteries are developed by depositing one or more

electroactive materials as a solid layer in the cell, decoupling the battery's energy from its power capability.

Examples of flow batteries include redox flow batteries and zinc-bromine hybrid flow batteries [27]. Flow batteries have the advantages of flexible/modular layout, due to separation of power (i.e. reactor) and energy (i.e. electrolyte tanks) components. Moreover, these batteries benefit from a faster response time and a longer cycle life, as there are no solid-solid phase changes. On the negative side, flow batteries require complicated instrumentation for control and thermal management of the reactor. Also, the energy densities provided by flow batteries is rather low compared to other technologies such as lithium-ion [21].

2.1.4.5 Lithium-ion batteries

Over the past decade, lithium-ion batteries have achieved significant penetration into various markets, where high specific energy and power densities are desirable [28]. There are several types of lithium-ion batteries in commercial use, such as, lithium cobalt oxide (LCO), lithium-ion iron phosphate (LFP), lithium-ion nickel manganese cobalt oxide (NMC), lithium nickel cobalt aluminium oxide (NCA) and lithium-titanate (LTO). Table 2.4 provides a summary of the performance capabilities for the mentioned lithium-ion battery technologies.

Whilst LCO batteries dominate the portable consumer electronics market, LFP and NMC batteries are gaining popularity amongst EV/HEV designers. Fig. 2.2 depicts an EV example incorporating a 20 kWh LFP battery pack. Other applications of LFP and NMC batteries include electric unmanned-aerial vehicles (e-UAV) and the recently emerging smart grid technology [29]. In contradiction to LFP and NMC batteries, NCA batteries have a less favourable performance, especially at low temperatures where the power and energy capabilities are reported to be considerably lower [30].

Due to their more stable lithium-titanate anode structures, LTO batteries are the safest type of lithium-ion batteries available in the market, which can achieve faster charge times and higher discharge currents. As a result, LTO batteries are now being

considered for large-scale grid-tie energy storage applications, such as, load balancing, peak shaving and improving the frequency response of the grid [31].
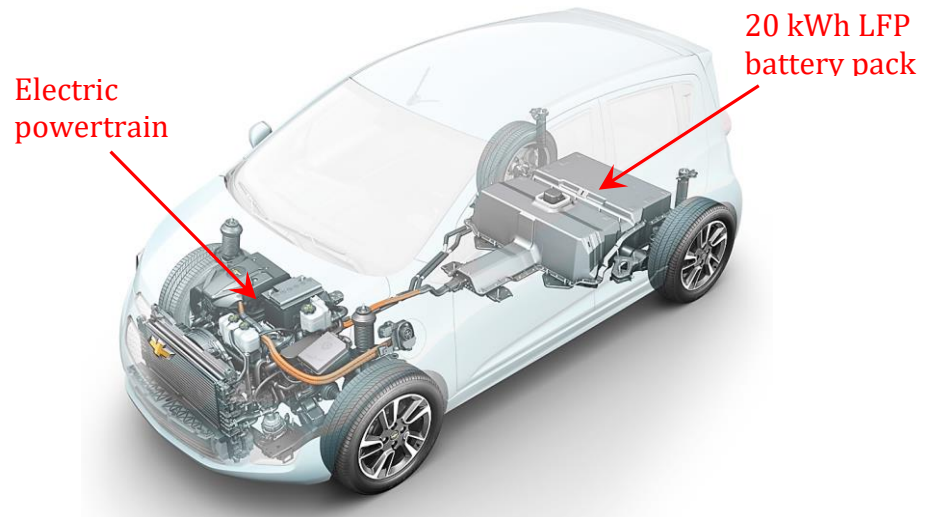
Fig. 2.2 Photo of an EV design (courtesy of Chevrolet) and its LFP battery pack

The high levels of ongoing academic and industrial research on lithium-ion batteries, together with the advancements in manufacturing techniques are setting the tone for an increasing trend in large-scale adoption of lithium-based batteries. Therefore, this particular chemistry is chosen as the subject of study in this thesis, with a view to later develop an online state monitoring system for the commercially available NMC and LFP cells. It is worth noting that the algorithms developed in this thesis are also applicable to other battery chemistries, given knowledge of certain battery model parameters are available at initialisation step.

Table 2.4 Comparison of different lithium-ion battery technologies [2], [5], [32]

Specification	LCO/NCA	LFP	NMC	LMO	LTO
Nominal cell voltage:	3.6–3.7 V	3.2 V	3.65 V	3.7–3.8 V	2.3 V
Specific Power:	1,500 W.kg^{-1}	150–500 W.kg^{-1}	300–1,500 W.kg^{-1}	700–1300 W.kg^{-1}	3,000–5,100 W.kg^{-1}
Specific Energy:	90–200 Wh.kg^{-1}	100–140 Wh.kg^{-1}	100–240 Wh.kg^{-1}	90–120 Wh.kg^{-1}	70 Wh.kg^{-1}
Energy Density:	400–640 Wh.l^{-1}	125–250 Wh.l^{-1}	250–640 Wh.l^{-1}	245–430 Wh.l^{-1}	170 Wh.l^{-1}
Peak currents:	Charge: < 1C	Charge: 1C	Charge: 1C	Charge: 1C	Charge: 5C
	Discharge: 3C	Discharge: > 10C	Discharge: > 3C	Discharge: < 10C	Discharge: < 10C
Operating temperatures:	Charge: 0–45°C	Charge: 0–45°C	Charge: 0–45°C	Charge: 0–45°C	Charge: -20–45°C
	Discharge: -20–60°C	Discharge: -30–60°C	Discharge: -20–60°C	Discharge: -40–65°C	Discharge: -30–60°C
Abuse tolerance:	Low	Low	Very low	Low	Moderate
Self-discharge per day:	0.1–0.3%	< 0.1%	< 0.2%	< 0.2%	0.1–0.4%
Cycle life (to 80% capacity):	< 1,000	1,500+	1,000+	< 1,000	10,000+

2.2 Battery Management System

In most real-world applications, a single cell will not be able to generate enough power to complete a given task. Therefore, battery packs, consisting of many cells connected in series and/or parallel formations are designed to achieve specified power and energy outputs. In order to keep the cells within their recommended operating envelope, battery management systems (BMS) are usually integrated into the pack design, serving as the "brain" of the battery system. As a result, at first, this section aims to provide an overview of modern BMS architectures and some of the typical tasks performed. Thereafter, the focus is brought to the *state-of-the-art* of advanced battery monitoring algorithms and online battery modelling and identification techniques, which is the main topic of study in this thesis.

2.2.1 Overview
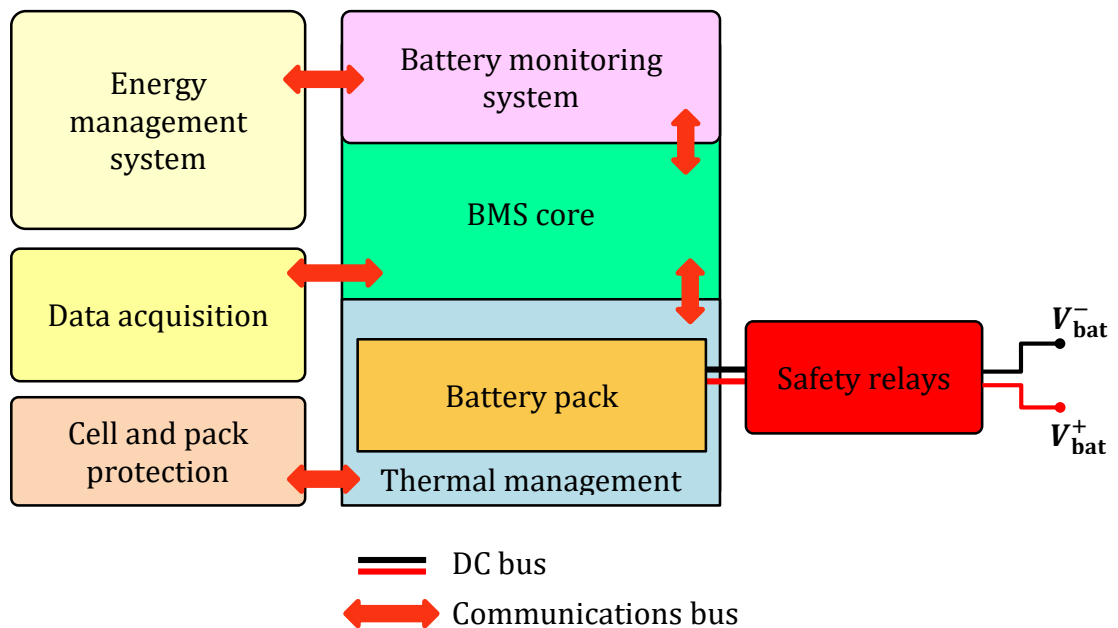
Fig. 2.3 General structure of a typical BMS

Most battery technologies require a BMS to not only ensure a safe operation, but also to help the battery perform at its highest energy and power capabilities, without violating the recommended operating limits. To achieve this goal, the BMS takes on

a variety of responsibility, which are visualised in Fig. 2.3. The most important tasks performed by a BMS include the following:

- Data acquisition;
- Cell protection;
- Cell balancing;
- Thermal management;
- Energy management;
- Battery state monitoring.

2.2.1.1 Data acquisition

In BMS, data acquisition (DAQ) includes the measurement and conditioning (e.g. low-pass filtering) of some of the most relevant battery data, which are then fed into other decision-making BMS units. The most relevant measurements are the voltages taken from every cell in a battery pack, the current that flows in parallel modules in a pack and temperatures of each cell or at least some thermally-critical points in the pack. The voltage and current measurements must be taken at proper sampling frequencies in order to be able to capture the important transient effects.

Whilst voltage measurement accuracies of less than 3 mV are achievable using low-cost sensors, the accurate acquisition of the battery/cell current in large-scale BES applications with over 20,000 cells is a more challenging task. In such applications, battery/cell current is usually measured using a shunt resistor or a hall sensor. Whereas shunt resistors suffer from temperature-induced drifts, hall sensors are prone to offset-induced errors, requiring a regular re-calibration. Therefore, in literature, the attentions have been brought to more advanced model-based battery conditioning techniques [33] that can adaptively account for the voltage and current sensor-induced errors. Moreover, through appropriate modelling of the BESS, it is possible to reduce the total number of temperature sensors required, without compromising the performance of the BMS as a whole [34].

2.2.1.2 Cell protection

The cell protection block involves both analogue and digital supervisory circuits that are responsible for ensuring that the cell will never violate the specified limits of a safe operating area (SOA) at any time. These limits include the lower and upper voltage thresholds, maximum discharge/charge current levels and the minimum and maximum operating temperatures that are allowable for a safe operation. For example, in conventional BMSs, the battery charging power is reduced to a minimum at low temperatures in order to prevent lithium plating in the cells and thus permanent damage to the battery. In more recent works (e.g. [35]–[37]), researchers have developed various battery protection techniques, using transistor switches to disconnect the current path to the faulted cells in a module. However, due to on-state conduction losses in semiconductor devices and the difficulty in predicting their behaviour under fault conditions, this method of protection may not be practicable large-scale safety-critical applications.

2.2.1.3 Cell balancing
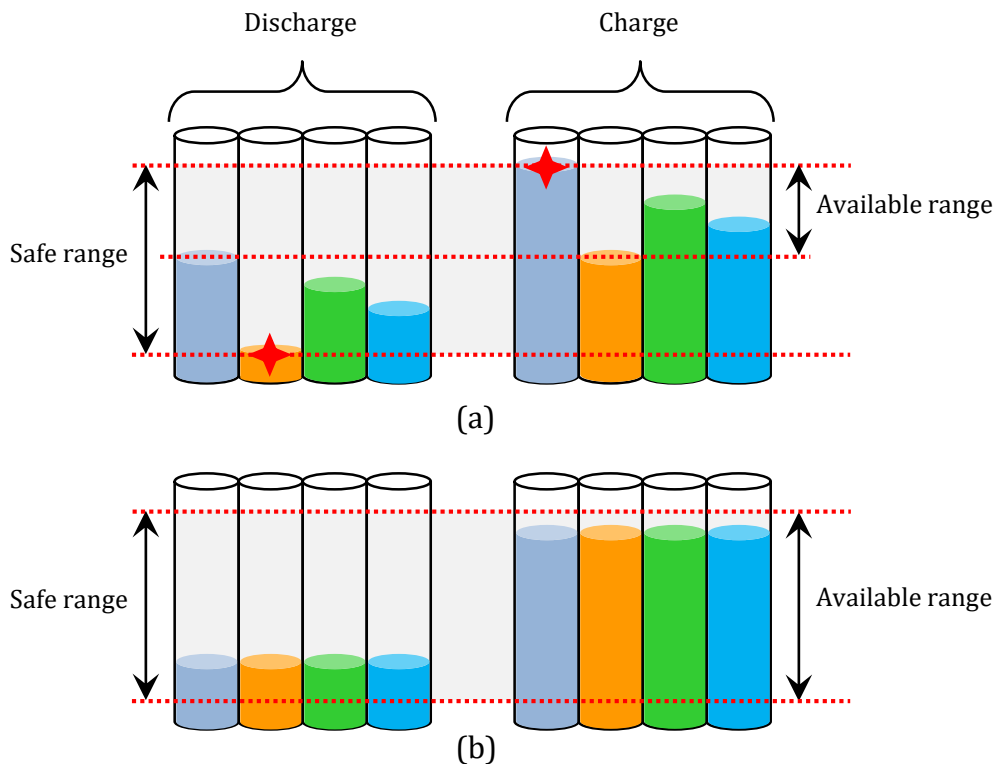
Fig. 2.4 Operational limitations of series-connected cells with (a) no balancing and (b) proper balancing

51

Cell balancing, also known as charge equalisation, is an important operational facet of any modern BMS. An illustration of this concept is presented in Fig. 2.4. Over the lifetime of a battery pack, the voltages and capacities of the series-connected cells may vary at different rates, which can significantly limit the overall performance of the battery pack. Therefore, by charge-balancing the cells in modules, it is possible to improve the energy and power delivery of the battery.

In literature, cell balancing methods are generally classified into two main categories of passive and active. Passive methods (e.g. [38], [39]) use electrical components such as resistors in order to limit the voltages of those cells that have higher capacities by losing the excess energy as heat. Although simple, passive methods suffer from large inefficiencies, making them a rather unattractive approach for large-scale BES applications. On the other hand, active methods (e.g. [40]–[42]) can achieve far better energy efficiencies by transferring the energy from those cells with higher capacities to the ones with reduced capacities. As depicted in Fig. 2.5, this is usually achieved by using DC-DC converter designs such as forward, full-bridge and buck-boost topologies. As a result, active methods require complex control algorithms with additional electronic interfaces, which can be costly.
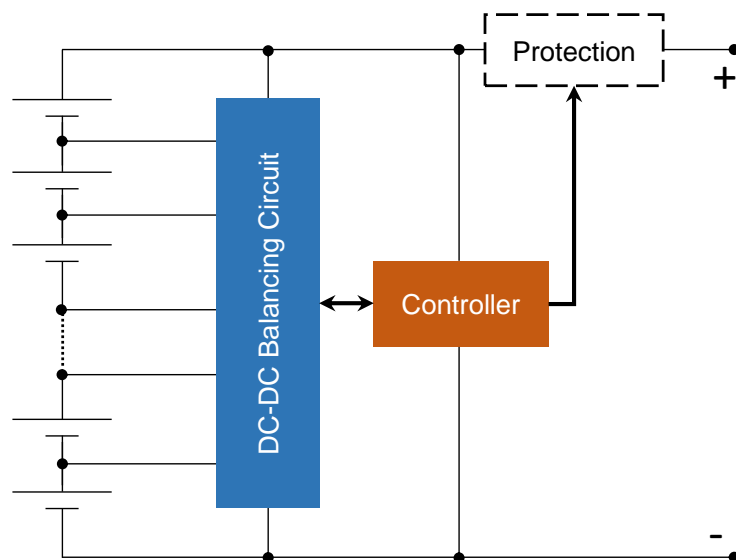
Fig. 2.5 Block schematic of typical active cell balancing in a pack

2.2.1.4 Thermal management
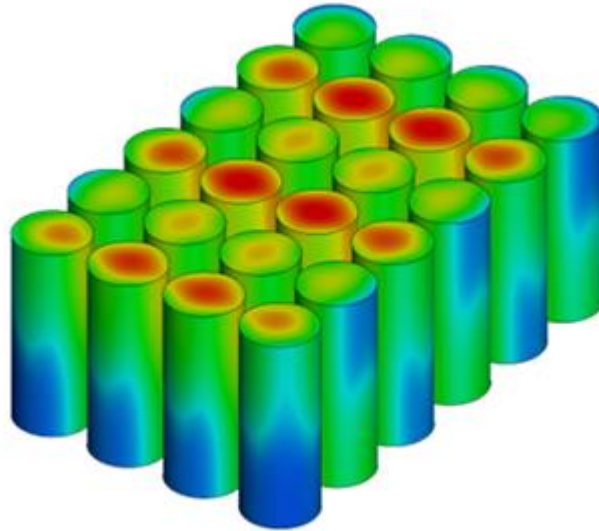
Fig. 2.6 An illustration of uneven thermal distribution over adjacent cylindrical cells in a module

Effective thermal management is a necessity for the optimal operation and lifetime extension of high-performance battery packs [43]. Moreover, as shown in Fig. 2.6, uneven thermal distribution in the battery pack can further exacerbate the charge balance in the incorporated cells, reducing the battery's performance capabilities. Therefore, depending on cell geometries and application conditions, the battery pack is often equipped with either an active or passive thermal management system.

The active systems are usually realised by using fans or pumps to circulate a coolant around the modules, extracting the heat from the battery pack. Typical coolants are air [44]–[46], liquid [47] or carbon dioxide [48]. In contrast, passive cooling systems exploit the physical properties of different coolants implanted between adjacent cells in a pack to absorb the heat generated during operation. These coolants are usually composed of phase-change materials (PCM) [49]–[51] with excellent heat absorption capabilities. Other methods include a recently developed thermoelectric cooler based on the Peltier effect [52] and a flexible hydrogen-based thermal management system [53].

2.2.1.5 Energy management
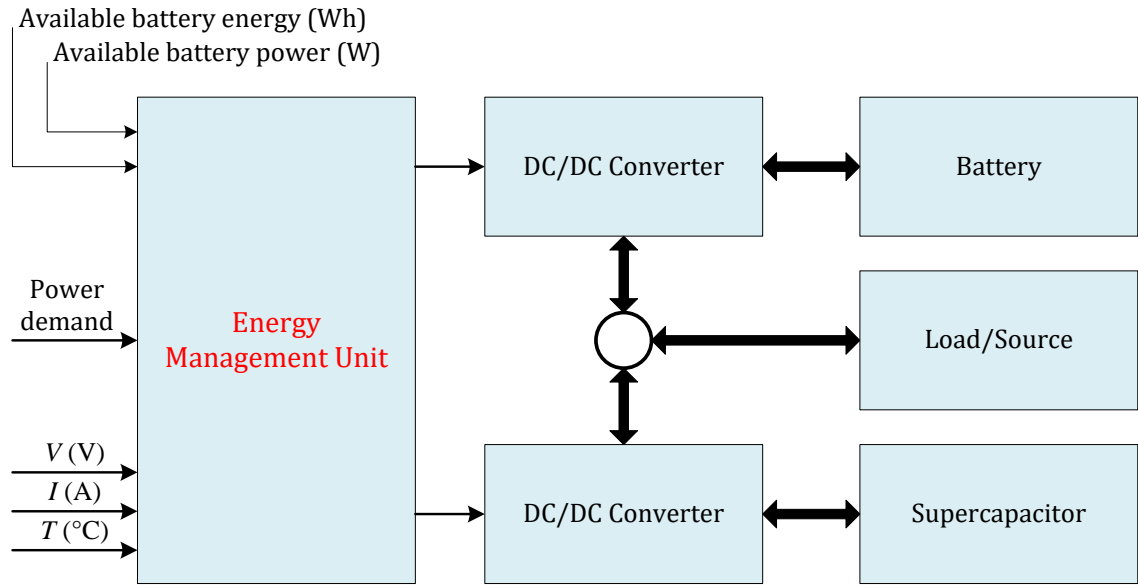
Fig. 2.7 General operation of energy management unit for CESSs

Irrespective of the constituent chemistry, a battery is considered a high energy density device. In most practical applications such as in EV/HEVs or grid-tie utility storage, in order to be able to respond quickly to fast-transient power demands, composite energy storage systems (CESS) are adopted [54]–[56]. These systems are usually comprised of high energy density batteries for long-time energy demands, and high power density ultra/super capacitors for short-time transient power requirements. Fig. 2.7 outlines the operation of a typical battery-supercapacitor CESS. This system, as well as any other CESS, requires a proper energy management system that can take care of charge balancing between multiple battery banks and other energy storage devices.

There are many energy and/or power management strategies for battery batteries [57]–[60]. Most of these strategies are based on the current and possibly future predictions of the battery states (e.g. SOC, SOP and SOH) provided by the battery monitoring system, to calculate the difference between the demanded and available sink/source power. Subsequently, if the power demand exceeds the battery's ratings at a given time, the energy management system will act immediately to limit the battery power output through the converter unit. This operation is a necessity

for the optimal utilisation of the battery devices, without imposing any serious damage on them.

2.2.1.6 Battery state monitoring
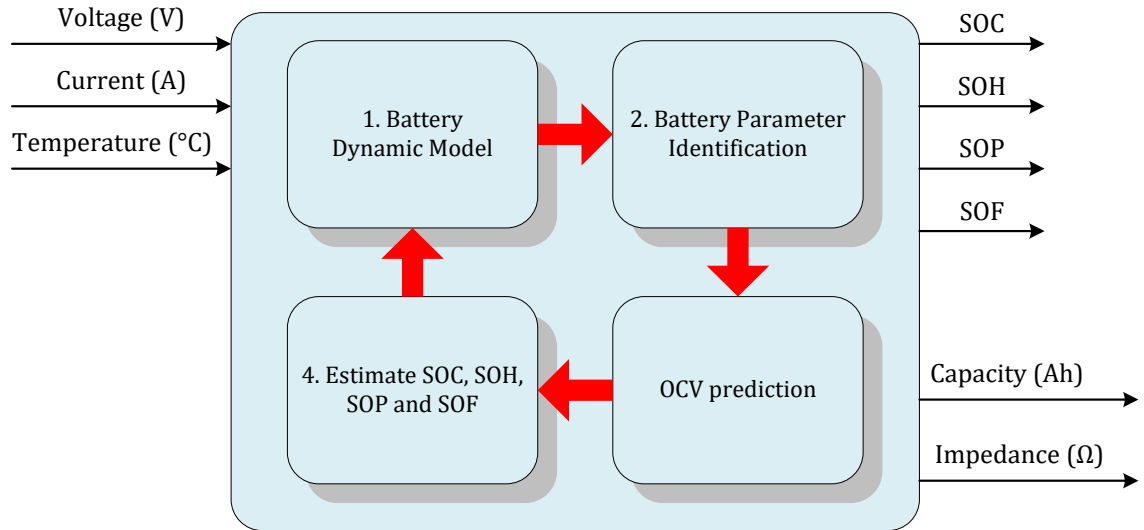
Fig. 2.8 Overview of underlying tasks performed by a battery monitoring system

For an effective and robust energy management algorithm, various battery states are required to be identified online. To this end, battery state monitoring algorithms are developed to provide the other decision-making units (e.g. energy management unit) within the BMS with a reasonable estimate of the battery's most favourite states (i.e. SOC, SOP and SOH). One common challenge in most battery state monitoring algorithms is the time-variability of the battery characteristics, including battery capacity and impedance parameters, due to varying operating conditions and battery ageing [61]. Therefore, the incorporated battery monitoring algorithm must be able to adaptively correct for these variations to produce an accurate and reliable set of battery state estimates.

The overall structure of a battery state monitoring system is illustrated in Fig. 2.8. In most battery monitoring algorithms, often a dynamic model representation of the battery system is used to aid with the online estimation of SOC, SOP, and SOH. Every step in time, the algorithm attempts to make an estimation of the battery impedance parameters, including the series resistance and its Ah capacity. Thereafter, using the

dynamic model structure, a prediction for the battery's OCV is made, which is then applied to either a look-up table or a predefined empirical function to estimate SOC in real time. Consequently, this information is processed into those algorithms responsible for SOP, SOF and SOH estimation, in order to realise a comprehensive battery monitoring system.

2.2.2 Review of Battery SOC Estimation Algorithms

This section reports on various approaches to battery SOC estimation. These can be summarised into two main categories, namely, the direct and indirect methods. The direct techniques include the easily implementable coulomb-counting method and the OCV methods. Whereas the former method suffers from sensor noise and initialisation-induced offsets, the latter requires a very long period of no-load connection to establish an accurate measurement for the battery's OCV. Consequently, these two methods are often combined in practice to form the basis for the indirect model-based SOC estimation techniques.

2.2.2.1 Coulomb-counting method

Coulomb-counting is an easily implementable technique for SOC estimation, where given an initial value, SOC (t_0), the time integral of the terminal current can be taken as an indicator for the battery's available charge.

$$\text{SOC}(t) = \text{SOC}(t_0) - \frac{\eta}{Q_{\text{nom}}} \int_{t_0}^{t} I(\tau) \cdot d\tau \qquad (2.14)$$

where $I(\tau)$ is the battery current, $Q_{\text{nom}} = C_{\text{nom}} \times 3600\text{s}$ and η (for charge $\eta < 1$ and for discharge $\eta = 0$) is the battery's coulombic efficiency. And C_{nom} is the battery's nominal capacity in ampere-hours. Conventionally, the current direction is negative during charge (i.e. $\text{sign}(I) < 0$) and positive during discharge (i.e. $\text{sign}(I) > 0$). Due to the open-loop nature of the coulomb-counting method described by (1), the predicted SOC is prone to large sensor offset and drift errors. Moreover, by using the nominal capacity as the denominator in (2.14), the resultant SOC may be under- or over-estimated.

2.2.2.2 OCV-based estimation

Additionally, SOC can be predicted based on a predefined relationship with the battery's EMF or OCV, as illustrated in Fig. 2.9. However, this technique requires a long period of no-load connection to establish an OCV measurement, making it impractical for online applications. Also, it can be argued that for those cell chemistries with flat OCV curves (e.g. lithium-ion iron phosphate), OCV-based techniques can produce unstable SOC estimates. This gives rise to more advanced model-based estimators used in BMS applications. Such methods often employ a model representation of the battery's dynamics whose parameters can be utilised as good indicators for various battery states, including SOC and SOH. In these techniques, the advantages of coulomb-counting are combined with an OCV-based method to realise a simple, yet efficient approach for the SOC estimation of various battery technologies, including lithium-ion.
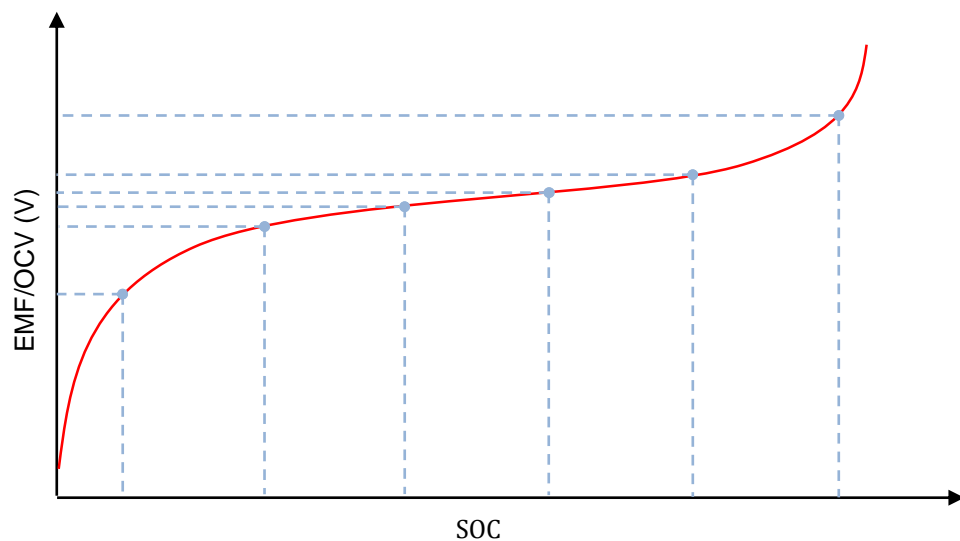
Fig. 2.9 A typical OCV-SOC relationship for a lithium-ion battery

As stated above, for an accurate SOC estimation, the battery's final EMF value must be established after a long period of OCV relaxation. The battery relaxation is mainly dominated by the internal electrochemical and thermodynamic processes that occur inside it. Depending on the battery's conditions, relaxation can take up to several hours, particularly when imposed to high charge/discharge current levels and operating at low temperature and near-empty SOC conditions.

There are several methods proposed in literature to estimate EMF by considering only the initial part of the OCV relaxation curve after a load disconnection. In [62], the authors have used a semi-log scale to plot the OCV relaxation curve against time. Then by considering two asymptotes, OCV is estimated as function of $\log(t)$. The model parameters are found using laboratory-based experiments on new batteries. The main drawback of this method is that, as the battery ages, the parameters used to model the voltage relaxation trajectory become increasingly unreliable.

Alternatively, adaptive techniques are developed to account for the variations in model parameters with battery ageing. The hypothesis is to use the first few minutes of the OCV relaxation after a load-disconnection to determine the OCV model parameters; thus the battery's EMF can be obtained and utilised for an accurate SOC estimation. For example, in [63], the authors have proposed an exponential function to relate the battery's EMF to the OCV as,

$$V_{\text{OC}}(t) = \text{EMF} - \big(\text{EMF} - V_{\text{OC}}(t_0)\big) \cdot e^{-t/\tau}. \tag{2.15}$$

The advantage of this simple model is that, the two unknowns (i.e. EMF and τ) are easily obtainable based on the first ten minutes of no-load connection. However, the work of [64] shows significant inaccuracies in the EMF prediction by this model. To further improve the performance of the exponential function given in (2.15), in [65], the authors have developed a more complex empirical model to describe the OCV relaxation in lithium-ion batteries. The proposed model is expressed as,

$$V_{\text{OC}}(t) = \text{EMF} - \frac{\gamma}{t^{\alpha} \cdot (\log(t))^{\beta}} \tag{2.16}$$

where EMF, γ, α and β are the model parameters and are identified online using a least-squares method. The performance of the OCV model represented by (2.16) has only been tested on small 1.1 Ah lithium-ion cells and its universality across other lithium-ion cell chemistries remains to be judged [64].

2.2.2.3 Book-keeping methods

The book-keeping methods use look-up tables for relating various battery characteristics to SOC for online BMS implementations. For example, in [66] and [67], SOC is proposed to be estimated by measuring the battery voltage, current and temperature, and relating it to a predefined function $SOC = f(V, I, T)$ that is parameterised while the battery is new. Although simple to realise, book-keeping SOC estimation methods are not practically fit for dynamic power applications. Moreover, the stored functions are only valid for the characterised batteries and the effect of ageing is not considered.

2.2.2.4 Impedance-based estimation

Battery impedance has been previously used as a basis for SOC estimation in lead-acid, NiMH, NiCd and lithium-ion battery applications (e.g. [68]–[72]). This approach to SOC estimation is similar to the OCV-based method, except in this case, the OCV-SOC function/look-up table is replaced with an impedance-SOC relationship. However, as shown in [73] and [74], battery impedance is heavily affected by SOC, SOH and other operating conditions such as temperature and current. Thus, impedance parameters alone are unable to provide an accurate SOC estimate as the battery ages. Furthermore, the sensitivity of the impedance to SOC is shown to be much lower than that to temperature. Therefore, a highly accurate temperature measurement system is required to compensate for the effects of temperature on impedance. Moreover, due to rapid temperature variations and uneven thermal distribution in large battery packs, high accuracies with impedance-based SOC estimation methods are impossible.

2.2.2.5 Model-based estimation

Model-based estimators (e.g. [75]–[79]), as the name suggests, employ deterministic model representations of the battery system in an effort to relate the terminal signals (i.e. voltage, current and temperature) to the battery's SOC. Essentially, the measurements are considered as model inputs to compute the battery's OCV while in operation. Then, the SOC-OCV relationship is used to provide an estimate for SOC in real time. Similar to previously mentioned OCV relaxation

models, the parameters of the model structures used in online SOC estimation algorithms vary significantly throughout the battery's lifetime. On the other hand, the adaption of model parameters with respect to operating conditions and battery ageing is only practical for relatively simple model structures. Nevertheless, model-based SOC estimation methods are increasingly becoming popular in applications where battery operation cannot be interrupted for characterisation purposes.

2.2.2.6   Observer-based methods

Alternatively, adaptive observers can be carefully designed to estimate various battery states and parameters in real time. Recently in [80], the authors have considered the nonlinearities and uncertainties in the OCV-SOC relationship to develop an improved observer-based SOC estimator. Other examples of observer-based SOC estimators and their usefulness in lithium-ion battery applications are reported in [80]–[87]. These methods benefit from simplicity and reasonably high accuracy levels. However, battery parameter adaption due to ageing is still an issue. To solve this, Rahimi-Eichi *et al.* [88] has proposed a piecewise linear mapping of the OCV-SOC relationship together with a moving-window least-squares method to estimate SOC, as well as battery impedance parameters in real time. In another approach taken in [89], the battery terminal signals are observed over a short period of time, depending on the excitability of the input signals. Then, using a simple battery model consisting of an OCV and series-resistance element, and an ordinary least-squares method, the battery's OCV is determined and used for SOC estimation.

2.2.2.7   Kalman Filter (KF) based estimators

The Kalman Filter (KF) is a recursive set of robust equations that allows for an stochastic identification of dynamic systems [90]. It finds applications over a wide range of disciplines, including the energy and power management of BES systems. The ordinary KF is mostly used with rather simple and linear battery model structures. For example, in [91] and [92] the authors apply the KF algorithm to find the battery's OCV, which is then used to estimate SOC. Alternatively, to compensate for the nonlinearities inherent to electrochemical devices and complex battery models, extensions of the ordinary KF algorithm are used.

The Extended Kalman Filter (EKF) is the most popular version of the nonlinear KF, where the model states and parameters are linearised about the filter's current trajectory. Examples of battery states monitoring using EKF include [93]–[100]. It may be argued that the EKF suffers from linearisation inaccuracies and the stochastic measurement noise characteristics can vary with battery and sensor ageing. Consequently, other advanced versions of the KF algorithm such as sigma-point KF (SPKF) have been introduced for battery identification purposes. Examples of SPKF include, the unscented KF (UKF) and the central-difference KF (CDKF), whose applicability to battery state estimation has been validated in [101]–[107].

The disadvantage of all KF-based estimators is that, for a proper implementation, a reasonable *a priori* knowledge of the model parameters and measurement and process noise covariance are required. Subsequently, inaccurate setting of the filter's initial conditions can lead to either divergence or an extremely slow convergence. To overcome this issue in battery identification problems, researchers have used adaptive KF (AKF) [92], adaptive EKF (AEKF) [108]–[114] or adaptive SPKF (ASPKF) [115] to estimate the nonlinear model parameters and measurement noise covariance in real time, at the expense of additional computational power.

Another disadvantage associated with KF estimators is that, the process and measurement noises are assumed to follow a Gaussian distribution with a mean value of zero. However, this assumption may not be true in most real battery applications, leading to further exacerbation of the filter's convergence behaviour and overall accuracy. As a result, particle filters (PF) and unscented-particle filters (UPF) are employed in [116]–[119] to achieve better results compared to KFs, at a cost of significantly increased computational power and memory consumption.

2.2.2.8 Machine learning techniques

Artificial neural networks (ANNs) [120]–[124], fuzzy logic (FL) [125]–[127] and support vector machines (SVMs) [128]–[132] have also found usage in BMS applications. These approaches are similar in implementation to the model-based methods described previously, except that SOC is represented by, for example ANNs, instead of a deterministic model structure. The advantages of such approaches is

that *a priori* knowledge of the battery parameters is no longer required. However, due to the requirement for large training datasets of various forms, these approaches for SOC estimation are often precluded form online BMS applications. Furthermore, due to the open-loop nature of such techniques, adaption to battery ageing and other factors such as manufacturing variations is not possible.

In more recent machine-learning approaches, the estimated SOC is used as one of the system inputs and the output, being the terminal voltage, is compared to the actual battery voltage to produce an error term. Then, by using an appropriate observer or one of the KF variants, closed-loop SOC estimation can be realised as in [133]–[135], which can adapt to battery parameter variations due to ageing and varying operating conditions; thus online training of the underlying models become possible. However, this brings with it some additional problems such as, tremendous computational power requirements and over-fitting, which precludes these techniques from online BMS applications that are intended to be implemented on low-cost microcontrollers.

2.2.3 Review of Battery Capacity Estimation Methods
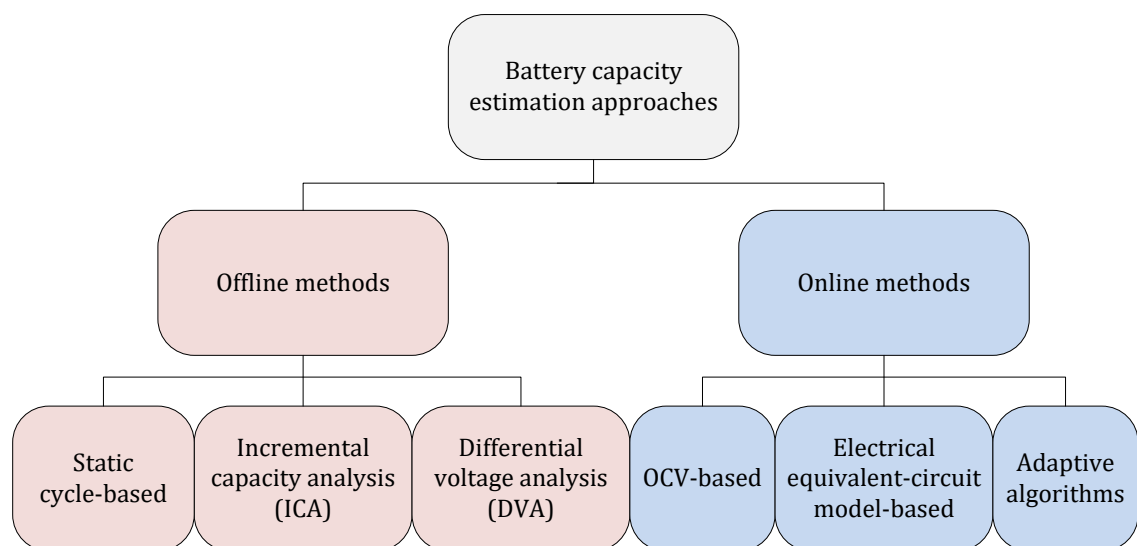
Fig. 2.10 Methods presented in literature for battery capacity estimation

Battery capacity is a direct indicator of the amount of available energy that a battery can supply from a fully charged state. Due to the advancements in battery manufacturing techniques, capacity variations in the battery/cells of the same chemistry and dimensions are usually very small. However, over the lifetime of the battery, its rate of capacity degradation can vary, depending on the usage and operating conditions. Therefore, it is important to be able to predict and monitor such variations, which can help prevent power shortages and/or failure in more safety-critical power applications. In this section, a description of the various offline and online methods proposed in literature for battery capacity estimation is provided. These methods are summarised in Fig. 2.10.

2.2.3.1 Offline approaches to capacity estimation

A simple method for battery capacity characterisation is to impose it with a full charge/discharge cycle and measure the amount of charge that leaves the battery during the discharge half-cycle. However, this method requires for the battery to be 'offline', where a full capacity measurement cycle can be performed; thus, it is not applicable to most BES applications (e.g. in EV/HEVs).

Other examples of offline capacity estimation methods include incremental capacity analysis (ICA) and differential voltage analysis (DVA) [136]–[138]. These methods involve charging and discharging the battery with a low current level in incremental or detrimental SOC steps, in an effort to gain a better understanding of the battery capacity loss mechanisms. Once the battery's OCV has reached a final equilibrium potential, the evolution of the incremental capacity (IC) curves as a function SOC and temperature are investigated to reveal the gradual changes in the underlying electrochemical properties of the battery. Similar to the static cycle-based method, ICA and DVA capacity estimation requires constant-current charging and discharging phases, which may not be available in certain applications.

2.2.3.2 Online approaches to capacity estimation

The online battery capacity estimation methods can be classified into two main groups; those based on a predefined OCV-SOC relationship and those based on adaptive estimation of electrical equivalent-circuit models. The first group methods

(e.g. [139]–[141]) consider the changes in the battery's OCV, with respect to SOC over a specified charge/discharge period. The ampere-hour capacity is then calculated by re-arranging equation (2.14) and solving for C_{nom}. Although easy to implement, this method requires the battery to be fully rested before an OCV measurement can be taken.

The methods from the second group (e.g. [64], [142]) are similar in principle to the first group methods, except that the battery's OCV is obtained from an electrical equivalent-circuit model. Eventually, the predicted OCV is applied to either a look-up table with static parameters, or to a polynomial function with adaptable parameters to estimate SOC and battery capacity.

Alternatively, battery capacity can be considered as a slow time-varying parameter of a dynamic model structure, where by applying one of the adaptive techniques described in section 2.2.2 for SOC estimation, battery capacity can also be obtained. For example, in [95], the authors have proposed a multiscale framework for the EKF estimation of battery SOC and capacity, whilst in [143], a joint EKF approach has been adopted. Other examples of adaptive battery capacity estimation methods include, the recursive least-squares (RLS) in [144] and [145], dual EKF in [100], [140], [146], dual SPKF in [106] and a combination of KF-based and subspace parameter estimation methods in [92] and [147]. These methods can achieve a fairly accurate capacity estimate, at the expense of increased computational power for intensive numerical operations such as inversion of large-dimensional covariance matrices.

2.2.4 Review of Battery Impedance Characterisation Methods

In modern battery monitoring systems, impedance parameters often serve as a good indicator and/or recalibration means for various battery states including SOC, SOH, SOP and SOF. During operation, the impedance parameters can vary significantly due to both internal and external factors. The internal factors are the battery's SOC, SOH and heat generation due ohmic losses, whilst the external factors may include ambient temperature, current and previous history of battery usage [148]. As a

result, many reaches have been reported on both online and offline battery impedance characterisation techniques, as summarised in Fig. 2.11.
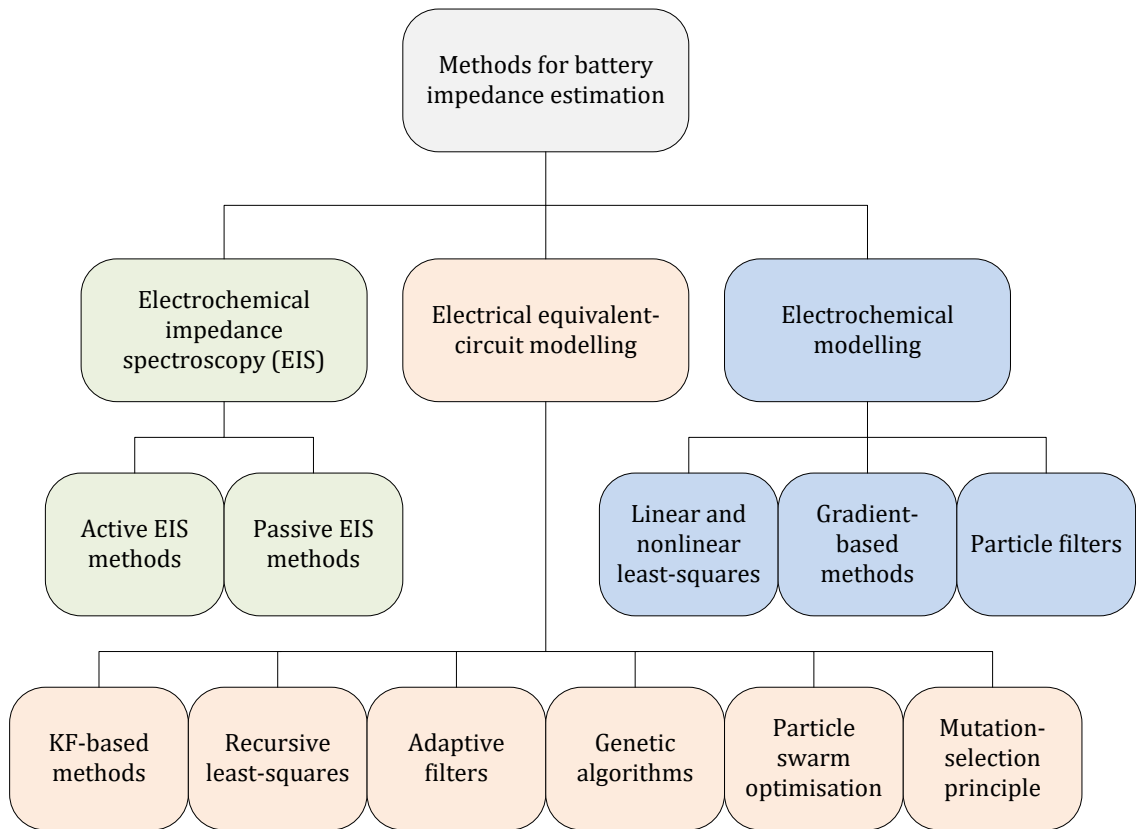
Fig. 2.11 Summary of battery impedance estimation methods [61]

2.2.4.1 *DC pulsed-current direct method*
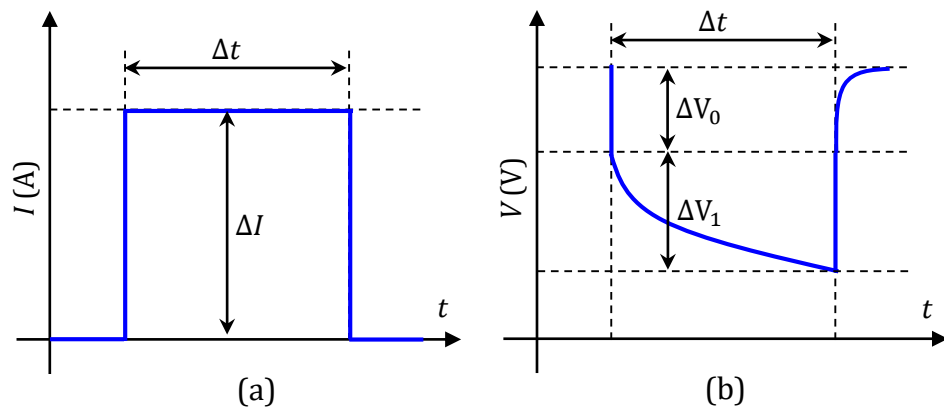
Fig. 2.12 Typical battery (a) current and (b) voltage responses obtained from a pulsed-current step for DC resistance calculation

A simple method to determine the battery's overall DC resistance is to inject it with a pulsed-current signal and measure the corresponding voltage response, as shown in Fig. 2.12, where ΔI is the amplitude and Δt is the period of the of the injected current pulse. Typically, Δt ranges from milliseconds to seconds, depending on the test regime applied (e.g. HPPC). Subsequently, the battery's ohmic or series-resistance, which is inherent to the cell's internal composition, can be calculated using Ohm's law as,

$$R_\text{s} = \frac{\Delta V_0}{\Delta I}. \tag{2.17}$$

The second voltage drop ΔV_1 occurs as a result of those elements impeding the transfer of charge in a battery. These elements include the short time-constant charge-transfer resistance and the double-layer capacitance at the electrodes. Moreover, due to the diffusion of the active species, a concentration gradient builds up, resulting in a change in the battery's EMF [65]. Therefore, considering the voltage drops due to ΔV_1, equation (2.17) can be rewritten as,

$$R_\text{int} = \frac{\Delta V_0 + \Delta V_1}{\Delta I}. \tag{2.18}$$

In most applications, equation (2.18) is considered sufficient for the purpose of power prediction. However, this crude approach does not fully describe the underlying battery dynamics. Moreover, the pulsed-current method largely depends on the period Δt of the applied stimulant, and can only be performed at a single frequency. As a result, such direct methods are only applicable to those applications, where accurate battery impedance estimation is not a necessity.

2.2.4.2 Electrochemical impedance spectroscopy (EIS)

EIS is a widely used experimental technique for the identification of a battery's internal processes occurring at different time-constants. This technique is often implemented either actively or passively in order to capture a battery's charge transfer dynamics over a specified band of frequencies.

The general principle of EIS is to apply a sinusoid to the battery under test and measure its response from which the electrical impedance is calculated. The input signal can either be a voltage (potentiostatic) or current (galvanostatic) sinusoid. For potentiostatic EIS testing, the battery impedance is defined in (2.19).

$$Z(\omega) = \frac{U}{I(\omega)} = |Z|\angle\phi(\omega) \tag{2.19}$$

U is the amplitude of the voltage response; $I(\omega)$ is the response current, where $\omega = 2\pi f$ is the angular frequency; $\phi(\omega)$ is the phase shift; $Z(\omega)$ is the complex-valued impedance and $|Z|$ is the absolute magnitude. It is also possible to express $Z(\omega)$ in a Cartesian plane, with a real part Z' and an imaginary part Z'' as,

$$\left.\begin{aligned}
Z(\omega) &= Z' + jZ'' \\
Z' &= |Z| \cdot \cos(\phi) \\
Z'' &= |Z| \cdot \sin(\phi) \\
|Z| &= \sqrt{Z'^2 + Z''^2}
\end{aligned}\right\} \tag{2.20}$$
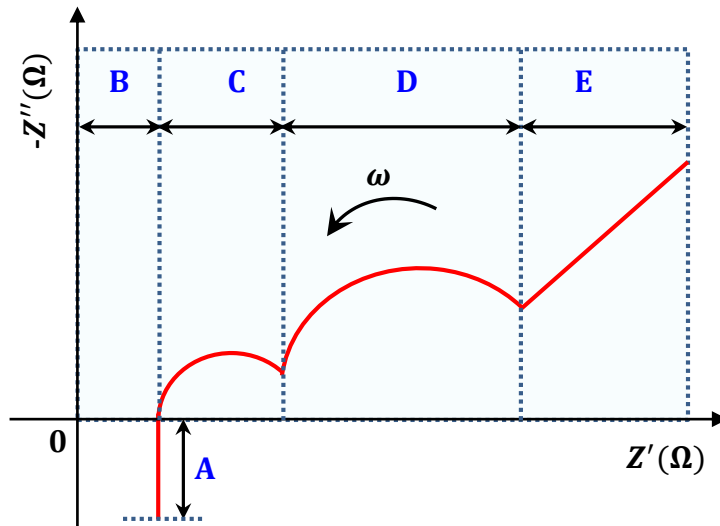
Fig. 2.13 Theoretical impedance spectrum for a lithium-ion cell

A theoretical impedance spectrum for a lithium-ion battery is demonstrated in Fig. 2.13 and in this case consists of five different regions. Each region has a physical interpretation, which, in terms of battery dynamics, can be explained as follow:

A) Inductive reactance caused by the battery geometry and metallic interconnections;

B) Internal ohmic resistance due to the current collectors, separator and the movement of ions through the electrolyte;

C) First semi-circle often associated with a solid electrolyte interface (SEI) film [149] formed over the surface of anode;

D) Second semi-circle occurring due to the double-layer capacitance and charge transfer resistance at the electrodes;

E) Finally, this region represents the long time-constant processes associated with the diffusion of active species.

On the basis of EIS operation, many battery monitoring systems have been reported in literature (e.g. [150]–[152]). On the down side, these active techniques require complex circuitry to perform on-board signal generation and data acquisition. Alternatively, passive EIS methods are developed in [153]–[155] to eliminate the requirements for extra circuitry. Instead, these methods use the fluctuations caused by dynamic loads to estimate the battery's impedance. However, due to the linear approximations used in such methods, the effects of current and temperature on battery impedance is often neglected. Moreover, the persistence of excitation criterion [156] might not be satisfied at all times, leading to loss of vital information at frequencies outside the signal's range.

2.2.4.3 Methods based on electrochemical modelling

Depending on the order of the governing partial differential equations (PDE), electrochemical models can achieve highly accurate descriptions of the battery dynamics. For example, in [157]–[160], by using adaptive PDE observers and nonlinear least-squares methods, battery's SOC and resistance are estimated simultaneously online. On the other hand, in [161], the authors have used a control-oriented single-particle model structure in combination with a gradient-based

recursive method to estimate the battery's total resistance. Another electrochemical model-based approach is reported in [162], where a particle filter is employed for SOC and impedance parameter estimation.

A common disadvantage to all the methods discussed above is the complexity of the model structures and the revolutionary system identification methods that are used to estimate the battery impedance parameters. Moreover, the parameters identified for electrochemical models cannot be easily related to any physical qualities of the battery (e.g. SOP or SOH). As a result, electrochemical models for battery impedance estimation are less frequently applied in online battery monitoring systems.

2.2.4.4 *Methods based on electrical equivalent-circuit modelling*

Electrical equivalent-circuit models have been found useful in many online battery state and parameter estimation algorithms. Fig. 2.14 illustrates an exemplary simple equivalent-circuit model structure, where OCV is defined as a function of SOC, R_{int} represents the battery's total internal resistance and V_{T} is the terminal voltage. By using such models, it is possible to relate the obtained battery parameters to real battery states, including SOP and SOH. Moreover, due to their relatively simplified numerical approaches, equivalent-circuit models are highly desirable for online BMS implementations on low-cost microcontroller platforms.
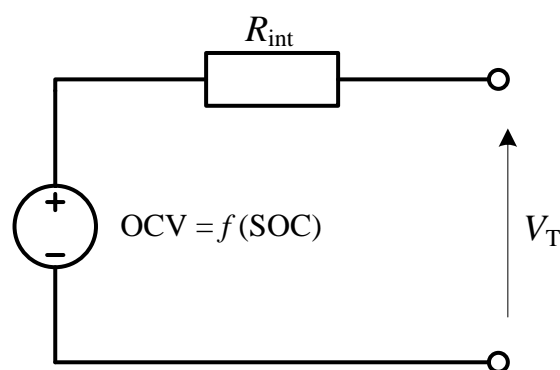
Fig. 2.14 Simple electrical equivalent-circuit battery model

There are various techniques reported in literature that can be applied to equivalent-circuit models to extract the battery impedance parameters in real time. Some of the most sighted techniques are listed below:

- KF-based methods;
- Recursive-least-squares methods;
- Non-recursive least-squares methods;
- Other adaptive approaches.

KF-based methods are not only useful in online battery state estimation problems, but can also be implemented in different formats to simultaneously identify the battery's impedance parameters. For example, in [163]–[165], the authors adopt a joint EKF approach to real-time battery identification, where system unknowns are stacked up in a single EKF for simultaneous estimation of the model states and parameters. The disadvantage of joint EKF for online applications is the increased number of large matrix operations (e.g. matrix inversions) due to the high dimension of the augmented state model. Alternatively, the dual EKF (e.g. [140], [146], [166]) and the dual SPKF (e.g. [146]) are employed in BMS applications to separate the process of state and parameter estimation by using two individual filters running in parallel. Due to the recursive nature of such system identification methods, the requirements for storage memory is very low; therefore their implementations on low-cost microcontrollers is achievable.

Least-squares techniques have also been applied to online battery parameter estimation problems. In [136], [137], [144], [145], [167], the authors have applied different variations of the least-squares method, such as, recursive least-squares (RLS), recursive least-mean-squares (RLMS) and weighted RLS (WRLS) to identify different battery model structures in real time. Compared to KF-based approaches, these techniques are computationally less intensive. However, they are less robust in cases where persistence of excitation is poorly conditioned. In [168], a moving window least-squares approach to battery parameter estimation was taken in an effort to improve the filter's convergence. This was achieved at the expense of increased memory consumption for storage of battery data sampled in a 'window'.

Non-recursive least-squares techniques are useful in situations where the underlying battery model structure is either highly nonlinear [169]–[171] or fractional with no ideal components [172]–[175]. This technique operates based on the principle of measuring and storing battery data over a period of time, and

applying the least-squares optimisation procedure to fit a battery model of interest to the measured data. Due to the high computational power and storage memory requirements, these techniques are often implemented offline in laboratory-based conditions to validate the performance of the underlying battery model structure.

In addition to KF-based and recursive least-squares methods, other adaptive approaches to online battery parameter identification have been reported. For example, in [176]–[179], a sliding-mode observer is proposed to estimate the battery parameters in real time. The use of evolutionary techniques for battery identification have also been reported in literature. These include genetic algorithms (e.g. [180]) and particle-swarm optimisation (e.g. [181]) methods. Although higher estimation accuracies are achievable compared to least-squares-based methods, however, the requirements for tremendous computational power and memory consumption precludes these techniques from most online BMS applications.

2.2.5 Review of Battery SOH Estimation Methods

As stated previously, SOH is the ability of the battery to provide its rated energy over its lifetime. The most common understanding of SOH is that, when the battery is new, SOH is defined as 100%, and when its energy delivery capabilities drop to a predefined level, SOH is said to have reached 0%. In certain BES applications, SOH can also be related to the power capability of the battery (SOH_{pwr}), as well its energy-based definition (SOH_{enr}).

2.2.5.1 Energy- and power-based SOH estimation

In general, as the battery ages, its capacity fades away, whilst its impedance grows larger. As a result, these two parameters can be used to determine the battery's energy- and power-based SOH levels (i.e. SOH_{enr} and SOH_{pwr}), respectively. This is a convenient way of characterising the SOH for batteries used in EV/HEVs and large-scale grid-tie energy storage sites, as battery's capacity and impedance parameters are readily available using the methods described in sections 0 and 0.

SOH can also be determined without explicitly having to estimate the battery's capacity and/or impedance. For example, in [70] the authors use the voltage drops measured for lithium-ion batteries under load conditions to obtain a DC resistance value; therefore the resulting SOH can be related to the battery's SOH_{pwr}. FL-based methods have also been reported in [182]–[184] for SOH estimation, where the model inputs consist of measured and/or calculated battery characteristics, including impedance parameters. The resulting SOH, however, does not reflect on a degradation in one particular battery characteristic, but provides a more general indication of the battery's condition (e.g. new, mid-life or EOL).

Alternative approaches to SOH estimation have been proposed in [185] and [186]. In these works, the authors have employed a lifetime model of a lithium-ion battery, and by observing various conditions (e.g. SOC, number of cycles and temperature), the battery's SOH is estimated. Ultimately, the recursive ANN and SVM methods are applied to the battery's lifetime model to adapt to varying operating conditions and improve the quality of the SOH estimate. However, these techniques require for extensive model-training datasets, which are almost always attained using accelerated ageing tests. Therefore, the validity of such SOH estimation methods could be reduced under real application conditions.

The SOH level used for determination of the battery's end-of-life (EOL) can vary amongst different applications. For example in EV/HEVs, the battery is said to have reached its EOL when SOH_{enr} reaches 80% of the nominal capacity, or when SOH_{pwr} drops by a factor two. Whilst a battery's SOH estimate might indicate that it has reached the criteria for replacement, the same battery could be perfectly fine for another secondary application. However, significant changes in the battery's internal characteristics means that there is an increased probability of battery failure. Therefore, extra monitoring and protection circuitry might be required.

2.2.5.2 Remaining useful life (RUL) prediction
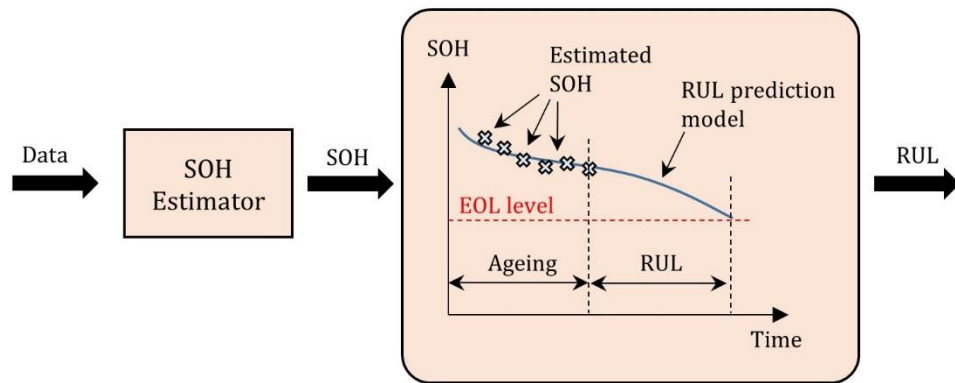
Fig. 2.15 Concept of RUL prediction based battery's SOH

A battery's remaining useful life (RUL) is usually defined as the remaining time or the number of charge/discharge cycles before it reaches 0% SOH. Fig. 2.15 presents the basic concept of RUL prediction, consisting of two parts. The first part involves the estimation of the battery's SOH using one of the methods discussed earlier. The second part includes an appropriate RUL model that takes SOH and other battery properties as a function of either time or cycle number to predict when the battery will reach its EOL threshold. Recent works on such RUL prediction approaches include [187]–[192]. Depending on the employed algorithms (e.g. SVM in [193]), battery RUL prediction can be computationally intensive. Nevertheless, the main challenge is to try and train the underlying RUL model based on the SOH data obtained during the early stages of battery ageing. This is similar to a battery lifetime model that can be parameterised online, according to imposed the load profile.

2.2.6 Review of Battery SOP Characterisation Methods

For a proper operation of the energy management system discussed in section 2.2.1.5, battery SOP prediction algorithms are employed. For instance, in EV/HEVs, knowledge about the available quantity of discharge power can help the energy management system make intelligent control decisions, preventing sudden power drops during acceleration and serious damage to the battery's health. Most battery energy management strategies (e.g. [194]) are reported to have a short power

prediction horizon. This means that the estimated battery power is only valid over a predefined time interval. In the following sections, the most commonly used SOP prediction methods by battery energy management strategies are discussed.

2.2.6.1 Book-keeping methods

Similar to book-keeping methods described in section 2.2.2.3 for SOC estimation, direct approaches to battery power prediction are also based on the interdependence of various battery states and parameters. In these methods, usually some direct relationships between, for example, battery's SOC, voltage and temperature with the demanded pulse power signal are established in laboratory conditions, and the results are stored in a non-volatile memory unit of the BMS for online implementations [195]–[197].

There are various pulse power characterisation procedures reported in [198]–[200] to help with the initial parameterisation of look-up tables or empirical functions for new batteries. However, as the battery's characteristics change due to ageing and other stress factors, the SOP values predicted by these methods become very inaccurate; thus some level of adaption to varying operating conditions is necessary. Moreover, the storage of multi-dimensional look-up table or best-fit function parameters requires a significant amount of memory, which suggests that these methods may not be suitable for embedded BMS applications.

2.2.6.2 Online model-based approaches

To overcome the challenges in direct SOP prediction approaches, model-based techniques have been developed in [201]–[206]. These methods employ model representations of the underlying battery dynamics to produce a more accurate estimation of the battery's available charge/discharge power. In order to ensure convergence of the battery model parameters in varying operating conditions, similar adaptive techniques discussed in section 2.2.4 for battery impedance estimation can be employed.

Model-based SOP prediction algorithms are to date, one of the most favoured techniques applied in many battery energy management strategies. This is owed to

their reduced complexity and minimum requirements for non-volatile storage of the initial model parameters. However, a trade-off exists for larger BES applications (e.g. grid-tie applications). Some researchers (e.g. [194]) have proposed to employ a separate model for each individual cell in a battery pack to produce a highly-accurate SOP estimate. The main drawback of such approach is that a significant amount of memory and computing power is required to identify the parameters of every cell model. An alternative solution to online power characterisation of larger battery packs was proposed in [78], where a more complex battery model is used to describe the dynamics of the pack as a whole.

2.3 Setup for Experimental Verification of Battery Monitoring

This section describes the experimental setup used to verify the algorithms hypothesised in this thesis based on a high-precision MACCOR battery tester, together with a Solartron EIS analyser. The tests for verification are carried out over a range of operating temperatures that required a bespoke thermal chamber to be designed and built. Furthermore, to validate the dynamic performance of the developed battery state and parameter estimation techniques, a set of current profiles are derived based on the power requirements for an EV traction battery under some prescribed driving cycles. The hardware and setup and the experimental procedures were designed for two variations of lithium-ion cell chemistry. The experimental setup presented in this section will be used throughout this thesis, unless stated otherwise.

2.3.1 Battery Testing Equipment

2.3.1.1 Lithium-ion test cells
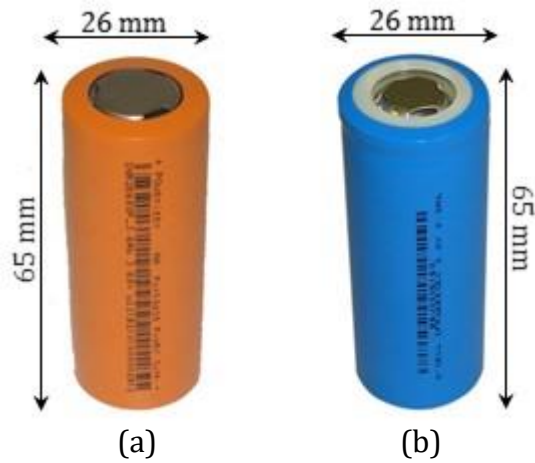
Fig. 2.16 Cylindrical lithium-ion test cells, (a) NMC and (b) LFP

The universality of the proposed algorithms is verified on two variations of lithium-ion battery cells, namely the NMC and LFP, as depicted in Fig. 2.16. These cells are of the cylindrical 26650 type with specification outlined in Table 2.5. These two lithium-ion cell variants are widely used in EV traction battery packs for their enhanced safety characteristics and superior energy and power densities. Moreover, due to the rapidly growing interest in these cells for other large-scale applications (e.g. LFP battery packs for gird-tie storage), they are chosen as the subject of study in this thesis. However, the algorithms developed here are not limited to NMC and LFP cell types, as they can be modified for other battery chemistries as well, without any fundamental changes to the algorithm

Table 2.5 Specifications for lithium-ion test cells at 25°C

Parameter	NMC	LFP
Nominal voltage (range):	3.65 V (2.75 – 4.2 V)	3.2 V (2.0 – 3.65 V)
Nominal capacity:	3600 mAh	3300 mAh
Impedance @ 1 kHz:	20 mΩ	30 mΩ

2.3.1.2 Experimental setup
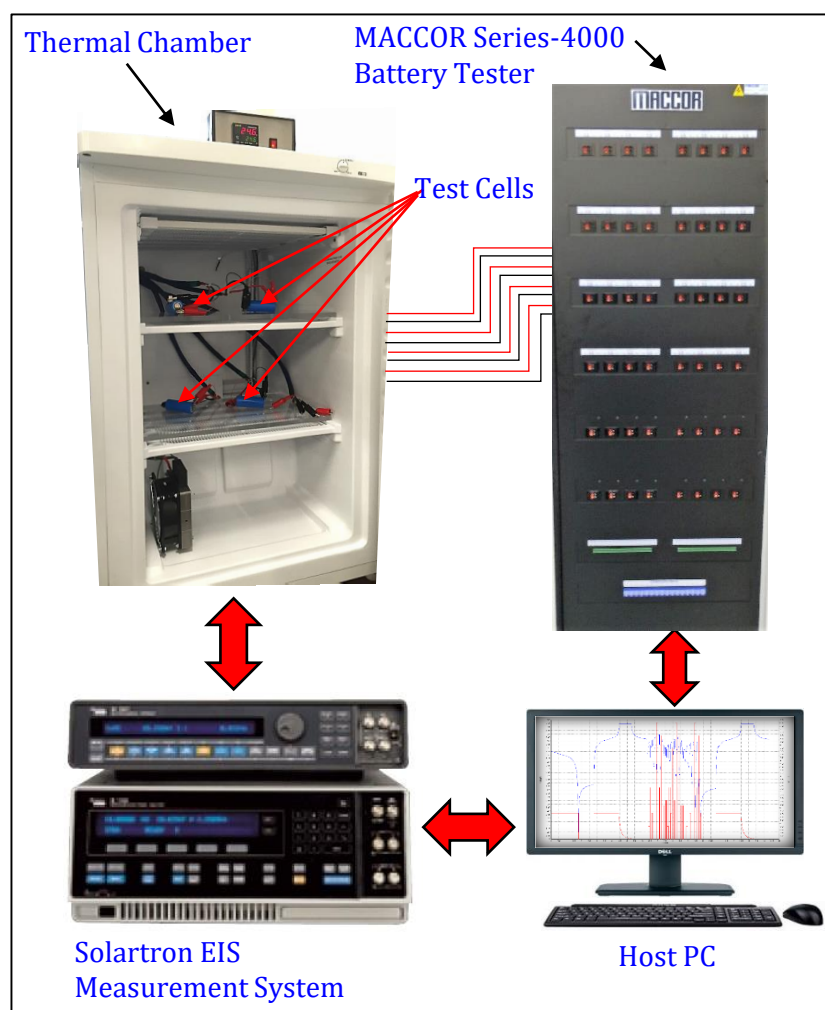
Fig. 2.17 Hardware configuration for lithium-ion cell testing in this thesis

The experimental setup used in this thesis, as illustrated in Fig. 2.17, features a multi-channel MACCOR 4000-series battery tester, which is equipped with 32 test channels. Each channel has a maximum control and measurement rate of 10 ms at 0-20 V and 0-10 A, with measurement accuracies of ±0.02% and ±0.05% for the voltage and current sensors, respectively.

The ambient temperature is controlled through a built-in-house thermal chamber with ±1°C accuracy. A desktop computer is used to provide software control and data storage for later analysis. Since the current sensor offset of the MACCOR system is relatively small and the sampling rate is reasonably high, it is safe to assume that the integral of the throughput current over the charge/discharge period represents

a true measurement of SOC. Finally, a Solartron 1260 electrochemical interface is used in conjunction with a Solartron 1287 frequency response analyser to perform a series of EIS tests.

2.3.2 Generation of Dataset
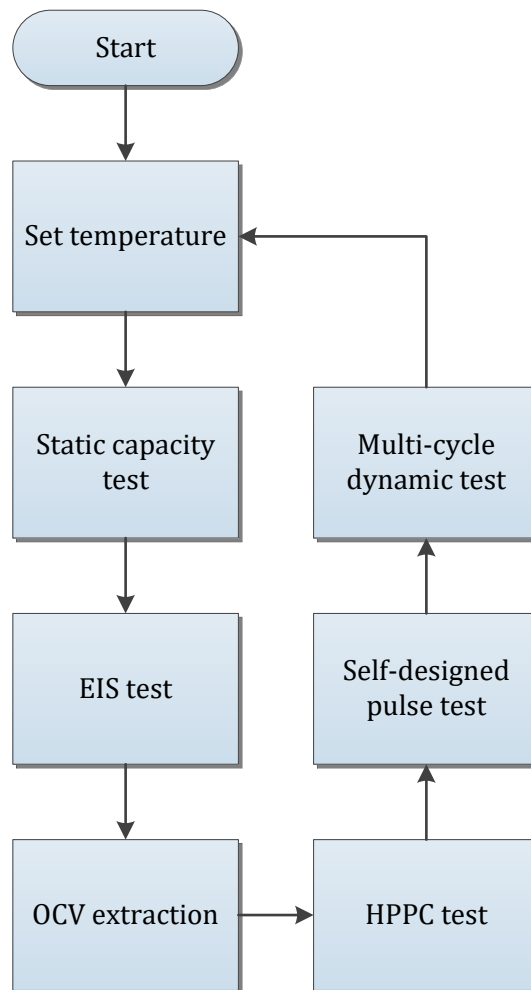
Fig. 2.18 Sequence of cell testing procedures undertaken in this thesis

In order to gather a comprehensive dataset, a test sequence as presented in Fig. 2.18, is designed and implemented. The test sequence starts with incubating the test cells in the thermal chamber for a period of 24 hours. The chosen dwell time is long enough for the small cylindrical cells to reach a thermal and electrochemical equilibrium prior to any characterisation test. Five temperature settings of 5, 15, 25, 35 and 45°C are chosen to provide a better understanding of the temperature

dependency of various battery states and parameters under both static and dynamic operating conditions. Throughout the tests, the thermal distribution over the test cells' surfaces is assumed constant, and the internal temperature variations due to high charge/discharge current rates are neglected. The following sections provide a description for the remaining test procedures.

2.3.2.1 Static capacity test

Prior to any test, each cell undergoes a capacity measurement cycle, which consists of a 0.5 C constant-current discharge, until the end-of-discharge voltage has been reached. This is to remove any residual charge left in the cell. After a one-hour rest period the cell is re-charged using the standard constant-current constant-voltage (CCCV) scheme at the manufacturer's recommend current and voltage levels. Then, following a one-hour rest, the cell under test is discharged at a 0.5 C current level. The quantity of charge removed from the cell is recorded as its maximum discharge capacity at the set temperature.

2.3.2.2 EIS test procedure

Fig. 2.19 EIS procedure for NMC and LFP test cells

Upon the completion of the static capacity test, each cell is recharged to SOC = 100% using the CCCV scheme. A zero-current relaxation period of 1 hour is allowed to ensure that the cell has reached a partial equilibrium, prior to each EIS test step in the sequence illustrated in Fig. 2.19. The relaxation period is chosen as a trade-off between accuracy and experiment time. The sweep bandwidth is fixed at 5 mHz to 5 kHz, with a resolution of 15 steps per decade. The amplitude of the excitation sinusoidal voltage is chosen as 8 mV. This is low enough to avoid any nonlinearities due to charge modification, but high enough for good noise immunity. An EIS test is

performed at every ΔSOC = 10%, starting from SOC = 100%. A discharge current of 0.5 C is applied to move SOC down to next step. This procedure is repeated until the cell reaches its lower voltage threshold (i.e. SOC = 0%.). The complex impedance data obtained are then used to identify a suitable order-number for a dynamic equivalent-circuit model and to verify the performance of the proposed battery impedance parameter estimation techniques in this thesis.

2.3.2.3 Open-circuit voltage (OCV) extraction
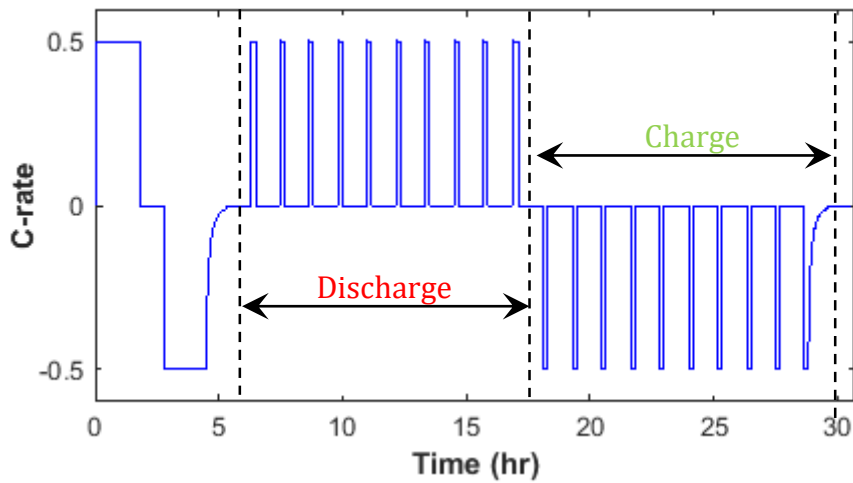
Fig. 2.20 Pulsed-current profile for cell OCV extraction

In this thesis, the relationship between the test cells' OCV and SOC is realised through a polynomial function, whose order is to be reported in Chapter 4. To this end, a pulsed-current and relaxation test profile, as shown in Fig. 2.20, is designed and implemented at different operating temperatures. The test profile begins with a full discharge at a constant current of 0.5 C, until the lower voltage thresholds are reached for both cell chemistries. Then, the cell under test is re-charged to 100% SOC using the CCCV charging scheme. After a relaxation period of 1 hour, the first OCV is recorded at SOC = 100%. Furthermore, the cells are discharged in steps of ΔSOC = 10% at a current level of 0.5 C for both cell chemistries, followed by one-hour rest periods. This sequence is repeated until the cells are fully discharged. The OCV measurements during the charge half-cycle are also obtained using a similar procedure, where the cells are charged in steps of ΔSOC = 10% at a current of 0.5 C.

2.3.2.4 Hybrid pulse power characterisation (HPPC)

The Hybrid-Pulse-Power-Characterisation (HPPC) test is a standard procedure developed by the Partnership for New Generation Vehicles (PNGV) [198] and is used to determine the power and energy capability of a rechargeable battery under both discharge and regenerative charging scenarios. Fig. 2.21 illustrates a single cycle HPPC waveform, which consists of a 1 C current pulse of 18 s duration
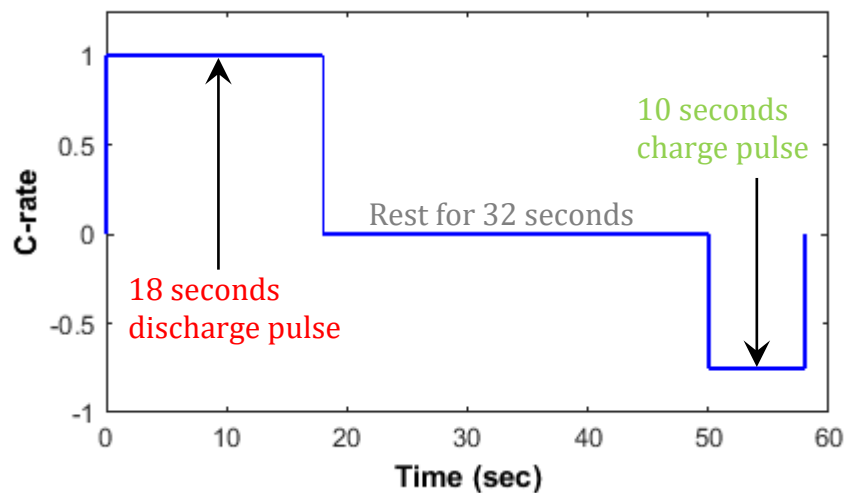
Fig. 2.21 A single cycle HPPC current profile [198]

for discharge and a 0.75 C current pulse of 10 s duration for regenerative charging, separated by a rest period of 32 s. The complete profile starts with a preamble CCCV charge step. Thereafter, the HPPC pulses, are applied to the cell under test over the SOC range of 10% to 90%, in steps of ΔSOC = 10%. A discharge current pulse of 0.5 C is used adjust the SOC level and a 1-hour rest period is allowed between the HPPC pulse repetitions. This particular current profile is used in this thesis to create a reference framework for verification of the SOP prediction algorithm to be reported.

2.3.2.5 Self-designed pulse test
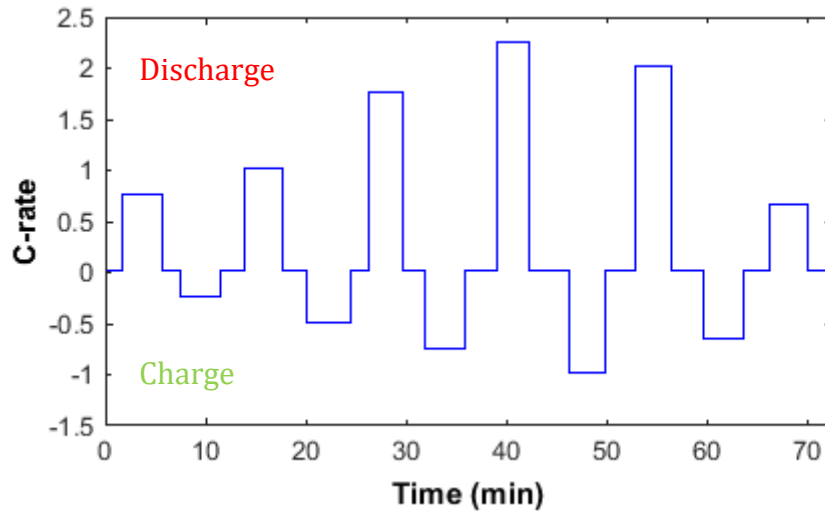
Fig. 2.22 Self-designed pulsed-current profile for dynamic cell excitation

The dynamic performance of the proposed SOC estimation algorithm in this thesis is verified using a self-designed pulsed-current profile. As shown in Fig. 2.22, the profile consists of both charge and discharge pulses of different amplitudes and periods, providing a dynamic excitation of the NMC and LFP test cells, whilst modifying the cell's SOC using discharge/charge current pulses which gradually increase in amplitude. The lengths of the relaxation periods in between discharge/charge steps are chosen arbitrarily; though, long enough to allow for a recovery to occur. Note that the profile has a predominant discharge characteristic as to remove charge from the cell, until it is fully discharged.

2.3.2.6 Battery power requirements for an EV design

It is a respectable approach to test any newly developed BMS algorithm under real-world operating conditions. The state monitoring algorithms to be reported in this thesis are no exception and thus require verification under current profiles that, in contrast to constant-current loads, are more dynamic and a better representative of the EV operation in real world. Therefore, a set of drive-cycle-based current profiles, consisting of both discharge and regenerative charge pulses need to be developed.

$$\frac{1}{2}\rho A C_d (V - V_w)^2$$

$$F_t$$

$$MgC_{rr}\cos(\theta)$$

$$Mg\sin(\theta)$$

$$\theta$$

$$Mg\cos(\theta)$$

$$Mg$$
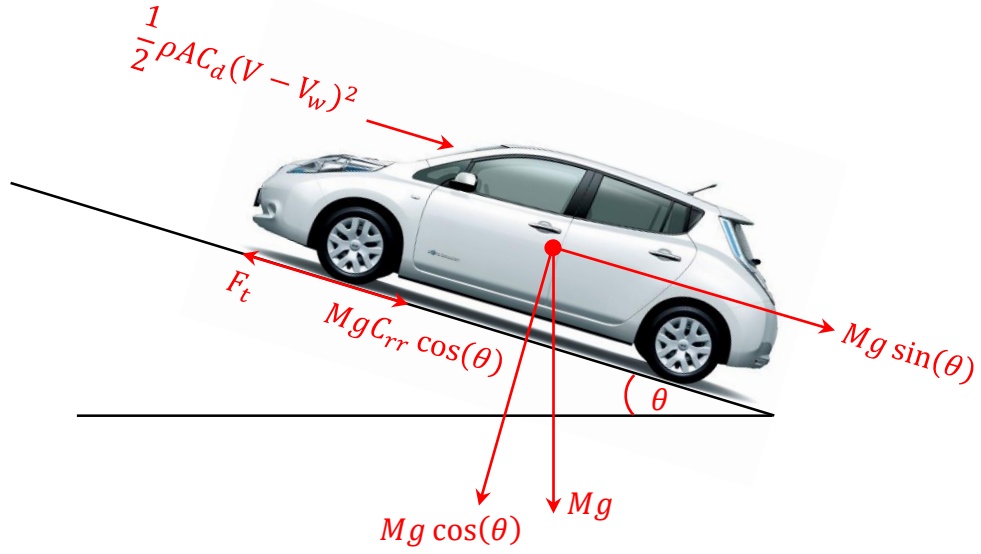
Fig. 2.23 Free-body diagram illustrating the forces applied on a Nissan Leaf EV

In this thesis, the electric power consumption for the propulsion of a battery-powered EV is calculated and scaled accordingly for safe testing of the NMC and LFP cells. Without loss of generality, in this thesis, the power calculations are performed for an old version of the Nissan Leaf EV. The EV model is based on the mechanical and aerodynamic forces that must be overcome to propel the vehicle. In general, the acceleration of an EV is determined by a force-balanced equation, which is given by Newton's second law as,

$$M\alpha = F_t - \sum F_r \tag{2.21}$$

where $M = 1521$ kg is the vehicle's overall mass, α is the acceleration, F_t is the total traction force provided by the powertrain and $\sum F_r$ is the sum of all resistive forces acting on the vehicle. The resistive forces usually are comprised of the friction between the tires and the road surface, aerodynamic drag and a resistance due to the track slope. Now, considering the free-body diagram illustrated in Fig. 2.23, the total resistive forces can be estimated using equation (2.22) [207].

$$\sum F_r = MgC_{rr}\cos(\theta) + \frac{1}{2}\rho AC_d(V - V_w)^2 + Mg\sin(\theta) \qquad (2.22)$$

where $g = 9.81 \text{ ms}^{-2}$ is the gravitational acceleration, $C_{rr} = 0.012$ is the rolling-resistance coefficient, $\rho = 1.225 \text{ kgm}^{-3}$ is the ambient air density, $A = 2.27 \text{ m}^2$ is the vehicle's frontal area, C_d is the aerodynamic drag coefficient, V is the speed of the vehicle, V_w is the speed of wind, and θ is the slope angle. Thus, by rearranging equations (2.21) and (2.22), the EV's total traction force can be calculate as,

$$F_t = M\alpha + MgC_r\cos(\theta) + \frac{1}{2}\rho AC_d(V - V_w)^2 + Mg\sin(\theta). \qquad (2.23)$$

Finally, the instantaneous power required to accelerate the EV up to a demanded velocity, or maintain it at a given constant velocity can be expressed as,

$$P = F_tV = M\alpha V + MgC_rV\cos(\theta) + \frac{1}{2}\rho AC_dV(V - V_w)^2 + MgV\sin(\theta). \qquad (2.24)$$

Here, the EV is assumed to be running on a relatively flat surface (i.e. $\theta \approx 0°$). During the initial stage of acceleration, the traction battery must be able to provide the power required to overcome mainly the rolling resistance in the tires. It should be noted that during deceleration, α becomes negative. This implies that the vehicle's kinetic energy can be used to overcome the resistive forces acting on it, whilst the excess can be converted into electrical energy and stored in the battery for later use. Now, considering the power equation expressed by (2.24), it is possible to approximate the instantaneous current C-rate required of the traction battery to achieve a step change in the EV's dynamic velocity.

$$\Delta E = P \cdot \Delta t, \qquad \Delta Q = \frac{\Delta E}{V_{\text{nom}}}, \qquad I_{\text{bat}} = \frac{\Delta Q}{\Delta t}, \qquad C_{\text{rate}} = \frac{I_{\text{bat}}}{C_{\text{bat}}},$$
$$I_{\text{cell}} = C_{\text{rate}} \cdot C_{\text{cell}}$$

$$(2.25)$$

where ΔE is the instantaneous electrical energy required over a period of Δt seconds; ΔQ is the resulting change in the ampere-second capacity; V_{nom} is battery pack's nominal voltage; I_{bat} is the amplitude of the current demanded from the battery pack; C_{bat} is the battery's nominal capacity; C_{rate} is the required C-rate current; and I_{cell} is the cell-level current demand based on a cell with an Ah capacity of C_{cell}. Conventionally, the direction of current flow in a battery is considered positive for discharge and negative for charge. Also, it should be noted that, since the current demand profile calculated based on equation (2.25) is an approximation, it is safe to assume that the EV's electrical and mechanical systems operate under a best-case scenario (i.e. $\approx 100\%$ efficiency).

Fig. 2.24 Composition of Nissan Leaf's 24 kWh LMO battery pack [208]

Fig. 2.24 above depicts the composition of the battery pack employed in a Nissan Leaf [209]. It is comprised of 48 modules in series, where each module is made up of 4 cells, arranged in a 2-series-2-parallel (2S2P) formation. Each cell has a nominal voltage of 3.75 V, with a capacity of 32.5 Ah. Therefore, by summing the cell voltages in series, and the capacities in parallel, V_{nom} and C_{nom} for the complete pack can be calculated as 360 V and 65 Ah, respectively. However, in practice, only 60 Ah of the pack's total capacity is made available to avoid battery operation in highly non-linear SOC regions. These two parameters are then applied to equation (2.25) to

obtain the cell-level current profile for the LFP and NMC test cells (see Table 2.5), when imposed to a dynamic EV drive cycle. Two standard speed profiles are used here; the New European Drive Cycle (NEDC) and the Artemis Motorway drive cycle.

2.3.2.7 New European Drive Cycle (NEDC)

(a)

(b)
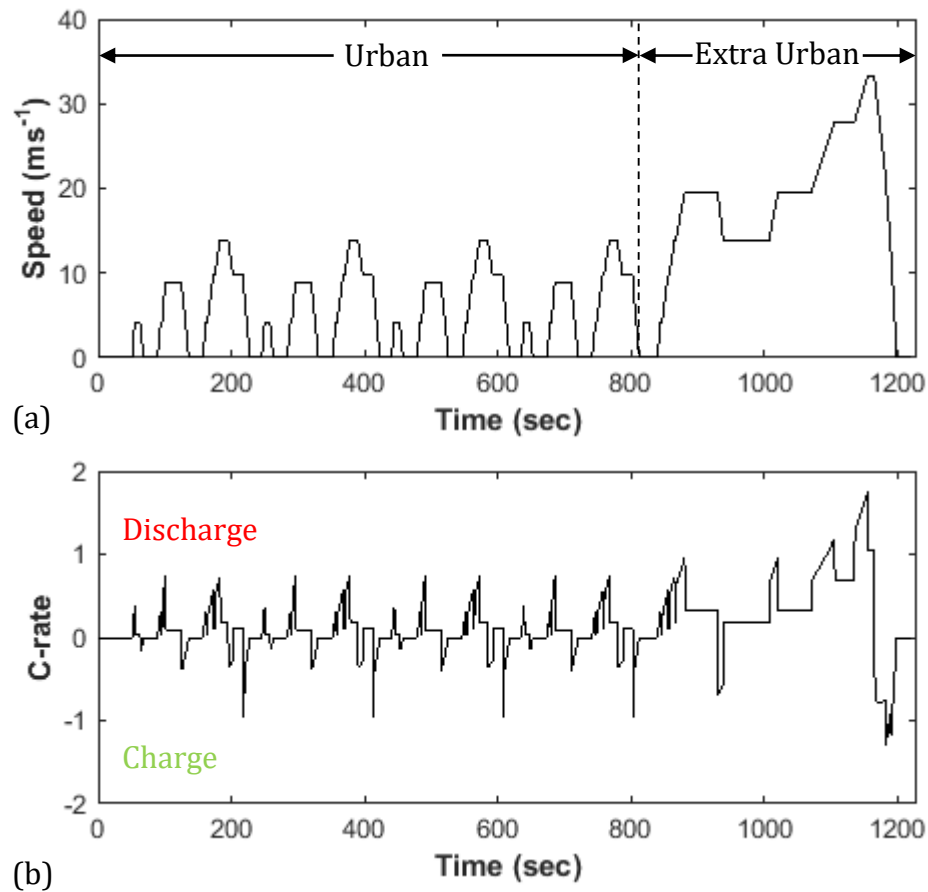
Fig. 2.25 (a) speed and (b) C-rate profile for energy-specific NEDC drive cycle

The NEDC is a relatively modest drive cycle that is regularly used in the European Union for type approval of light-duty vehicle models, including EV/HEVs [210]. As depicted in Fig. 2.25(a), this dynamic profile consists of periods of constant acceleration, deceleration or regenerative braking and speed, which is particularly useful when testing for the energy capability or range of an EV's traction battery.

Despite the unrealistic driving patterns observed in the NEDC profile, it is employed by many researchers to serve as a laboratory-based platform for online verification of different SOC estimation techniques. In this thesis, the C-rate profile derived

based on the NEDC drive cycle data is scaled accordingly and applied to each LFP and NMC test cell at a range of different operating temperatures. This is to gather a valuable dataset for the verification of the battery SOC and parameter estimation techniques to be reported under dynamic discharge conditions.

2.3.2.8 Artemis Highway Free Urban (ArtHiUFL) drive cycle
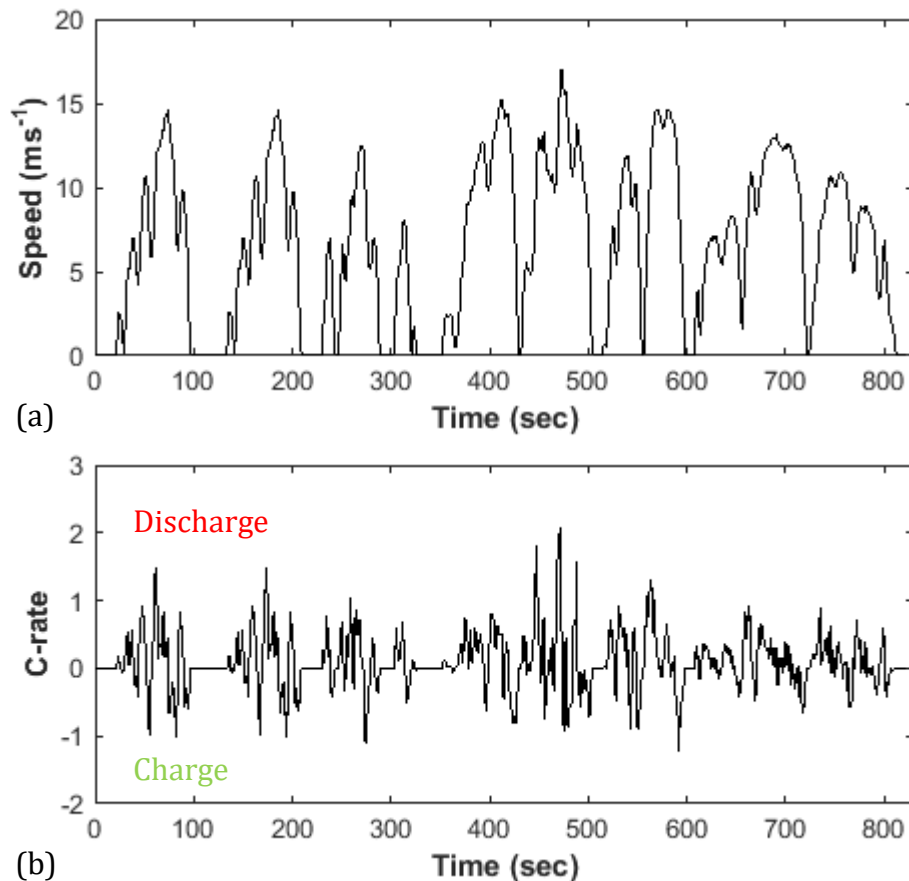
Fig. 2.26 (a) speed and (b) C-rate profile for power-specific ArtHiUFL drive cycle

Using more than one transient profile for the verification of newly developed BMS algorithms is a respected approach. As a result, another European drive cycle, namely the ArtHiUFL (see Fig. 2.26), is adopted to generate a more realistic dataset for further validation of the proposed battery parameter estimation techniques. As can be seen in Fig. 2.26(a), the ArtHiUFL speed profile consists of short moments of intense acceleration and deceleration, which in terms of electrical power required of the traction battery can be interpreted as a high-amplitude discharge or charge current pulse. Therefore, the results obtained from this particular profile at various

temperatures are used to investigate the dynamic performance of a proposed impedance-based battery power prediction algorithm.

2.4 Chapter conclusions

This Chapter has reported on the *state-of-the-art* of various battery technologies and their applications. It was shown that, due to their enhanced energy and power capabilities, lithium-ion batteries are becoming the preferred solution to many energy storage and supply problems. Also, it was discussed that without optimisation of battery monitoring algorithms, the future uptake of lithium-ion batteries in safety-critical applications would remain a challenge. Therefore, in this Chapter, a comprehensive review of the current battery state and parameter estimation techniques has been provided. The operational battery states of interest in BMS applications, and in this thesis, have been identified as SOC, SOH and SOP. Similarly, the battery parameters of interest are impedance and capacity. In general, battery states and parameter estimation methods can be categorised into inferred, book-keeping, model-based and filter- or observer-based groups. Model-based techniques are very popular for online BMS applications. This is owed to the physical relationship that exists between different model parameters and battery operating conditions, which can serve as good indicators for not only SOC, but also for SOH and SOP as well. Finally, the experimental setup adopted in this thesis is described; it offers two variants of lithium-ion cell chemistry (i.e. NMC and LFP), professional battery testing equipment and dynamic profiles derived based on standard EV/HEV drive-cycle data. These dynamic profiles are employed for online verification of the proposed battery identification techniques under 'realistic' application conditions.

Chapter **3**

A Low-Cost µP-Based Power Cycler for Online Lithium-ion SOH Estimation and RUL Prediction

Despite the many advantages of rechargeable batteries, their capacity degradation still remains an issue in most power applications. The SOH is a qualitative measure of the battery's charge storage capability, which is a key factor in determining the battery's end-of-service-life or RUL; thus, preventing unintended power shortages. There are many researches on battery SOH estimation algorithms, however, almost all of the proposed techniques in literature are verified using expensive laboratory-based battery testing equipment and powerful computers which may not be a practical choice for most applications. Therefore, in this Chapter, a low-cost microprocessor-based battery power cycler, for the purpose of SOH characterisation is designed and implemented. Moreover, an online SOH estimation technique is proposed, which is embedded on the microprocessor unit for real-time operation. Finally, an empirically-derived model for battery remaining-useful-life or RUL prediction is developed based on the first 3-4% of SOH degradation. The performance of the proposed hardware design and the SOH estimation technique are experimentally verified on two 3.3 Ah LFP cells, imposed to a series of constant-current degradation cycles at 1C current level and a controlled ambient temperature of 25°C.

3.1 Introduction

One of the main issues associated with the utilisation of rechargeable batteries in power applications is the degradation of their ability to convert and store electrical energy to chemical energy and vice versa. This property is better known as SOH, which was discussed in Chapter 2, section 2.2.5. The SOH is an inherent characteristic of the electrochemical energy storage devices such as batteries, where the formation of the SEI layer called the solid electrolyte interphase (SEI) over the negative electrode causes an increase in the battery's equivalent series resistance and a decrease in the maximum charge storage capability of the battery [149]. The SOH estimation plays an important role in the following:

- Early diagnosis of the close-to-failure cells in a battery pack;
- Estimating the end-of-cycle-life of a safety critical battery-powered system;
- Improved prediction of the battery functionality in response to a particular power demand;
- Optimisation of the performance of a particular BMS.

Various SOH estimation techniques have been presented in literature with each having its own advantages and drawbacks. Many of these techniques estimate the SOH through the characterisation of the battery's internal parameters [211][212]. These parameters may include the battery's charge/discharge impedance, current rate, terminal voltage, temperature and SOC, each of which vary dynamically according to the imposed application profile. For example in [213] the author has used the battery's maximum releasable capacity to estimate the SOH of Li-ion batteries. Gould *et al.* [92] have used a modified second-order Randle's model together with a Kalman filter estimator for online prediction of the SOH for Li-ion batteries. Another SOH estimation technique for Li-ion batteries is realised in [177] that uses the battery's SOC and a dual-sliding-mode observer. Micea *et al.* [214] have addressed the issue of the SOH prediction for NiMH batteries in embedded system applications and proposed a new SOH estimation technique based on a second-order parabolic regression model which estimates the battery's capacity fade online. In [137], an alternative approach to online estimation of the battery SOH is used based on a support vector regression model and the incremental capacity analysis

of the battery. Although the techniques presented by the authors demonstrate good performance, due to their computational power requirements, their integration for real-time applications is not practical.

Almost all the research presented in literature on various BMS algorithms are validated on host personal computers (PC). This has been perceived as a motivation to develop a low-cost micro-processor (μP) based platform for the cycling and SOH estimation of lithium-ion battery cells. To this end, this Chapter initially puts its focus on the design of a bidirectional μP-based power cycler that is capable of measuring and monitoring the cell's terminal voltage, current and temperature of battery cells of lithium-ion chemistry. Thereafter, an online SOH estimation technique is proposed based on the linear approximation of the relationship between the cell's terminal voltage and removed ampere-hour charge over the linear region of the cell's operation. The proposed technique is then implemented on the μP unit and experimentally verified on two LFP cell variants of lithium-ion chemistry. Finally, an empirically derived mathematical function is used to predict the cells' RUL. The findings of this Chapter have been presented in [215].

3.2 An Online SOH Estimation Technique

As mentioned in Chapter 2, the SOH is a qualitative measure of the battery's capacity fade due to the irreversible ageing process and is largely dependent on the battery's SOC, operating temperature, current rate and other external stress factors [216]. In a typical power application, the battery's terminal voltage and current are readily available to the incorporated BMS. The maximum discharge capacity or Q_{max} (i.e. integral of battery current over discharge time) measured in ampere-hour is a commonly used parameter for the estimation of battery's SOH. A definition for SOH can be given in the form of,

$$\mathrm{SOH}(\%) = \frac{Q_{\mathrm{max}}(n)}{Q_{\mathrm{max}}(0)}, \qquad n = 1, 2, \ldots, N \qquad (3.1)$$

where $Q_{\mathrm{max}}(0)$ and $Q_{\mathrm{max}}(n)$ are the maximum charge released from a completely new and aged batteries/cells, respectively. However, in applications such as in EV/HEVs, for various reasons including over- and under-voltage protection and linear-behavioural operation, the battery voltage is restricted to a smaller operating range, where the battery behaviour is fairly linear. This prohibits the battery from being fully charged or discharged, making Q_{max} unattainable; thus, the online implementation of the SOH estimation technique based on direct measurement of Q_{max} becomes impractical.

As a result, an online SOH estimation technique is developed in this Chapter. The experimental cell ageing data on a lithium-ion cell from the NASA public database [217] have been adopted to verify the proposed SOH estimation technique prior to any experimental work on real lithium-ion cells. The public dataset consists of 168 cycles of charge and discharge on a 2 Ah lithium-ion cell at a temperature of 24°C. The charging process was carried out in a constant-current (CC) mode at 1.5 A until the cell's voltage reached 4.2 V and then continued in a constant-voltage (CV) mode until the charge current dropped to 20 mA. The discharge was then performed at a CC rate of 2 A until the voltage reached 2.7 V. The cell's SOH after every successive cycle is then calculated using the measured discharge capacity and equation (3.1).

Fig. 3.1(a) illustrates the relationship between the cell's discharge capacity and terminal voltage as a function of SOH. Within the linear region of cell's operation, (i.e. between $\sim$10-90% SOC) the non-linear Q-V relationship can be approximated to that of a straight line given as,

$$Q_{\mathrm{max}}^{\mathrm{lin}} = aV_{\mathrm{t}}^{\mathrm{lin}} + b \qquad (3.2)$$

where $Q_{\mathrm{max}}^{\mathrm{lin}}$ and $V_{\mathrm{t}}^{\mathrm{lin}}$ are the battery's maximum Ah capacity and terminal voltage, respectively, measured over the battery's linear region of operation. The parameters a and b are determined online by fitting (3.2) to the acquired data using a linear least squares method to be reported in section 3.3.3. Fig. 3.1(b) presents the linearised cell capacity as a function of terminal voltage for the public NASA ageing dataset.
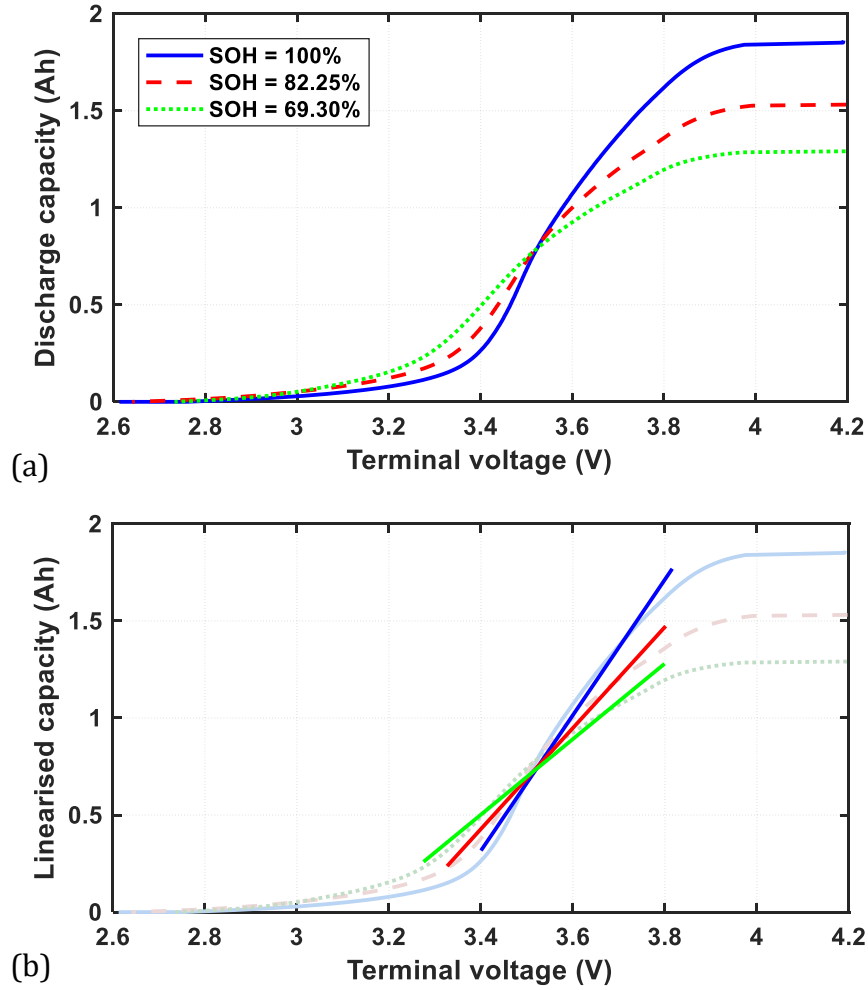
Fig. 3.1 Relationship between cell discharge capacity and terminal voltage as a function of SOH, (a) measured and (b) linearised

It is evident that as the cell's SOH deteriorates, the slope of the linear fit declines with, indicating a loss in the cell's maximum charge-storage capacity. Therefore, a quantitative definition for the cell's SOH can be derived and given as,

$$\widehat{SOH}(n) = \frac{a(n)}{a(0)} \times 100\% \qquad (3.3)$$

where $a(n)$ and $a(0)$ are the slopes for the nth cycle and that of a new cell, respectively.

Fig. 3.2 presents the measured and estimated SOH results, using (3.3), which pose a good agreement with each other, verified against an average percentage-point error

of less than ±0.5%. Due to the temperature and load dependency of the cell terminal voltage, any small variations in these two variables would greatly affect the accuracy of the SOH model. For example, at 90th cycle, a spike in the error plot shown by Fig. 3.2(b) is observable, which can be attributed to changes in the test cell's conditions, causing such large estimation error. Thus, for applications with dynamic load profiles, it is advantageous to use the cell's OCV relationship with the battery's maximum releasable charge capacity when approximating the slope of the Q-V profile. Although, the OCV must be estimated while the battery is operating online, which will necessitate for more advanced algorithms to solve.

(a)

(b)
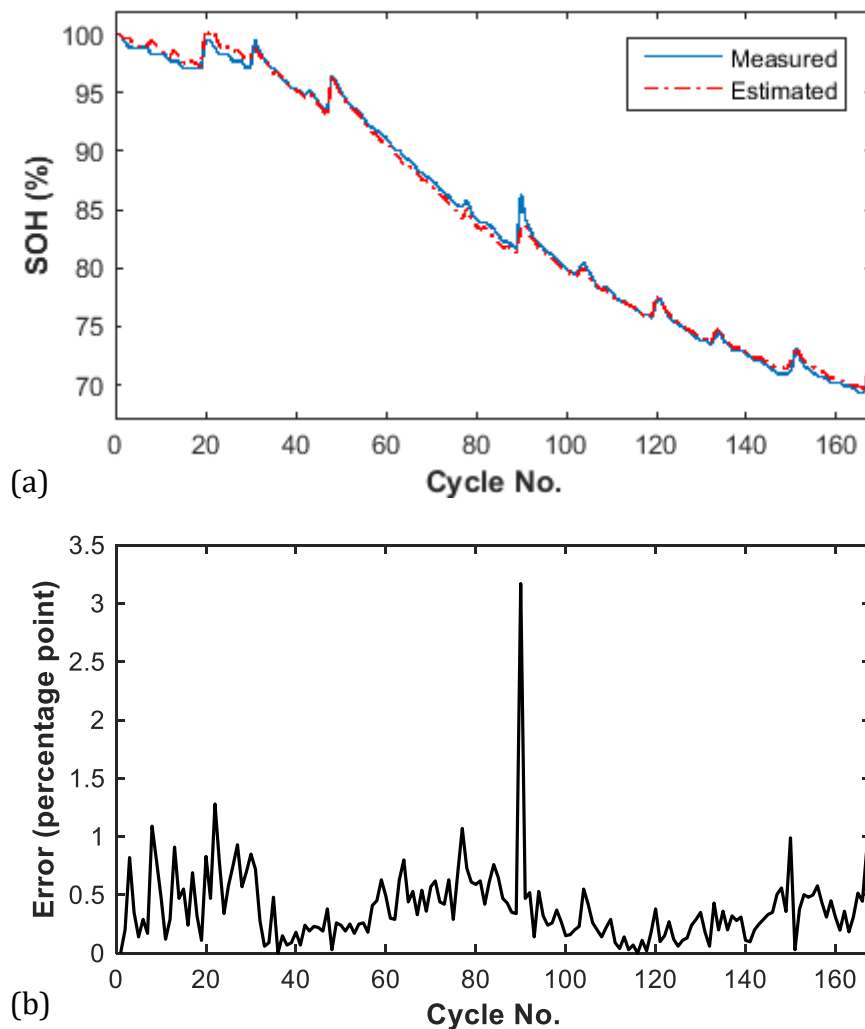
Fig. 3.2 Comparison of the measured and estimated SOH for the public NASA dataset

3.3 µP-Based Cell Power Cycler Design and Implementation

The cell power cycler proposed in this thesis (see photo displayed in Fig. 3.3) benefits from an inexpensive design by sharing the same components for both charging and discharging circuitry. Fig. 3.4 shows the block diagram of the proposed system, consisting of an 8-bit Atmel µP unit which can be programmed to control the switch between the charge and discharge modes, whilst allowing for up to sixteen 10-bit ADC channels for data logging. The single-channel power cycler is rated at 10 A – 5 V. The mode switching is realised by a double-pole double-throw (DPDT) relay, which configures the electrical path between the cell under test and the charger or discharger circuitry accordingly. A second DPDT relay is also employed to provide a complete isolation of the cell terminals for safety purposes. The µP unit is sourced with a regulated 12 V power supply (VCC), whereas, the DC link for battery charging (V_{dc}) is provided by an external power supply at 7 V.
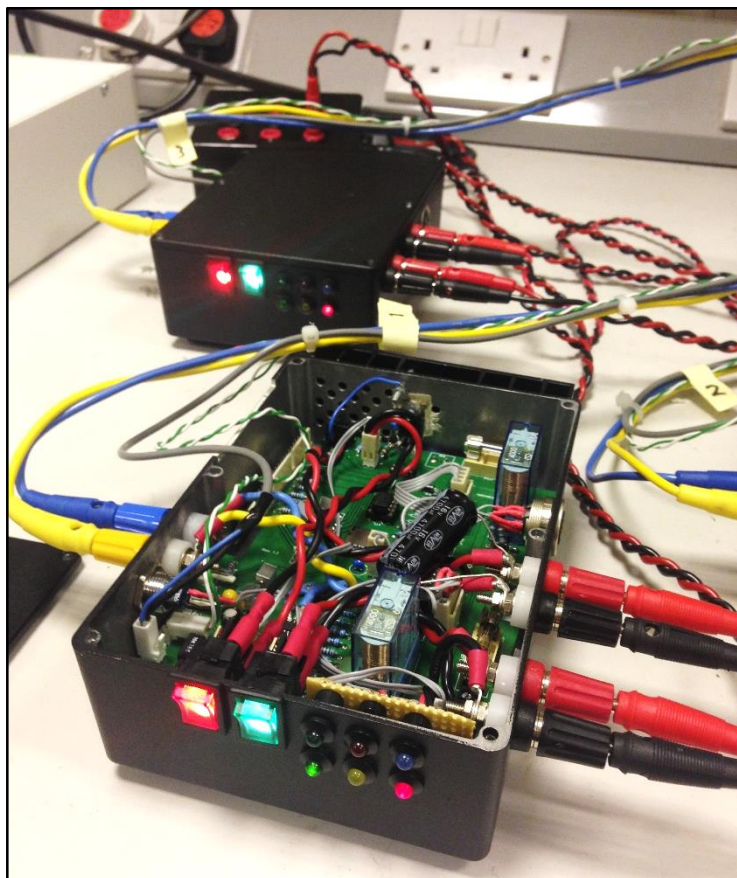
Fig. 3.3 Photograph of the proposed lithium-ion cell cycler on test bench
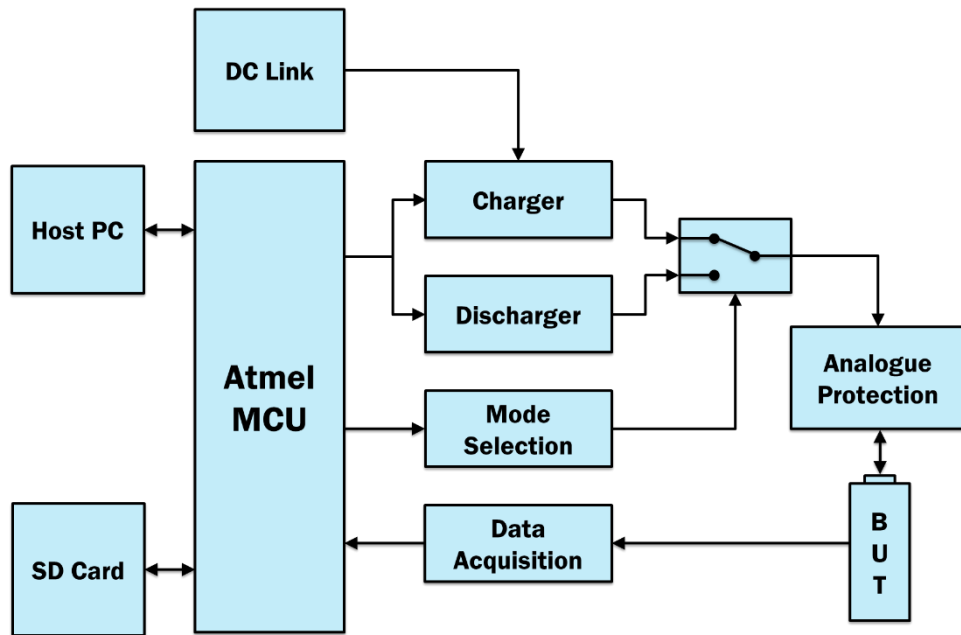
Fig. 3.4 Block diagram for the proposed lithium-ion cell power cycler design

The μP unit is also responsible for controlling the amount of charge being injected or removed from the battery cell by sampling its terminal voltage and current in order to create a feedback control loop. The acquired data can then be written onto a micro SD card for storage and sent via a serial peripheral interface (SPI) to a host computer for real-time monitoring and SOH estimation purposes.

3.3.1 Hardware Configuration

Fig. 3.5(a) and (b) show the block diagrams for the charger and discharger circuits, respectively. In both modes of operation, a power MOSFET is implemented as a linear current controller to allow a maximum charge/discharge current of 10 A to/from the cell under test. To drive the MOSFET, a second order low-pass filter is designed (with a corner frequency of f_c = 1 Hz) in order to convert the digital pulse-width-modulated (PWM) command signal from the Atmel μP unit into a clean analogue reference signal for the op-amp gate driver. Therefore, by regulating the PWM duty cycle, the rate of charge injection or removal from the cell under test can be fully controlled.

The maximum output current for the charger is calculated as,

$$I_{c(max)} = \frac{V_{ref} - V_c}{R_s + R_i} \tag{3.4}$$

where V_{ref} is the low-pass filtered input signal to the op-amp, V_c is the cell's open circuit voltage (OCV), R_s is the shunt resistance and R_i is the cell's equivalent series resistance. Equation (3.4) shows that for a cell under charge, the maximum charging current is determined by the amplitude of the PWM signal at 100% duty cycle, and the shunting resistance.

The voltage source to the charging circuit is taken from an external power supply whose level is calculated based on the assumption that, at maximum load current, the MOSFET is biased to its pinch-off point in order to avoid excessive resistive losses. Thus, by using Kirchhoff's voltage law, the maximum DC voltage, V_{dc}, required for constant-current charging can be given as,

$$V_{dc} = I_{c(max)}\left(R_{ds(ON)} + R_s + R_i\right) + V_c \tag{3.5}$$

where $R_{ds(ON)}$ is the MOSFET's on-state resistance.

The total dissipative power during the charge and discharge processes can be given by equations (3.6) and (3.7), respectively.

$$P_{diss} = I_c^2(r_{ds} + R_s + R_i) \tag{3.6}$$

$$P_{diss} = I_d^2(r_{ds} + R_d + R_i) \tag{3.7}$$

where r_{ds} is the series-resistance of the MOSFET operating in its linear region as given by (3.8). In the discharge mode, R_d is the shunt resistance and I_d is the controlled discharging current as per (3.9).
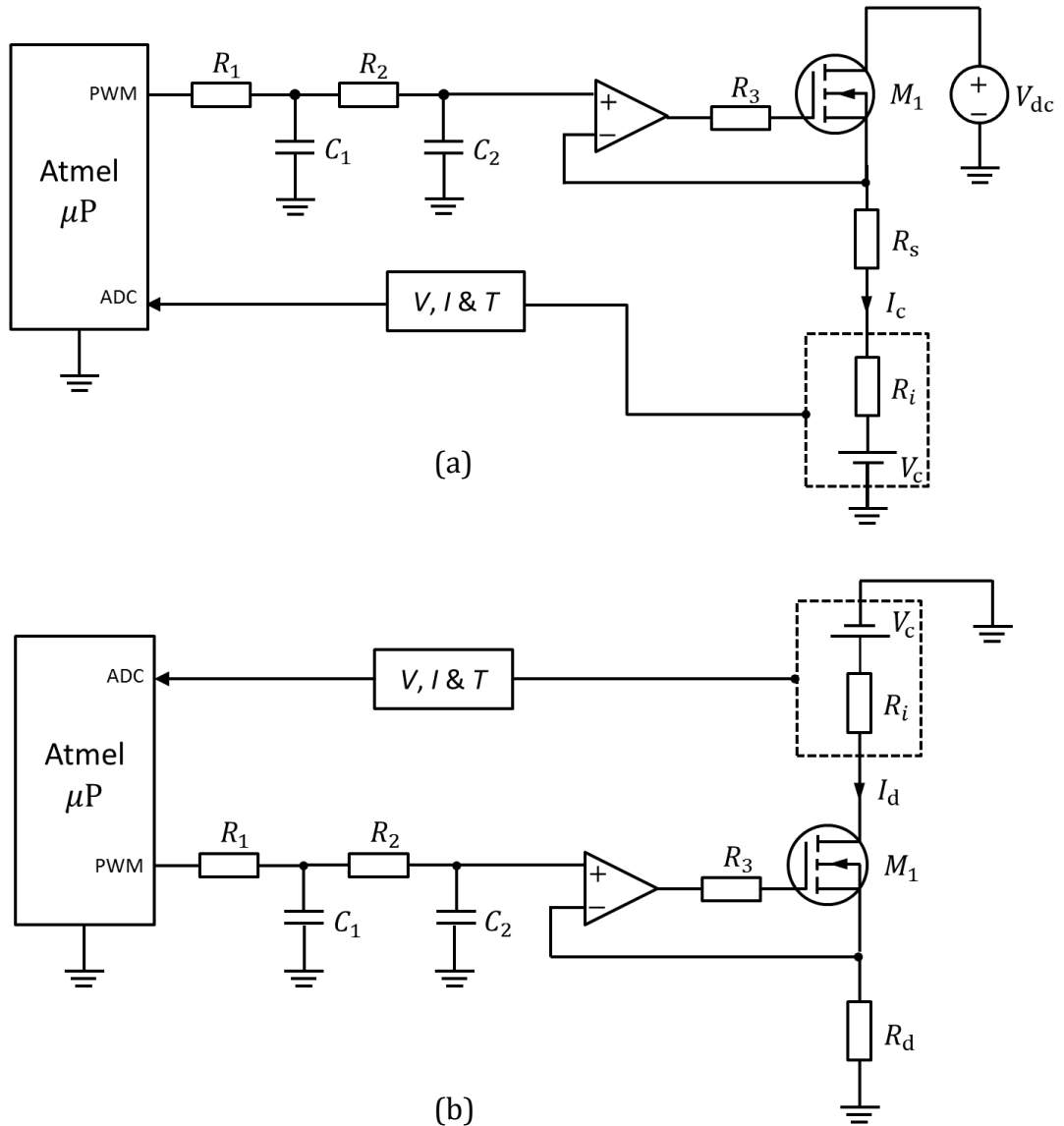
Fig. 3.5 Schematic diagrams for (a) charge and (b) discharge modes of operation

$$r_{ds} = \left(\frac{V_c}{I_d}\right) - (R_i + R_d) \tag{3.8}$$

$$I_d = \frac{V_{ref}}{R_d}. \tag{3.9}$$

Due to the electrochemical nature of batteries, it is vital to keep them within their safe operating conditions to prevent fire and explosion. The μP is responsible for protecting the device under test (DUT) from over- or under-charge conditions. For

additional safety, an analogue watchdog circuit is also added to act in case of a μP or ADC failure.
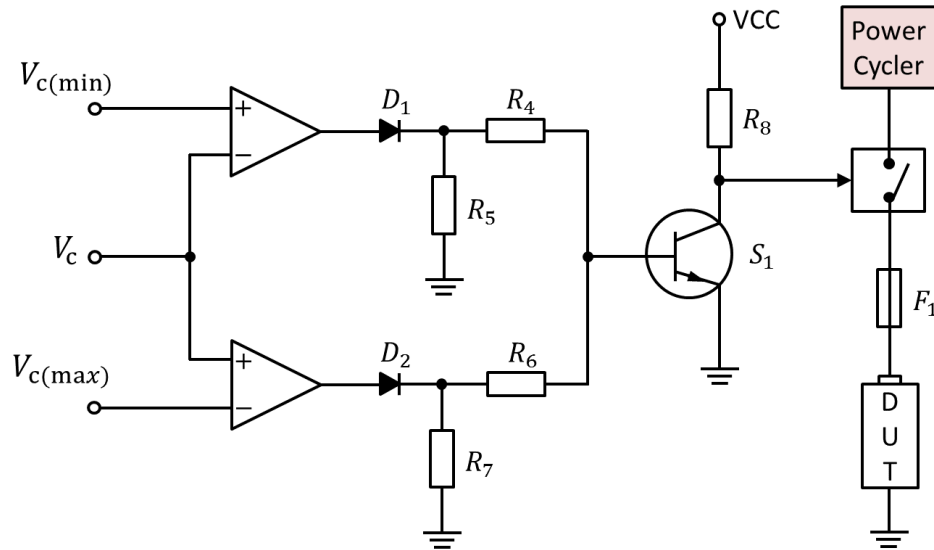
Fig. 3.6 Analogue cell protection circuit diagram

As shown in Fig. 3.6, the protection circuit consists of two comparators which continuously measure and compare the cell voltage against the minimum ($V_{c(min)}$) and maximum ($V_{c(max)}$) reference values. In the event of an over- or under-voltage, the respective comparator will force the transistor S_1 to close to isolate the cell terminals completely. The system is also fused at 10 A to protect the cell from over-currents. Finally, Table 3.1 is provided to summarise the chosen design parameters.

Table 3.1 Summary of design parameters

Parameter	Value
V_{dc}	7 V
$I_{c(max)}, I_{d(max)}$	10 A
R_s, R_d	100 mΩ
$R_{ds(ON)}$	20 mΩ
R_1, R_4, R_6	1 kΩ
R_3	10 Ω
R_2, R_8	10 kΩ
R_5, R_7	100 kΩ

3.3.2 Control Software
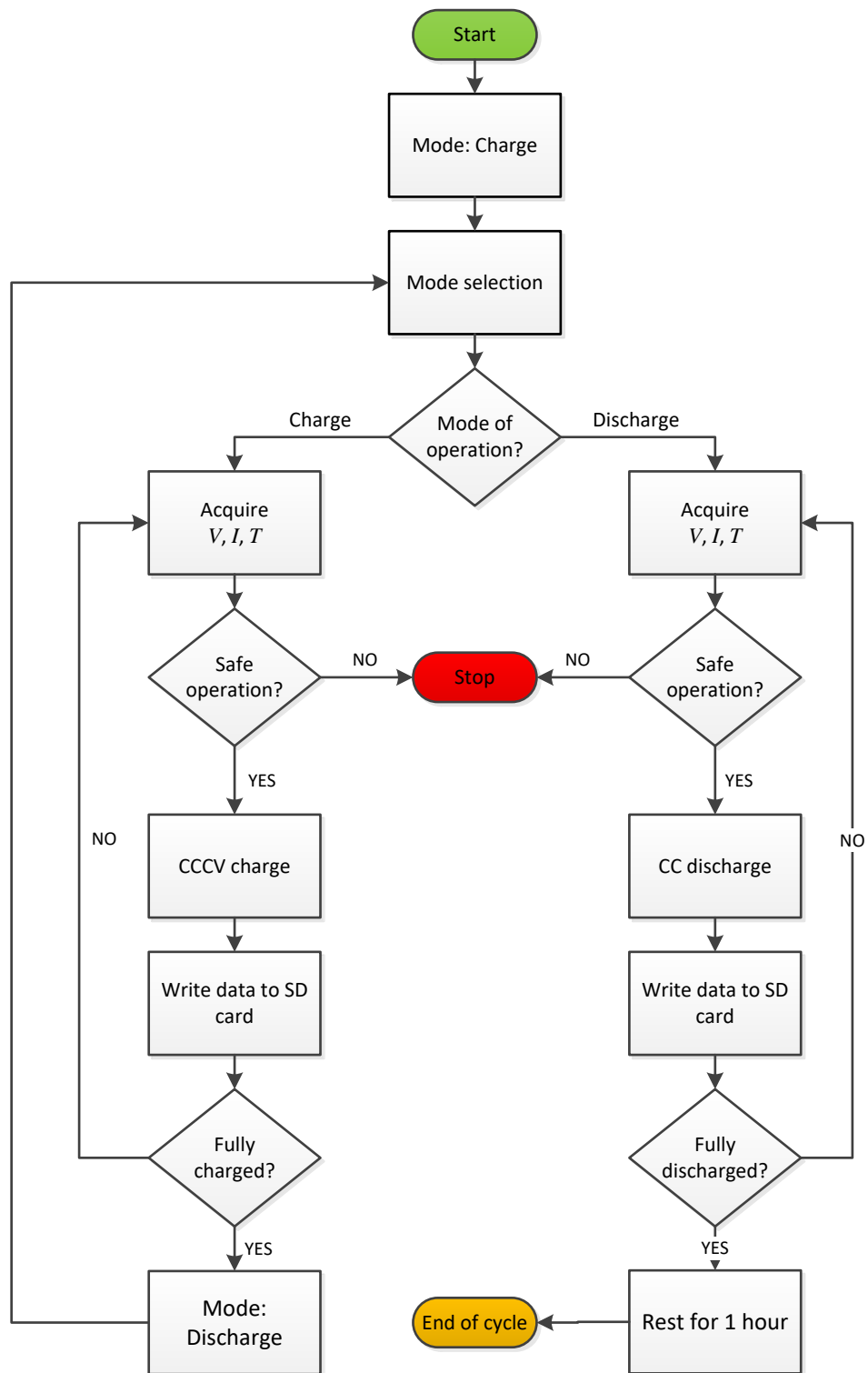
Fig. 3.7 Software flowchart showing procedure for one charge and discharge cycle

A software program for the 8-bit μP unit is developed, as depicted in Fig. 3.7. On start-up, the battery parameters (charge and discharge currents, safe ambient

operating temperature ranges, end-of-charge and end-of-discharge voltage thresholds, etc.) are read directly from the SD card. Upon the completion of initialisation, the controller starts by charging the DUT under a constant-current constant-voltage (CCCV) scheme.

During the constant-current (CC) charging mode, the PWM duty cycle is regulated accordingly to yield the commanded charge current. As the cell reaches its end-of-charge voltage, the controller switches to constant-voltage (CV) charging mode until the charge current drops to the cut-off threshold. Once the cell is fully charged, a zero-current relaxation period is allowed before changing to the discharge mode. Similar to the CC charging, under the CC discharge regime the PWM duty cycle is controlled to source the demanded current. The cell is then discharged until its terminal voltage reaches its end-of-discharge value. Throughout each cycle, relevant parameters (i.e. terminal voltage, current and temperature) are stored on an 8GB SD memory card.

3.3.3 Linear Least-Squares Method for μP Implementation

In order to obtain the parameters for the Q-V model given by (3.2) online using the 8-bit μP unit, a linear least-squares method, as described in [218] is adopted in this Chapter. First, the straight-line fitting problem over a set of N data points (x_i, y_i) is defined in a general form as,

$$y(x; a, b) = a + bx \qquad (3.10)$$

where y is the linearised cell capacity (i.e. $Q_{\max}^{\text{lin}}$), x is the terminal voltage (i.e. $V_{\text{t}}^{\text{lin}}$), and a and b are the model parameters in (3.2). Now, assuming the uncertainty σ_i associated with each measurement y_i is unknown (i.e. unweighted data $\sigma_i = 1$), and that x_i is known, the chi-square merit function given by (3.11) can be used to assess the resulting fit quality over the measured Q-V data.

$$\chi^2(a, b) = \sum_{i=1}^{N} \left(\frac{y_i - a - bx_i}{\sigma_i} \right)^2 \tag{3.11}$$

where, assuming the current and voltage measurement errors are normally distributed, (3.11) will yield a maximum likelihood parameter estimation of a and b. It should be noted that, if the measurement errors are not normally distributed, then a maximum likelihood estimate might not be achievable; though, they may still be useful in a practical sense. Subsequently, to obtain a maximum likelihood estimate of the parameters a and b, the chi-square function (3.11) must be minimised. This occurs when the derivatives of $\chi^2(a, b)$ with respect to a and b are equal to zero.

$$0 = \frac{\partial \chi^2}{\partial a} = -2 \sum_{i=1}^{N} \frac{y_i - a - bx_i}{\sigma_i^2}$$

$$0 = \frac{\partial \chi^2}{\partial b} = -2 \sum_{i=1}^{N} \frac{x_i(y_i - a - bx_i)}{\sigma_i^2}. \tag{3.12}$$

These two conditions may be re-written in a suitable form for online implementation on any μP such that,

$$S \equiv \sum_{i=1}^{N} \frac{1}{\sigma_i^2}, \quad S_x \equiv \sum_{i=1}^{N} \frac{x_i}{\sigma_i^2}, \quad S_y \equiv \sum_{i=1}^{N} \frac{y_i}{\sigma_i^2}, \quad S_{xx} \equiv \sum_{i=1}^{N} \frac{x_i^2}{\sigma_i^2},$$

$$S_{xy} \equiv \sum_{i=1}^{N} \frac{y_i x_i}{\sigma_i^2} \tag{3.13}$$

Rewriting (3.12) in terms of the sums defined in (3.13) yields,

$$aS + bS_x = S_y$$

$$aS_x + bS_{xx} = S_{xy}. \tag{3.14}$$

Therefore, the solution for the equation above with two unknowns (i.e. a and b) can be calculated as,

$$\Delta \equiv SS_{xx} - (S_x)^2$$

$$a = \frac{S_{xx}S_y - S_xS_{xy}}{\Delta} \qquad (3.15)$$

$$b = \frac{SS_{xy} - S_xS_y}{\Delta}.$$

Using equation (3.15), the best-fit parameters a and b (in a least-squares sense) for the linearised Q-V function (3.2) are computed. Thus, battery's SOH after every cycle can be estimated online using the definition given by (3.3).

3.4 Experimental Validation
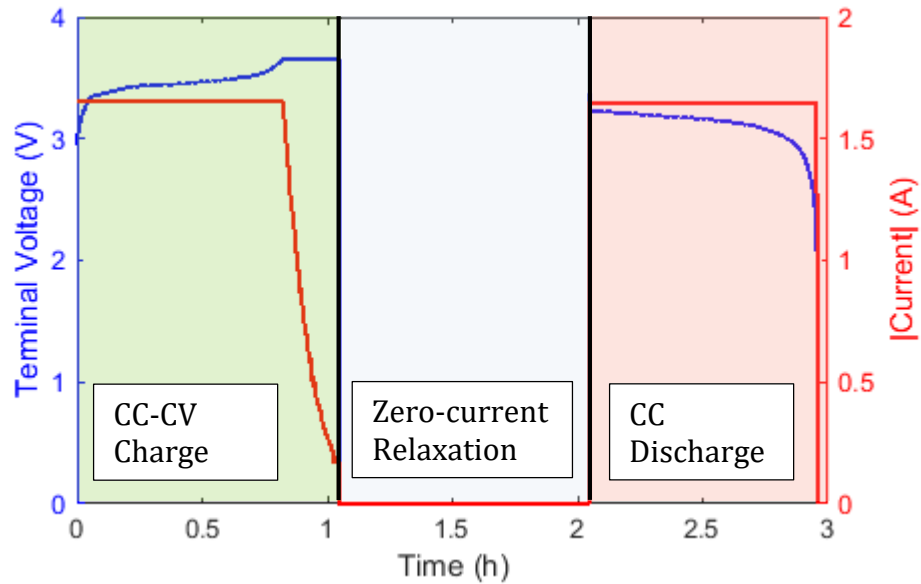
Fig. 3.8 Example of a degradation cycle, current and voltage waveforms

In order to validate the performance of the cell power cycler, together with the proposed SOH estimation method, and its application to battery RUL prediction, three new 3.3 Ah LFP cells (see Table 2.5 for test cell specifications) have been subjected to a series of degradation cycles, as presented in Fig. 3.8. Each cycle begins with a CCCV charging scheme at 3.3 A (1C) until the terminal voltage of the cell under test reaches 3.65 V and then continued in a CV mode until a current level of 300 mA is reached. Once the cell is fully charged, a zero-current relaxation period of 1 hour is allowed to ensure that the cell's internal state has reached a stable condition. Then

the cell is further applied with a CC discharge current of 3.3 A (1C) until its voltage drops to a cut-off value of 2.0 V.

Whilst the cell under test is being discharged, the measured terminal voltage and current are used to estimate the amount of charge being removed from the cell for the Q-V function generation. Thereafter, based on the generated Q-V dataset, the slope of the linear fit given in (3.2) is estimated for each cycle using the linear least-squares method described previously. Throughout the whole experiment, the test cells were kept in a thermally-controlled chamber at 25°C; thus, the validity of the SOH estimation technique proposed here at other operating temperatures requires further investigation which is outside of the scope of this Chapter.

The estimated SOH for the two candidate LFP cells using the SOH model developed in previous section are compared with that obtained from maximum discharge capacity measurements using (3.1); LFP cell 1 completed 200 charge/discharge cycles, while, LFP cell 2 went through 250 cycles. The results are presented in Fig. 3.9 and Fig. 3.10. During the first 100 cycles, LFP 1 experiences a SOH degradation of 2.5%, whereas for LFP 2, a degradation of around 4% is observed. It can be seen that the SOH estimated for the two test cells over the first 100 cycles have been estimated with an absolute error of less than 1 percentage point. This gives confidence to the performance capability of the proposed SOH model as implemented on the μP-based cell power-cycler.

As discussed in Chapter 2, section 2.2.5.2, RUL prediction is of necessity for a proper battery prognostic and health management [219]. Thus, an exponential RUL model is proposed herein, which is given as a function of cycle number, n, to predict the battery's RUL as a percentage of its maximum deliverable amp-hour capacity.

$$\text{RUL} = \frac{\exp(n^\alpha)}{(n^\beta - \zeta)} \times 100\% \qquad (3.16)$$

where the parameters α and β are rate-determining factors, while ζ is an offset, all to be identified offline, using a nonlinear least-squares method in MATLAB

(Levenberg-Marquardt algorithm). Notice that the estimated SOH quantities by the AVR μP unit are saved on the SD card and transferred to a host PC over the USB serial port for offline data-processing purposes.

The identified RUL model parameters for both LFP test cells, based on the SOH levels estimated for the first 100 cycles using the SOH model of (3.3) are presented in **Error! Reference source not found.**. As can be seen in Fig. 3.9 and Fig. 3.10, the measured SOH results for the LFP 1 appear to be more spread than those of the LFP 2. This can be attributed to the fact that the cells were tested in separate enclosures filled with sand for safety purposes, and stacked on top of each other, thus, causing an uneven temperature and capacity variation in the two LFP cells.

The parameters of the RUL model given by (3.16) are identified based on the first 100 power cycles (SOH estimates to the left of the dash line) and employed to train and identify the RUL model of (3.16). The results demonstrate excellent fit for both LFP test cells. According to the RUL prediction results attained at 100th cycle, LFP 1 was predicted to reach a SOH level of 96.77% after 197 cycles, whereas the actual SOH level at the 197th cycle was measured at 96.96%. Similarly, for LFP 2, it was predicted to reach a SOH level 94.54% after 250 cycles, whereas the actual SOH was measured at 94.68%.

It is evident that based on the first 100 cycles (~3-4% SOH degradation), the proposed battery RUL model, together with the online μP-based SOH estimation technique, is capable of producing a fairly accurate prediction for the degradation of the two LFP test cells. Despite the excellent performance of the proposed battery RUL prediction technique, its validity is limited to the number of completed cycles on each test cell. Further degradation cycles are required to verify the test cells' end-of-life cycle numbers, when their SOH level reaches 80%.

(a)

(b)
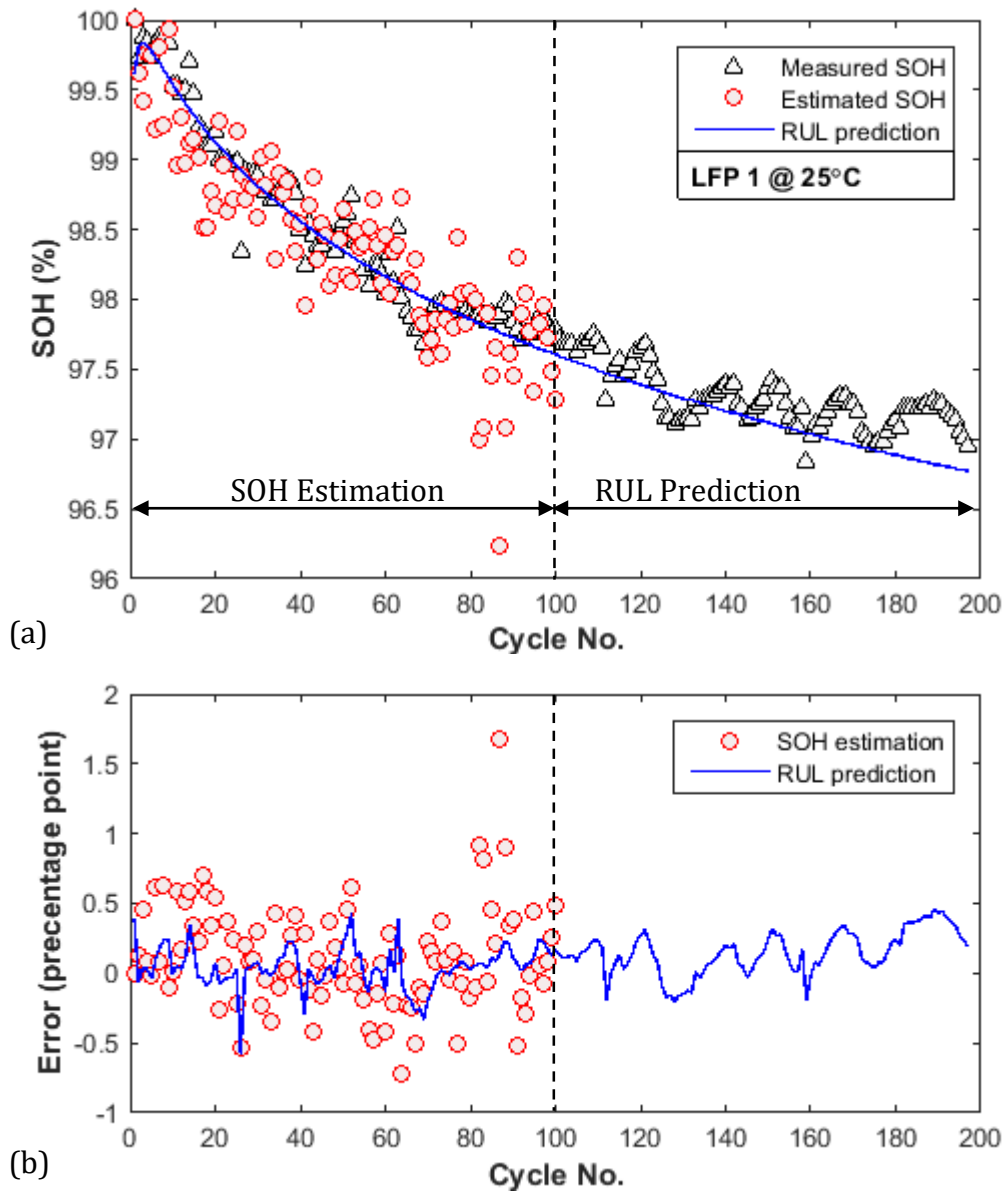
Fig. 3.9 SOH estimation and RUL prediction results for test cell LFP 1

Table 3.2 Identified RUL model parameters for the two LFP test cells

Test cell	α	β	ζ
LFP 1	-0.06658	-0.1938	-1.729
LFP 2	-0.08172	-0.2393	-1.733
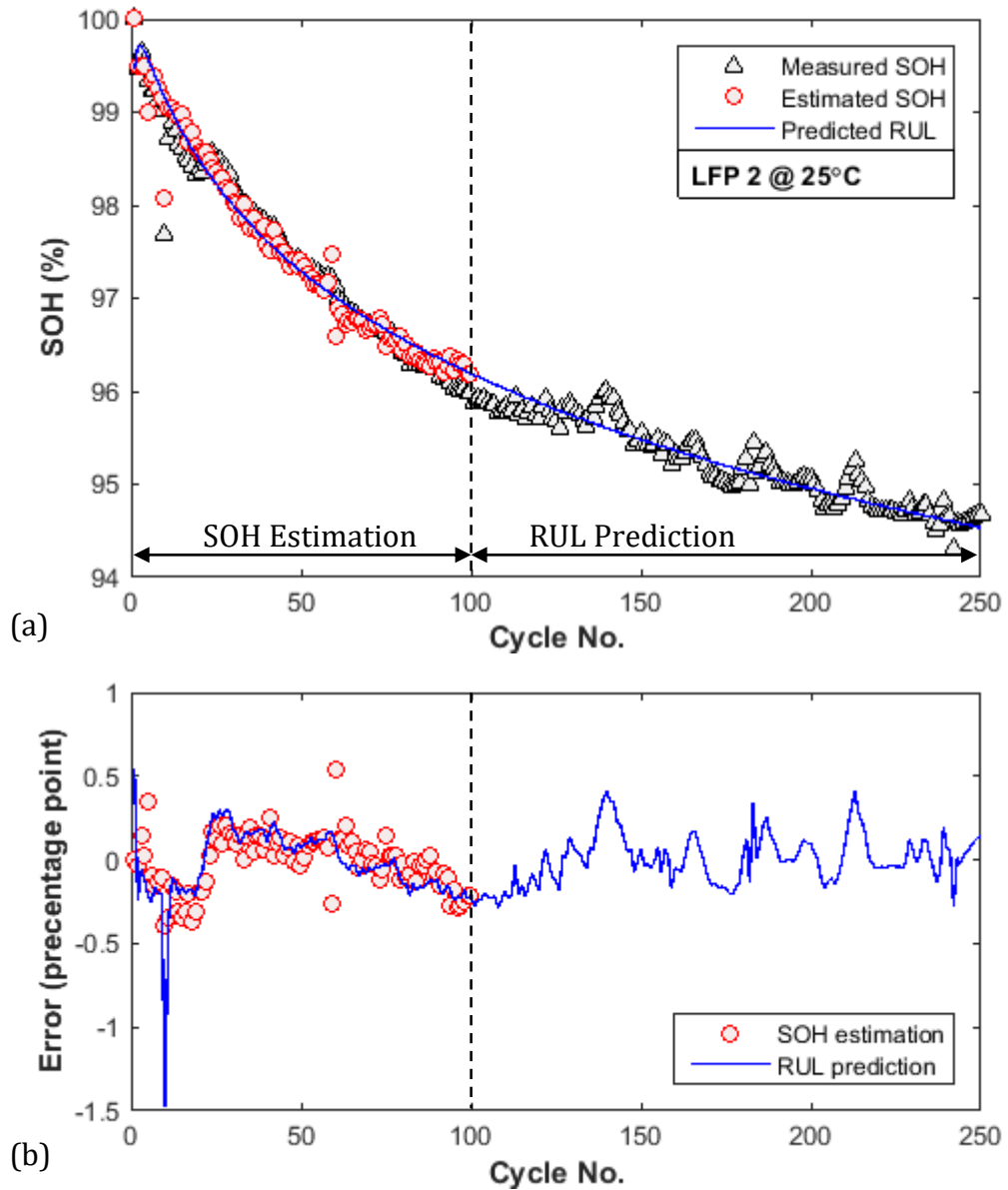
Fig. 3.10 SOH estimation and RUL prediction results for test cell LFP 2

3.5 Chapter Conclusions

In this Chapter 2, it was discussed that the SOH and RUL metrics play an imperative role in prognostics, and, thus, determining the end-of-service life of battery energy storage device to avoid any undesirable power shortages. The problem with most battery SOH estimation techniques proposed in literature is that they require for expensive lab-based testing equipment and powerful computers. As a result, this Chapter, at first, aimed to develop a low-cost μP-based lithium-ion cell power cycler

as a platform for the implementation of an online SOH estimation technique. The proposed technique included the linearisation of the relationship between the battery's terminal voltage and the released ampere-hour capacity during the linear region of battery operation. A direct relationship between the slope of the fitted straight line with the battery's age has been identified and demonstrated on a set of lithium-ion battery ageing dataset from NASA's public database. Moreover, the performance of the designed μP-based cell power cycler and the proposed SOH estimation technique has been experimentally verified on two new 3.3 Ah LFP cells. an excellent agreement between the measured and estimated SOH levels for the two cells has been observed, with an absolute percentage-point error of less than 1%. Finally, an empirically-derived model for the prediction of the test cells' remaining-useful-life or RUL has been developed. The RUL model parameters were identified offline based on the first 3-4% of SOH degradation (i.e. after 100 cycles for both LFP cells). According to the RUL model fitted using the SOH estimates obtained for the first 100 cycles, both cells' SOH at the end of 197th cycle for LFP1 and 250th cycle for LFP2 were predicted within ±0.5% percentage-point error, which is a significant achievement.

Chapter 4

An Experimental Study on Electrical Equivalent-Circuit Models for Real-Time Battery States Estimation

In Chapter 2, it was concluded that for online management of battery/cells, appropriate battery models, in terms of complexity and accuracy, are required. As a result, this Chapter reports on an experimental comparative study carried out on the most commonly used battery models in both motive and stationary BES applications. The models of interest include, the combined model, Rint model, two different hysteresis models, Randles model, a modified Randles model, and two resistor-capacitor (RC) network models with and without hysteresis included. To investigate the universality of the mentioned model structures, two lithium-ion cell variants of LFP and NMC are examined. For those models requiring a mathematical function to describe the OCV-SOC relationship, a polynomial function, whose order is empirically determined, is employed. Thereafter, a dual-EKF is designed to serve as an online cell model states (including SOC) and parameters estimator. The noise covariance matrices for the incorporated EKFs are estimated using an expectation maximisation (EM) method. Finally, the dynamic performance of the candidate models is experimentally verified. Analysis results on the ten cell models show that, both RC model structures provide the best dynamic performance with respect to terminal voltage, SOC and SOP estimation accuracy.

4.1 Introduction

As discussed in Chapter 2, a key function of the BMS is to assess and monitor the performance of the battery, through accurate characterisation of various battery states in real time. These states include the SOC, SOH, SOP and SOF. Whilst direct measurement techniques, such as coulomb-counting, are easy to implement for SOC estimation, they suffer largely from erroneous initialisation of SOC, drifts caused by current sensor noise, and battery capacity variations due to temperature and ageing. Moreover, the direct measurement of the other battery states of interest (i.e. SOH, SOP and SOF) for real-time applications is practically not possible.

Hence, battery models are often utilised within the BMS to indirectly infer and monitor the battery's various states through the measurement of its terminal voltage, current and surface temperature. In addition to the accurate characterisation of the battery states, a candidate model is also desired to be computationally efficient. In other words, there should be a balance between model accuracy and complexity so that it can easily be embedded on a simple and inexpensive microprocessor unit (MCU), similar to those found in EV/HEV BMS.

In literature, there are no studies that compare the accuracy and universality of the reported battery models for real-time estimation of SOC and SOP together. Therefore, this Chapter aims to carry out a systematic study on a number of selected electrical equivalent-circuit battery models for two variants on lithium-ion cell chemistry (i.e. LFP and NMC). The models of interest include the combined model, Rint model, one-state hysteresis model by Plett, Huria *et al.* hysteresis model, one- and two-*RC* models and one- and two-*RC* models combined with the hysteresis model proposed by Huria *et al* [220]. These models are nominated based on the number of their appearances in literature. The model parameters are then identified recursively using the nonlinear dual-EKF algorithm. It should be noted that the experimental results in this Chapter have been produced using the MACCOR battery tester as described in section 2.3.1.2.

4.2 Types of Battery Models

In general, the battery models presented in literature fall into one of the following categories:

1. Electrochemical or physics-based models;
2. Empirical or data-based models;
3. Equivalent electrical-circuit based models.

Electrochemical models (e.g. [221]–[225]) that aim to capture the dynamic behaviour of battery cells on a macroscopic scale often can achieve high accuracies. These models are defined by a high number of partial differential equations (PDEs) that must be solved simultaneously. The complexity of any electrochemical model is directly related to the number and order of the governing PDEs, which can lead to tremendous requirements for memory and computational power. Another issue that often precludes these models from real-time applications is that due to the large number of unknown variables, they are likely to run into over-fitting problems, increasing the uncertainty in the model's output. Alternatively, these models can be represented by a lower number of reduced order PDEs and by substituting boundary conditions and discretisation, real-time applications may become achievable (e.g. [226]–[228]). However, this comes at the expense of reduced SOC accuracy and yet the computational burden on the MCU remains questionable.

Data-based models (e.g. [229]–[231]) often adopt empirically derived equations from experimental data fittings to infer relationships between various battery parameters such as the terminal voltage, throughput current, surface temperature and SOC. Although these models benefit from simplicity and ease of implementation, they often suffer from inaccuracies of 5-20% [232], mainly due to the highly non-linear behaviour of a battery under a dynamic load profile. In [125], [233], the authors took a multiple-model approach to battery modelling using the local model networks (LMN). This technique interpolates between different local linear models to capture the battery's non-linearity due to SOC variations, relaxation, hysteresis, temperature and the battery current effects. One downside of the LMN modelling approach is the excessive requirements for different experiments to train the model

in first place. Generally, the data-based model parameters are not physically interpretable, which drops their popularity for *in situ* estimation and tracking of SOH and SOP. Furthermore, a large cell sample of the same chemistry is required to create a dataset for identification and training of data-based models.

In [146], [234], [235], Plett used a series of models including the combined, simple, zero-state hysteresis, one-state hysteresis and a non-linear enhanced self-correcting (ESC) model to adaptively estimate the battery's SOC. The latter model took into consideration the effects of the current direction, the SOC dependency of OCV hysteresis and the relaxation or the charge-recovery effect to improve the model accuracy for dynamic load profiles. In an attempt to model the OCV hysteresis behaviour together with the charge recovery effects, Roscher *et al.* [236] developed an empirical model whose parameters required off-line identification. In [220], Huria *et al.* proposed a mathematical model to describe the dynamics of the large hysteresis levels that exist amongst high-power lithium-ion cells. Further on in the Chapter, this model structure will be referred to as the adaptive hysteresis model.

The electrical equivalent-circuit models have gained a lot of interest amongst for real-time battery state estimation and power management purposes. This is due to their simplified mathematical and numerical approaches that minimise the necessity for computationally intensive procedures. Furthermore, there is often a strong physical relation between the constituent model parameters and the underlying electrochemical processes that occur within the battery cells. These models use passive electrical components, such as resistors and capacitors, to mimic the behavioural response of a battery. The simplest equivalent circuit model is in the form of an ideal voltage source in series with a resistor [76]. This model assumes that the demand current has no physical influence on the battery, i.e. no core temperature variations or undesired transition effects. To account for temperature variations, Howe *et al.* [237] proposed a sensor-less thermal-impedance battery model. More complicated equivalent models include parallel-connected resistor-capacitor (*RC*) branches with different time constants. Depending on the dynamics of the load profile and the required modelling accuracy, the number *RC* branches

may vary from one (e.g. [70], [232], [238], [239]) to two (e.g. [92], [169], [240]). Models of up to a fifth-order have also been proposed in literature (e.g. [241]).

4.3 Candidate Models for Online Implementation

The candidate battery model structures for the purpose of this comparative study are summarised in Table 4.1. These models form the basis for many real-time SOC, SOH, SOP and SOF estimation algorithms that appear in lithium-ion BMS applications. In this section, each model structure is described in terms of its constituent parameters, and using Kirchhoff's circuit laws, the input-output equations for each model structure is derived.

Table 4.1 Candidate battery models for online BMS implementations

Model	Description	Parameters
1.	Combined model, Equation (4.1)	$K_0, K_1, K_2, K_3, K_4, R_s$
2.	Rint model, (4.2)	R_s
3.	Huria *et al.* Hysteresis model, equation (4.3)	R_s, m
4.	Plett Hysteresis model, Equation (4.6)	R_s, h
5.	Randles' model, Equation (4.7)	R_s, R_d, R_t, C_b, C_s
6.	Modified Randles' model, Equation (4.9)	R_s, R_p, R_n, C_p, C_n
7.	One-*RC* model without Hysteresis, Equation (4.10)	R_s, R_1, C_1
8.	Two-*RC* model without Hysteresis, Equation (4.10)	R_s, R_1, R_2, C_1, C_2
9.	One-*RC* model with Hysteresis, Equations (4.10) + (4.3)	R_s, R_1, C_1, m
10.	Two-*RC* model with Hysteresis, Equations (4.10) + (4.3)	$R_s, R_1, R_2, C_1, C_2, m$

4.3.1 The Combined Model

The combined model [235] provides a very crude approximation of the battery's dynamics. As the name suggests, this model structure is a combination of the Shepherd model [230], Unnewehr and Nasar universal model [242] and the Nernst model [5]. The combination of these models results in a mathematical equation, which can be expressed as,

$$V_k = \underbrace{K_0 - \frac{K_1}{\text{SOC}_k} - K_2\text{SOC}_k + K_3\ln(\text{SOC}_k) + K_4\ln(1 - \text{SOC}_k)}_{V_{OC} = f(\text{SOC})} - I_k R_s \tag{4.1}$$

where V_k is the battery's terminal voltage and I_k is the throughput current. The battery's internal series-resistance is described by R_s and is a function of temperature and SOC. The constants K_0, K_1, K_2, K_3 and K_4 are used to describe the battery's OCV dependency on SOC. This model benefits from being linear in parameters and thus simplifies the identification procedure.

4.3.2 The Rint Model
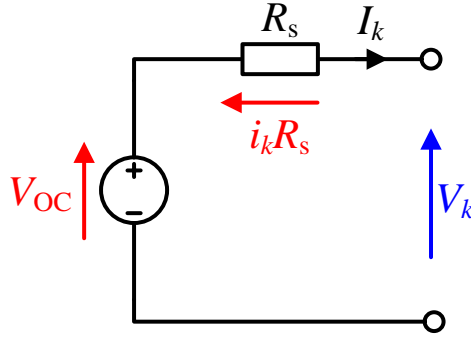
Fig. 4.1 Equivalent-circuit diagram for Rint model

The internal resistance or Rint model, as illustrated in Fig. 4.1, is comprised of an ideal voltage source V_{OC} to represent the battery's OCV as a function of SOC and a series resistor R_s that describes the internal ohmic losses [243]. This model structure is also linear in parameters and is very 'simple' to implement in real time. However, the model's output equation expressed by (4.2) is only a crude estimate of the battery's actual terminal voltage, which can result in large uncertainties in other model-based battery states (e.g. SOC and SOP).

$$V_k = V_{OC}(\text{SOC}_k) - I_k R_s. \tag{4.2}$$

4.3.3 The Hysteresis Models

The OCV extraction test procedure, as discussed in Chapter 2, was used to establish an OCV-SOC relationship for the two cell chemistries of interest to this thesis. The results are presented in Fig. 4.2. It can be noted that, the OCV curve obtained for the LFP cell has a relatively small rate of decent with respect to SOC than that observed for the NMC variant. This virtue makes LFP cells more appealing to those BES systems that require a fairly constant power over a wider operational SOC range.

Furthermore, the OCV obtained after a charge step for both LFP and NMC cells has a higher value than that of a discharge. In literature, this phenomenon is referred to as OCV hysteresis. In [220], the authors have shown that for high-power LFP cells, the hysteresis level decreases with increasing rest period which is allowed immediately after a charge or discharge step. This can be attributed to the thermodynamic origins of hysteresis [244] and requires for a long period of rest interval, in order for the cell to reach a final equilibrium potential.

The hysteresis levels obtained after a one-hour rest period for the two cell chemistries under study are presented in Fig. 4.2(b) and (d) respectively. It is apparent that the hysteresis level for the LFP chemistry is considerably higher than that obtained for the NMC chemistry. Moreover, within a conventional/conservative SOC range of 20% to 80%, the OCV curve for the LFP chemistry is fairly flat. This implies that for those OCV-based SOC estimators, even a small error in the voltage measurement within this region can result in a large deviation from the actual SOC value. Thus, for a more reliable SOC estimation, a model representation of the cell's hysteresis behaviour is of necessity.

To overcome the effects of hysteresis, different modelling approaches have been reported in literature (e.g. [245]). For those battery chemistries that pose a relatively small hysteresis level (e.g. NMC), often a direct approach is adopted [235]. This technique can be achieved either by evaluating the arithmetic mean or minimising the global squared-error between the charge and discharge OCV points attained separately for the same SOC level. However, for those chemistries with larger hysteresis levels (e.g. LFP), direct methods for hysteresis modelling would

lead to large uncertainties in the SOC estimates. Therefore, more comprehensive models can be employed to reduce such hysteresis-related uncertainties.
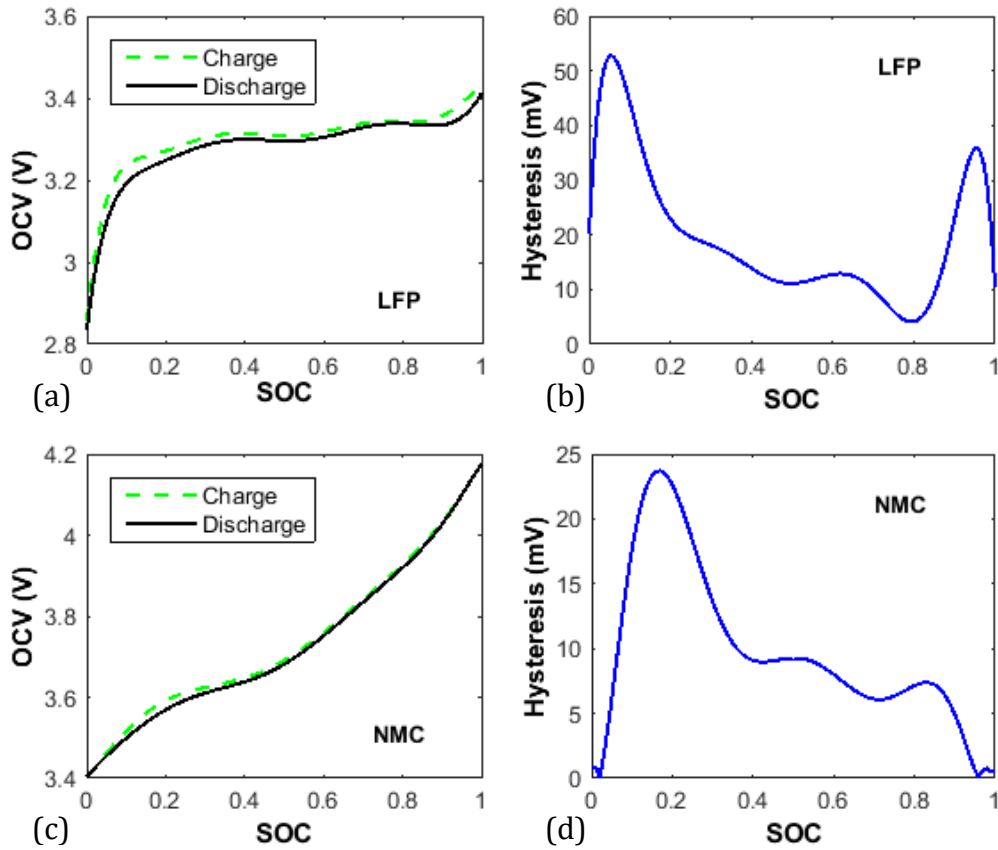
Fig. 4.2 Illustrating OCV and hysteresis level for (a)-(b) LFP and (c)-(d) NMC cell chemistries at 25°C

In [236], the authors develop an empirically-derived hysteresis model for LFP cells comprising of two parts; first part captures the dynamics of the OCV hysteresis as a function of SOC and an identifiable hysteresis factor that determines the position of the OCV curve with respect to the charge and discharge OCV curves, and the second part considers the SOC-dependent recovery effects (i.e. the time taken for the cell to reach a final equilibrium potential after a current interruption at a given SOC). This results in a comprehensive representation of the cell's OCV during operation. However, due to the empirical nature of the model structure, a training dataset is required to identify the model parameters off-line.

For the purpose of this study, we put the focus on the hysteresis models presented in [235] and [220], whose parameters can possibly be identified recursively in real time, without the necessity for various training datasets. Another example of online OCV hysteresis treatment can be found in [117]. The first hysteresis model is developed based on an algorithm presented by Huria *et al.* [220] and is defined as,

$$
\nabla V_{\text{OC}} = \frac{\mathrm{d}V_{\text{OC}}}{\mathrm{d}\text{SOC}} =
\begin{cases}
\dfrac{\mathrm{d}V_{\text{OC,ch}}}{\mathrm{d}\text{SOC}} + m(V_{\text{OC,ch}} - V_{\text{OC}}), & \text{for } \dfrac{\mathrm{d}\text{SOC}}{\mathrm{d}t} \geq 0 \\
\dfrac{\mathrm{d}V_{\text{OC,dis}}}{\mathrm{d}\text{SOC}} + m(V_{\text{OC,dis}} - V_{\text{OC}}), & \text{for } \dfrac{\mathrm{d}\text{SOC}}{\mathrm{d}t} < 0
\end{cases}
\qquad (4.3)
$$

which determines the gradient of $V_{\text{OC}} = f(\text{SOC})$ as a function of the rate-of-change of SOC and its distance away from the major hysteresis loop formed by the charge,$V_{\text{OC,ch}}$, and discharge, $V_{\text{OC,dis}}$, OCV curves. The dimensionless coefficient m determines how fast V_{OC} transitions towards $V_{\text{OC,ch}}$ or $V_{\text{OC,dis}}$ after a preceding charge or discharge current pulse respectively. In order to compare the performance of the two hysteresis models discussed in this section, algorithm (4.3) is combined with the Rint model (4.2) to give,

$$
V_k = V_{\text{OC}}(\text{SOC}_k) + \nabla V_{\text{OC,k}} - I_k R_s \qquad (4.4)
$$

where $\nabla V_{\text{OC,k}}$ is the V_{OC} derivative attained at time step k.

In [235], Plett developed a model to describe the hysteresis effects using a differential equation in both time and SOC such as,

$$
\frac{\mathrm{d}h(\text{SOC}, t)}{\mathrm{d}\text{SOC}} = \gamma \text{sgn}(\dot{\text{SOC}})\left(H(\text{SOC}, \dot{\text{SOC}}) - h(\text{SOC}, t)\right) \qquad (4.5)
$$

where $h(\text{SOC}, t)$ is a function to describe the hysteresis voltage, $H(\text{SOC}, \dot{\text{SOC}})$ defines the maximum positive and negative hysteresis as a function of SOC and rate-of-change of SOC, γ is a tuneable factor to control the rate-of-decay of hysteresis towards the major loop and $\dot{\text{SOC}} = \mathrm{d}\text{SOC}/\mathrm{d}t$ is the rate-of-change of SOC. Now, using

the SOC definition given by equation (2.14) in Chapter 2 and rearranging (4.5) as a differential equation in time only, the cell model's state-space equations become,

$$h_{k+1} = \exp\left(-\left|\frac{\eta I_k \gamma \Delta t}{Q_{\text{nom}}}\right|\right) h_k + \left(1 - \exp\left(-\left|\frac{\eta I_k \gamma \Delta t}{Q_{\text{nom}}}\right|\right)\right) H(\text{SOC}, \dot{\text{SOC}})$$

$$V_k = V_{\text{OC}}(\text{SOC}_k) - I_k R_{\text{s}} + h_k.$$

$$(4.6)$$

4.3.4 The Randles Model
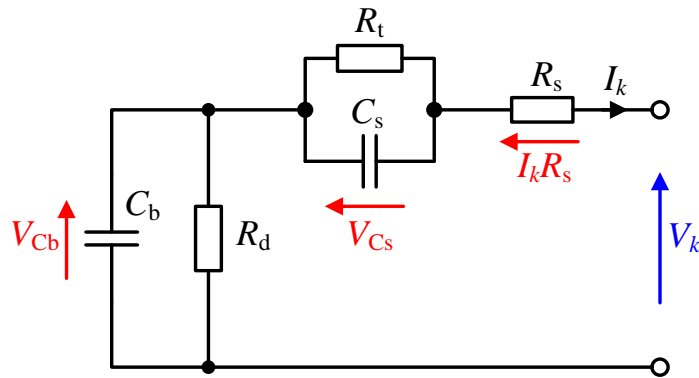
Fig. 4.3 Equivalent-circuit diagram for Randles model

The Randles model was originally developed for lead-acid batteries [96], [135], [216]. However, in recent years their utilisation in lithium-ion battery modelling has been sighted as well [246]. Fig. 4.3 shows the Randles' equivalent-circuit diagram for a typical lithium-ion cell, where R_{s} is the series resistance, R_{d} models the cell's no-load self-discharge (typically $\sim$70k Ω), C_{b} represents the bulk charge storage of the cell, C_{s} represents the electrodes' double-layer effect and R_{t} is the charge-transfer resistance. The voltage V_{Cb} across C_{b} is analogous to the cell's OCV and the model's output response can be expressed as,

$$\begin{bmatrix} V_{\mathrm{Cb}_{k+1}} \\ V_{\mathrm{Cs}_{k+1}} \end{bmatrix} = \begin{bmatrix} e^{\frac{-\Delta t}{R_{\mathrm{d}}C_{\mathrm{b}}}} & 0 \\ 0 & e^{\frac{-\Delta t}{R_{\mathrm{t}}C_{\mathrm{s}}}} \end{bmatrix} \begin{bmatrix} V_{\mathrm{Cb}_k} \\ V_{\mathrm{Cs}_k} \end{bmatrix} + \begin{bmatrix} R_{\mathrm{d}}\left(1 - e^{\frac{-\Delta t}{R_{\mathrm{d}}C_{\mathrm{b}}}}\right) & 0 \\ 0 & R_{\mathrm{t}}\left(1 - e^{\frac{-\Delta t}{R_{\mathrm{t}}C_{\mathrm{s}}}}\right) \end{bmatrix} I_k$$

$$V_k = V_{\mathrm{Cb},k} - V_{\mathrm{Cs},k} - I_k R_{\mathrm{s}}.$$

<div align="right">(4.7)</div>

Gould *et al.* [92] developed a new battery model through the star-delta transformation of the original Randles' circuit. This particular model, as shown in Fig. 4.4, consists of the same number of parameters as the Randles model with a slight modification in the way the transient states are represented.

In [92], it is shown that when applied with real-time state observers such as the Utkin and Kalman Filter, the parallel reconfiguration of the Randles' model states can yield a better SOC estimate. Thus, the adaptability of this model structure for online SOC and SOP estimation will be evaluated in this study. Consequently, mapping the Randles' model parameters as per (4.8) and solving for the output equation in discrete form, results in equation (4.9).
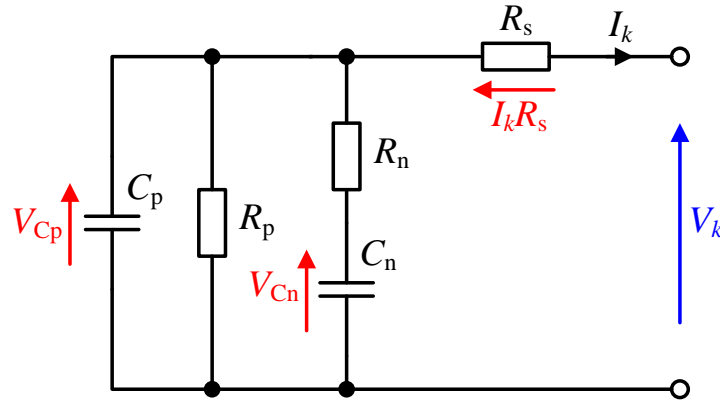
Fig. 4.4 Equivalent-circuit diagram for modified Randles model

$$C_{\mathrm{n}} = C_{\mathrm{b}}^2/(C_{\mathrm{b}} + C_{\mathrm{s}}), \qquad C_{\mathrm{p}} = C_{\mathrm{p}}C_{\mathrm{s}}/(C_{\mathrm{b}} + C_{\mathrm{s}}),$$

$$R_{\mathrm{n}} = R_{\mathrm{t}}(C_{\mathrm{b}} + C_{\mathrm{s}})^2/C_{\mathrm{b}}^2, \qquad R_{\mathrm{p}} = R_{\mathrm{d}} + R_{\mathrm{t}}$$

<div align="right">(4.8)</div>

$$
\begin{bmatrix} V_{\mathrm{Cp}_{k+1}} \\ V_{\mathrm{Cn}_{k+1}} \end{bmatrix} = \begin{bmatrix} e^{\frac{-\Delta t}{\tau_{\mathrm{p}}}} & \dfrac{R_{\mathrm{T}}}{R_{\mathrm{n}}}\left(1 - e^{\frac{-\Delta t}{\tau_{\mathrm{p}}}}\right) \\ \left(1 - e^{\frac{-\Delta t}{\tau_{\mathrm{n}}}}\right) & e^{\frac{-\Delta t}{\tau_{\mathrm{n}}}} \end{bmatrix} \begin{bmatrix} V_{\mathrm{Cp}_k} \\ V_{\mathrm{Cn}_k} \end{bmatrix} + \begin{bmatrix} R_{\mathrm{T}}\left(e^{\frac{-\Delta t}{\tau_{\mathrm{p}}}} - 1\right) & 0 \\ 0 & 0 \end{bmatrix} I_k
$$

$$
V_k = V_{\mathrm{Cp},k} - I_k R_{\mathrm{s}}
$$

$$(4.9)$$

where $R_{\mathrm{T}} = R_{\mathrm{p}}R_{\mathrm{n}}/\left(R_{\mathrm{p}} + R_{\mathrm{n}}\right)$, $\tau_{\mathrm{n}} = R_{\mathrm{n}}C_{\mathrm{n}}$ and $\tau_{\mathrm{p}} = R_{\mathrm{T}}C_{\mathrm{p}}$.

4.3.5 The Resistor-Capacitor (RC) Network Model
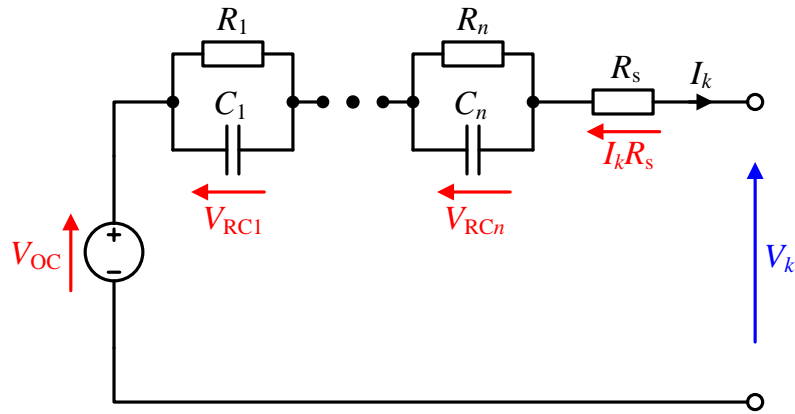
Fig. 4.5 Equivalent-circuit diagram for n-RC network model

The resistor-capacitor (RC) or the Thevenin equivalent-circuit model, as shown in Fig. 4.5, is a modification of the Rint model. This model is comprised of an ideal voltage source to represent the cell's OCV at partial equilibrium as a function of SOC, a series ohmic-resistance R_{s} and n number of series-connected parallel RC branches. Depending on the dynamics of the intended application, the number of the RC branches may vary. For most power applications, one RC branch is adequate (e.g. [168], [247], [248]) to describe the long time-constant reactions associated with the diffusion of active species into the electrolyte.

Considering applications with faster transients, the short time-constant reactions associated with the charge-transfer and the double-layer effect of the electrodes can be modelled with additional RC branches (e.g. [74], [249]–[251]). Without loss of

generality, the electrical behaviour of an n-th order RC model in its discrete form can be expressed as,

$$
\begin{bmatrix} V_{\text{RC1}_{k+1}} \\ \vdots \\ V_{\text{RC}n_{k+1}} \end{bmatrix} = \begin{bmatrix} e^{\frac{-\Delta t}{R_1 C_1}} & \cdots & 0 \\ \vdots & \ddots & \vdots \\ 0 & \cdots & e^{\frac{-\Delta t}{R_n C_n}} \end{bmatrix} \begin{bmatrix} V_{\text{RC1}_k} \\ \vdots \\ V_{\text{RC}n_k} \end{bmatrix} + \begin{bmatrix} R_1 \left(1 - e^{\frac{-\Delta t}{R_1 C_1}} \right) & \cdots & 0 \\ \vdots & \ddots & \vdots \\ 0 & \cdots & R_n \left(1 - e^{\frac{-\Delta t}{R_n C_n}} \right) \end{bmatrix} I_k
$$

$$
V_k = V_{\text{OC}}(\text{SOC}_k) - V_{\text{RC1}_k} - \cdots - V_{\text{RC}n_k} - I_k R_\text{s}.
$$

(4.10)

4.4 Formulation of Cell States Equations

In order to estimate lithium-ion cell states (i.e. SOC and SOP) using the model structures defined by equations (4.1) to (4.10), a set of equations in the discrete form is required. Subsequently, this section provides a description on the development of an empirically-deduced OCV function, which relates to the cell's SOC at discrete time intervals. Furthermore, in order to include SOC as an estimable state in the cell models' state-space equations, the coulomb-counting equation given in (2.14) is converted into a discrete form. Finally, a definition for the cells SOP is inferred based on the estimated cell's OCV and resistance parameters identified at a particular SOC value.

4.4.1 Inference of OCV-SOC Relationship

Upon the completion of the OCV extraction test procedure described in Chapter 2, section 2.3.2.3, the OCV values at ΔSOC = 10% steps, over the entire SOC range, were extracted. Fig. 4.6 presents the results obtained for both LFP and NMC reference test cells. The effect of hysteresis is often reported to be large for lithium-ion cells [220]. However, as can be observed, the test cells used here do not pose the typical hysteresis behaviour. Thus, by ignoring the hysteresis effect, in this thesis, the average of the OCV values obtained during both charge and discharge cycles are used to establish an OCV-SOC relationship for the two lithium-ion test cell variants.

As discussed in Chapter 2, for a reliable model-based cell state and parameter estimation, a sufficiently accurate function that relates the cell's OCV to its SOC is required. Various solutions have been proposed in literature. For example, in [168], Rahimi-Eichi *et al.* report on a piecewise linear OCV-SOC function, whose parameters are identified recursively using a reduced-order observer. Despite the simplicity offered by such OCV modelling approaches, they suffer largely from errors induced by the highly nonlinear OCV-SOC relationships, especially when SOC is either less than 10% or more than 90%.
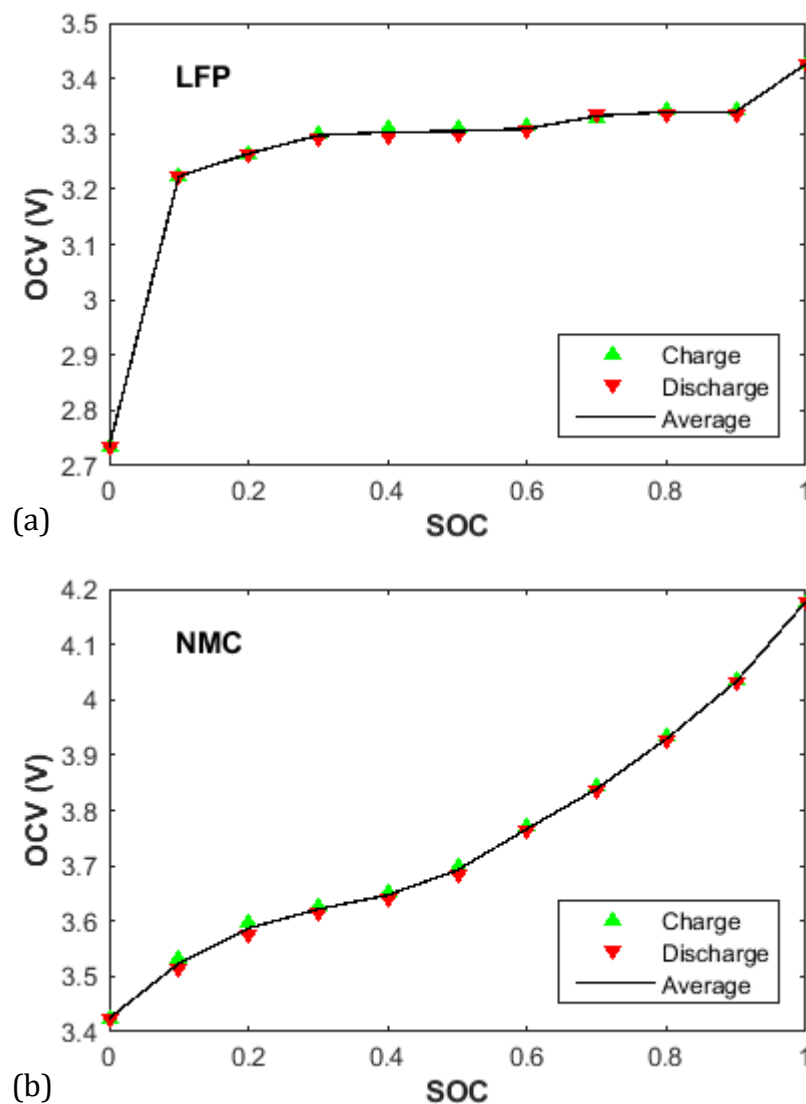
Fig. 4.6 OCV-SOC relationship for (a) LFP and (b) NMC reference cells at 25°C

Therefore, in this thesis, a nonlinear polynomial function is employed to accurately describe the OCV-SOC relationship.

$$V_{OC}(\text{SOC}) = a_i \text{SOC}_k^n + \cdots + a_1 \text{SOC}_k + a_0 \qquad (4.11)$$

where the coefficients a_i to a_0 are empirically determined, by curve-fitting the OCV-SOC data recorded at 10% SOC granularity and applying a nonlinear least-squares method in MATLAB. According to the work carried out in [142], ageing has a negligible effect on lithium-ion cells' OCV behaviour. Thus, the OCV coefficients identified for the LFP and NMC test cells here are stored in a look-up table for online implementations and need not to be updated recursively. This reduces the computational burden on low-cost MCUs that are typically found in motive and large-scale BES applications.

In order to determine a sufficient order-number for the OCV function given in (4.11), a statistical analysis is conducted. Polynomials of up to eighth order are fitted to the OCV-SOC data recorded for the two reference LFP and NMC cells, over their entire SOC range and at all test temperatures. Then, the residual norm, $\|e\|$, for each polynomial is calculated using (4.12) and is used as a goodness-of-fit indicator.

$$\|e\| = \sqrt{\sum_i \left(U_i - \widehat{U}_i\right)^2} \qquad (4.12)$$

where U_i is the measured and $\widehat{U}_i$ is the estimated OCV. The results are presented in Fig. 4.7. As can be noted, there exists an exponential trend line, which decays with increasing polynomial order-number and approaches a horizontal asymptote when order number is eight. Subsequently, an eighth-order polynomial is chosen herein as a sufficient order-number for the OCV function given in (4.11), to accurately describe the OCV-SOC relationship for both LFP and NMC cells.
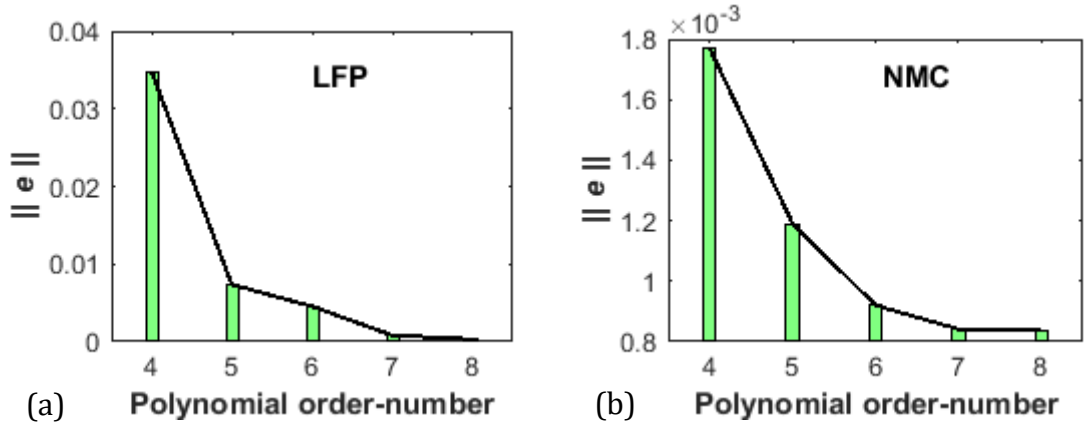
Fig. 4.7 Average residual norms obtained from curve-fitting high-order polynomials to OCV-SOC data measured for (a) LFP and (b) NMC cells

The fitted OCV curves at various temperatures are presented in Fig. 4.8. As can be seen, during the operational SOC range of both battery chemistries (i.e. 20% ≤ SOC ≤ 80%), the OCV-SOC relationship is almost independent of the operating temperature. This finding implies that for practical purposes, one can safely rely on only an OCV curve obtained at a reasonable temperature (e.g. at 25°C). However, to keep the modelling uncertainties at a minimum, in this Chapter, separate functions are fitted to represent the OCV-SOC relationship at each test temperature.

4.4.2 Discrete SOC Equation

In order to include SOC as an estimable state in the battery models' state-space equations (4.1) to (4.10), the coulomb-counter equation stated in (2.14) needs to be converted into a discrete form. Thus, assuming a small sampling period (in this case, $\Delta t = 100$ ms) and using a rectangular approximation yields,

$$\text{SOC}_{k+1} = \text{SOC}_k - \left(\frac{\eta \cdot \Delta t}{Q_{\text{nom}}}\right) I_k. \tag{4.13}$$
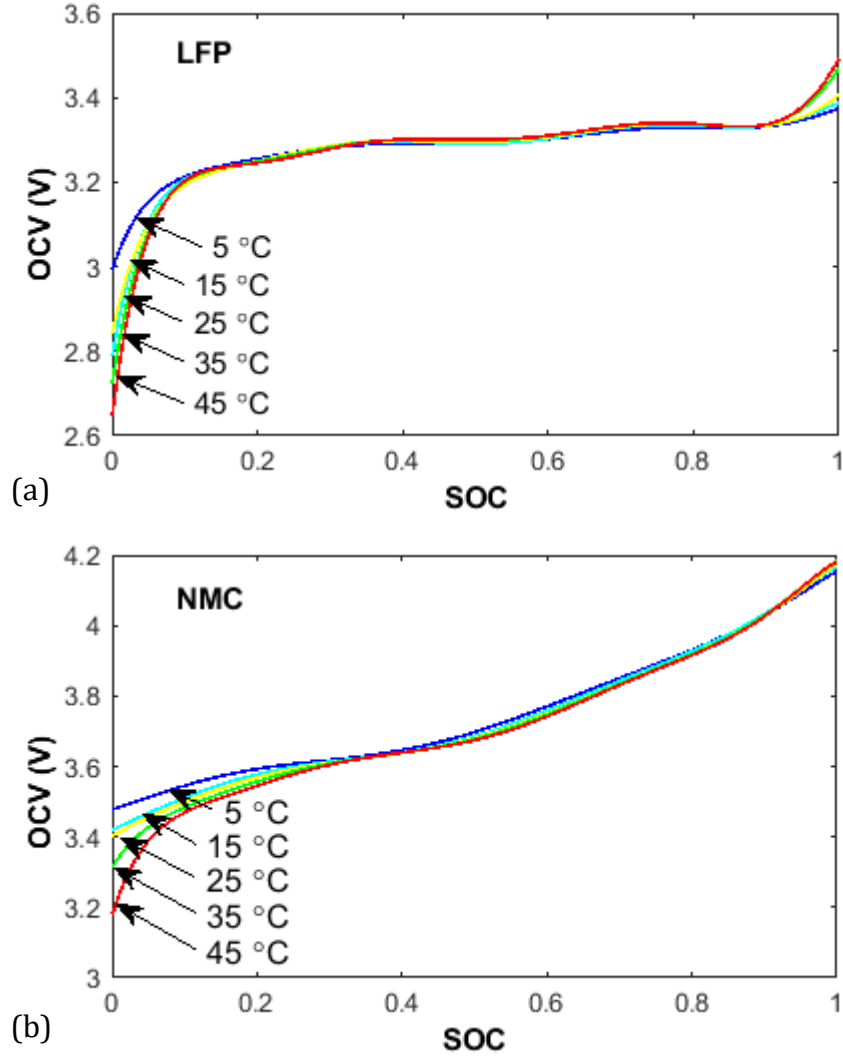
Fig. 4.8 Fitted average OCV curves for (a) LFP and (b) NMC cells, presented as a function of SOC and temperature

4.4.3 A Mathematical SOP Definition

Various quantitative definitions for SOP exist in literature (e.g. [194], [203], [252]), which are all associated with the battery's power capabilities. In this paper, we define SOP as the available source or sink power over a short period of Δt. Using $V_{\text{OC}} = f(\text{SOC})$ as defined in (2.25), the instantaneous discharge or charge power at time step k can be respectively calculated as,

$$P_{\text{dis},k} = \frac{V_{\min}(V_{\text{OC},k} - V_{\min})}{\hat{R}_{\text{eq}}} \tag{4.14}$$

$$P_{\text{ch},k} = \frac{V_{\text{max}}(V_{\text{max}} - V_{\text{OC},k})}{\hat{R}_{\text{eq}}} \qquad\qquad (4.15)$$

where V_{min} and V_{max} are the minimum and maximum threshold voltages recommended by the manufacturer for a safe operation and $\hat{R}_{\text{eq}}$ is an estimate for the cell's series-equivalent resistance.

Note that the value of $\hat{R}_{\text{eq}}$ in (4.14) and (4.15) can be approximated by applying the Thevenin's Theorem to the equivalent-circuit model under study. Alternatively, the voltage and current waveforms obtained for a sequence of HPPC pulses at every SOC value can be used to calculate a value for the cell's discharge or charge resistance as,

$$R_{\text{dis}} = \frac{V_0 - V_1}{I_{\text{dis}}}, \qquad R_{\text{ch}} = \frac{V_3 - V_2}{I_{\text{ch}}}. \qquad\qquad (4.16)$$

In equation (4.16), V_0 and V_1 are the cell voltages measured respectively at the start and end of a discharge current pulse, I_{dis}, of duration Δt seconds. Similarly, V_2 and V_3 are the voltage measurements taken for a charge current pulse I_{ch} of duration Δt seconds. The resulting resistances are analogous to the cell's internal resistances and can reflect on the power capability of a cell under operation. Consequently, any variations in the cell's internal resistance as a function of SOC and temperature can affect the quality of the SOP estimate at any time.

4.5 Dual-EKF System Identification

In Chapter 2, section 2.2.2.7, it was discussed that EKF is an *ad hoc* solution for the identification of non-linear time-varying systems, such as electrochemical cells. Using the EKF system identification method, the non-linear battery model describing the underlying dynamics of the system is linearised using the Taylor series expansion around the filter's current estimated trajectory. In order to simultaneously estimate both model states and parameters, the dual-EKF algorithm is adopted here. It should be noted that the ultimate goal of this Chapter is to review the online performance of the battery model structures presented in Table 4.1 and

not the online estimator. Therefore, the dual-EKF framework is chosen, as it is one of the most robust online system identification techniques applied in the battery energy and/or power management systems to overcome a wide range of problems (e.g. [118], [119], [165], [253]).

4.5.1 Underlying Theory

With the assumption that the cell terminal current I_k and voltage V_k are the only measurable quantities, the EKF state filter can be designed such that,

$$\mathbf{x}_{k+1} = f(\mathbf{x}_k, \mathbf{u}_k, \boldsymbol{\theta}_k) + \mathbf{w}_k$$

$$\mathbf{y}_k = h(\mathbf{x}_k, \mathbf{u}_k, \boldsymbol{\theta}_k) + \mathbf{v}_k \qquad (4.17)$$

$$\mathbf{w}_k \sim N(0, \mathbf{Q}^{\mathrm{x}}), \qquad \mathbf{v}_k \sim N(0, \mathbf{R}^{\mathrm{x}})$$

where $\mathbf{x}_k \in \mathbb{R}^n$ is a vector containing the model states to be predicted in a minimum variance sense, $\boldsymbol{\theta}_k \in \mathbb{R}^q$ contains the time-varying model parameters, $\mathbf{u}_k \in \mathbb{R}^p$ is the exogenous model input, $\mathbf{y}_k \in \mathbb{R}^m$ is the output and $\mathbf{w}_k \in \mathbb{R}^n$ and $\mathbf{v}_k \in \mathbb{R}^m$ are the zero-mean process and measurement noises of covariance $\mathbf{Q}^{\mathrm{x}}$ and $\mathbf{R}^{\mathrm{x}}$ respectively. The nonlinear function $f(\cdot, \cdot, \cdot)$ relates the states estimated at discrete time-step $k - 1$ to the states at the current time step k and $h(\cdot, \cdot, \cdot)$ maps the updated states to the measurements at time-step k. Assuming that the parameters vary slowly over time (i.e. minutes to hours), the weight EKF can be designed to adaptively provide an estimate of the true model parameters. Thus, the state-space model for the weight filter is given as,

$$\boldsymbol{\theta}_{k+1} = \boldsymbol{\theta}_k + \mathbf{r}_k$$

$$\mathbf{d}_k = h(\mathbf{x}_k, \mathbf{u}_k, \boldsymbol{\theta}_k) + \mathbf{e}_k \qquad (4.18)$$

$$\mathbf{r}_k \sim N(0, \mathbf{Q}^{\theta}), \qquad \mathbf{e}_k \sim N(0, \mathbf{R}^{\theta})$$

where the dynamics of changes in $\boldsymbol{\theta}_k$ are attributed to a small imaginary white noise $\mathbf{r}_k \in \mathbb{R}^p$ of covariance $\mathbf{Q}^{\theta}$ that evolves the parameters over time. The output

equation $\mathbf{d}_k \in \mathbb{R}^m$ is given as a measurable function of $\boldsymbol{\theta}_k$ and a white noise $\mathbf{e}_k \in \mathbb{R}^m$ of covariance $\mathbf{R}^\theta$ to account for the sensor noise and modelling uncertainties.

Due to the time-variability of the model parameters, it is imperative that the actual input/output cell data (e.g. voltage, current, etc.) convey continual information on the parameters to be estimated. This condition is referred to in system identification literature as the "persistence of excitation" (PE) [90].

In many real-time battery state estimation problems, the load-current profile may not fully satisfy the PE criterion. For those observer-based SOC estimators such as the extended Luenberger observer, sliding mode or adaptive observers, if the PE condition is not sufficiently satisfied, the gains tend to approach infinity and severe divergence occurs [90]. Nevertheless, the EKF algorithm seems to operate well under such conditions without any divergence (e.g. in [95], [130], [186], [254]).

A summary of the dual-EKF algorithm is presented in Table 4.2. Note that the algorithm is initialised by assuming *a prior* knowledge of the model states and parameters are available. However, in practice, initial system information are usually unknown. Thus, the states and the parameters are set to their best guess values at $k = 0$ so that $\widehat{\boldsymbol{\theta}}_0^+ = E[\boldsymbol{\theta}_0]$ and $\widehat{\mathbf{x}}_0^+ = E[\mathbf{x}_0]$.

Each time step, the algorithm first updates the state and parameter estimates $\widehat{\mathbf{x}}_k^-$ and $\widehat{\boldsymbol{\theta}}_k^-$ and their error covariance $\mathbf{P}_{\tilde{\mathbf{x}},k}^-$ and $\mathbf{P}_{\tilde{\theta},k}^-$ respectively, by propagating them forward in time. Note that for the parameter time-update equation (4.22), the new parameter estimate $\widehat{\boldsymbol{\theta}}_k^-$ is equal to the previous estimate $\widehat{\boldsymbol{\theta}}_{k-1}^+$ with an increase in its uncertainty due to the presence of the white process noise $\mathbf{r}_k$.

After a measurement has been taken at time step k, both filters take this measurement into consideration to update the state and parameter estimates $\widehat{\mathbf{x}}_k^+$ and $\widehat{\boldsymbol{\theta}}_k^+$ and their corresponding uncertainties as $\mathbf{P}_{\tilde{\mathbf{x}},k}^+$ and $\mathbf{P}_{\tilde{\theta},k}^+$ respectively. In (4.23) and (4.24), the measurement-update error covariance matrices $\mathbf{P}_{\tilde{\mathbf{x}},k}^+$ and $\mathbf{P}_{\tilde{\theta},k}^+$ are given in their Joseph forms to ensure a numerically robust algorithm [255]. It is noted that for the weight filter's measurement-update equations given in (4.24), the

total-differential $\mathbf{H}_k^\theta$ of the model output equation $h(\cdot,\cdot,\cdot)$ with respect to parameters θ_k is required. Therefore, by decomposing the total-derivative into partial-derivatives, $\mathbf{H}_k^\theta$ is computed recursively as the following set of equations,

$$\mathbf{H}_k^\theta = \left.\frac{\mathrm{d}h(\hat{\mathbf{x}}_k^-,\mathbf{u}_k,\theta_k)}{\mathrm{d}\theta_k}\right|_{\theta_k=\hat{\theta}_k^-}$$

$$\frac{\mathrm{d}h(\hat{\mathbf{x}}_k^-,\mathbf{u}_k,\hat{\theta}_k^-)}{\mathrm{d}\hat{\theta}_k^-} = \frac{\partial h(\hat{\mathbf{x}}_k^-,\mathbf{u}_k,\hat{\theta}_k^-)}{\partial\hat{\theta}_k^-} + \frac{\partial h(\hat{\mathbf{x}}_k^-,\mathbf{u}_k,\hat{\theta}_k^-)}{\partial\hat{\mathbf{x}}_k^-}\cdot\frac{\mathrm{d}\hat{\mathbf{x}}_k^-}{\mathrm{d}\hat{\theta}_k^-}$$

$$\frac{\mathrm{d}\hat{\mathbf{x}}_k^-}{\mathrm{d}\hat{\theta}_k^-} = \frac{\partial f(\hat{\mathbf{x}}_{k-1}^+,\mathbf{u}_{k-1},\hat{\theta}_k^-)}{\partial\hat{\theta}_k^-} + \frac{\partial f(\hat{\mathbf{x}}_{k-1}^+,\mathbf{u}_{k-1},\hat{\theta}_k^-)}{\partial\hat{\mathbf{x}}_{k-1}^+}\cdot\frac{\mathrm{d}\hat{\mathbf{x}}_{k-1}^+}{\mathrm{d}\hat{\theta}_k^-} \tag{4.19}$$

$$\frac{\mathrm{d}\hat{\mathbf{x}}_{k-1}^+}{\mathrm{d}\hat{\theta}_k^-} = \frac{\mathrm{d}\hat{\mathbf{x}}_{k-1}^-}{\mathrm{d}\hat{\theta}_{k-1}^+} - \mathbf{L}_{k-1}^{\mathrm{x}}\frac{\mathrm{d}h(\hat{\mathbf{x}}_{k-1}^-,\mathbf{u}_{k-1},\hat{\theta}_{k-1}^+)}{\mathrm{d}\hat{\theta}_{k-1}^+}.$$

Since $\mathbf{L}_{k-1}^{\mathrm{x}}$ is weakly related to the parameter estimates θ_k, it can be safely neglected in (4.19) to improve the computation efficiency of the weight filter. Furthermore, $\mathrm{d}\hat{\mathbf{x}}_{k-1}^+/\mathrm{d}\hat{\theta}_k^-$ is set to zero at $k = 0$ and the three total-derivatives are updated recursively.

4.5.2 Estimation of EKF Noise Statistics

The convergence and tracking performance of any KF-based system identification technique is largely dependent on the process and measurement noise statistics initialised at time-step $k = 0$. In most researches conducted on battery system identification using KF-based algorithms, these two statistical parameters are either tuned manually, which can be a tedious task, or set by experience. In this thesis, the expectation maximisation (EM) algorithm is employed to provide an iterative maximum-likelihood estimate for the filters' process and measurement noise statistical parameters (i.e. $\mathbf{Q}^{\mathrm{x}}$ and $\mathbf{R}^{\mathrm{x}}$ for the state EKF and $\mathbf{Q}^\theta$ and $\mathbf{R}^\theta$ for the weight EKF).

Table 4.2 Summary of the dual-EKF algorithm for battery model state and parameters estimation

Initialisation:

$$\widehat{\boldsymbol{\theta}}_0^+ = E[\boldsymbol{\theta}_0], \qquad \mathbf{P}_{\theta,0}^+ = E\left[(\boldsymbol{\theta} - \widehat{\boldsymbol{\theta}}_0^+)(\boldsymbol{\theta} - \widehat{\boldsymbol{\theta}}_0^+)^T\right]$$

$$\hat{\mathbf{x}}_0^+ = E[\mathbf{x}_0], \qquad \mathbf{P}_{x,0}^+ = E[(\mathbf{x} - \hat{\mathbf{x}}_0^+)(\mathbf{x} - \hat{\mathbf{x}}_0^+)^T]$$

(4.20)

Time-update equations for state filter:

$$\hat{\mathbf{x}}_k^- = f\left(\hat{\mathbf{x}}_{k-1}^+, \mathbf{u}_{k-1}, \widehat{\boldsymbol{\theta}}_k^-\right)$$

$$\mathbf{P}_{\tilde{x},k}^- = \mathbf{F}_{k-1}\mathbf{P}_{\tilde{x},k-1}^+\mathbf{F}_{k-1}^T + \mathbf{Q}_k^x$$

(4.21)

Time-update equations for weight filter:

$$\widehat{\boldsymbol{\theta}}_k^- = \widehat{\boldsymbol{\theta}}_{k-1}^+$$

$$\mathbf{P}_{\tilde{\theta},k}^- = \mathbf{P}_{\tilde{\theta},k-1}^+ + \mathbf{Q}_k^\theta$$

(4.22)

Measurement-update equations for state filter:

$$\mathbf{L}_k^x = \mathbf{P}_{\tilde{x},k}^-(\mathbf{H}_k^x)^T\left[\mathbf{H}_k^x\mathbf{P}_{\tilde{x},k}^-(\mathbf{H}_k^x)^T + \mathbf{R}_k^x\right]^{-1}$$

$$\hat{\mathbf{x}}_k^+ = \hat{\mathbf{x}}_k^- + \mathbf{L}_k^x\left[\mathbf{y}_k - h\left(\hat{\mathbf{x}}_k^-, \mathbf{u}_k, \widehat{\boldsymbol{\theta}}_k^-\right)\right]$$

$$\mathbf{P}_{\tilde{x},k}^+ = (\boldsymbol{I} - \mathbf{L}_k^x\mathbf{H}_k^x)\mathbf{P}_{\tilde{x},k}^-(\boldsymbol{I} - \mathbf{L}_k^x\mathbf{H}_k^x)^T + \mathbf{L}_k^x\mathbf{R}_k^x(\mathbf{L}_k^x)^T$$

(4.23)

Measurement-update equations for weight filter:

$$\mathbf{L}_k^\theta = \mathbf{P}_{\tilde{\theta},k}^-\left(\mathbf{H}_k^\theta\right)^T\left[\mathbf{H}_k^\theta\mathbf{P}_{\tilde{\theta},k}^-\left(\mathbf{H}_k^\theta\right)^T + \mathbf{R}_k^\theta\right]^{-1}$$

$$\widehat{\boldsymbol{\theta}}_k^+ = \widehat{\boldsymbol{\theta}}_k^- + \mathbf{L}_k^\theta\left[\mathbf{d}_k - h\left(\hat{\mathbf{x}}_k^-, \mathbf{u}_k, \widehat{\boldsymbol{\theta}}_k^-\right)\right]$$

$$\mathbf{P}_{\tilde{\theta},k}^+ = \left(\boldsymbol{I} - \mathbf{L}_k^\theta\mathbf{H}_k^\theta\right)\mathbf{P}_{\tilde{\theta},k}^-\left(\boldsymbol{I} - \mathbf{L}_k^\theta\mathbf{H}_k^\theta\right)^T + \mathbf{L}_k^\theta\mathbf{R}_k^\theta\left(\mathbf{L}_k^\theta\right)^T$$

(4.24)

Where,

$$\mathbf{F}_{k-1} = \frac{\partial f\left(\mathbf{x}_{k-1}, \mathbf{u}_{k-1}, \widehat{\boldsymbol{\theta}}_k^-\right)}{\partial \mathbf{x}_{k-1}}\Bigg|_{\mathbf{x}_{k-1}=\hat{\mathbf{x}}_{k-1}^+}, \qquad \mathbf{H}_k^x = \frac{\partial h\left(\mathbf{x}_k, \mathbf{u}_k, \widehat{\boldsymbol{\theta}}_k^-\right)}{\partial \mathbf{x}_k}\Bigg|_{\mathbf{x}_k=\hat{\mathbf{x}}_k^-},$$

$$\mathbf{H}_k^\theta = \frac{\mathrm{d}h(\hat{\mathbf{x}}_k^-, \mathbf{u}_k, \boldsymbol{\theta}_k)}{\mathrm{d}\boldsymbol{\theta}_k}\Bigg|_{\boldsymbol{\theta}_k=\widehat{\boldsymbol{\theta}}_k^-}.$$

(4.25)

In general, for a nonlinear joint-optimisation problem, where both model states and parameters are unknown, the EM algorithm performs a joint maximisation of the conditional probability density functions for both the states vector $\mathbf{x}_k$ and the parameters vector $\mathbf{\theta}_k$. The resulting algorithm can, thus, be used as an alternative to the dual-EKF estimator for online BES identification problems. However, this comes at an increased computational cost, which is a subject of study in its own merits. Alternatively, assuming the initial model states and parameters are known at time step $k = 0$ (e.g. from manufacturer's datasheet or through offline parameterisation techniques), the extended EM method, as reported in [256], can be applied to recursively identify $\mathbf{Q}$ and $\mathbf{R}$ for a set of persistently-exciting input/output data.

4.5.1.1   Estimation of process noise covariance Q

For a measurement vector, $\mathbf{y}_N$, of sample size N, the covariance $\mathbf{Q}$ of the zero-mean white process noise $\mathbf{w}_k \sim N(0, \mathbf{Q})$ can be defined as,

$$\mathbf{Q} = \frac{1}{N}\sum_{k=1}^{N} E\big[\mathbf{w}_k \mathbf{w}_k^{\mathrm{T}} | \mathbf{y}_N \big].\tag{4.26}$$

Then, considering the state-space equations given in (4.17), the process noise, $\mathbf{w}_k$, for a dual-EKF can be approximated using the first-order Taylor series expansion.

$$\mathbf{w}_k \approx \mathbf{x}_k - f\big(\mathbf{x}_{k-1|N}, \mathbf{u}_{k-1}, \mathbf{\theta}_{k-1|N}\big) - \mathbf{F}_{k-1|N}\tilde{\mathbf{x}}_{k-1|N}\tag{4.27}$$

where $\mathbf{F}_{k-1|N}$ is the Jacobian of the nonlinear function $f(\cdot)$ and $\tilde{\mathbf{x}}_{k-1|N} = \mathbf{x}_{k-1} - \mathbf{x}_{k-1|N}$. Subsequently, using (4.27), the outer product of $\mathbf{w}_k$, as required in (4.26), can be expressed as,

$$
\begin{aligned}
\mathbf{w}_k \mathbf{w}_k^{\mathrm{T}} = {} & \mathbf{x}_k \mathbf{x}_k^{\mathrm{T}} - \mathbf{x}_k f\big(\mathbf{x}_{k-1|N}, \mathbf{u}_{k-1}, \boldsymbol{\theta}_{k-1|N}\big)^{\mathrm{T}} - f\big(\mathbf{x}_{k-1|N}, \mathbf{u}_{k-1}, \boldsymbol{\theta}_{k-1|N}\big)\mathbf{x}_k^{\mathrm{T}} \\
& + f\big(\mathbf{x}_{k-1|N}, \mathbf{u}_{k-1}, \boldsymbol{\theta}_{k-1|N}\big) f\big(\mathbf{x}_{k-1|N}, \mathbf{u}_{k-1}, \boldsymbol{\theta}_{k-1|N}\big)^{\mathrm{T}} \\
& - \mathbf{x}_k \tilde{\mathbf{x}}_{k-1|N}^{\mathrm{T}} \mathbf{F}_{k-1|N}^{\mathrm{T}} + f\big(\mathbf{x}_{k-1|N}, \mathbf{u}_{k-1}, \boldsymbol{\theta}_{k-1|N}\big) \tilde{\mathbf{x}}_{k-1|N}^{\mathrm{T}} \mathbf{F}_{k-1|N}^{\mathrm{T}} \\
& - \mathbf{F}_{k-1|N} \tilde{\mathbf{x}}_{k-1|N} \mathbf{x}_k^{\mathrm{T}} + \mathbf{F}_{k-1|N} \tilde{\mathbf{x}}_{k-1|N} f\big(\mathbf{x}_{k-1|N}, \mathbf{u}_{k-1}, \boldsymbol{\theta}_{k-1|N}\big)^{\mathrm{T}} \\
& + \mathbf{F}_{k-1|N} \tilde{\mathbf{x}}_{k-1|N} \tilde{\mathbf{x}}_{k-1|N}^{\mathrm{T}} \mathbf{F}_{k-1|N}^{\mathrm{T}}.
\end{aligned}
$$

(4.28)

Now, according to Bayes' rules [255], the conditional expectation for a state vector $\mathbf{x}_k$ to be estimated, given measurements of up to and including $\mathbf{y}_N$ are available, can be expressed as,

$$
\begin{aligned}
E\big[\mathbf{x}_k \mathbf{x}_k^{\mathrm{T}} | \mathbf{y}_N\big] &= \mathbf{x}_{k|N} \mathbf{x}_{k|N}^{\mathrm{T}} + \mathbf{P}_{k|N} \\
E\big[\mathbf{x}_k \mathbf{x}_{k-1}^{\mathrm{T}} | \mathbf{y}_N\big] &= \mathbf{x}_{k|N} \mathbf{x}_{k-1|N}^{\mathrm{T}} + \mathbf{P}_{k,k-1|N}
\end{aligned}
$$

(4.29)

where the lagged covariance $\mathbf{P}_{k,k-1|N}$ is defined by,

$$
\begin{aligned}
\mathbf{P}_{k,k-1|N} &= E\left[\big(\mathbf{x}_k - \mathbf{x}_{k|N}\big)\big(\mathbf{x}_{k-1} - \mathbf{x}_{k-1|N}\big)^{\mathrm{T}}\right] \\
&= \mathbf{P}_{k|k} \mathbf{L}_{k-1|N}^{\mathrm{T}} + \mathbf{L}_{k|N}\big(\mathbf{P}_{k+1,k|N} - \mathbf{F}_k \mathbf{P}_{k|k}\big)\mathbf{L}_{k-1|N}^{\mathrm{T}}.
\end{aligned}
$$

(4.30)

Subsequently, by rearranging equations (4.28) to (4.30), the conditional expectation defined in (4.26) can be given as,

$$
\begin{aligned}
E\big[\mathbf{w}_k \mathbf{w}_k^{\mathrm{T}} | \mathbf{y}_N\big] = {} & \mathbf{x}_{k|N} \mathbf{x}_{k|N}^{\mathrm{T}} + \mathbf{P}_{k|N} + \mathbf{x}_{k|N} f\big(\mathbf{x}_{k-1|N}, \mathbf{u}_{k-1}, \boldsymbol{\theta}_{k-1|N}\big)^{\mathrm{T}} \\
& - f\big(\mathbf{x}_{k-1|N}, \mathbf{u}_{k-1}, \boldsymbol{\theta}_{k-1|N}\big)\mathbf{x}_{k|N}^{\mathrm{T}} \\
& + f\big(\mathbf{x}_{k-1|N}, \mathbf{u}_{k-1}, \boldsymbol{\theta}_{k-1|N}\big) f\big(\mathbf{x}_{k-1|N}, \mathbf{u}_{k-1}, \boldsymbol{\theta}_{k-1|N}\big)^{\mathrm{T}} - \mathbf{P}_{k,k-1|N} \mathbf{F}_{k-1|N}^{\mathrm{T}} \\
& - \mathbf{P}_{k,k-1|N}^{\mathrm{T}} \mathbf{F}_{k-1|N} + \mathbf{F}_{k-1|N} \mathbf{P}_{k-1|k-1} \mathbf{F}_{k-1|N}^{\mathrm{T}}.
\end{aligned}
$$

(4.31)

Finally, substituting (4.31) into (4.26) yields,

$$\mathbf{Q} = \frac{1}{N} \sum_{k=1}^{N} \left(\mathbf{w}_{k|N} \mathbf{w}_{k|N}^{\mathrm{T}} + \mathbf{P}_{k|N} + \mathbf{F}_{k-1|N} \mathbf{P}_{k-1|N} \mathbf{F}_{k-1|N}^{\mathrm{T}} - \mathbf{P}_{k,k-1|N} \mathbf{F}_{k-1|N}^{\mathrm{T}} \right.$$
$$\left. - \mathbf{P}_{k,k-1|N}^{\mathrm{T}} \mathbf{F}_{k-1|N} \right)$$

(4.32)

where $\mathbf{w}_{k|N} = \mathbf{x}_{k|N} - f\left(\mathbf{x}_{k-1|N}, \mathbf{u}_{k-1}, \boldsymbol{\theta}_{k-1|N} \right)$.

4.5.1.2   Estimation of measurement noise covariance R

Similar to $\mathbf{Q}$ estiamtion, for the same sample of size N, the measurement noise covariance $\mathbf{R}$ can be defined as,

$$\mathbf{R} = \frac{1}{N} \sum_{k=1}^{N} E\left[\mathbf{v}_k \mathbf{v}_k^{\mathrm{T}} | \boldsymbol{y}_N \right]$$

(4.33)

where $\mathbf{v}_k \sim N(0, \mathbf{R})$ is the zero-mean white-colour noise introduced by the current and voltage sensors. Then, using $\mathbf{v}_k = \mathbf{y}_k - h(\mathbf{x}_k, \mathbf{u}_k, \boldsymbol{\theta}_k)$ as per (4.17), the measurement noise, $\mathbf{v}_k$, can be approximated using the first-order Taylor series expansion and given as,

$$\mathbf{v}_k \approx \mathbf{y}_k - h\left(\mathbf{x}_{k|N}, \mathbf{u}_k, \boldsymbol{\theta}_{k|N} \right) - \mathbf{H}_{k|N} \tilde{\mathbf{x}}_{k|N}$$

(4.34)

where $\mathbf{H}_{k|N}$ is the Jacobian of the nonlinear function $h(\cdot)$ and $\tilde{\mathbf{x}}_{k|N} = \mathbf{x}_k - \mathbf{x}_{k|N}$. Subsequently, using (4.34), the outer product of $\mathbf{v}_k$, as required in (4.33), can be expressed as,

$$\mathbf{v}_k \mathbf{v}_k^{\mathrm{T}} = \mathbf{y}_k \mathbf{y}_k^{\mathrm{T}} - \mathbf{y}_k h\left(\mathbf{x}_{k|N}, \mathbf{u}_k, \boldsymbol{\theta}_{k|N} \right)^{\mathrm{T}} - \mathbf{y}_k \tilde{\mathbf{x}}_{k|N} \mathbf{H}_{k|N}^{\mathrm{T}} - h\left(\mathbf{x}_{k|N}, \mathbf{u}_k, \boldsymbol{\theta}_{k|N} \right) \mathbf{y}_k^{\mathrm{T}}$$
$$+ h\left(\mathbf{x}_{k|N}, \mathbf{u}_k, \boldsymbol{\theta}_{k|N} \right) h\left(\mathbf{x}_{k|N}, \mathbf{u}_k, \boldsymbol{\theta}_{k|N} \right)^{\mathrm{T}} + h\left(\mathbf{x}_{k|N}, \mathbf{u}_k, \boldsymbol{\theta}_{k|N} \right) \tilde{\mathbf{x}}_{k|N}^{\mathrm{T}} \mathbf{H}_{k|N}^{\mathrm{T}}$$
$$- \mathbf{H}_{k|N} \tilde{\mathbf{x}}_{k|N} \mathbf{y}_k^{\mathrm{T}} + \mathbf{H}_{k|N} \tilde{\mathbf{x}}_{k|N} h\left(\mathbf{x}_{k|N}, \mathbf{u}_k, \boldsymbol{\theta}_{k|N} \right)^{\mathrm{T}} + \mathbf{H}_{k|N} \tilde{\mathbf{x}}_{k|N} \tilde{\mathbf{x}}_{k|N}^{\mathrm{T}} \mathbf{H}_{k|N}^{\mathrm{T}}.$$

(4.35)

For a normally-distributed measurement noise, it is known that, $E[\tilde{\mathbf{x}}_{k|N}] = E[\mathbf{x}_k - \mathbf{x}_{k|N}] = 0$ and $E[\tilde{\mathbf{x}}_{k|N}\tilde{\mathbf{x}}_{k|N}^{\mathrm{T}}] = E\left[(\mathbf{x}_k - \mathbf{x}_{k|N})(\mathbf{x}_k - \mathbf{x}_{k|N})^{\mathrm{T}}\right] = \mathbf{P}_{k|N}$. Hence, the conditional expectation defined in (4.33) can be derived and given as,

$$
\begin{aligned}
E[\mathbf{v}_k\mathbf{v}_k^{\mathrm{T}}|\mathbf{y}_N] = \mathbf{y}_k\mathbf{y}_k^{\mathrm{T}} &- \mathbf{y}_k h(\mathbf{x}_{k|N}, \mathbf{u}_k, \boldsymbol{\theta}_{k|N})^{\mathrm{T}} - h(\mathbf{x}_{k|N}, \mathbf{u}_k, \boldsymbol{\theta}_{k|N})\mathbf{y}_k^{\mathrm{T}} \\
&+ h(\mathbf{x}_{k|N}, \mathbf{u}_k, \boldsymbol{\theta}_{k|N})h(\mathbf{x}_{k|N}, \mathbf{u}_k, \boldsymbol{\theta}_{k|N})^{\mathrm{T}} + \mathbf{H}_{k|N}\mathbf{P}_{k|N}\mathbf{H}_{k|N}^{\mathrm{T}}
\end{aligned}
$$

$$(4.36)$$

Finally, by substituting (4.36) into (4.33), $\mathbf{R}$ can be estimated as,

$$
\mathbf{R} = \frac{1}{N}\sum_{k=1}^{N}\left(\mathbf{v}_{k|N}\mathbf{v}_{k|N}^{\mathrm{T}} + \mathbf{H}_{k|N}\mathbf{P}_{k|N}\mathbf{H}_{k|N}^{\mathrm{T}}\right) \tag{4.37}
$$

where $\mathbf{v}_{k|N} = \mathbf{y}_k - h(\mathbf{x}_{k|N}, \mathbf{u}_k, \boldsymbol{\theta}_{k|N})$.

4.5.1.3   Initialised Q and R Values

Using the input/output data obtained for the reference LFP and NMC cells under the self-designed pulsed-current test, and a sample size of $N = 1000$, equations (4.32) and (4.37) were applied to the dual-EKF algorithm to estimate the state and weight filters' noise covariance. The chosen sample size implies that for the sampling period of $\Delta t = 100$ ms used here, there will be 100 seconds of data in every window. This allows for those model parameters with slow transients to be assumed steady over the period of 100 seconds. Finally, by taking the arithmetic mean of $\mathbf{Q}$ and $\mathbf{R}$ values obtained for both LFP and NMC cells, the process and measurement noise covariance for both EKFs are initialised as per (4.38). The filter parameters are kept the same for both LFP and NMC cells. This is to ensure a fair assessment on the cell model's performance for the two lithium-ion cell variants.

$$\mathbf{Q}_0^x = \text{diag}_n\{1 \times 10^{-6}\}, \qquad \mathbf{P}_{\tilde{x},0}^+ = \text{diag}_n\{10\}, \qquad \mathbf{R}_0^x = \text{diag}_m\{10\}$$

$$\mathbf{Q}_0^\theta = \text{diag}_q\{1 \times 10^{-8}\}, \qquad \mathbf{P}_{\tilde{\theta},0}^+ = \text{diag}_q\{10\}, \qquad \mathbf{R}_0^\theta = \text{diag}_m\{10\}$$

$$(4.38)$$

where $\text{diag}\{\cdot\}$ is a diagonal matrix of size $n \times n$ for $\mathbf{Q}_0^x$ and $\mathbf{P}_{\tilde{x},0}^+$, $q \times q$ for $\mathbf{Q}_0^\theta$ and $\mathbf{P}_{\tilde{\theta},0}^+$, and $m \times m$ for $\mathbf{R}_0^x$ and $\mathbf{R}_0^\theta$ matrices, respectively. Note that the error covariance matrices $\mathbf{P}_{\tilde{x},0}^+$ and $\mathbf{P}_{\tilde{\theta},0}^+$ are set to a large value at the initialisation time-step $k = 0$ in order to account for any uncertainties in the filters' initial conditions.

4.6 Experimental Results and Discussion

This section provides a description of the test procedures used in this Chapter, for the purpose of model training and validation. The dynamic performance and generality of each model structure is verified using two sets of lithium-ion cells. An analysis on the ten model structures is conducted with respect to SOC and SOP estimation, with different initial conditions.

4.6.1 Test Procedures

The generality of the battery models given in Table 4.1 is demonstrated using three identical cells of LFP and NMC chemistries. The specifications for the test cells are presented in Chapter 2, Table 2.5. The datasets for model training and validation are generated using the sequence outlined in Chapter 2, Fig. 2.18. The data obtained for one of each cell-chemistry is used for model training purposes, whereas the data gathered for the other four cells are utilised for verification of the identified model parameters and their dynamic performances.

As for any electrochemical device, the energy storage capacity of batteries is greatly influenced by the ambient temperature in which they operate at. For practical reasons, most coulomb counters are normalised using the battery's nameplate or nominal capacity, which can lead to erroneous SOC estimates at different operating temperatures. Therefore, the test cells here are initially treated with a capacity

measurement cycle (see Chapter 2, section 2.3.2.1), replacing Q_{nom} in the SOC equation given by **Error! Reference source not found.** with the cells' actual capacities at the test temperatures.

In order to verify the EKF-identified equivalent cell resistances, each cell is characterised using the EIS method (see Chapter 2, section 2.3.2.2) and the results are compared. Thereafter, the two LFP and NMC reference cells are applied with an OCV extraction test (see Chapter 2, section 2.3.2.3), in order to establish a polynomial function to describe their OCV-SOC relationships. The derived functions are then included in the output equations of those models whose OCVs are expressed as a function of SOC.

The dependency of available cell power with respect to ambient temperature and SOC is experimentally demonstrated here by using the HPPC procedure as prescribed in Chapter 2, section 2.3.2.4. Finally, the results from the self-designed pulsed-current test and a multi-cycle NEDC are used to verify the dynamic performance of the ten model structures under study, with respect to voltage, SOC and SOP accuracy.

The self-designed test (see Fig. 4.9) is performed over the full SOC range of 100% to 0%. The multi-cycle NEDC profile (see Fig. 4.10) is carried out over the SOC range of 90% to 10% and consists of 14 consecutive NEDC repetitions, separated by 15-minute rest periods. Note that prior to any of the aforementioned tests, a discharge-charge cycle is performed to ensure the cells are at an initial SOC of 100%. For the NEDC test, the SOC range of 90% to 10% is chosen in order to avoid the highly nonlinear regions of cell operation, above and below these limits respectively. Subsequently, a 0.5C current rate is used to discharge the cell under test from 100% to 90% SOC, followed by a one-hour rest period.

4.6.2 Measured Cell Capacities

The measured capacities for all six test cells at 0.5C current rate, over the temperature range of 5°C to 45°C, are presented in Fig. 4.11. As for any battery chemistry, cold temperatures can have a drastic effect on LFP and NMC cells. At low

temperatures, lithium-ion cells experience an increase in their internal resistances, due to the strong dependency of the kinetic and ionic transport properties on close-to-zero and sub-zero temperatures [257]. As a result, a significant capacity loss is observed at 5°C for both LFP and NMC cells. Conversely, at high temperatures, the rate of the electrochemical reactions that occur inside the cells are increased, resulting in a higher quantity of releasable energy; thus, improving the cell capacity. However, continuous operation at elevated temperatures will cause an accelerated deterioration of the cell's SOH.
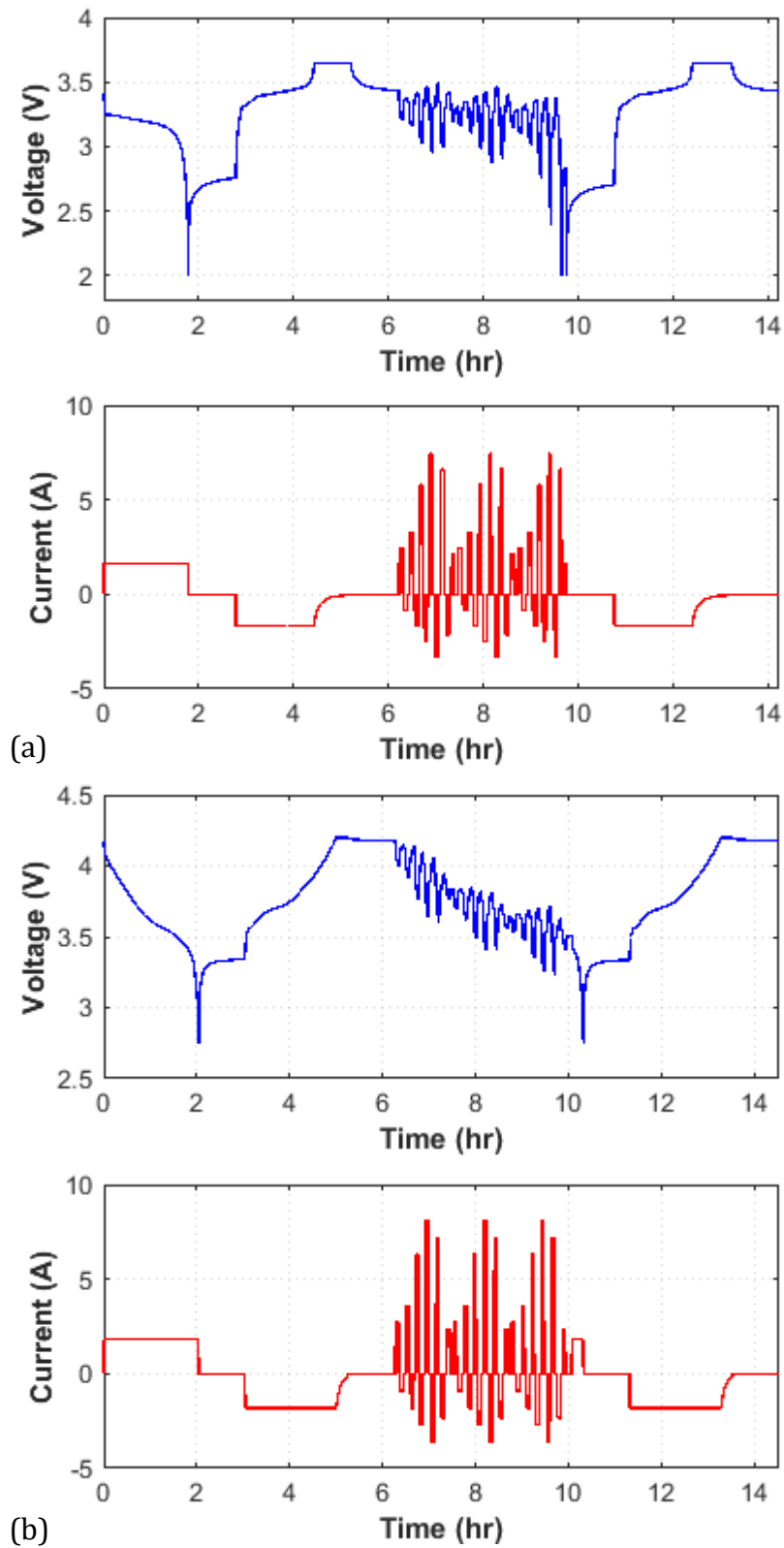
Fig. 4.9 Voltage and current waveforms for (a) one LFP cell and (b) one NMC cell under the self-designed pulsed-current test at 25°C
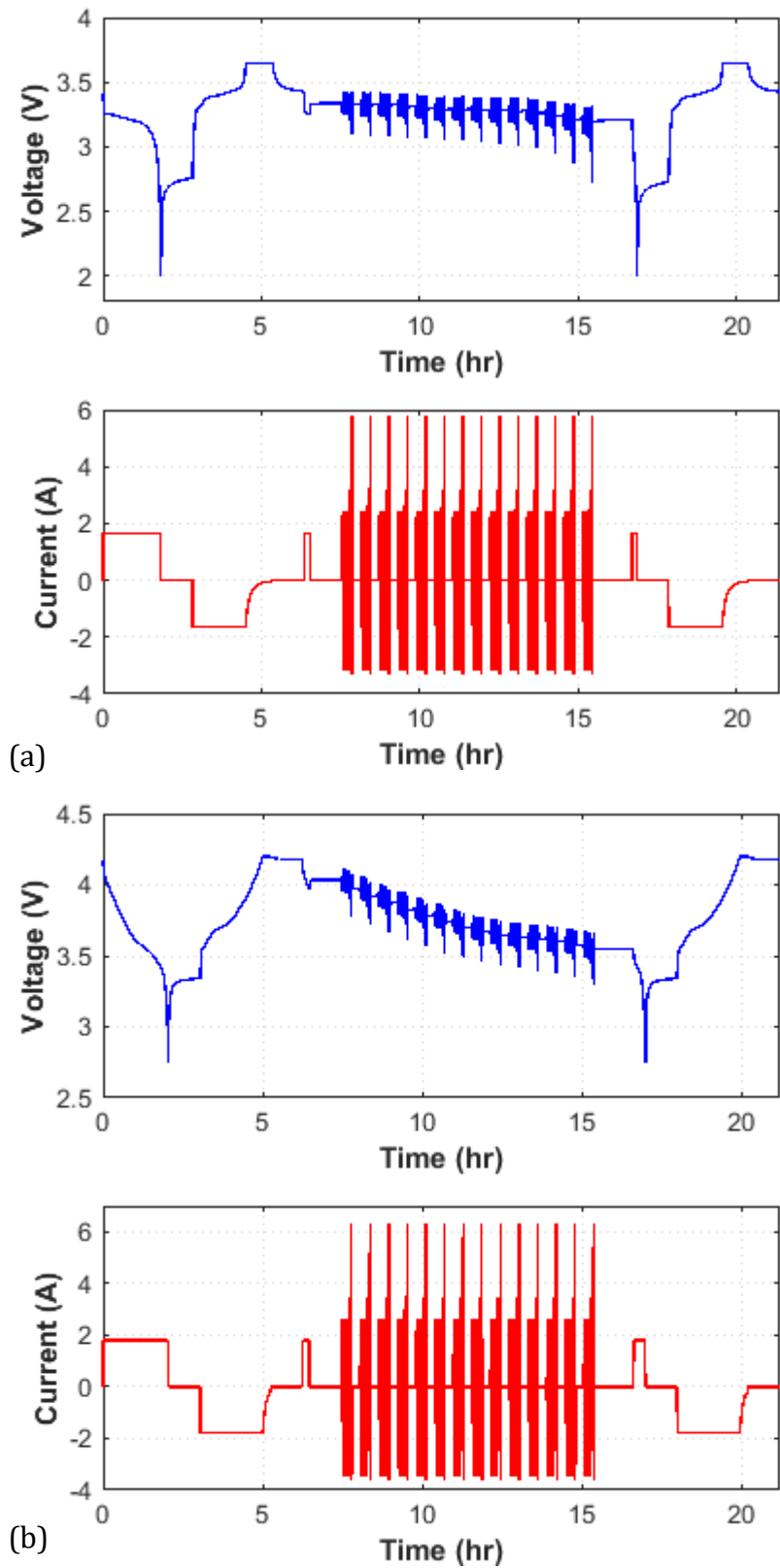
Fig. 4.10 Voltage and current waveforms for (a) one LFP cell and (b) one NMC cell under the multi-cycle NEDC test at 25°C
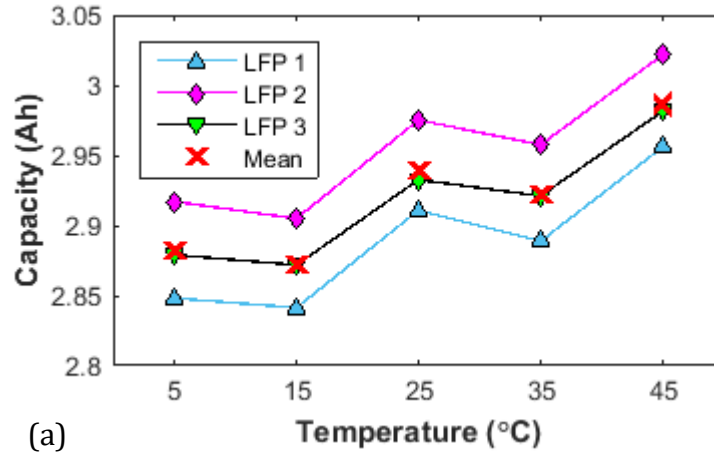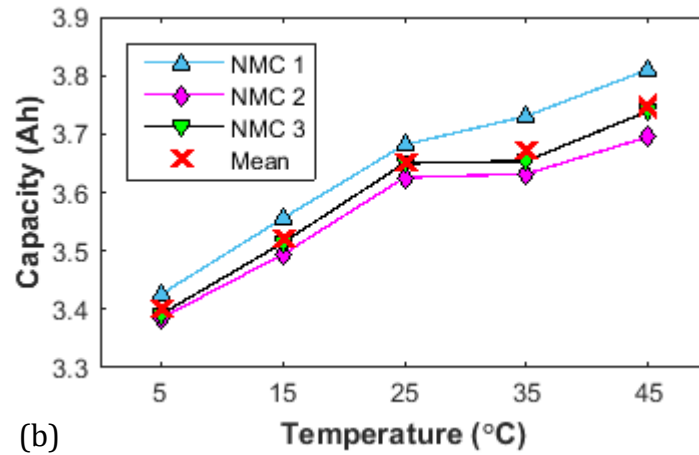
Fig. 4.11 Experimentally determined capacities for (a) LFP and (b) NMC test cells, measured at 0.5C current rate (discharge)

4.6.3 Voltage Estimation

A statistical analysis of the test results was performed. Fig. 4.12 presents the average root-mean-squared-error (RMSE) voltage for each set of LFP and NMC cells for the self-designed pulse test results. In order to mitigate the SOC dependency of the OCV functions, the true SOC values obtained using the coulomb-counting technique were used to compute the RMSE values for each model structure. It is evident that the Rint model has the largest error for both lithium-ion cell chemistries. This is due to the absence of any transient states as to capture the underlying dynamics of the electrochemical and thermodynamic processes.
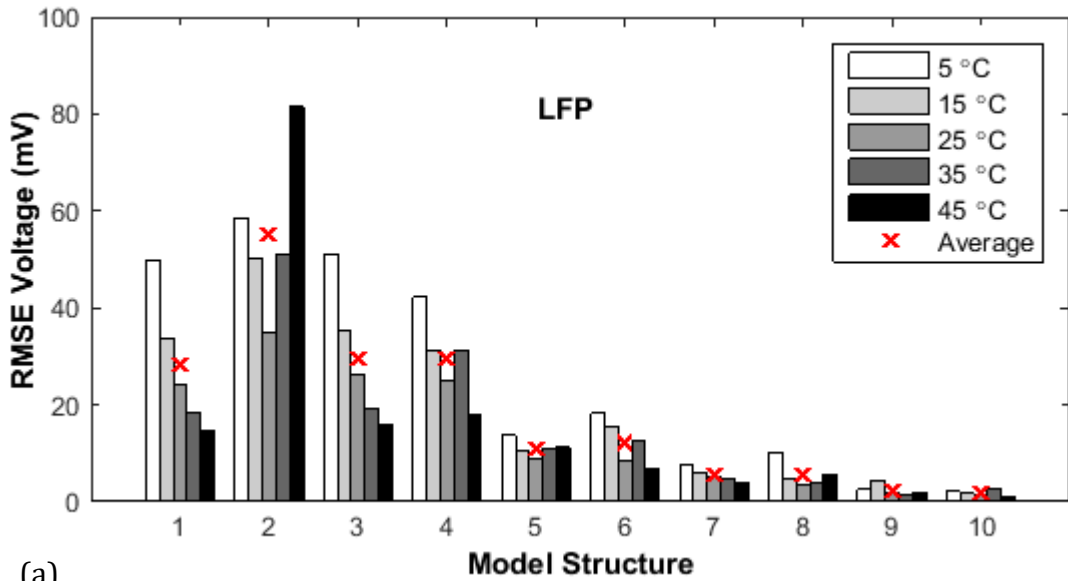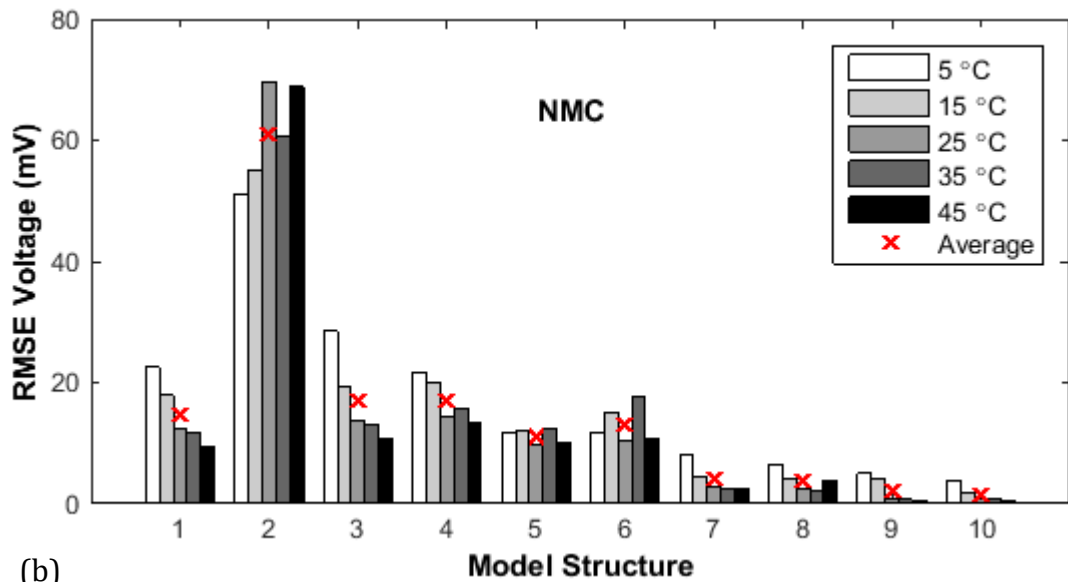
Fig. 4.12 Average modelling error on models of Table 4.1 for the self-designed test for (a) LFP and (b) NMC set of cells over the temperature range of 5 to 45°C

The hysteresis models perform consistently better compared to the simple Rint model. This improvement is attributed to the fact that there exists a hysteresis level for both LFP and NMC cell chemistries, which needs considering for more accurate cell modelling. Although similar results are achieved by the two hysteresis models (structures 3 and 4), the model structure proposed by Huria *et al.* [220] is comparatively more favourable in real-time applications, as it only has one identifiable parameter to be estimated online. This further reduces the

computational burden on the BMS. The Randles and the modified Randles models both have two capacitors to include the OCV and the transients associated with the diffusion effects respectively. However, a large error is induced due to the instabilities in the battery model states.

Compared to other structures, the one- and two-*RC* models both demonstrate excellent modelling capabilities. These two models have a separate empirical function as to describe the cell's OCV as a function of SOC. It is observable that by including the OCV hysteresis as one of the EKF states, an even better modelling result in terms of RMSE is achievable.

In order to study the SOC estimation and tracking capability of each model structure, the results for the multi-cycle NEDC test over the SOC range of 10-90% were used. The dual-EKF algorithm was initialised with the best-guess values for the model parameters and the SOC state was set to its true value. Fig. 4.13 presents the estimated cell voltage for one NEDC cycle at SOC = 64% for one of the LFP test cells. The results obtained for the NMC cells pose a similar behaviour. It can be noted that the two-*RC* model structure with hysteresis included has the closest fit to the true cell voltage.

4.6.4 SOC Estimation

Fig. 4.14 illustrates the resulting model-based SOC estimation errors obtained for the multi-cycle NEDC current profile, over the temperature range of 5°C to 45°C. The average SOC errors for the three LFP set of cells are shown in Fig. 4.14(a) and those for the NMC set of cells are shown in Fig. 4.14(b). The EKF SOC state for all models was correctly initialised to 90% and the filter and hysteresis states were set to zero. It can be noted that at low operating temperatures, the induced SOC error is the largest. This is due to the fact that at low temperatures, the inherent electrochemical reactions are significantly slower. Thus, it becomes more difficult to model the underlying cell dynamics, leading to a larger modelling and SOC error.
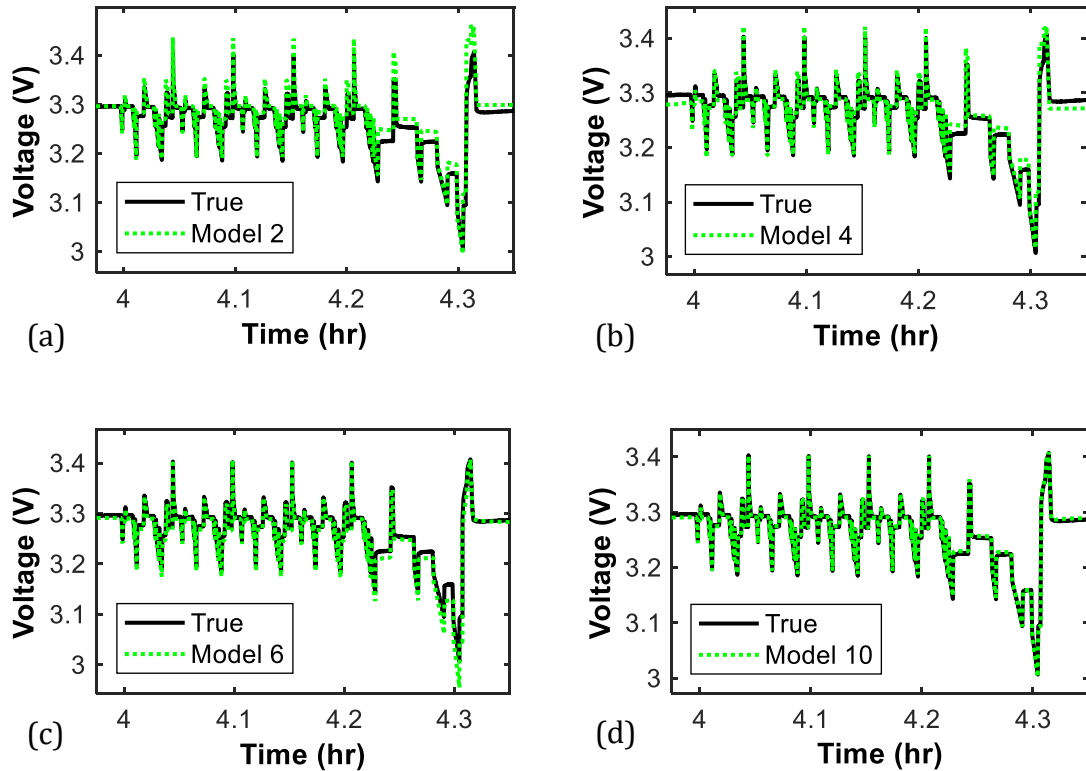
Fig. 4.13 Estimated voltage from one NEDC drive cycle for (a) Rint model, (b) one-state Hysteresis model, (c) modified Randles model, and (d) two-*RC* model with hysteresis for one LFP cell at 25°C

The average SOC errors in Fig. 4.14 show that, the one- and two-*RC* model structures pose a considerably better performance for SOC estimation in real time for both test cell chemistries. This can be attributed to the enhanced characterisation of the charge-transfer and diffusion effects by the model states. Moreover, by including the hysteresis effects in the *RC*-network model structures, a further improvement in the SOC estimate can be achieved.

Thus far, the SOC estimation results presented have been obtained using correct initialisation for the EKF's SOC state. In practice, the EKF would be initialised with a best-guess value for SOC, which is usually realised based on OCV measurements prior to a load connection and/or using the cell's most recent history of usage. Either way, it is important to understand the SOC filter's behaviour with respect to erroneous initial conditions.

143
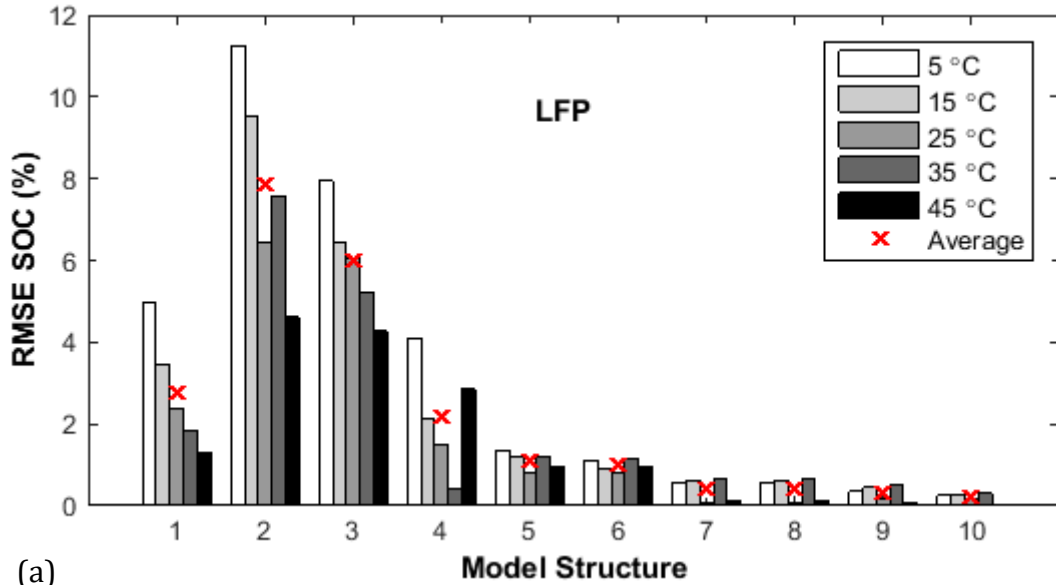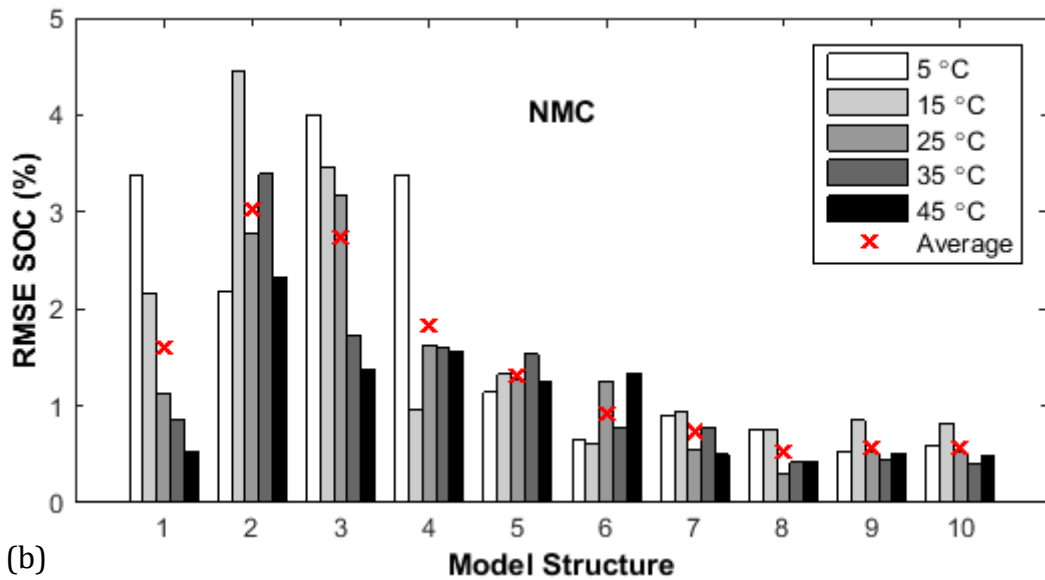
Fig. 4.14 Average SOC estimation error on models of Table 4.1 for the multi-cycle NEDC profile for (a) LFP and (b) NMC cells over the temperature range of 5 to 45°C

Using the measurements recorded for the pulsed-current test profile at 25 °C, SOC was estimated for all the LFP and NMC test cells under three different EKF initialisation scenarios. Firstly, the SOC state was correctly initialised to 100%. The results are presented in Table 4.3. As can be seen, all of the model structures are able to achieve a SOC estimate that is within the standard ±5% error bounds, given a correct initialisation of the SOC state is provided. Secondly, the SOC state was intentionally initialised to 80% instead of 100% to verify the filter's convergence.

The results are presented in Table 4.4. It is evident that compared to other model structures, both *RC* models with and without the hysteresis included achieved outstanding SOC estimation errors. Finally, the SOC state was incorrectly set to 60% instead of 100%. Similar results are obtainable as presented in Table 4.5. It should be noted that the SOC error statistics for the three SOC initialisation cases given here were computed by excluding the first hour of the SOC data. This allowed for a reasonable convergence towards the actual SOC to be established for all of the model structures, before the RMSE for each SOC case was calculated.

As presented in Table 4.4 and Table 4.5, the best SOC estimation results with incorrectly initialised filter states are realised with the hysteresis model '3' and the one- and two-*RC* models '7' and '8' respectively. It is apparent that including the transient effects in a cell model not only improves the characterisation of a cell under load conditions in real time (see Fig. 4.12), but also results in a more robust SOC estimator. Furthermore, to reduce the uncertainties in the SOC estimate, the hysteresis functions can possibly be merged with the *RC* models resulting in a better SOC convergence.

Table 4.3 SOC estimation results for the self-designed pulsed-current test profile at 25°C with correct initialisation of 100%

Model	LFP			NMC		
	Average Error (%)	Maximum Error (%)	Standard deviation of error	Average Error (%)	Maximum Error (%)	Standard Deviation of Error
1.	3.93	5.27	1.53e-4	5.24	6.80	1.46e-3
2.	2.13	9.63	1.94e-3	3.09	11.11	6.08e-3
3.	3.17	14.35	1.10e-3	2.80	9.78	7.77e-3
4.	2.73	8.93	3.22e-3	4.95	14.76	1.46e-2
5.	3.88	5.86	2.61e-3	6.47	16.32	3.78e-3
6.	3.03	6.02	7.21e-4	2.20	5.21	8.43e-3
7.	2.66	10.74	1.05e-3	2.15	7.98	5.95e-3
8.	2.65	10.64	1.06e-3	2.15	7.78	5.99e-3
9.	1.39	8.58	6.56e-4	2.89	9.69	6.55e-3
10.	1.44	6.78	1.35e-3	2.15	7.96	5.99e-3

Table 4.4 SOC estimation results for the self-designed pulsed-current test profile at 25°C with incorrect initialisation of 80%, when actual SOC = 100%

Model	LFP			NMC		
	Average Error (%)	Maximum Error (%)	Standard deviation of error	Average Error (%)	Maximum Error (%)	Standard Deviation of Error
1.	13.19	14.82	5.6e-4	5.23	7.17	2.06e-3
2.	6.33	11.39	6.5e-3	3.09	10.91	4.2e-3
3.	3.40	14.65	1.6e-3	2.80	9.79	6.2e-3
4.	6.96	13.67	1.1e-2	4.95	16.16	1.0e-2
5.	3.62	6.47	3.5e-3	6.47	15.72	3.41e-3
6.	5.07	9.46	2.9e-4	2.20	6.79	2.70e-3
7.	3.03	11.18	8.5e-4	2.15	8.03	5.16e-3
8.	3.02	11.06	9.0e-4	2.14	8.01	5.16e-3
9.	2.28	11.03	6.8e-4	2.89	9.69	7.05e-3
10.	2.01	8.37	1.4e-3	2.15	8.01	5.11e-3

Table 4.5 SOC estimation results for the self-designed pulsed-current test profile at 25°C with incorrect initialisation of 60%, when actual SOC = 100%

Model	LFP			NMC		
	Average Error (%)	Maximum Error (%)	Standard deviation of error	Average Error (%)	Maximum Error (%)	Standard Deviation of Error
1.	13.45	14.82	4.57e-3	10.00	10.78	1.05e-3
2.	19.58	35.74	6.24e-4	3.54	10.94	2.97e-3
3.	3.72	14.70	2.35e-3	3.27	9.80	5.28e-3
4.	16.20	31.63	2.86e-3	6.56	16.52	1.03e-2
5.	8.61	16.98	2.87e-3	6.60	15.98	3.15e-3
6.	11.42	21.17	4.93e-4	2.55	5.97	1.95e-3
7.	3.12	11.25	8.50e-4	2.33	8.07	4.55e-3
8.	3.12	11.12	8.50e-4	2.32	8.05	4.50e-3
9.	2.47	11.17	3.21e-4	2.78	9.69	7.35e-3
10.	2.34	8.80	5.69e-4	2.34	8.06	4.40e-3

4.6.5 SOP Characterisation

Using the HPPC and the DC resistance identification method described in Chapter 2, section 2.2.4.1, the cells' internal resistances and their available discharge powers (i.e. SOP), over the SOC range of 90% to 10%, are obtained. The averaged resistance and SOP results for the two sets of LFP and NMC cells are presented in Fig. 4.15 and Fig. 4.16, respectively.
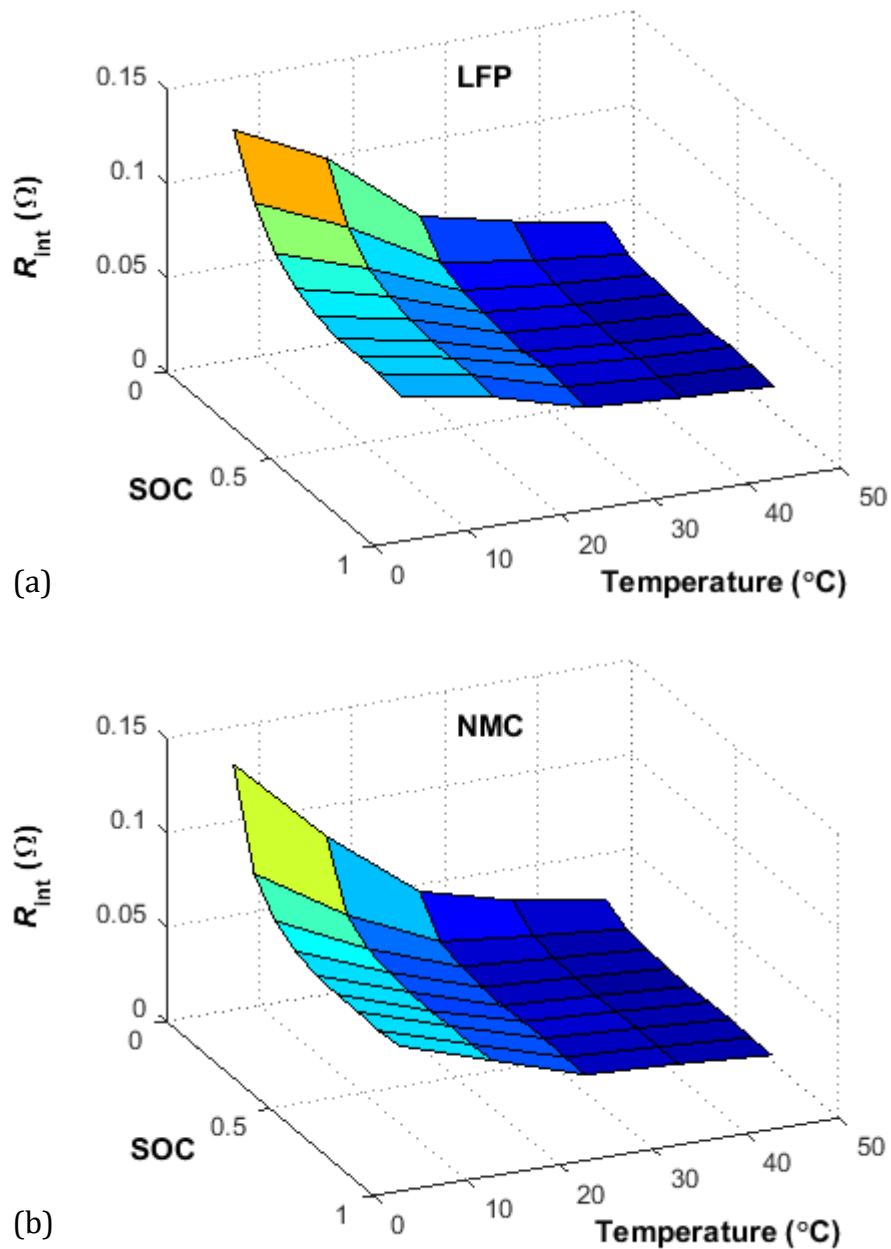
Fig. 4.15 Comparison of average internal resistances for (a) LFP and (b) NMC test cells, obtained using the HPPC method
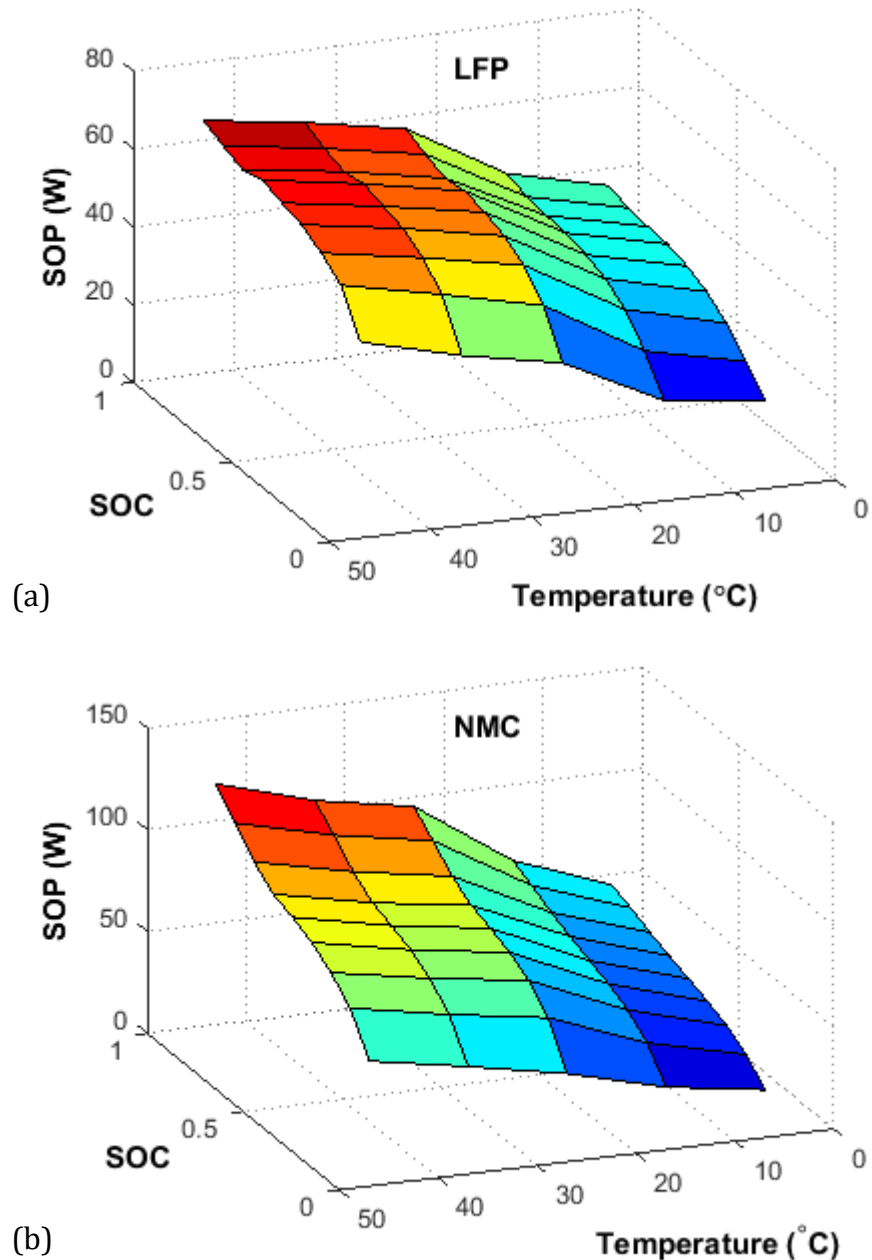
Fig. 4.16 Comparison of calculated discharge power using the HPPC method for (a) LFP and (b) NMC cells

Whereas Fig. 4.15(a) and Fig. 4.15(b) demonstrate the variation of the discharge cell resistance, Fig. 4.16(a) and Fig. 4.16(b) display how the cells' SOP values for a fixed current-pulse duration (in this case 18 seconds) may vary with respect to SOC and temperature for the LFP and NMC cells respectively. It can be noted that at high temperature and SOC values, the cell resistance is smallest for both chemistries, resulting in a larger quantity of power being available for discharge. Moreover, at

high SOC values, the corresponding OCV is also larger, which further improves the cell's capability to source power, without violating the safe operating voltage thresholds.

As defined by (4.14) and (4.15), the quality of the estimated instantaneous discharge or charge power largely depends on the accuracy of the identified cell resistance under various operating scenarios. Using the EKF-identified model parameters obtained for each test cell under a single HPPC repetition at 25 °C and SOC = 90%, the Thevenin equivalent circuit resistance, R_{eq}, for every model structure is calculated. The obtained model-based cell resistances for each set of chemistries are then averaged and compared to the average of the resistances calculated by equation (2.18) for the same HPPC profile. The results are presented in Table 4.6. It is evident that the two-RC model and the one-RC with adaptive hysteresis model provide the best estimates for the cell's equivalent resistance, which can be used to improve the quality of the model-based SOP estimate. Additionally, the EKF identified R_{eq} parameter for SOP predictions is shown to have a very low mean error for all model structures.

In order to further demonstrate the reliability of the dual-EKF algorithm for battery model identification, the EIS method is implemented as described in Chapter 2, section 2.3.2.2 in order to identify the 2-RC model parameters for one NMC test cell as a function of SOC. The results are compared against those attained using the dual-EKF algorithm at 20% and 80% SOC levels and are presented in Table 4.7 and Table 4.8 respectively. It is apparent that despite the lack of persistent excitation of the NEDC current profile, the EKF algorithm is capable of tracking the SOC-dependent variations in the battery model parameters. This is true, if and only if a sufficiently accurate *a priori* knowledge of the model parameters is available at the initialisation step. Otherwise, the input signal is required to completely satisfy the persistent excitation criterion [258].

Note that for a reliable SOP assessment, an accurate SOC estimate is also required, which in turn reflects on the accuracy of the cell's predicted OCV in (4.14) and (4.15). Thus, the two-RC model structure can be nominated as an optimum choice, with only

two estimable states and five identifiable parameters, for an accurate cell dynamic modelling and joint SOC and SOP estimation. Alternatively, for cell chemistries with large inherent hysteresis levels, the one-RC with hysteresis model is preferred.

Table 4.6 Comparison of EKF-identified R_{eq} with those calculated for the LFP and NMC cells for a single HPPC repetition at 25°C and SOC = 100%

Model	LFP		NMC	
	EKF Identified R_{eq} (mΩ)	Mean Error (mΩ)	EKF Identified R_{eq} (mΩ)	Mean Error (mΩ)
1.	35.5	8.1	26.5	7.8
2.	38.4	5.2	28.3	6.0
3.	45.6	2.0	46.4	12.1
4.	38.4	5.2	28.3	6.0
5.	37.9	5.7	29.4	4.9
6.	36.4	7.2	27.8	6.5
7.	48.2	4.6	29.5	4.8
8.	47.0	3.4	30.2	4.1
9.	46.0	2.4	32.7	1.6
10.	47.3	3.7	36.6	2.3

Table 4.7 Comparison of identified parameters for two-RC model structure using the accurate EIS method against the dual-EKF method for LFP cell at SOC = 20%

Parameter	EIS Identified	EKF Identified	Absolute Error
R_s (mΩ)	25.47	25.55	0.08
R_1 (mΩ)	13.30	10.35	2.95
C_1 (F)	1424	1561	137
R_2 (mΩ)	13.83	12.41	1.42
C_2 (F)	6.2	6.8	0.60

Table 4.8 Comparison of identified parameters for two-*RC* model structure using the precise EIS method against the dual-EKF method for LFP cell at SOC = 80%

Parameter	EIS Identified	EKF Identified	Absolute Error
R_s (mΩ)	24.02	24.09	0.07
R_1 (mΩ)	13.63	13.92	0.29
C_1 (F)	1355	1293	62
R_2 (mΩ)	9.39	9.64	0.25
C_2 (F)	5.9	5.8	0.10

4.7 Chapter Conclusions

This Chapter has systematically reviewed the most common lumped-parameter equivalent circuit models used in lithium-ion battery energy storage applications based on their number of appearances in literature. The merits for comparison were modelling accuracy in terms of average root-mean-squared-error for two sets of lithium-ion cells of different electrode chemistries, namely the LFP and NMC. The generality of each model structure was examined over a temperature range of 5°C to 45°C. The battery models' parameters and states were recursively estimated using a nonlinear system identification technique based on the dual-EKF algorithm. Furthermore, the dynamic performance of each model structure for joint estimation of SOC and SOP were discussed. The results suggested that the two-*RC* model structure, with two estimable states and five identifiable parameters, is an optimum choice for implementation of most battery energy and power management strategies. Alternatively, for cell chemistries with large inherent hysteresis levels, the one-*RC* model with hysteresis included is preferred without an increase in complexity.

Chapter 5

Sensitivity of Equivalent-Circuit *RC* Model to Battery Parameterisation Error

---

In Chapter 4, it was determined that an RC network model structure provides the highest level of accuracy when compared to other electrical equivalent-circuit battery models. It was also discussed that the identified battery parameters are prone to changes due to different operating conditions such as temperature, C-rate, SOC and SOH. Hence, when estimating various battery states based on an equivalent-circuit model, it is of utmost importance to update the model parameters in real time. Otherwise, misleading information regarding the battery's performance might be produced by the BMS algorithm. Consequently, in this Chapter, a frequency-domain analysis on the EIS-obtained impedance data for the NMC and LFP cell chemistries is performed, in order to establish the minimum order-number required to accurately model the underlying cell dynamics. Thereafter, a sensitivity analysis is carried out on the chosen RC model order with respect to the constituent model parameters. This allows for a better understanding of the impact that erroneous or static model parameters can have on the quality of the model-based battery states estimates such as SOC, SOP and SOH.

5.1 Introduction

In Chapter 4, it was observed that, modern BMS algorithms employ accurate battery models to estimate various battery states, such as SOC, SOH and SOP in real time. It also was deduced that, for LFP and NMC cell chemistries, the *RC*-network electrical equivalent-circuit model, as depicted in Fig. 4.5, can achieve high accuracy depending on the chosen model order. Generally, as the order of the employed model structure increases, so does the number of identifiable parameters; thus, more computational power and memory is required to implement the BMS algorithm online. Therefore, there is a trade-off between required modelling accuracy and the number of incorporated *RC* branches, which will be explored for the LFP and NMC cells.

In contrast to electrochemical and empirically-associated battery models, the parameters in an *RC*-network model usually have a physical interpretation to them, which can be particularly useful in SOP and SOH estimation. However, as for any other battery model structure, the parameters of an *RC* model are prone to variations that are caused by the conditions under which the battery is operating. These conditions include the battery's SOC, temperature and age [61]. Failing to account for these induced parameter deviations can result in erroneous battery state estimates, which is a common problem in those BMS algorithms that use static battery parameters. Thus, it is imperative to gain an understanding of the battery's sensitivity to these external stress factors.

In this Chapter, upon the identification of a suitable order number for the *RC* network model structure given in Fig. 4.5, its response sensitivity with respect to the constituent model parameters is both theoretically and experimentally analysed. The initial model parameters in this sensitivity study are accurately identified using the offline EIS technique and a nonlinear least-squares method. Then, each parameter is manually varied in steps of ±10% of its obtained best-fit value, up to a maximum of ±50% deviation, and the corresponding model response is simulated for analysis purposes.

5.2 *RC*-Network Equivalent-Circuit Battery Model

As explored in Chapter 4, depending on the desired accuracy and the dynamics of the intended application, different battery models have been developed by researchers. Amongst them, the *RC*-network electrical equivalent-circuit model is found to be the most effective in describing the underlying dynamics of LFP and NMC lithium-ion cells.

In most battery management problems, including in EV/HEVs, often one or two *RC* branches are used to describe the battery's dynamic response in real time. However, the model order-number in the reported works is chosen arbitrarily. Therefore, prior to conducting a sensitivity analysis on the *RC* battery model, this section puts its focus on the identification of a minimum order-number for the n-*RC* model structure given in Fig. 4.5.

5.2.1 EIS Analysis of LFP and NMC cells

The impedance spectra and the resulting Bode plots obtained for two of the test cells at a temperature of 25°C and 80% SOC are respectively presented in Fig. 5.1(a) and Fig. 5.1 (b). As can be seen, the spectra for both test cells cross the real axis at point α. This high-frequency impedance element relates to the cell's series resistance and is usually obtained around 1 kHz.

Between α and β, the spectrum for the NMC cell shows a depressed semi-circle that is associated with the growth of SEI layer [61] as a function of SOH. However, for the LFP test cell, the effect of the SEI is so small that it is not visible in the obtained spectrum. Thus, only one depressed semi-circle is observable between α and γ, which is due to the combination of the SEI film, and the charge-transfer resistance and double-layer effect of the electrodes.
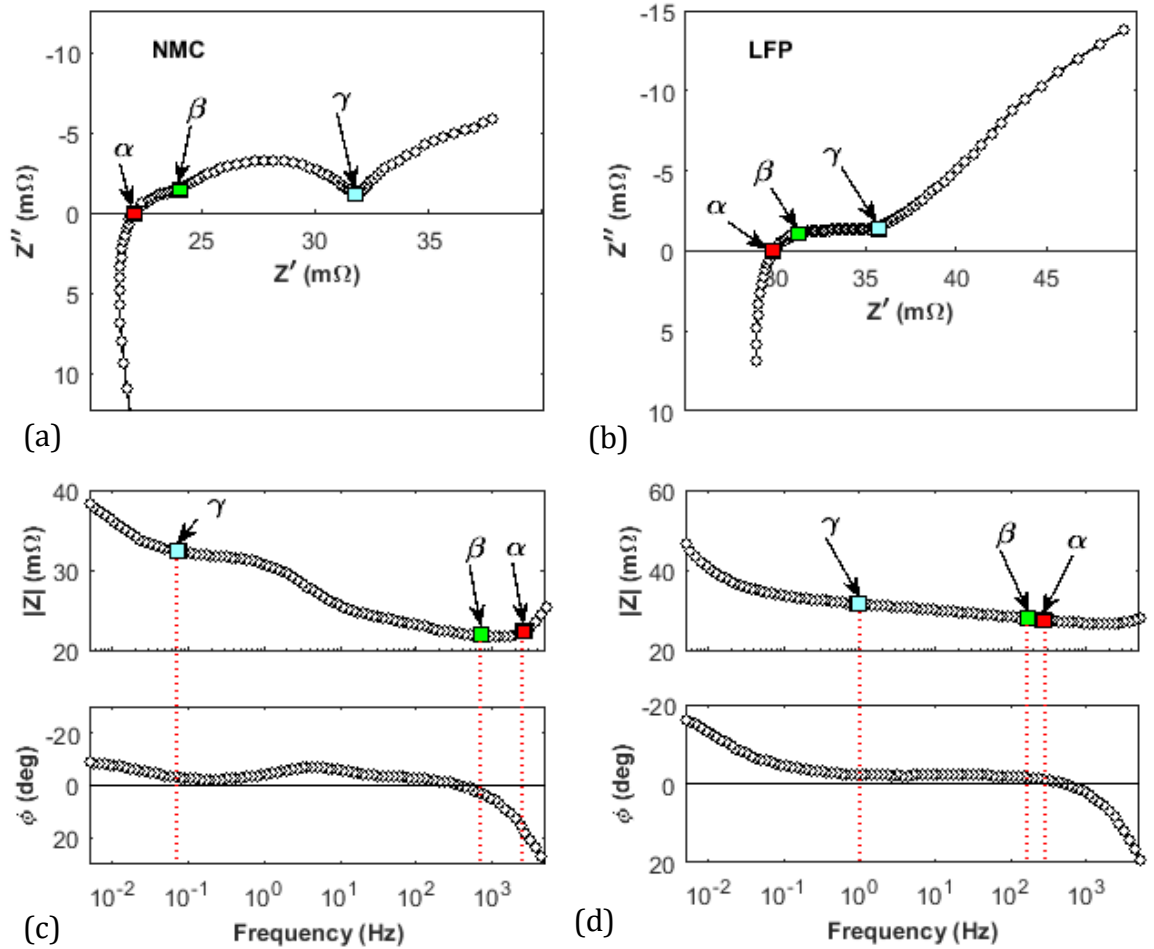
Fig. 5.1 Exemplary Nyquist plots (a)–(b) and Bode plots (c)–(d) obtained at 25°C and 80% SOC for an NMC and LFP test cell, respectively

Towards the low end of the spectrum (i.e. beyond point γ), a diffusional impedance is observed [259]. Modelling this low-frequency impedance element can be accurately achieved by the use of non-ideal electrical components, such as the diffusion Warburg impedance element (Z_W) or the constant-phase-element (CPE) [241]. These elements are defined as electrically imperfect resistors and capacitors, whose parameter identification in real time can lead to prohibitive requirements for memory and computational power. Furthermore, due the lack of physical meaning, these non-ideal elements are often precluded from online BMS applications. Therefore, equivalent-circuit *RC* models with ideal circuit elements are often adopted to represent the battery's impedance response in online applications.
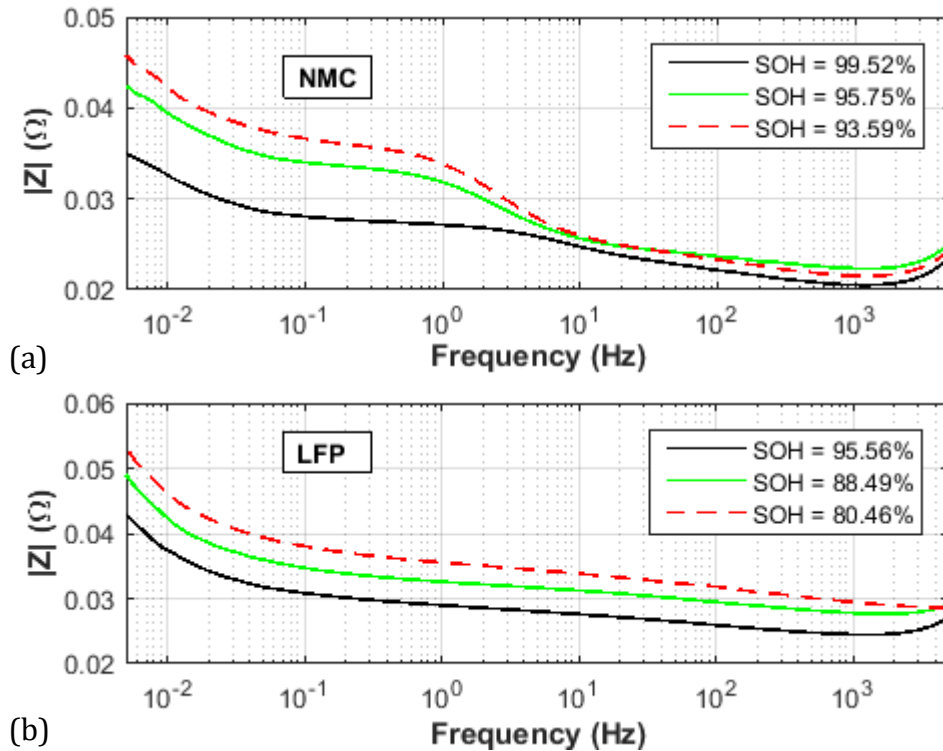
Fig. 5.2 Variation of impedance magnitudes with respect to cell ageing for (a) NMC and (b) LFP cells

Fig. 5.2 demonstrates the effect of ageing on the magnitude of the measured impedance for the NMC and LFP cells at 25°C and 80% SOC. In both cases, an increasing trend between the cell's age and the measured impedance can be observed. This effect is most profound towards the lower end of the frequency spectrum, where diffusional impedance occurs. This particular impedance element conveys vital information on the main charge storage capacity of the cell and can serve as a good indicator for SOH and SOP.

Fig. 5.3(a)–(b) illustrate the variation in the measured impedance for the NMC3 and LFP3 test cells, as a function of SOC. It is evident that as the SOC level drops, the cell impedance grows. This is due to the build-up of a potential gradient between the two cell electrodes. As the cell is further discharged, it becomes increasingly more difficult for the positive active species to push against this potential gradient and migrate from one electrode to another. Similar to ageing, the effect of varying SOC on impedance is stronger at lower frequencies.
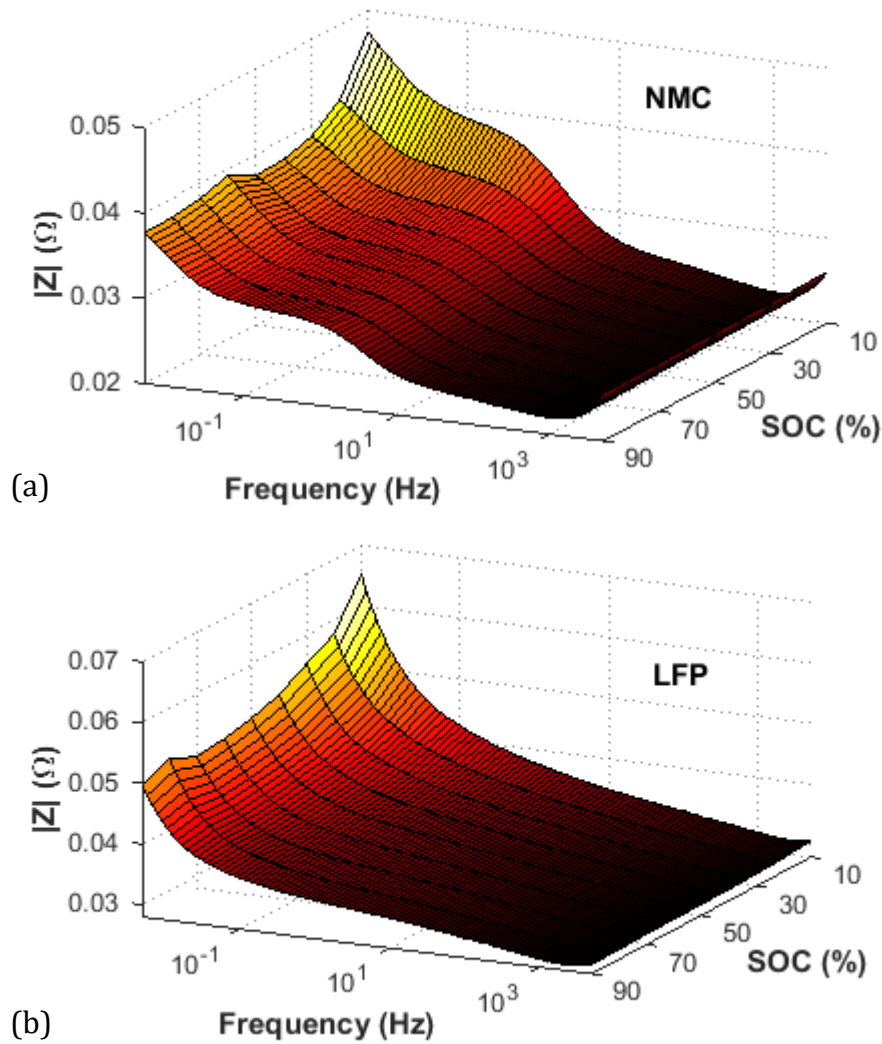
Fig. 5.3 Variation of cell impedance with respect to SOC for (a) NMC and (b) LFP cells obtained at 25°C

As well as low SOC, cold temperatures can also have a drastic effect on NMC and LFP cell impedances. This is demonstrated in Fig. 5.4. This effect occurs because at low temperatures, the boundary region between the cell electrodes and the electrolyte solidifies, exacerbating the cell's charge- and power-transfer capabilities. On the other hand, as the operating temperature increases, the cell impedance drops, resulting in a boost in the cell's power capabilities. However, operating lithium-ion cells at high temperatures can speed up the formation of the SEI layer and thus deteriorate the cells' lifetime faster. Nonetheless, to realise a more accurate model-based battery states monitoring system, it is vital to adapt to these SOC- and temperature-induced nonlinearities in the battery/cell impedance parameters.

(a)

(b)
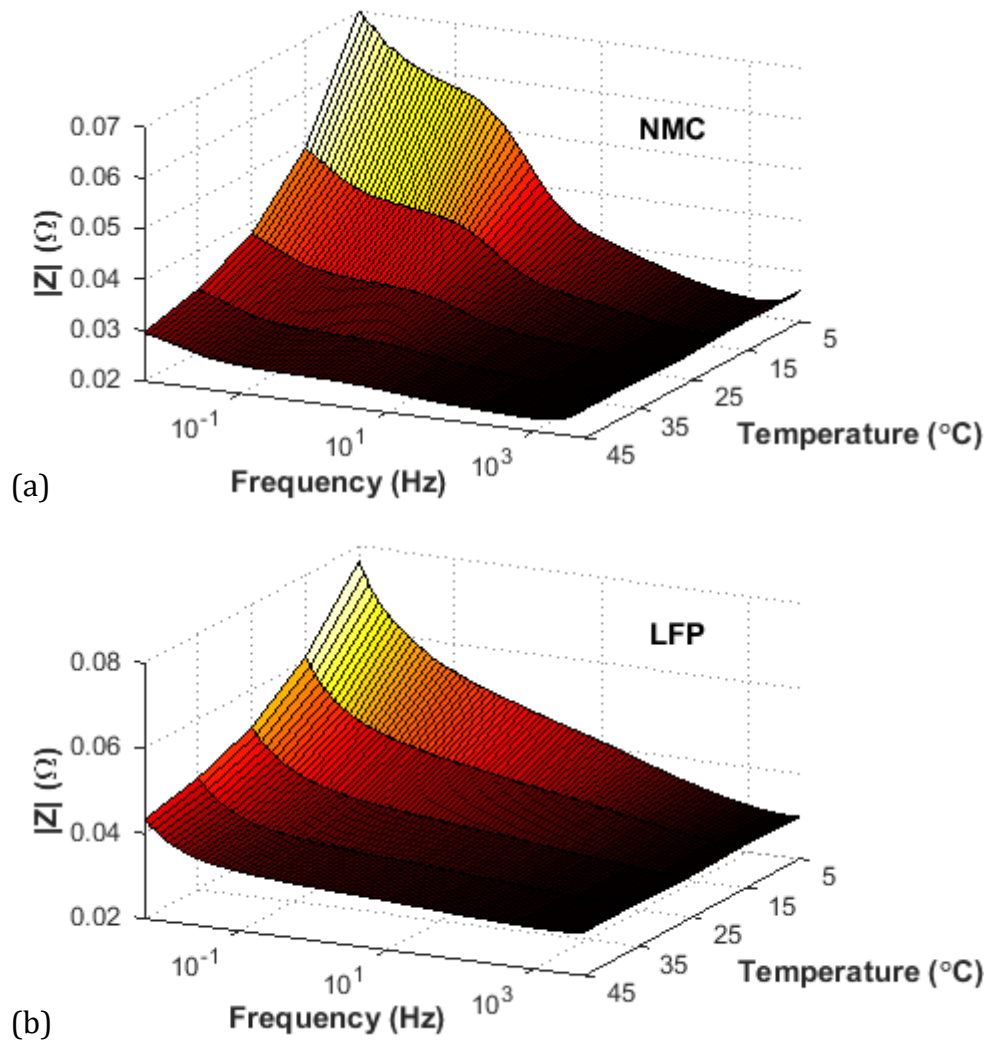
Fig. 5.4 Variation of cell impedance with respect to ambient temperature for (a) NMC and (b) LFP cells obtained at 80% SOC

5.2.2 Model Transfer Function

At its simplest, EIS is a pure sine-swept method which involves the injection of a voltage or a current sinusoid into the system, whilst measuring the amplitude and the phase of the resulting current or voltage response. There are two types of systems that can be characterised using the EIS technique; one-port and two-port networks. As depicted in Fig. 5.5, in a one-port network, the voltage and current are measured at the same port, allowing for the self-impedance of the system to be calculated. Whereas, in a two-port system, the voltage and current measurements are taken from different ports.
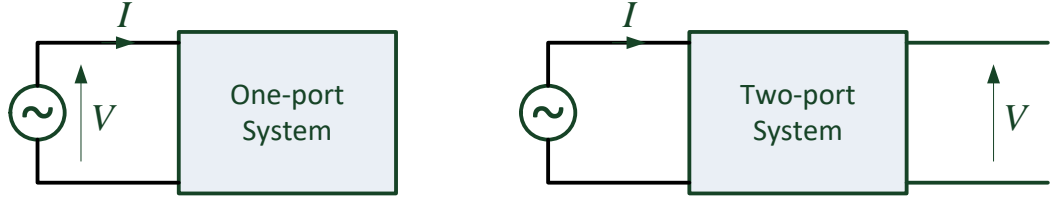
Fig. 5.5 Difference between a one- and two-port system for a sine-swept impedance characterisation using the EIS technique

In this case, the battery is a one-port system where using the potentiostatic EIS method (refer to Chapter 2, section 2.2.4.2 for more details on EIS), a voltage sinusoid is applied at the battery terminals and the sine-wave response current is measured at the same terminals. Thus, using equation (2.19), the battery's self-impedance can be expressed in the frequency domain as

$$Z_{\text{bat}}(\omega) = \frac{V}{I(\omega)} = |Z_{\text{bat}}(\omega)| \angle \phi_{\text{bat}}(\omega) \tag{5.1}$$

where V is the sinusoid voltage injected into the battery during EIS testing; $I(\omega)$ is the measured response current at angular frequency ω; $\phi_{\text{bat}}(\omega)$ is the phase angle between the input voltage and the response current; and $Z_{\text{bat}}(\omega)$ is the battery's complex impedance.

A continuous transfer-function representation of the n-RC battery model is required to be able to curve-fit the RC models of different order to the EIS-attained battery impedance data, and to perform a sensitivity analysis on the chosen model order. To this end, the battery model's output equation in the time domain is first derived by applying the Kirchhoff's voltage law to the circuit diagram in Fig. 4.5.

$$V_{\text{o}}(t) = V_{\text{OC}}(\text{SOC}) - [V_{\text{RC1}}(t) + \cdots + V_{\text{RC}n}(t)] - I_{\text{i}}(t) \cdot R_{\text{s}} \tag{5.2}$$

where $V_{\text{o}}(t)$ is the time-domain output voltage, $I_{\text{i}}(t)$ is the input current, $I_{\text{i}}(t) \cdot R_{\text{s}}$ is the series voltage drop, and $V_{\text{RC}n}(t)$ is the transient voltage drop across the n-th RC branch. Then, using Kirchhoff's current law, an equation for $V_{\text{RC}n}(t)$ is derived.

$$I_i(t) = i_{Rn}(t) + i_{RCn}(t) = \frac{V_{RCn}(t)}{R_n} + C_n \frac{dV_{RCn}}{dt}$$

(5.3)

$$\therefore V_{RCn}(t) = I_i(t) \cdot R_n - R_n C_n \frac{dV_{RCn}}{dt}.$$

Replacing $V_{RC1 \to n}$ in (5.2) with (5.3) and taking the Laplace transform of the resulting differential equation yields

$$V_o(s) = \mathcal{L}[V_o(t)] = V_{OC}(SOC) - \mathcal{L}[V_{RC1} + \cdots + V_{RCn} + I_i(t) \cdot R_s]$$

(5.4)

$$= V_{OC}(SOC) - \mathcal{L}[V_{RC1}] - \cdots - \mathcal{L}[V_{RCn}] - \mathcal{L}[I_i(t) \cdot R_s].$$

where $V_{OC}(SOC)$ is a SOC-dependent DC bias due to the battery's OCV and it is assumed to be in a steady-state condition. Given the time-domain definition of $V_{RCn}(t)$ in (5.3), and using the linearity, superposition and the differentiation properties of the Laplace transform, the battery model's output equation in the s-domain is obtained and expressed as,

$$V_o(s) = V_{OC}(SOC)$$
$$- I_i(s) \left[R_s + \left(\frac{R_1}{R_1 \cdot sC_1 + 1} \right) + \cdots + \left(\frac{R_n}{R_n \cdot sC_n + 1} \right) \right].$$

(5.5)

Subsequently, by rearranging (5.5), the self-impedance or transfer function of the n-RC battery model can be obtained.

$$Z_{mdl}(s) = \frac{V_{OC}(SOC) - V_o(s)}{I_i(s)}$$

(5.6)

$$= R_s + \left(\frac{R_1}{R_1 \cdot sC_1 + 1} \right) + \cdots + \left(\frac{R_n}{R_n \cdot sC_n + 1} \right)$$

Finally, direct mapping of $s \to j\omega$ allows for the magnitude and the phase of the battery model's frequency response to be calculated using equation (5.7).

$$Z_{\text{mdl}}(s) = Z_{\text{mdl}}(j\omega) = |Z_{\text{mdl}}(\omega)|\angle\phi_{\text{mdl}}(\omega) \tag{5.7}$$

where $|Z_{\text{mdl}}(\omega)|$ is the magnitude and $\phi_{\text{mdl}}(\omega)$ is the resulting phase angle of the model's frequency response as a function of angular frequency.

5.2.3 Minimum *RC* Model Order Selection

Most BMS algorithms are designed to run at frequencies below 10 Hz. This is due to the imposed hardware limitations such as cost, memory and processing power of the incorporated μP unit. As a result, it is not possible to properly reveal the battery's dynamics at higher frequencies using embedded system identification techniques. This is particularly pertinent as those impedance elements occurring at the lower end of the spectrum (i.e. beyond γ in Fig. 5.1) contain more useful information on the battery's current conditions with respect to SOH, SOC and temperature.

Therefore, in this thesis, the cell dynamics are modelled over a reduced frequency band of 5 mHz to 5 Hz. In order to properly capture the cell's diffusional impedance elements within the defined frequency band, an optimum order (in terms of accuracy and complexity) must be chosen for the equivalent-circuit *RC* model. An analysis is therefore carried out to investigate the performance of several *RC* model structures of up to fifth order (i.e. n = 1, 2, 3, 5).

Using the EIS-obtained complex impedance, the *RC* model parameters (i.e. R_s, R_1, C_1, etc.) are identified using the (offline nonlinear least-squares method) Levenberg-Marquardt algorithm [260]. Subsequently, the model parameters are identified via the minimisation of an error term, defined as

$$|\epsilon|^2 = \left(\ln|Z_{\text{bat}}(\omega)| - \ln|Z_{\text{mdl}}(\omega)| \right)^2 + \left(\phi_{\text{bat}}(\omega) - \phi_{\text{mdl}}(\omega) \right)^2 \tag{5.8}$$

where $|\epsilon|^2$ is the square error between the logarithmic moduli and the phases of the transfer function defined by (5.6) and those obtained through EIS testing.

Upon the completion of parameter identification for the NMC and LFP test cells, the response of the *RC* model structures under study were simulated. Fig. 5.6 compares the actual EIS complex data obtained at 25°C and 80% SOC over the desired frequency bandwidth of 5 mHz to 5 Hz to that presented by the RC model structures of up to fifth order. In both cases, the 1-*RC* model yields the poorest performance due to the lack of modelling capabilities to fully capture the non-ideal impedance elements at low frequencies. Note that as the *RC* model order increases, so does the goodness of the fitted impedance spectrum. However, a trade-off must be made between accuracy and complexity.

The model complexity is assessed based on the number of identifiable model parameters and the amount of time taken to estimate them. In order to achieve a fair assessment, the maximum number of iterations allowed for the optimisation algorithm is set at 600 per model parameter. Furthermore, the bounds on the same parameters for different model orders are all set to $\mathbb{R}_{>0} = \{x \in \mathbb{R} \mid x > 0\}$. The analysis is performed on datasets generated using all the six lithium-ion cells given.

Finally, the model accuracy is measured by the average of the RMSE values obtained between the magnitude of the EIS datasets at several SOC and temperature settings and the output from the *RC* models under study. This is defined as,

$$\text{RMSE} = \sqrt{\frac{1}{\omega_1 - \omega_0} \int_{\omega_0}^{\omega_1} \left(|Z_{\text{bat}}(\omega)| - |Z_{\text{mdl}}(\omega)| \right)^2 \cdot d\omega} \qquad (5.9)$$

where $\omega_1 = 2\pi \times 5 \text{ rads}^{-1}$ and $\omega_0 = 2\pi \times 0.005 \text{ rads}^{-1}$ are, respectively, the maximum and minimum angular frequencies measured by the ESI system (refer to setup shown in Fig. 2.19). The impedance magnitudes, both measured and simulated, are presented in a logarithmic scale.
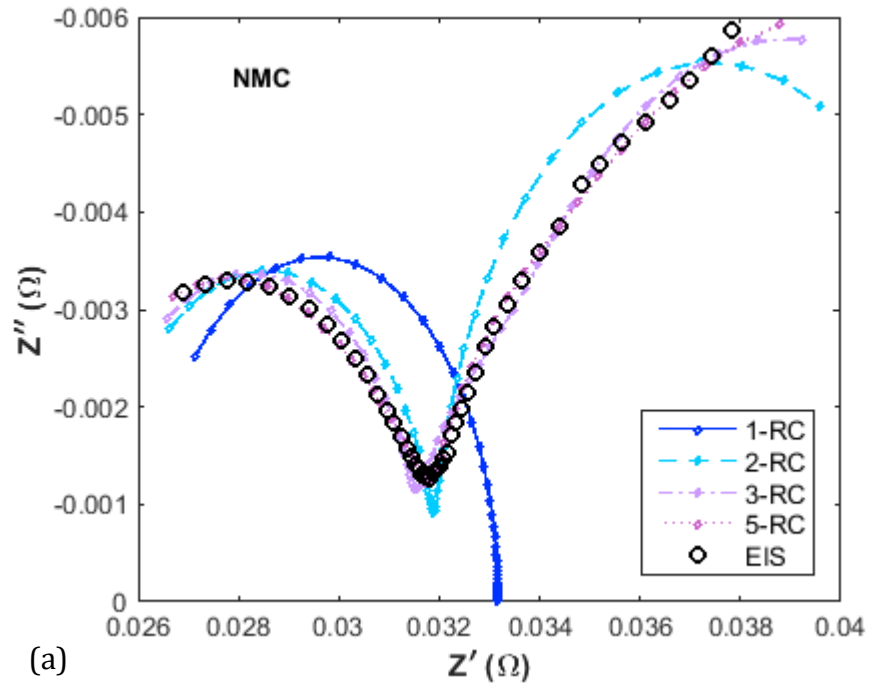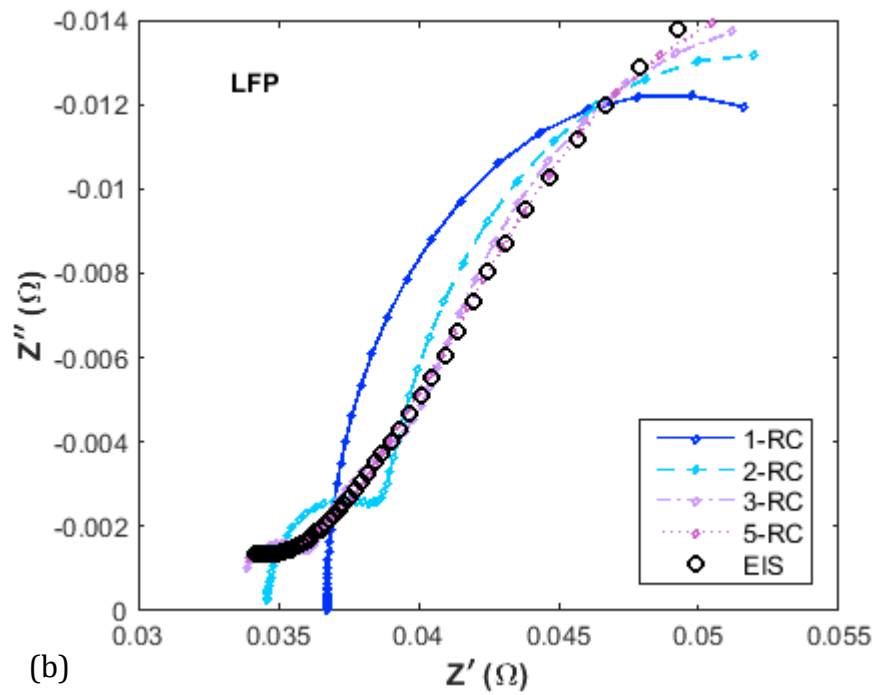
Fig. 5.6 Comparison of EIS data obtained for (a) NMC and (b) LFP test cells and fitted *RC* models of up to fifth order at 25°C and 80% SOC over the frequency range of 5 mHz to 5 Hz

A relationship between *RC* model order, accuracy and complexity is established and the results are presented in Fig. 5.7. It is evident that the average RMSE for both NMC and LFP cell variations decreases exponentially with the increasing model order number. However, with increased order-number, the model complexity increases and the duration of the identification process becomes disadvantageous.
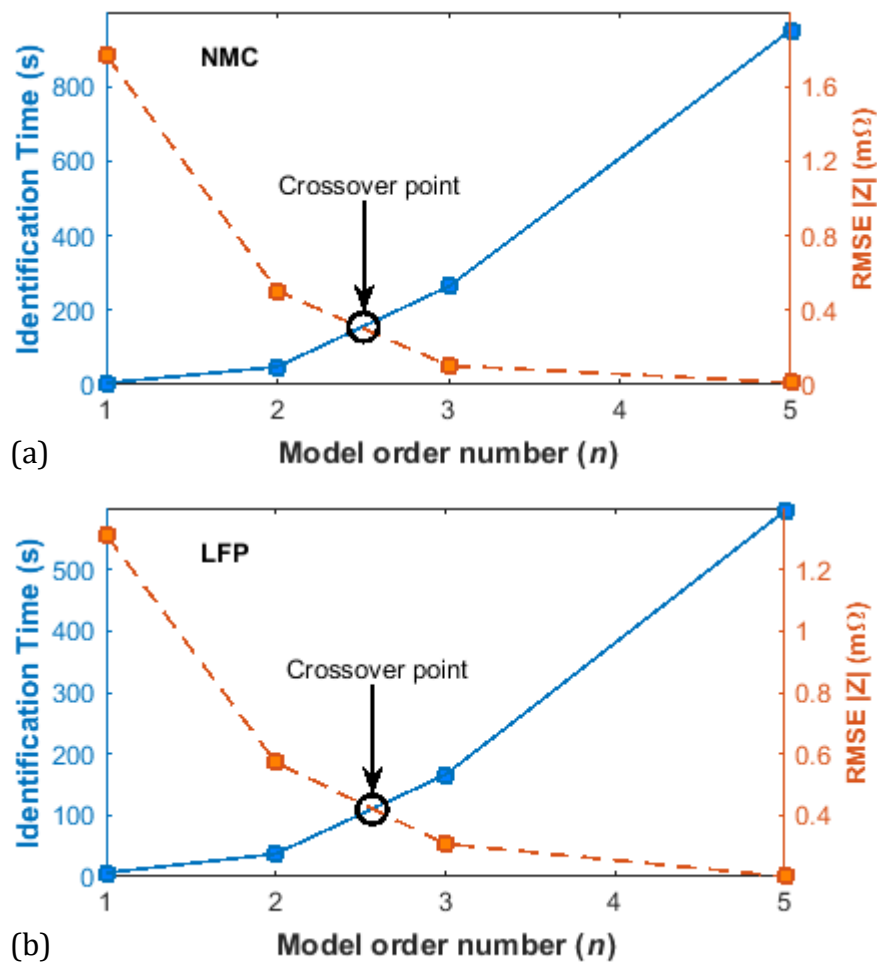
Fig. 5.7 Comparison of model accuracy and elapsed time for parameters identification of *RC* models for (a) NMC and (b) LFP test cells

Therefore, considering the trade-off crossover point between the two curves of model complexity (i.e. average identification time) and accuracy (i.e. average RMSE) in Fig. 5.7, it is determined that a minimum order number of $n = 2$ is required to properly capture the low-frequency dynamics of an NMC or LFP lithium-ion cell. It should be noted that the optimum model order number indicated by crossover point is not realisable per se. Thus, a 2-*RC* battery model structure is chosen in this thesis

for battery modelling and identification purposes. In this case, R_1 and C_1 are used to approximate the battery's diffusional impedance and R_2 and C_2 are used to represent the short time-constant transients associated with the charge-transfer resistance and the double-layer capacitance, respectively.

5.3 Mathematical Analysis

Partial derivatives can be used to conduct sensitivity analyses in a computationally efficient way [261]. Using this approach for the 2-RC battery model in hand, a dimensionless sensitivity coefficient $S_\rho(s)$ can be mathematically defined for every model parameter by calculating the partial derivative of the transfer function (5.6) with respect to a parameter ρ.

$$S_\rho(s) = \lim_{\Delta\rho \to 0} \left(\frac{\Delta Z_{\text{mdl}}(s)/Z_{\text{mdl}}(s)}{\Delta\rho/\rho} \right) = \frac{\partial Z_{\text{mdl}}(s)}{\partial\rho} \cdot \left(\frac{\rho}{Z_{\text{mdl}}(s)} \right) \qquad (5.10)$$

where $\Delta Z_{\text{mdl}}(s)$ is a change in model output caused by a change $\Delta\rho$ in the parameter ρ. The factor $\rho/Z_{\text{mdl}}(s)$ is used to normalise $S_\rho(s)$ by removing the effect of units. Subsequently, the coefficients for each model parameter can be achieved as follows.

For R_s:

$$S_{R_s}(s) = \frac{R_s}{Z_{\text{mdl}}(s)} \cdot \frac{\partial Z_{\text{mdl}}(s)}{\partial R_s} \qquad (5.11)$$

$$\frac{\partial Z_{\text{mdl}}(s)}{\partial R_s} = 1 \qquad (5.12)$$

$$\frac{R_s}{Z_{\text{mdl}}(s)}$$
$$= \frac{(C_1 C_2 R_1 R_2 R_s)s^2 + (C_1 R_1 R_s + C_2 R_2 R_s)s + R_s}{(C_1 C_2 R_1 R_2 R_s)s^2 + (C_1 R_1 R_2 + C_2 R_1 R_2 + C_1 R_1 R_s + C_2 R_2 R_s)s + R_1 + R_2 + R_s}.$$

$$(5.13)$$

For R_1:

$$S_{R_1}(s) = \frac{R_1}{Z_{\text{mdl}}(s)} \cdot \frac{\partial Z_{\text{mdl}}(s)}{\partial R_1} \tag{5.14}$$

$$\frac{\partial Z_{\text{mdl}}(s)}{\partial R_1} = \frac{1}{(C_1^2 R_1^2)s^2 + (2R_1 C_1)s + 1} \tag{5.15}$$

$$\frac{R_1}{Z_{\text{mdl}}(s)}$$

$$= \frac{(C_1 C_2 R_1^2 R_2)s^2 + (C_1 R_1^2 + C_2 R_2 R_1)s + R_1}{(C_1 C_2 R_1 R_2 R_s)s^2 + (C_1 R_1 R_2 + C_2 R_1 R_2 + C_1 R_1 R_s + C_2 R_2 R_s)s + R_1 + R_2 + R_s}. \tag{5.16}$$

For C_1:

$$S_{C_1}(s) = \frac{C_1}{Z_{\text{mdl}}(s)} \cdot \frac{\partial Z_{\text{mdl}}(s)}{\partial C_1} \tag{5.17}$$

$$\frac{\partial Z_{\text{mdl}}(s)}{\partial C_1} = -\frac{R_1^2 s}{(R_1 C_1 s + 1)^2} \tag{5.18}$$

$$\frac{C_1}{Z_{\text{mdl}}(s)}$$

$$= \frac{(C_1^2 C_2 R_1 R_2)s^2 + (R_1 C_1^2 + C_2 R_2 C_1)s + C_1}{(C_1 C_2 R_1 R_2 R_s)s^2 + (C_1 R_1 R_2 + C_2 R_1 R_2 + C_1 R_1 R_s + C_2 R_2 R_s)s + R_1 + R_2 + R_s}. \tag{5.19}$$

For R_2:

$$S_{R_2}(s) = \frac{R_2}{Z_{\text{mdl}}(s)} \cdot \frac{\partial Z_{\text{mdl}}(s)}{\partial R_2} \tag{5.20}$$

$$\frac{\partial Z_{\text{mdl}}(s)}{\partial R_2} = \frac{1}{(C_2 R_2 s + 1)} - \frac{C_2 R_2 s}{(C_2 R_2 s + 1)^2} \qquad (5.21)$$

$$\frac{R_2}{Z_{\text{mdl}}(s)}$$

$$= \frac{(C_1 C_2 R_1 R_2^2)s^2 + (C_2 R_2^2 + C_1 R_1 R_2)s + R_2}{(C_1 C_2 R_1 R_2 R_s)s^2 + (C_1 R_1 R_2 + C_2 R_1 R_2 + C_1 R_1 R_s + C_2 R_2 R_s)s + R_1 + R_2 + R_s}.$$

$$(5.22)$$

For C_2:

$$S_{C_2}(s) = \frac{C_2}{Z_{\text{mdl}}(s)} \cdot \frac{\partial Z_{\text{mdl}}(s)}{\partial C_2} \qquad (5.23)$$

$$\frac{\partial Z_{\text{mdl}}(s)}{\partial C_2} = -\frac{R_2^2 s}{(C_2 R_2 s + 1)^2} \qquad (5.24)$$

$$\frac{C_2}{Z_{\text{mdl}}(s)}$$

$$= \frac{(C_1 C_2^2 R_1 R_2)s^2 + (R_2 C_2^2 + C_1 R_1 C_2)s + C_2}{(C_1 C_2 R_1 R_2 R_s)s^2 + (C_1 R_1 R_2 + C_2 R_1 R_2 + C_1 R_1 R_s + C_2 R_2 R_s)s + R_1 + R_2 + R_s}.$$

$$(5.25)$$

Note that the sensitivity coefficients given by equations (5.11), (5.14), (5.17), (5.20) and (5.23) are expressed as a function of complex frequency 's'. Hence, to be able to compare the coefficients of different parameters over the entire frequency range of interest, the geometric mean of the magnitude of $S_\rho(s)$ for each parameter is calculated using equation (5.26) [262], where $|S_\rho(\omega_i)| \in [0,1]$ and n_s is sample size.

$$\bar{S}_\rho = \left(\prod_{i=1}^{n_s} |S_\rho(\omega_i)| \right)^{\frac{1}{n_s}} = \sqrt[n_s]{|S_\rho(\omega_1)| \cdot |S_\rho(\omega_2)| \cdots |S_\rho(\omega_{n_s})|}. \qquad (5.26)$$

Consequently, the model parameters identified at 25°C and averaged over the entire SOC range of 0% to 100% as given per Table 5.1, are applied to equations (5.11)-(5.25) in order to conduct a sensitivity analysis on the 2-*RC* battery model. The results for the NMC and LFP cells are presented in Fig. 5.8(a) and (b) respectively.

Table 5.1 Average 2-*RC* model parameters for the entire SOC range obtained using the EIS method at 25°C

Cell	$\bar{R}_s$ (mΩ)	$\bar{R}_1$ (mΩ)	$\bar{C}_1$ (F)	$\bar{R}_2$ (mΩ)	$\bar{C}_2$ (F)
NMC	24.5	18.4	1700	11.4	8.094
LFP	32.8	8.55	984	5.8	162

(a)

(b)
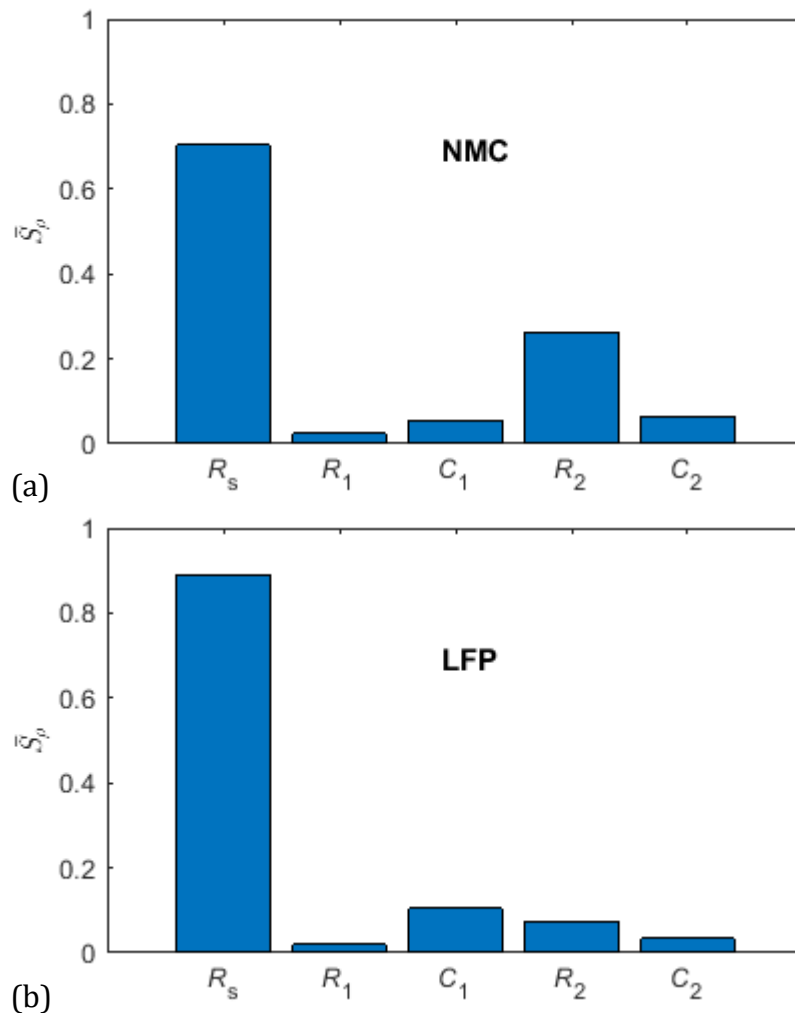
Fig. 5.8 Theoretical sensitivity of the 2-*RC* battery model to its constituent parameters for (a) NMC and (b) LFP cells

As can be seen, the 2-RC model's sensitivity with respect to R_s is greatest for both NMC and LFP cells. This is in accordance with the outcome of equation (5.12), which implies that any deviations in the model response caused by variations in R_s is almost instantaneous, unlike any other RC parameter. For both cell chemistries, the effect of diffusional resistance R_1 is mathematically found to be smallest. However, variations exist amongst the same RC parameters, when curve-fitted to different cell chemistry data.

In the NMC case, the effect of short time-constant transients (i.e. R_2 and C_2) on model sensitivity is evidently larger when compared to that of the long time-constant diffusional transients (i.e. R_1 and C_1). On the other hand, the model sensitivity calculated for the LFP cell with respect to C_1 is found to be largest, in comparison to other RC parameters. This is due to the fact that for the LFP cell, as demonstrated in Fig. 5.1(d), there is a large phase-change at the lower end of spectrum, which means that the cell's diffusional impedance is mostly caused by a capacitive reactance (i.e. C_1).

The theoretical sensitivity results presented imply that, for an accurate battery modelling and state estimation in an online application, model parameters must be identified in real time. This will ensure that any variations in the parameters with respect to SOC, temperature and any other external stress factors are accounted for during identification to result in a better model-based estimate of certain battery states such as SOP.

5.4 Significance of Model Sensitivity to SOP Estimate

As discussed in Chapter 2, battery impedance can serve as a good indicator for SOP. This means that for a reliable BMS algorithm incorporating SOP estimation, any variations in the model-based impedance parameters can result in an erroneous SOP estimate. Hence, it is imperative to gain an understanding of the SOP sensitivity with respect to the battery's impedance. To this end, assuming steady-state conditions, the discharge and charge SOP definitions given by (4.14) and (4.15), respectively, can be expressed as a function of angular frequency.

$$\text{SOP}_{\text{dis}}(\omega) = \frac{V_{\text{min}}(V_{\text{OC}} - V_{\text{min}})}{|Z_{\text{bat}}(\omega)|} \tag{5.27}$$

$$\text{SOP}_{\text{ch}}(\omega) = \frac{V_{\text{max}}(V_{\text{max}} - V_{\text{OC}})}{|Z_{\text{bat}}(\omega)|} \tag{5.28}$$

where V_{min} and V_{max} are the minimum and maximum battery voltage thresholds, V_{OC} is the battery's OCV and $|Z_{\text{bat}}(\omega)|$ is the magnitude of the battery's complex impedance. Now, due to the presence of $|Z_{\text{bat}}(\omega)|$ in (4.14) and (4.15), the value of SOP given is frequency dependent and therefore, to obtain a geometric average of the maximum deliverable power by the battery over the frequency band of interest, SOP can be re-defined as,

$$\overline{\text{SOP}}_{\text{dis}} = \frac{V_{\text{min}}(V_{\text{OC}} - V_{\text{min}})}{\bar{Z}_{\text{bat}}} \tag{5.29}$$

$$\overline{\text{SOP}}_{\text{ch}} = \frac{V_{\text{max}}(V_{\text{max}} - V_{\text{OC}})}{\bar{Z}_{\text{bat}}} \tag{5.30}$$

$$\tag{5.31}$$
$$\bar{Z}_{\text{bat}} = \left(\prod_{i=1}^{n_{\text{s}}} |Z_{\text{bat}}(\omega_i)| \right)^{\frac{1}{n_{\text{s}}}}$$
$$= \sqrt[n_{\text{s}}]{|Z_{\text{bat}}(\omega_1)| \cdot |Z_{\text{bat}}(\omega_2)| \cdots |Z_{\text{bat}}(\omega_{n_{\text{s}}})|}$$

where $\bar{Z}_{\text{bat}}$ is the geometric mean of the battery impedance magnitudes measured over the frequency band of $\omega_0 = 2\pi \times 0.005\ \text{rads}^{-1}$ to $\omega_1 = 2\pi \times 5\ \text{rads}^{-1}$. It should be noted that for an n-RC battery model with a good fit, $\bar{Z}_{\text{bat}}$ can be replaced by $\bar{Z}_{\text{mdl}}$. Therefore, the sensitivity of SOP estimate with respect to the battery impedance modelled by the 2-RC model can be expressed as,

$$\Delta\overline{\text{SOP}}_{\text{dis}} = \frac{V_{\text{min}}(V_{\text{OC}} - V_{\text{min}})}{\Delta\bar{Z}_{\text{mdl}}} \tag{5.32}$$

$$\Delta \overline{\mathrm{SOP}}_{\mathrm{ch}} = \frac{V_{\max}(V_{\max} - V_{\mathrm{OC}})}{\Delta \bar{Z}_{\mathrm{mdl}}} \qquad (5.33)$$

$$\therefore \Delta \overline{\mathrm{SOP}} \propto \frac{1}{\Delta \bar{Z}_{\mathrm{mdl}}}. \qquad (5.34)$$

Using equation (5.34), it can be determined that for the same input signal, changes in SOP are inversely proportional to changes in the transfer-function response given by (5.6) with $n = 2$. Now, considering this relationship, the average magnitudes of the 2-*RC* model responses obtained at 50% SOC for the NMC and LFP cells are used to conduct a sensitivity analysis with respect to parameters $\{R_{\mathrm{s}}, R_1, C_1, R_2, C_2\}$.

To capture the effect of each model parameter on the impedance response of the 2-*RC* model, the parameter under study is varied from -50% to +50% of its best-fit value in steps of $\Delta 10\%$. Thereafter, a quantitative assessment of the induced modelling errors is performed using the RMSE equation defined in (5.9) as,

$$\mathrm{RMSE} = \sqrt{\frac{1}{\omega_1 - \omega_0} \int_{\omega_0}^{\omega_1} \left(\left| Z_{\rho_0}^{\mathrm{mdl}}(\omega) \right| - \left| Z_{\rho_i}^{\mathrm{mdl}}(\omega) \right| \right)^2 \cdot d\omega} \qquad (5.35)$$

where the error term is calculated between the impedance magnitude simulated using the best-fit model parameter, $\left| Z_{\rho_0}^{\mathrm{mdl}}(\omega) \right|$, and that obtained as a result of a parameter swing, $\left| Z_{\rho_i}^{\mathrm{mdl}}(\omega) \right|$.

Fig. 5.9 presents the sensitivity of the 2-*RC* model's impedance response to erroneous model parameters. The results shown here are averaged over the cell's entire SOC range of 0% to 100% to provide a global relationship between the incorporated model parameters and the response given by transfer-function (5.6). As expected by the mathematical analysis conducted previously, the effect of parameter R_{s} is most dominant for both NMC and LFP cells. For example, a change of $\Delta R_{\mathrm{s}} = +50\%$ has resulted in a deviation of 12 mΩ and 16 mΩ in the impedance magnitudes simulated for the NMC and LFP cells, respectively. This equates to a

deviation error of 25% (percentage-point) for the NMC cell and 30% (percentage-point) for the LFP cell, when using equations (5.32) and (5.33) to estimate SOP.
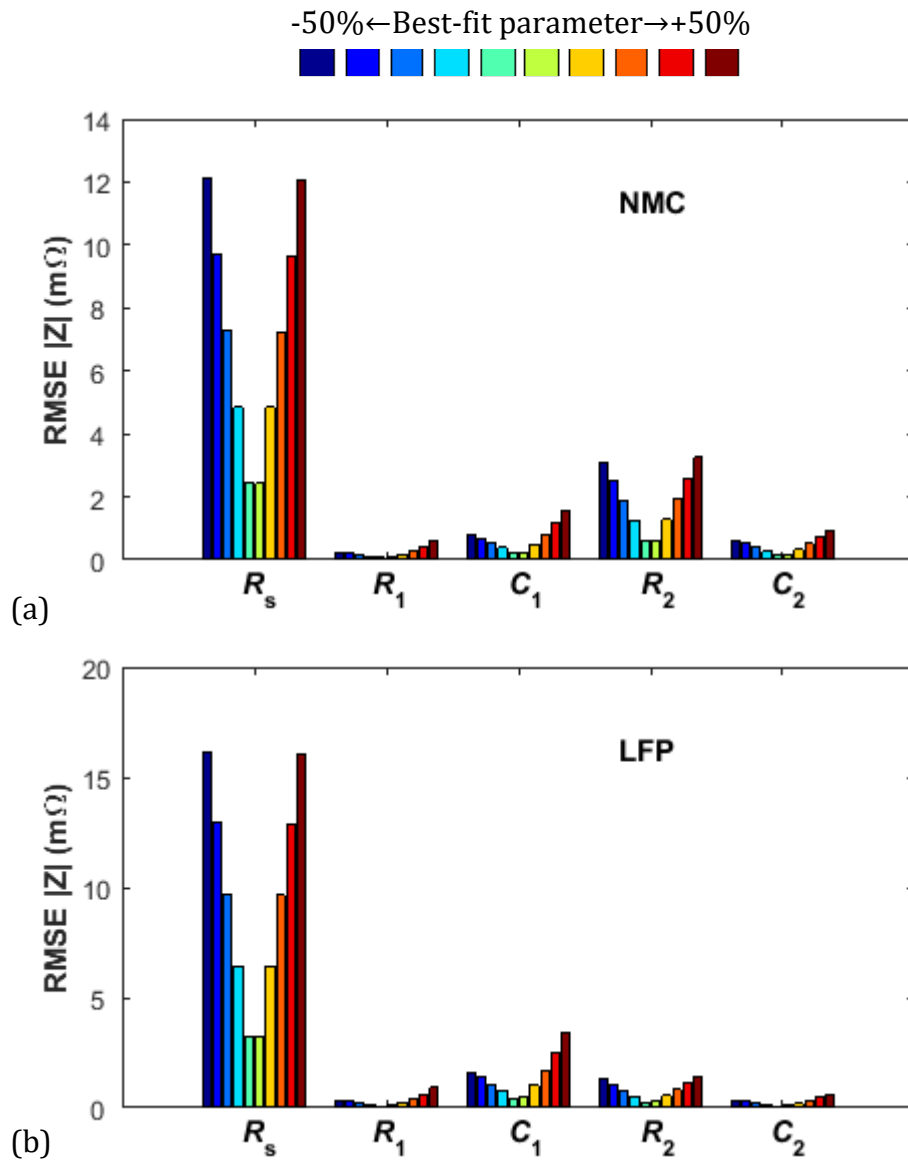
Fig. 5.9 Sensitivity of the 2-RC model-based battery impedance response to erroneous model parameters, simulated for (a) NMC and (b) LFP lithium-ion cells

From Fig. 5.9, it can be determined that R_1 is the least influential parameter in terms of model sensitivity in both cell chemistries, where a change of $\Delta R_1 = +50\%$ results in only a small SOP deviation of 1.7% for the NMC and 2.4% for the LFP cell. However, variations exist between the same parameters identified for the two variations of lithium-ion cells. Comparatively, the model-based impedance

magnitude for the LFP cell poses a greater sensitivity to swings in the diffusional capacitance parameter (i.e. C_1), whereas in the NMC cell, the impact of charge-transfer resistance (i.e. R_2) is more pronounced.

5.5 Chapter Conclusions

This Chapter has provided an analytical determination of a suitable order-number for the *RC* network battery model. To this end, a frequency-domain analysis on the EIS-attained impedance data for the two test cells of NMC and LFP chemistries has been performed. The results implied that a minimum order-number of two is required to accurately model the battery dynamics, without over-complicating the model structure. Through a partial-derivative approach, a comparable dimensionless coefficient representing the model's sensitivity with respect to its constituent elements has been carried out. In addition, the sensitivity of the battery's instantaneous available power (i.e. SOP) with respect to the impedance parameters has been analysed. Overall, the results suggest that for an accurate model-based SOP estimate in an online application, a robust system identification technique is required which accounts for parameter variations due to changing operating conditions such as temperature, SOC and SOH.

Chapter **6**

Dual-EKF Initialisation Using PRBS for Adaptive Battery Parameters Identification

---

In Chapter 5, it was discussed that the 2-RC battery model response is fairly sensitive to parameterisation error, which could result in misleading information on the battery's performance capabilities, especially the SOP. This necessitates for an online battery identification method which can adapt to those parameter variations induced by varying operating conditions. Thus, in this Chapter, at first, the convergence and tracking capabilities of the dual-EKF algorithm for battery SOC and model parameters is investigated with respect to unknown initial conditions. Thereafter, a hybrid battery identification technique is put forward to reduce the uncertainties in the model estimates produced by the dual-EKF algorithm. The proposed technique is comprised of a carefully designed pseudorandom binary sequences (PRBS), used to properly excite the cells over a prescribed frequency band. The 2-RC battery model parameters are then extracted using a nonlinear least-squares method, in an effort to correctly initialise the dual-EKF algorithm. The performance of the proposed hybrid battery identification technique is experimentally verified against a more accurate impedance spectroscopy (i.e. the EIS) method. The model parameter/variables estimated using the PRBS-initialised dual-EKF algorithm are then used to obtain an online estimate for the battery's charge/discharge power capability, i.e. the SOP.

6.1 Introduction

In the previous Chapter, it was discussed that for an accurate model-based battery state estimation, especially for SOP, it is crucial to consider the time-variability of the incorporated battery parameters in a 2-RC equivalent-circuit model. The nonlinear Kalman filter system identification technique introduced in Chapter 4 achieves this through a robust set of recursive equations, given the filters' statistical parameters are initialised correctly. To this end, an expectation-maximisation method was adopted to provide an accurate set of noise statistical parameters for both state and weight filters in the dual-EKF algorithm. However, when it comes to the initialisation of the model states and parameters themselves, the filters' response becomes very sensitive to erroneous initial conditions.

In order to initialise the dual-EKF algorithm for the real-time estimation of both battery states and parameters, a sufficient knowledge of the unknown parameters to be estimated is often a necessity. In case of erroneous initial battery states, such as SOC, depending on the dynamic structure of the employed battery model, convergence of the battery states is achievable. Although, the rate of convergence can vary for different conditions. Difficulty arises when there exists a large uncertainty in the initial model parameters, i.e. in $\boldsymbol{\theta}_k = \{R_s, R_1, C_1, R_2, C_2\}$. This is due to the fact that, although the 2-RC network model representation of the battery dynamics is linear in states, the relationship between the incorporated parameters is heavily nonlinear. As a result, convergence towards the expected parameter values might not be possible under erroneous initial parameter settings.

Furthermore, due to the time-variability of the modelled battery parameters, the input/output signal (i.e. terminal current/voltage signal) must be persistently exciting at all times [156]. This pre-condition is a necessity for any online parameter identification technique to be able to properly reveal the contents of the battery's dynamics, whilst running in real time. However, in many real battery systems (e.g. in EVs), the current signal may not be sufficiently exciting at all times (e.g. during open-circuit or static charge/discharge periods). In practice, the dual-EKF algorithm, as opposed to those observer-based estimators as discussed in Chapter 2 (e.g. sliding-mode observer), seems to operate well without any divergence [90].

This is true, if and only if, a sufficient knowledge of the model parameters is available at the initialisation step [258]. Otherwise, convergence might never be achieved; even though the error covariance matrices for the weight filter in the dual-EKF could be approaching zero. In most dual-EKF-based BMS algorithms, the battery model parameters are often initialised/calibrated through an offline process, such as EIS, which can be impractical in certain motive and intermittent BESS applications. Therefore, in most cases, the initial parameters are either set arbitrarily based on experience, or they are approximated by using the information provided in the manufacturer's datasheet. It is also possible to identify the battery model parameters using various time-domain techniques (e.g. the HPPC method [198]). However, the obtained results will only be valid at a single frequency, which is directly dependent on the period of the injected signal.

As a result, at first, this Chapter investigates the performance of the dual-EKF algorithm for battery SOC and parameter estimation under erroneous initial conditions. Thereafter, a new hybrid battery identification technique is introduced which revolves around pseudorandom binary sequences (PRBS) for battery excitation whilst in open-circuit mode, which allows for accurate initialisation of the parameters vector in the dual-EKF estimator. It should be noted that the experimental results in this Chapter have been produced using the MACCOR battery tester as described in section 2.3.1.2.

6.2 Dual-EKF Performance Under Incorrect Initial Conditions

In this section, the performance of the dual-EKF algorithm with respect to erroneous initial conditions is investigated, with a view to later develop a hybrid battery identification technique which not only improves the quality of the online-identified battery parameters, but also improves the accuracy of battery SOP. This is a significant achievement, especially for those batteries nearing their end-of-life threshold (e.g. 20% power degradation in EVs) whereby accurate monitoring of SOP, the battery's degraded power capabilities can be taken into account when responding to a particular load profile.

6.2.1 Formulation of State-Space Equations

In Chapter 4, the state-space representation of the n-RC battery model was given as per equation (4.10). In this Chapter, the state-space equations required for the selected RC model order of $n = 2$ are derived from first principles.
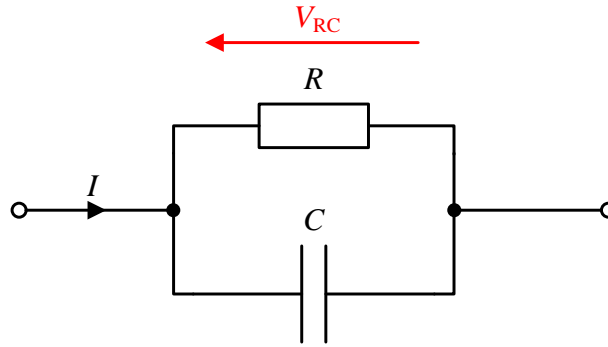
Fig. 6.1 Equivalent-circuit diagram for the 2-RC network battery model

Considering the single RC branch depicted in Fig. 6.1, the transient voltage-drop across V_{RC} across the resistor R and the capacitor C with respect to input current I can be realised. Now, according to Kirchhoff's current law, the amount of current flowing into the branch must be equal to that leaving it. Thus,

$$I = \frac{V_{\mathrm{RC}}}{R} + C\frac{dV_{\mathrm{RC}}}{dt} \tag{6.1}$$

Rearranging equation (6.1) leads to a first-order differential equation which can be solved by using the technique of separable variables.

$$V_{\mathrm{RC}} - IR = -RC\frac{dV_{\mathrm{RC}}}{dt} \iff \int_{V_{\mathrm{RC}}(t_0)}^{V_{\mathrm{RC}}(t_1)} \frac{1}{V_{\mathrm{RC}} - IR} \cdot dV_{\mathrm{RC}} = -\frac{1}{RC}\int_{t_0}^{t_1} 1 \cdot dt$$

$$\iff \ln\left(V_{\mathrm{RC}} - IR\right)\Big|_{V_{\mathrm{RC}}(t_0)}^{V_{\mathrm{RC}}(t_1)} = -\frac{t}{RC}\Big|_{t_0}^{t_1} \tag{6.2}$$

$$\iff \ln[V_{\mathrm{RC}}(t_1) - IR] - \ln[V_{\mathrm{RC}}(t_0) - IR] = -\frac{(t_1 - t_0) = \Delta t}{RC}$$

$$\therefore V_{\mathrm{RC}}(t_1) = [V_{\mathrm{RC}}(t_0) - IR]e^{-\frac{\Delta t}{RC}} + IR$$

where $V_{\mathrm{RC}}(t_0)$ is the initial voltage across the RC branch at discrete time-step k, $V_{\mathrm{RC}}(t_1)$ is the voltage across the same branch at discrete time-step $k+1$ and Δt is the sampling period; note that $t_1 > t_0$. Subsequently, an expression for the transient voltage-drop across each branch of the 2-RC battery model given in Fig. 4.5 can be deduced in discrete form and given as,

$$\left. \begin{aligned} V_{\mathrm{RC1}_{k+1}} &= \left(V_{\mathrm{RC1}_k} - I_k R_1\right)e^{-\frac{\Delta t}{R_1 C_1}} - I_k R_1 \\[2mm] V_{\mathrm{RC2}_{k+1}} &= \left(V_{\mathrm{RC2}_k} - I_k R_2\right)e^{-\frac{\Delta t}{R_2 C_2}} - I_k R_2 \end{aligned} \right\} \tag{6.3}$$

Finally, by applying the superposition theorem to the 2-RC equivalent-circuit model, the state-space equations in discrete time required for the dual-EKF algorithm can be realised and expressed as,

$$\boldsymbol{f}(\cdot) = \begin{bmatrix} x_1 \\ x_2 \\ x_3 \end{bmatrix} = \begin{bmatrix} \mathrm{SOC}_{k+1} \\ V_{\mathrm{RC1}_{k+1}} \\ V_{\mathrm{RC2}_{k+1}} \end{bmatrix}$$

$$= \begin{bmatrix} 1 & 0 & 0 \\ 0 & e^{\frac{-\Delta t}{\tau_1}} & 0 \\ 0 & 0 & e^{\frac{-\Delta t}{\tau_2}} \end{bmatrix} \begin{bmatrix} \mathrm{SOC}_k \\ V_{\mathrm{RC1}_k} \\ V_{\mathrm{RC2}_k} \end{bmatrix}$$

$$+ \begin{bmatrix} -\dfrac{\eta \Delta t}{Q_{\mathrm{actual}}} & 0 & 0 \\[3mm] 0 & R_1\left(1 - e^{\frac{-\Delta t}{\tau_1}}\right) & 0 \\[3mm] 0 & 0 & R_2\left(1 - e^{\frac{-\Delta t}{\tau_2}}\right) \end{bmatrix} I_k \tag{6.4}$$

$$\boldsymbol{\theta}_k = [R_{\mathrm{s}}, R_1, \tau_1, R_2, \tau_2]^{\mathrm{T}}$$

$$\boldsymbol{h}(\cdot) = V_k = V_{\mathrm{OC}}(\mathrm{SOC}_k) - V_{\mathrm{RC1}_k} - V_{\mathrm{RC2}_k} - I_k R_{\mathrm{s}}$$

where $f(\cdot)$ and $h(\cdot)$ are the nonlinear state transition and observation models respectively and $\tau_1 = R_1 C_1$ and $\tau_2 = R_2 C_2$ are long and short transient time-constants respectively. Now, assuming the state-filter gain $\mathbf{L}_k^x$ is weakly related to the parameters vector $\boldsymbol{\theta}_k$, the Jacobian matrices required for the recursive dual-EKF algorithm presented in Table 4.2 can be computed as,

$$\mathbf{F}_{k-1} = \frac{\partial \boldsymbol{f}(\cdot)}{\partial \mathbf{x}_k}\bigg|_{\mathbf{x}_k = \hat{\mathbf{x}}_{k-1}^+} = \begin{bmatrix} 1 & 0 & 0 \\ 0 & e^{\frac{-\Delta t}{\tau_1}} & 0 \\ 0 & 0 & e^{\frac{-\Delta t}{\tau_2}} \end{bmatrix} \qquad (6.5)$$

$$\left.\begin{aligned} \mathbf{H}_k^\theta &= \frac{\mathrm{d}h(\cdot)}{\mathrm{d}\boldsymbol{\theta}_k}\bigg|_{\boldsymbol{\theta}_k = \hat{\boldsymbol{\theta}}_k^-} = \frac{\partial \boldsymbol{h}(\cdot)}{\partial \hat{\boldsymbol{\theta}}_k^-} + \frac{\partial \boldsymbol{h}(\cdot)}{\partial \hat{\mathbf{x}}_k^-} \cdot \frac{\mathrm{d}\hat{\mathbf{x}}_k^-}{\mathrm{d}\hat{\boldsymbol{\theta}}_k^-} \\[2mm] \frac{\mathrm{d}\hat{\mathbf{x}}_k^-}{\mathrm{d}\hat{\boldsymbol{\theta}}_k^-} &= \frac{\partial \boldsymbol{f}(\cdot)}{\partial \hat{\boldsymbol{\theta}}_k^-} + \frac{\partial \boldsymbol{f}(\cdot)}{\partial \hat{\mathbf{x}}_{k-1}^+} \cdot \frac{\mathrm{d}\hat{\mathbf{x}}_{k-1}^+}{\mathrm{d}\hat{\boldsymbol{\theta}}_k^-} \\[2mm] \frac{\partial \boldsymbol{h}(\cdot)}{\partial \hat{\boldsymbol{\theta}}_k^-} &= \begin{bmatrix} -I_{k-1} & 0 & 0 & 0 & 0 \end{bmatrix} \\[2mm] \frac{\mathrm{d}\hat{\mathbf{x}}_k^-}{\mathrm{d}\hat{\boldsymbol{\theta}}_k^-} &= \begin{bmatrix} 0 & 0 & 0 & 0 & 0 \\ 0 & a_{2,2} & a_{2,3} & 0 & 0 \\ 0 & 0 & 0 & a_{3,4} & a_{3,5} \end{bmatrix} \end{aligned}\right\} \qquad (6.6)$$

where,

- $a_{2,2} = -I_{k-1} \cdot (\exp(\Delta t/\tau_1^2) - 1);$
- $a_{2,3} = (\Delta t/\tau_1^2) \cdot (\hat{x}_{2,k}^- - R_1 I_{k-1}) \exp(-\Delta t/\tau_1);$
- $a_{3,4} = -I_{k-1} \cdot (\exp(\Delta t/\tau_2^2) - 1);$ and
- $a_{3,5} = (\Delta t/\tau_2^2) \cdot (\hat{x}_{3,k}^- - R_2 I_{k-1}) \exp(-\Delta t/\tau_2).$

6.2.2 A Steady-State Definition for SOP

As discussed previously, battery impedance parameters play a crucial role in the determination of the battery's instantaneous power capabilities. According to equations (5.32) and (5.33), for the estimation of battery SOP in real time, the impedance magnitude of the 2-RC equivalent-circuit model is required. Now,

considering the transfer function given by (5.6), under steady-state conditions, as $s \to 0$, battery model impedance reduces to,

$$\left[Z_{\mathrm{mdl}}(s) \right]_{s=0} = \left[R_{\mathrm{s}} + \left(\frac{R_1}{R_1 \cdot sC_1 + 1} \right) + \left(\frac{R_2}{R_2 \cdot sC_2 + 1} \right) \right]_{s=0} \tag{6.7}$$

$$Z_{\mathrm{mdl}}^{s \to 0} = R_{\mathrm{s}} + R_1 + R_2.$$

Equation (6.7) implies that for the online estimation of battery SOP using the 2-RC model and the dual-EKF algorithm, the effects of the parameters C_1 and C_2 are negligible under steady-state conditions. Therefore, by substituting $Z_{\mathrm{mdl}}^{s \to 0}$ into equations (5.32) and (5.33), the steady-state SOP definitions for discharge and charge can be obtained.

$$\mathrm{SOP_{dis}} = \frac{V_{\min}(V_{\mathrm{OC}} - V_{\min})}{R_{\mathrm{s}} + R_1 + R_2} \tag{6.8}$$

$$\mathrm{SOP_{ch}} = \frac{V_{\max}(V_{\max} - V_{\mathrm{OC}})}{R_{\mathrm{s}} + R_1 + R_2}. \tag{6.9}$$

From equations (6.8) and (6.9), it can be deduced that for an accurate and reliable SOP estimate, the dual-EKF estimator must be able to produce a convergent estimate for the resistive elements of the 2-RC equivalent-circuit battery model.

6.2.3 EFK Response to Unknown Initial Battery Parameters

In order to gain a better understanding of the dual-EKF algorithm's performance capabilities for battery parameter identification under unknown initial conditions, the experimental results obtained for an NMC cell under a dynamic load profile based on the ArtHiUFL drive cycle, as described in Chapter 2, section 2.3.2.8, are used here. Ultimately, the aim of the ArtHiUFL test profile is to provide a realistic and dynamic operating condition for the validation of the proposed hybrid battery identification technique in this Chapter.

It should be noted that, a rather conservative operating SOC range of 80% to 20% is assumed here. Fig. 6.2 presents the current and voltage waveforms measured for the NMC cell under test; 28 consecutive ArtHiUFL cycles have been applied to discharge it from an initial SOC of ~80% down to 20%.
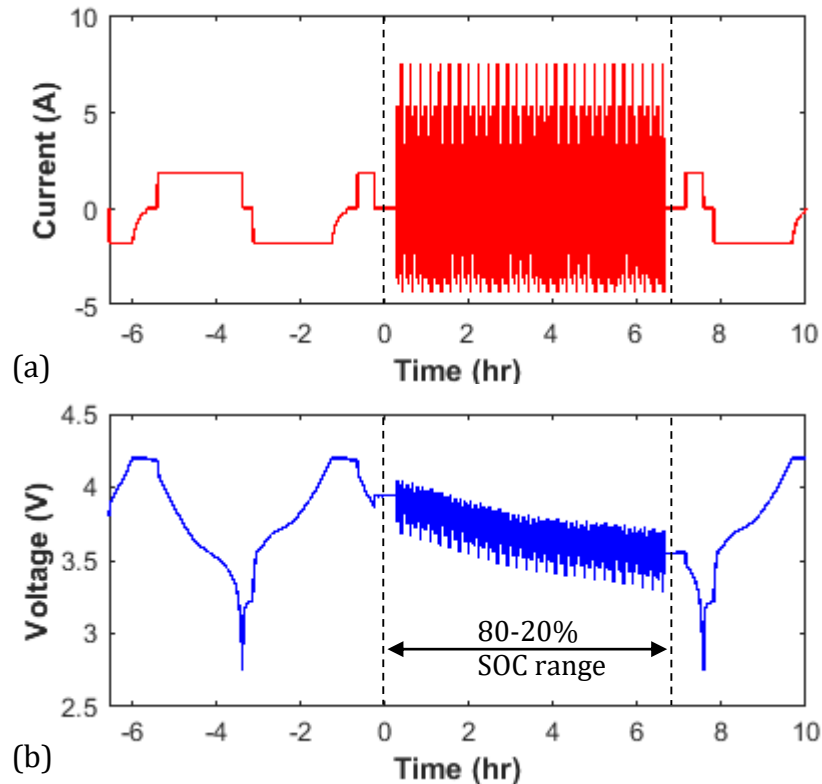
Fig. 6.2 The (a) current and (b) voltage waveforms obtained for the multi-ArtHiUFL drive cycle when applied to an NMC test cell at 25°C

The chosen SOC range has been employed by many researchers previously as a safe range for battery operation, without extension into the nonlinear regions of the battery's operating envelope [10]. Moreover, due to the regenerative nature of the current demands in motive and intermittent BESS applications (e.g. in EVs and grid-tie storages), the battery is usually charged up to 80% nominal capacity, enabling a better charge acceptance in cases of regenerative currents. Similarly, operating or keeping the battery at low SOC values can have an adverse effect on the battery's lifetime in the long run.

In the following sub-sections, the dual-EKF's performance capability in terms of voltage, SOC and parameter estimation errors is explored for two cases; case 1, dual-EKF initialised with best-guess *RC* model parameters taken from the cell datasheet, and, case 2, dual-EKF initialised with *a priori* knowledge of the *RC* model parameters, through curve fitting of the EIS-attained complex impedance data at 25°C and 80% SOC.

Table 6.1 Initial *RC* model parameters for dual-EKF battery identification

Parameters	R_s (mΩ)	R_1 (mΩ)	C_1 (F)	R_2 (mΩ)	C_2 (F)
From datasheet	20	10	1000	10	100
EIS-attained	26.95	12.6	1853	3.2	17.08

Table 6.1 provides the *RC* model parameters for the two filter initialisation scenarios. It should be noted that for both cases, the initial SOC state is intentionally set to 20% instead of true 79.12%. This is to demonstrate the convergence and robustness of the EKF SOC estimator, even under datasheet initialisation of the *RC* model parameters. The state and weight filters in the dual-EKF algorithm are initialised according to (6.10).

$$\mathbf{x}_0 = \begin{bmatrix} \text{SOC}_0 \\ V_{\text{RC1},0} \\ V_{\text{RC2},0} \end{bmatrix} = \begin{bmatrix} 0.2 \\ 0 \\ 0 \end{bmatrix}, \qquad \boldsymbol{\theta}_0 = [R_s, R_1, \tau_1, R_2, \tau_2]^{\mathrm{T}}$$

$$\mathbf{Q}_0^{\mathrm{x}} = \text{diag}_n\{1 \times 10^{-8}\}, \qquad \mathbf{P}_{\tilde{\mathrm{x}},0}^{+} = \text{diag}_n\{10\}, \qquad \mathbf{R}_0^{\mathrm{x}} = \text{diag}_m\{0.1\}$$

$$\mathbf{Q}_0^{\theta} = \text{diag}_q\{1 \times 10^{-12}\}, \qquad \mathbf{P}_{\tilde{\theta},0}^{+} = \text{diag}_q\{10\}, \qquad \mathbf{R}_0^{\theta} = \text{diag}_m\{10\}$$

$$(6.10)$$

where diag{·} is a diagonal matrix of size 3×3 for $\mathbf{Q}_0^{\mathrm{x}}$ and $\mathbf{P}_{\tilde{\mathrm{x}},0}^{+}$, 5×5 for $\mathbf{Q}_0^{\theta}$ and $\mathbf{P}_{\tilde{\theta},0}^{+}$, and 1×1 for $\mathbf{R}_0^{\mathrm{x}}$ and $\mathbf{R}_0^{\theta}$ matrices, respectively. Note that the error covariance matrices $\mathbf{P}_{\tilde{\mathrm{x}},0}^{+}$ and $\mathbf{P}_{\tilde{\theta},0}^{+}$ are set to a large value at initialisation. This is to account for any uncertainties in both EKFs' initial conditions. However, for the EIS-obtained

initial parameters, since the weight EKF is initialised with *a prior* knowledge, the initial error covariance is set to a small value, in this case $\mathbf{P}^{+}_{\tilde{\theta},0} = \text{diag}_5\{1\}$.

6.2.1.1   EKF terminal voltage response
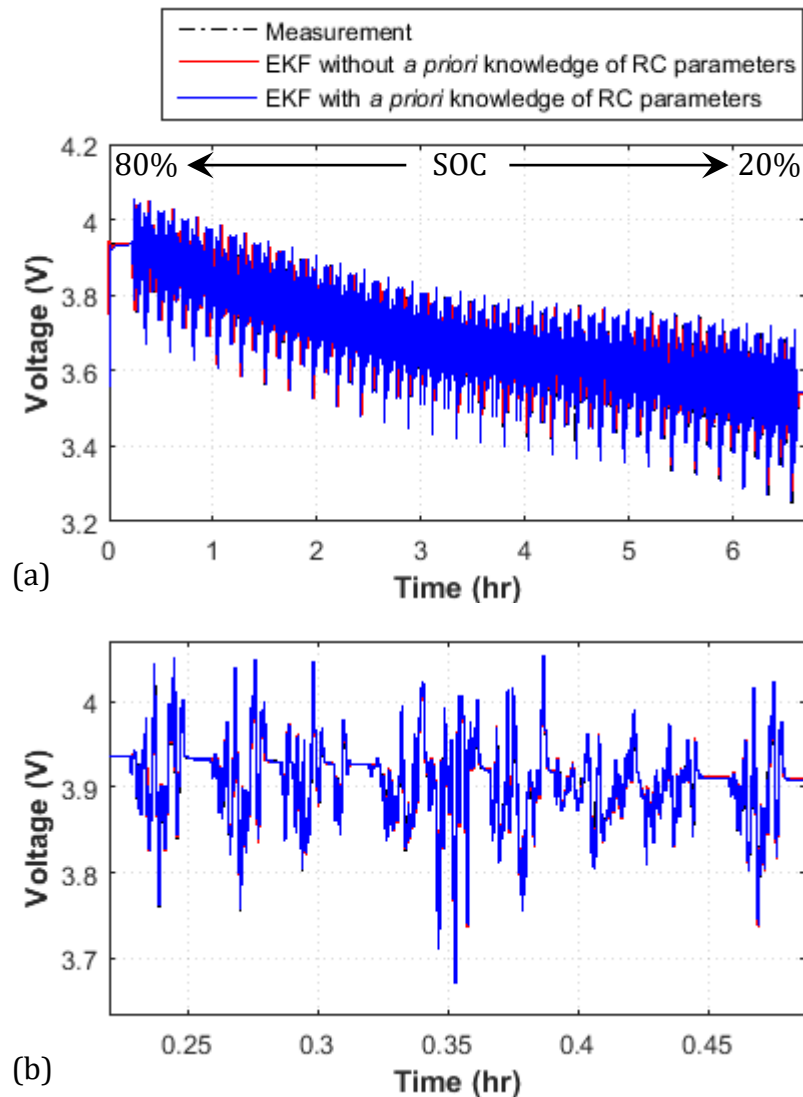
Fig. 6.3 Voltage reponse of the dual-EKF algorithm with respect to correct and erroeneous initial *RC* model parameters, (a) complete and (b) single repetition of Artemis-based test profile

Fig. 6.3 compares the response of the dual-EKF algorithm when initialised with and without *a priori* knowledge of the *RC* battery model parameters. As can be seen, despite the erroneous initial parameters for the latter case, the filter provides a very good estimate of the cell's terminal voltage. This is due to the fact that cell voltage is

directly available to the filer as one of its observable quantities; thus, it is easier to minimise the error between prediction and observation, yielding an accurate estimate for the cell's terminal voltage.

Table 6.2 RMSE performance of the dual-EKF estimator for battery parameters identification, with and without a sufficient knowledge of initial *RC* parameters

Initial condition	RMSE (mV)
Without *a priori* knowledge of *RC* parameters	1.7
With *a priori* knowledge of *RC* parameters	0.89

Table 6.2 presents the voltage RMSE values calculated for the dual-EKF initialised with the aforementioned model parameters. Note that the RMSE has been calculated from the time that voltage estimate satisfied a 5% error bound with respect to the measured signal. This ensured that large errors in the model states during the convergence phase did not skew the results. From the presented RMSE results, it can be said that, the dual-EKF algorithm's performance in battery terminal voltage estimation is not significantly improved by correctly initialising the model parameters, rather than using some generic datasheet parameters.

6.2.1.2   SOC estimation performance

Similar to the voltage estimates, the SOC estimates obtained for the two filter initialisation scenarios were plotted on a same graph, as shown in Fig. 6.4. Despite the large errors in the initial SOC sate and the battery model parameters, the state EKF delivers a satisfactory performance by converging to the reference SOC (denoted as Ref. SOC in Fig. 6.4) within the first 15 minutes of filter initialisation. This is owed to the fairly accurate OCV-SOC relationship that has been empirically derived for the NMC test cell in Chapter 4. Although, for the case with *a priori* knowledge of the *RC* model parameters, the convergence rate of the state filter has improved by approximately a factor of a half.
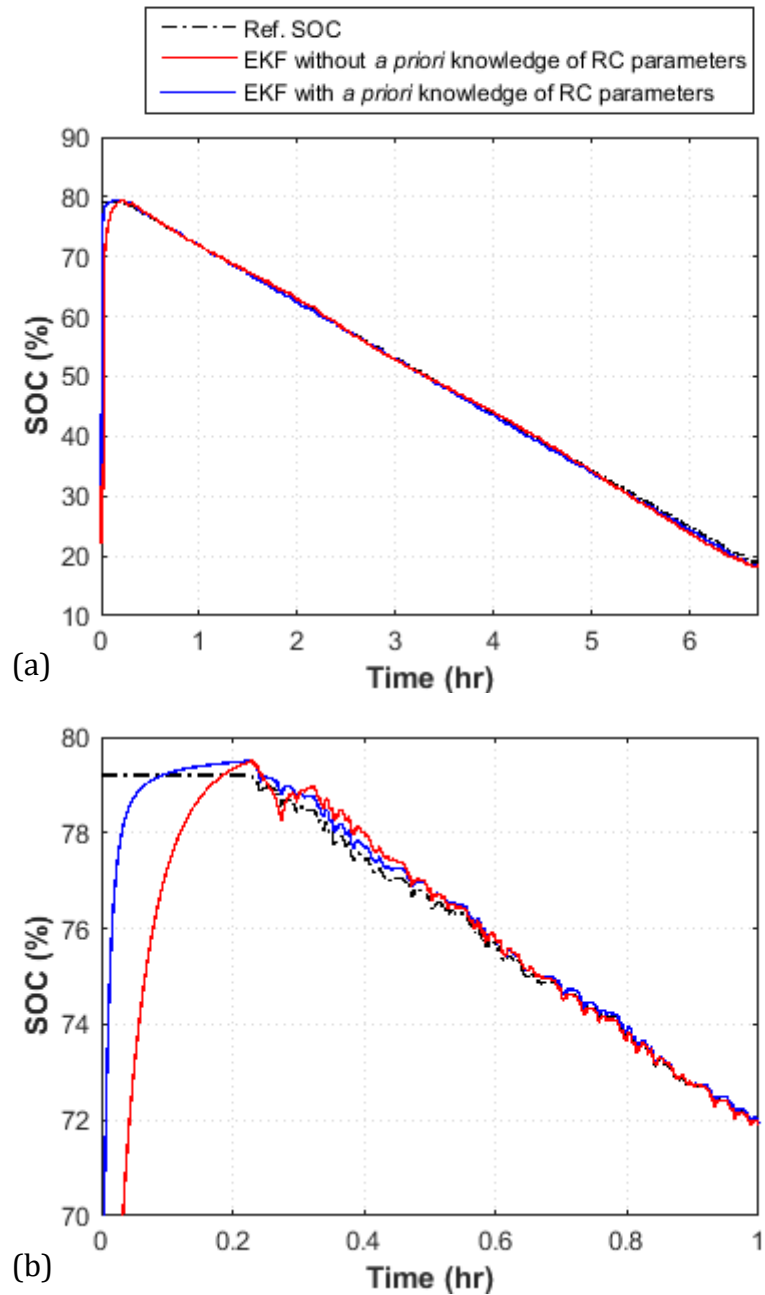
Fig. 6.4 The SOC estimation performance of the dual-EKF algorithm with respect to correct and erroeneous initial model parameters, (a) complete and (b) zoom view

Finally, Table 6.3 presents the RMSE values calculated for the SOC estimates, from the moment that the 5% error-bound criterion has been met. Evidently, under both scenarios of dual-EKF weight-filter initialisation, the state filter produces a SOC estimate with less than 1% error. This outcome demonstrates the robustness of the dual-EKF algorithm, regardless of the accuracy of the initial model parameters.

Table 6.3 RMSE performance of the dual-EKF estimator for battery SOC estimation, with and without a sufficient knowledge of initial *RC* parameters

Initial condition	RMSE SOC (%)
Without *a priori* knowledge of *RC* parameters	0.88
With *a priori* knowledge of *RC* parameters	0.49

6.2.1.3 EKF battery parameter identification performance

Fig. 6.5 compares the parameter estimation capability of the dual-EKF algorithm for both correct and incorrect initial conditions. It is evident that, despite its excellent SOC state estimation performance, the dual-EKF is significantly affected by incorrect initial battery parameters, resulting in a non-convergent estimator for online battery parameter identification. This can be attributed to two facts; lack of persistence of excitation of the input current signal, and, very slow time-variability of the battery parameters. Both of which can have a detrimental effect on the performance of the weight filter in the dual-EKF algorithm.

Therefore, by having *a priori* knowledge of the battery parameters when initialising the weight filter in the dual-EKF algorithm, it is possible to achieve a true estimate for the resistive-element *RC* model parameters in real time, which is key to proper operation of various battery power management strategies. As a result, in this Chapter, a hybrid battery identification technique is put forward. The proposed technique involves the application of an online impedance spectroscopy whilst the battery is in open-circuit mode. This is to realise a correct initialisation of the weight EKF at the current battery conditions, and once in closed-circuit mode, the dual-EKF algorithm is implemented to identify the model parameters in real time. A more detailed description of the concept is provided in the next section.
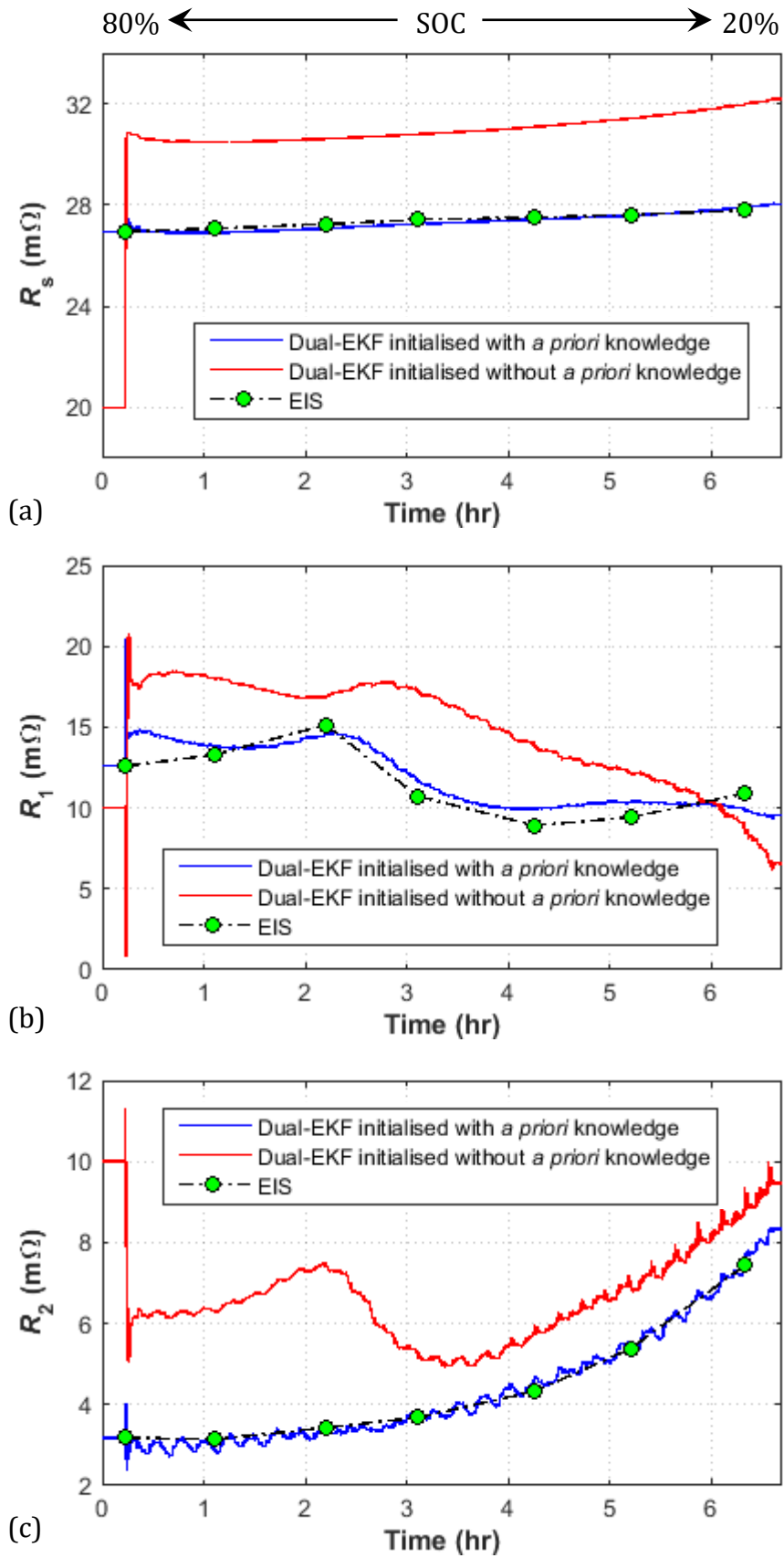
Fig. 6.5 Comparison of resistive-element 2-*RC* battery model parameters identified with and without *a priori* knowledge of the initial conditions through EIS

6.3 A Hybrid Battery Identification Technique

The proposed hybrid battery identification technique revolves around an online impedance spectroscopy method, namely the pseudorandom binary sequences (PRBS), which is essentially a band-limited white-noise-alike random signal that allows for the realisation of a proper battery excitation over a prescribed frequency band. The PRBS excitation is conducted while the battery is in the open-circuit mode (i.e. zero-current relaxation mode). Once in the closed-circuit mode (i.e. under load conditions), the dual-EKF is initialised with the PRBS-attained 2-RC model parameters and implemented recursively to yield an adaptive estimate for the RC parameters in real time.

6.3.1 Concept

Fig. 6.6 demonstrates the concept of the of the proposed hybrid battery parameter identification. The sequence of the procedures undertaken is summarised as follows. Whilst the battery is in the open-circuit mode (i.e. zero load-current), a carefully designed PRBS excitation signal is injected into the battery. The period of the PRBS signal designed for excitation of the NMC and LFP cells used in this thesis is 102 seconds. This means that the proposed technique can be conveniently applied to a motive BESS while resting (e.g. after a full charge in an EV) to serve two purposes; 1) to provide an online diagnosis tool for the detection of early cell/battery failures; 2) to better utilise the dual-EKF algorithm for not only the estimation of SOC, but also for the estimation of other battery states, such as SOP and SOF, whose realisation relies largely on accurate battery impedance parameters.

In order to ensure a steady-state condition prior to PRBS excitation, the cells under test are required to relax for a period of 30 minutes. This time-limit is chosen as a result of an investigation carried out on the cells' OCV hysteresis behaviour with respect to zero-current rest period. Fig. 6.7 and Fig. 6.8 present the charge and discharge OCV measurements with their resulting hysteresis levels as a function of SOC and rest time, gathered for the NMC and LFP cells, respectively. From these two

figures, it is evident that for both cell types, the OCV hysteresis level achieved after a 30-minute rest is very close to that measured after a 1-hour rest period. Thus, it can be safely assumed that a steady-state condition can be reached by the test cells after the chosen rest period of 30 minutes, prior to conducting the online PRBS excitation test.
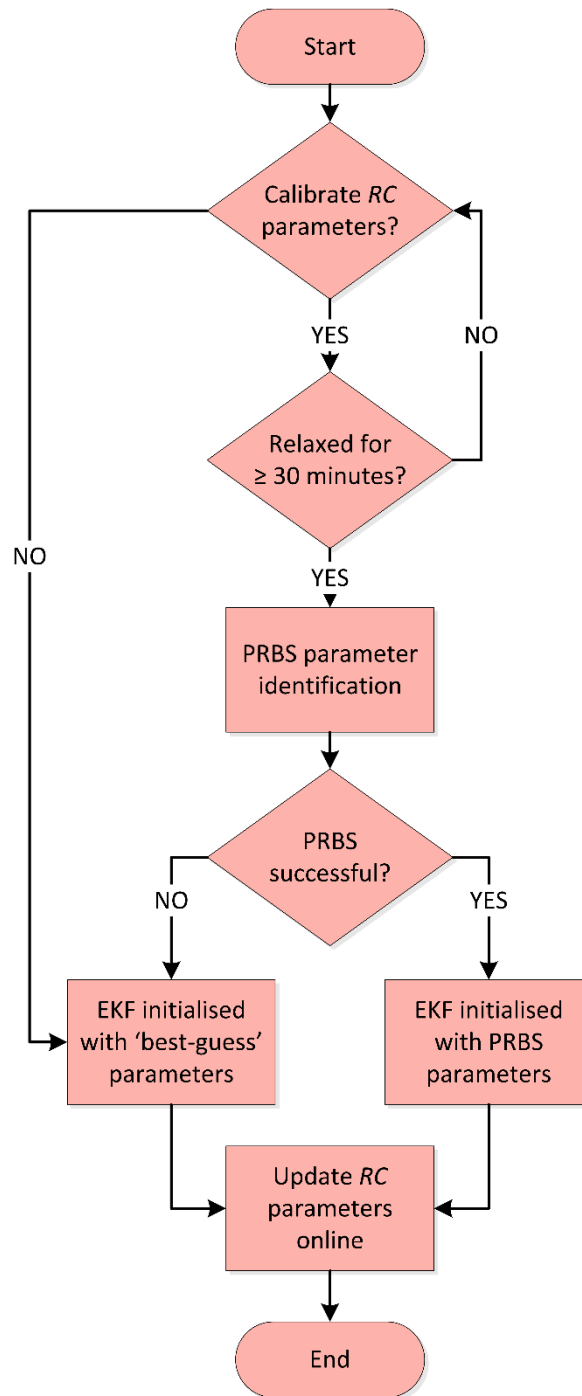
Fig. 6.6 Block diagram demonstrating the concept of the proposed hybrid battery parameter identification
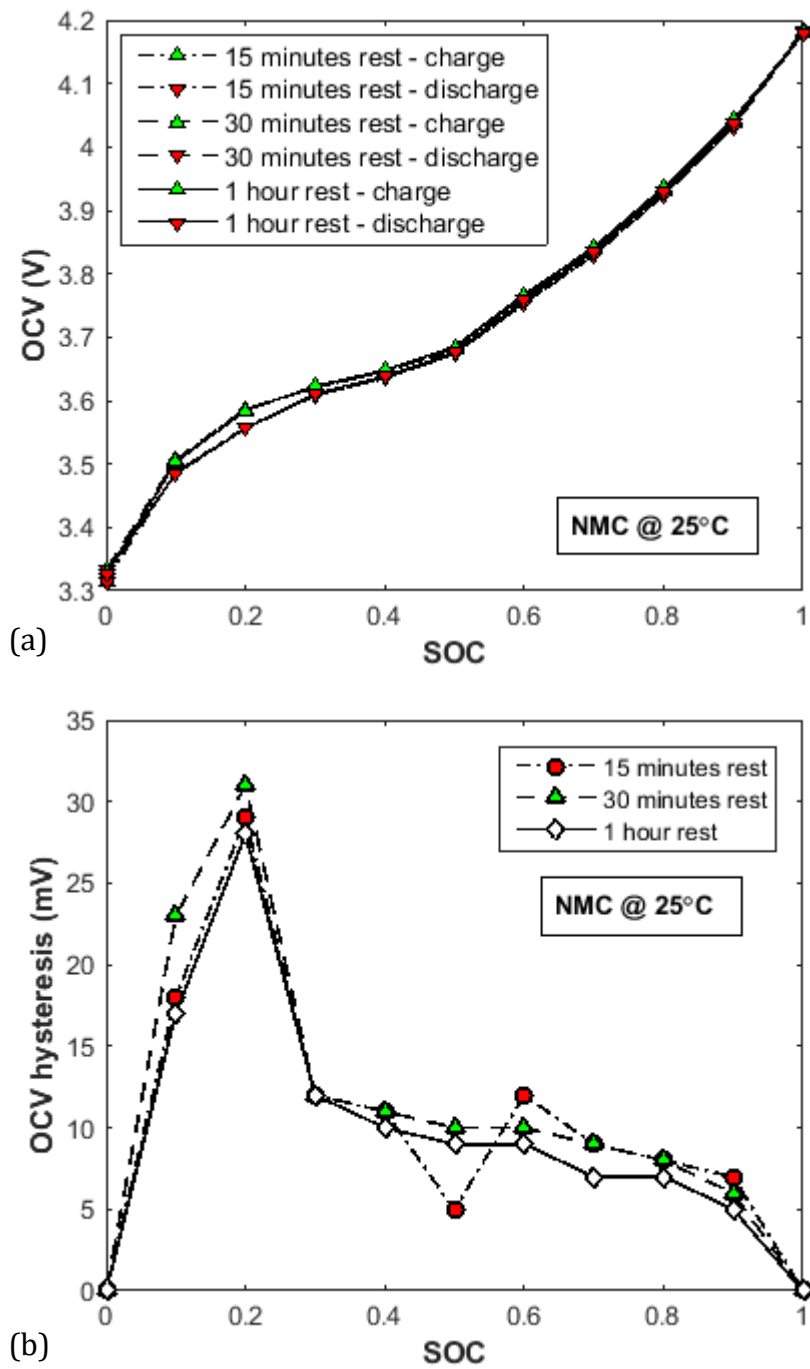
Fig. 6.7 OCV measurements as a function of SOC obtained for the NMC cell after a 15-minute, 30-minute and 1-hour rest period at 10% SOC intervals and 25°C
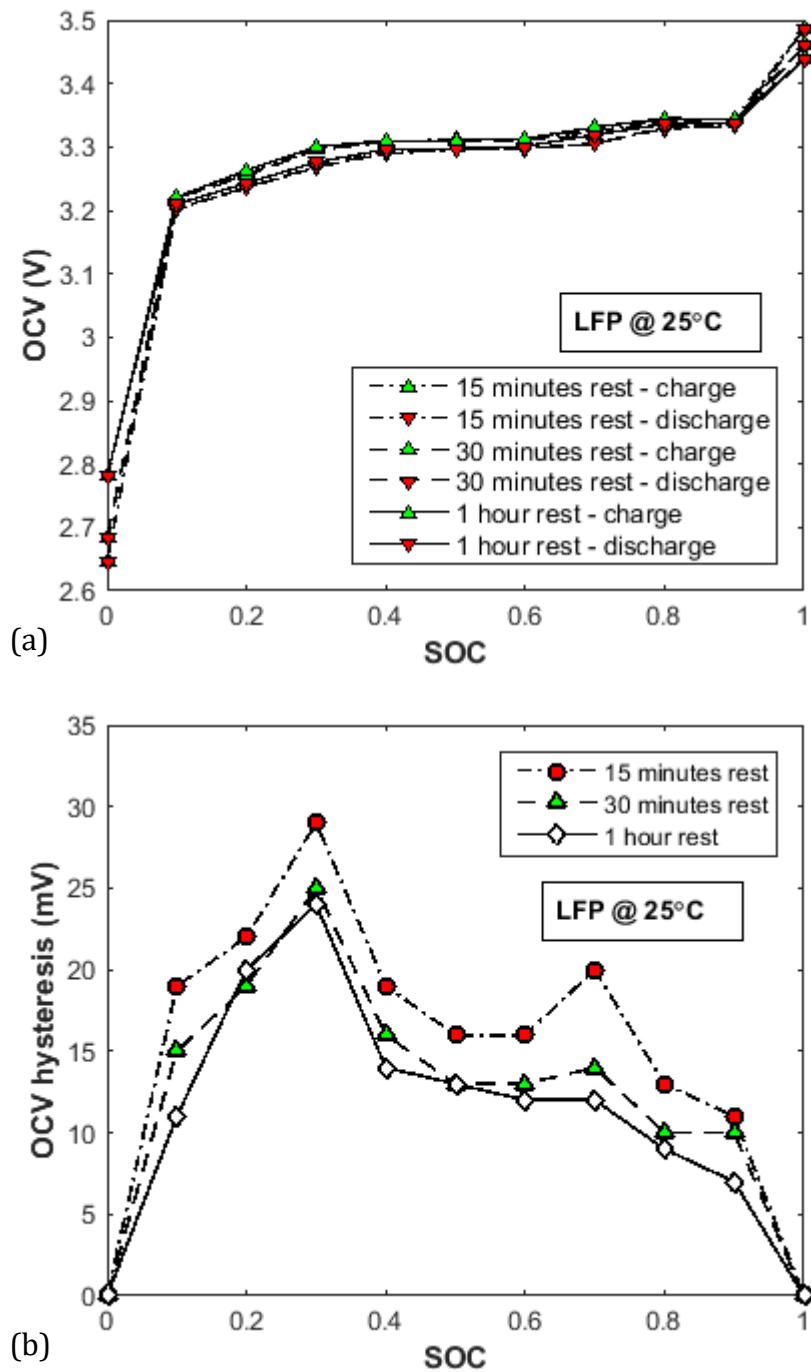
Fig. 6.8 OCV measurements as a function of SOC obtained for the LFP cell after a 15-minute, 30-minute and 1-hour rest period at 10% SOC intervals and 25°C

Upon the completion of the PRBS excitation, the nonlinear least-squares identification method described in Chapter 5 is applied to the obtained complex impedance data. The identified parameters are then fed forward to the weight EKF in the dual-EKF algorithm. Thereafter, the *RC* model parameters are recursively

updated through the dual-EKF algorithm [166] to account for any SOC- and/or temperature-induced variations in real time.

Should the battery experience a severe change in its operating conditions, such as changes in the ambient temperature or returning to open-circuit mode after supplying/sourcing a harsh load demand, the PRBS identification method can be repeated to accomplish 1) an online diagnosis of the internal status of the battery, and, 2) re-initialisation of the RC model parameters in the weight EKF to avoid divergence. In case the PRBS excitation procedure is interrupted due unpredictable consumer behaviour, the parameters vector in the dual-EKF algorithm is provided with 'best-guess' values (e.g. datasheet parameters) at the time of initialisation. Next section puts its focus on the theoretical design and practical implementation of a 10-bit 10 Hz PRBS signal for the excitation of the LFP and NMC test cells.

6.3.2 PRBS Generation for Online Initialisation of EKF

PRBS is a special type of random signal that finds usage over a wide range of identification problems (e.g. [263]). This particular technique, as opposed to costly and time-consuming sine-swept methods, provides a simple and inexpensive alternative for the identification of dynamic systems.

A typical PRBS sequence is comprised of binary 'zeros' and 'ones' that are switched at a pre-determined pattern. The outcome is a perturbation signal that resembles properties akin to a band-limited white noise [264]. The most commonly-used PRBS's are those based on maximum-length sequences. These sequences are often generated in either hardware or software environments, using a number of linear-feedback shift registers (LFSR) with modulo-two (XOR) feedback taken from some pre-determined tap positions [264].

When designing a PRBS signal, there are two base parameters that must be carefully selected. These include the source clock frequency (f_{clk}) and the number of shift registers (n), which in turn define the PRBS frequency bandwidth and the test duration.
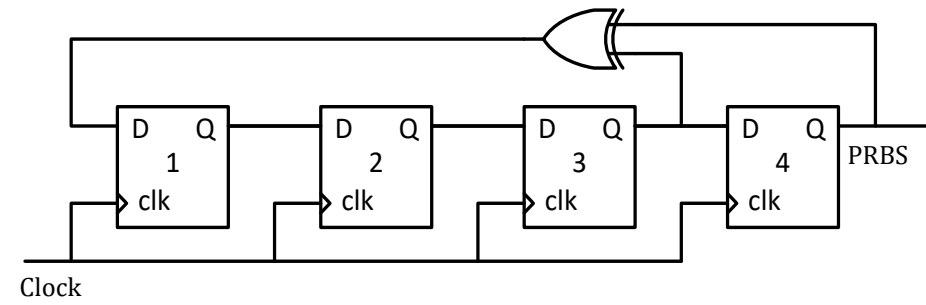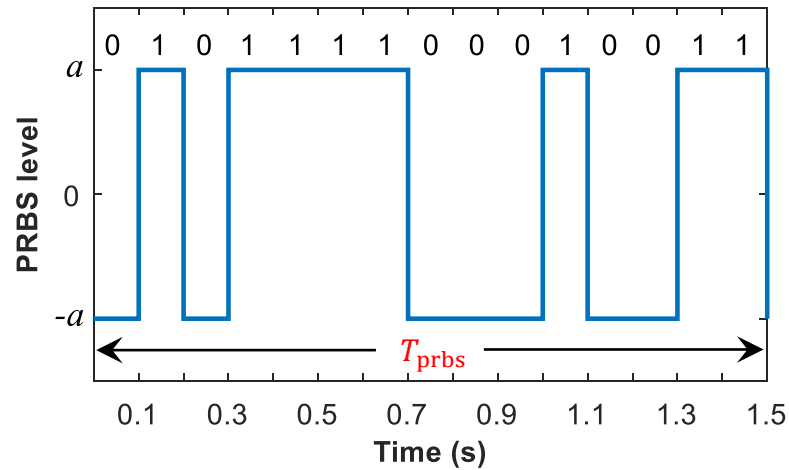
Fig. 6.9 Example of a 4-bit 10 Hz PRBS generator showing (a) configuration of LFSRs with feedback tap positions and (b) time-domain bit stream of one complete sequence

Therefore, a theoretical analysis is conducted herein to determine f_{clk} and n for the battery identification problem in hand. Fig. 6.9 depicts the register configuration and resulting pulses for an exemplary PRBS with $n = 4$ and $f_{clk} = 10$ Hz. Note that the PRBS is in bipolar form, shifting between $-a$ for a 'zero' and $+a$ for a 'one'. This leads to a relatively balanced perturbation signal that will charge and discharge the battery in a way, so that the net quantity of stored energy stays unaffected.

For a maximum-length PRBS, the test duration T_{prbs} can be defined as,

$$T_{prbs} = \frac{N}{f_{clk}} \tag{6.11}$$

where $N = 2^l - 1$ is the sequence length and l is the PRBS bit-length. In [265] and [266] the authors have shown that by analysing the signal power spectral density (PSD), the bandwidth over which the PRBS data is useable can be established. Fig. 6.10 presents the PSD for the 4-bit 10 Hz PRBS exemplary sequence given in Fig. 6.9, where the power spectrum is represented by discrete power points separated by f_{clk}/N. As can be observed, the corresponding PSD has a *sinc* function characteristic, which can be described by (6.12).
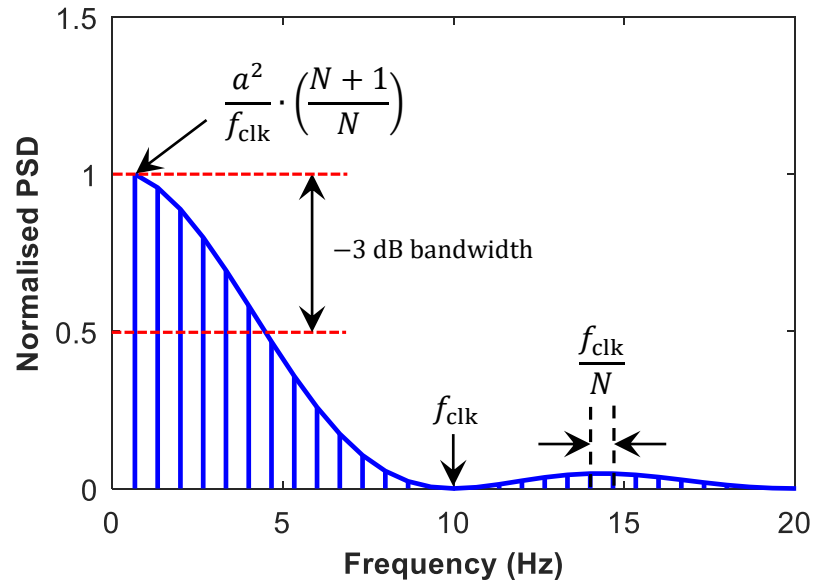
Fig. 6.10 Normalised PSD for the simulated 4-bit 10 Hz PRBS

$$S_{\text{xx}}(f) = \frac{a^2(N+1)}{N \cdot f_{\text{clk}}} \left[\frac{\sin(f\pi/f_{\text{clk}})}{f\pi/f_{\text{clk}}} \right]^2. \tag{6.12}$$

The band-limit of a PRBS is defined by the frequency at which its power is attenuated by -3 dB (i.e. power drops by half). This event occurs when,

$$\left[\frac{\sin(f\pi/f_{\text{clk}})}{f\pi/f_{\text{clk}}} \right]^2 = 0.5 \Rightarrow f_{\text{max}} \approx \frac{f_{\text{clk}}}{2.25}. \tag{6.13}$$

Now, considering the lower band-limit as $f_{\min} = f_{\text{clk}}/N$ and using $f_{\max}$ from (6.13), the theoretical frequency band (f_{band}) over which the PRBS information are useful can be given as,

$$f_{\text{band}} = f_{\text{clk}} \left(\frac{1}{2.25} - \frac{1}{N} \right)$$

$$f_{\text{norm}} = \frac{f_{\text{band}}}{f_{\max}} = 1 - \frac{2.25}{N}$$

(6.14)

where f_{norm} is the normalised frequency band.

From the comprehensive frequency-domain analysis conducted earlier in Chapter 5, it was determined that for lithium-ion cells of LFP and NMC types, the impedance is most useful over the low end of the attained spectrum (i.e. 5 mHz $\leq f \leq$ 5 Hz). Now, according to (6.14), a PRBS clock frequency of $f_{\text{clk}} = 11.25$ Hz should be sufficient to capture the battery dynamics over the frequency band of interest. However, to be able to use the MACCOR battery tester (see Fig. 2.17) as a PRBS excitation and acquisition device, a clock frequency of $f_{\text{clk}} = 10$ Hz is chosen herein, yielding a maximum frequency band-limit of 4.44 Hz.

In order to maintain the white-noise-like properties of the generated PRBS and to avoid spectral leakage during analysis, the sequence must be captured as a whole. This leads to the consideration for the required number of shift registers (i.e. bit-length), which in turn dictates the duration of the test as given by (6.11) and the amount of data that must be acquired. Fig. 6.11 illustrates the effect of increasing PRBS bit-length on test bandwidth (f_{nom}) and duration (T_{prbs}).

As can be seen, the normalised bandwidth increases exponentially with increasing PRBS bit-length. However, the exponential increase in test duration becomes disadvantageous. It follows that there exists a trade-off, which appears to be between $l = 8$ and $l = 14$. H, a bit-length of $l = 10$ is chosen, leading to a PRBS perturbation signal that is conveniently less than two minutes long and covers a theoretical frequency range of 0.01 Hz $\leq f \leq$ 4.44 Hz. This range is low enough to

properly stimulate the lower-frequency dynamics of the lithium-ion battery cells used in this paper. Finally, to achieve a maximum-length sequence with a 10-bit PRBS, *XOR* feedback must be taken from the seventh and the tenth shift registers [264].
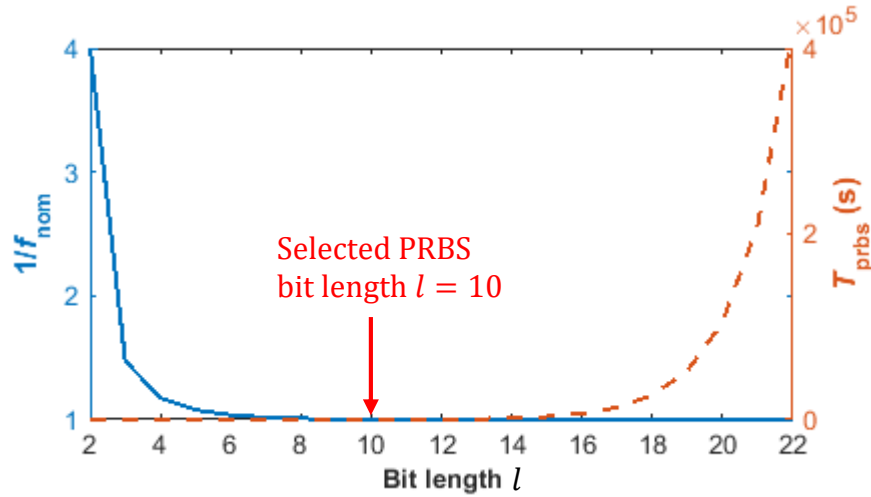
Fig. 6.11 Relationship between PRBS bit-length, normalised bandwidth and resulting test duration

Since battery current is the easiest variable to adjust, it is chosen here as the controllable input signal and the terminal voltage represents the output. Extracts of the acquired voltage and current for an NMC cell is given in Fig. 6.12. In order to compute the complex impedance of the battery system, a conversion of the signals in time-domain to frequency-domain is required. This is often realised by taking the discrete Fourier transform (DFT) of the acquired input/out data [267]. Thus, the impedance transfer function of the battery system under test can be identified as,

$$Z_k(f) = \frac{\mathcal{F}\{V_k\}}{\mathcal{F}\{I_k\}}; \ \ f = k\frac{f_s}{n_s}; \ \ n_s = N\left(\frac{f_s}{f_{clk}}\right); \ \forall \, k \le n_s - 1 \qquad (6.15)$$

where $\mathcal{F}\{\cdot\}$ denotes the Fourier transform, f_s is the sampling rate and n_s is the number of samples in a dataset. According to Nyquist-Shannon sampling theorem, the chosen sampling rate must be at least twice the highest frequency (i.e. $f_s \ge 2 \times$

f_{clk}). However, in this thesis, a practical sampling rate of $f_s = 10 \times f_{clk} = 100$ Hz is used to further reduce the risk of spectral leakage during the DFT operation.
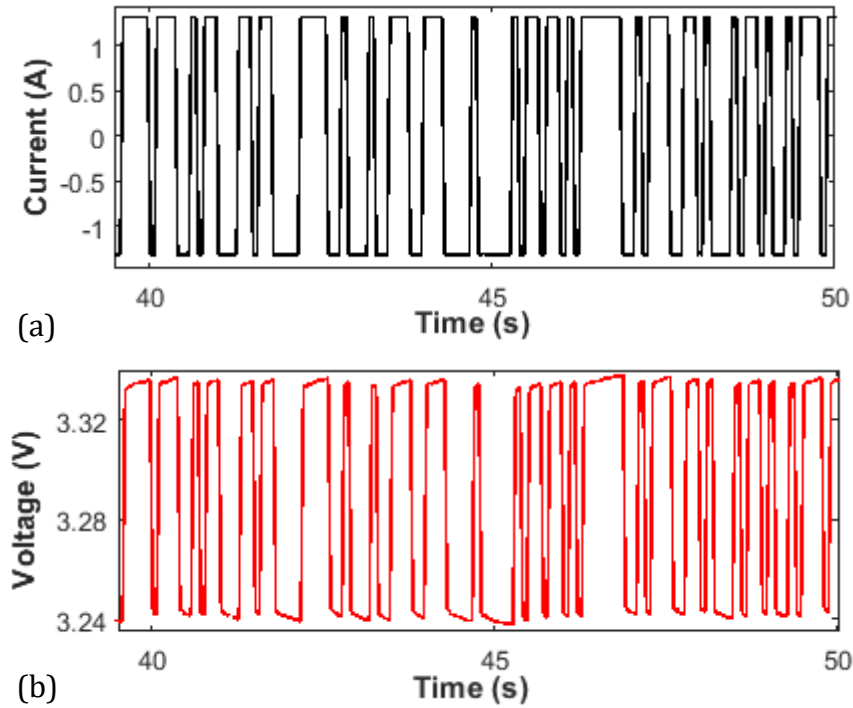
Fig. 6.12 Extracts of the acquired (a) input current and (b) response voltage for an NMC test cell

6.4 Application to Online Battery SOP Estimation

In order to verify the performance of the proposed hybrid battery identification technique, both in open- and short-circuit modes, two tests have been devised and implemented on the 3.5 Ah NMC and 3.3 Ah LFP test cells.

First, a modified HPPC test, as depicted in Fig. 6.13 for the NMC cell, has been designed. As shown in Fig. 6.14, this test consists of a standard HPPC test, as described in Chapter 2, section 2.3.2.4, followed by a 10-bit 10 Hz PRBS excitation signal. This profile has been repeated over the SOC range of 90% to 10%. The amplitudes of the current pulses were scaled to ±0.4C for both cell variants, in order to achieve a proper excitation of the cells under test without inducing a large SOC deviation.
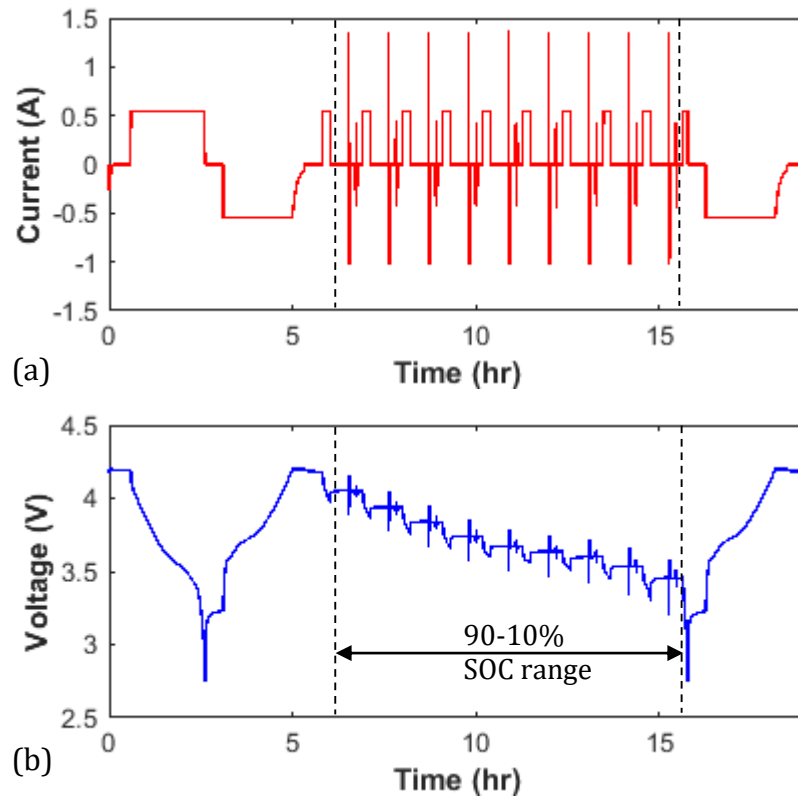
Fig. 6.13 The (a) current and (b) voltage waveforms obtained for the modified HPPC test when applied to an NMC cell at 25°C

Fig. 6.15(a) and (b) present the SOC results for the NMC and LFP test cells, when applied with ±0.4C pulses over one complete PRBS sequence, respectively. As can be seen, the chosen pulse amplitude has resulted in a maximum SOC deviation of only 0.05 percentage-point for the NMC cell, and 0.06 percentage-point for the LFP cell. Moreover, the SOC state immediately before and after the PRBS injection are the same, confirming a balanced excitation signal. In addition, a 10-minute relaxation period has also been allowed between the HPPC test and PRBS injection to a steady-state condition has been reached.

It should be noted that, due to the white-noise-alike properties of the PRBS signal (i.e. having a flat spectrum over the entire frequency band), the overall state of the system under test is not affected greatly, i.e. the PRBS is balanced. This can be evidently observed in Fig. 6.16, where the voltages measured immediately before and after the PRBS injection for the NMC cell follow the same trajectory of OCV relaxation.
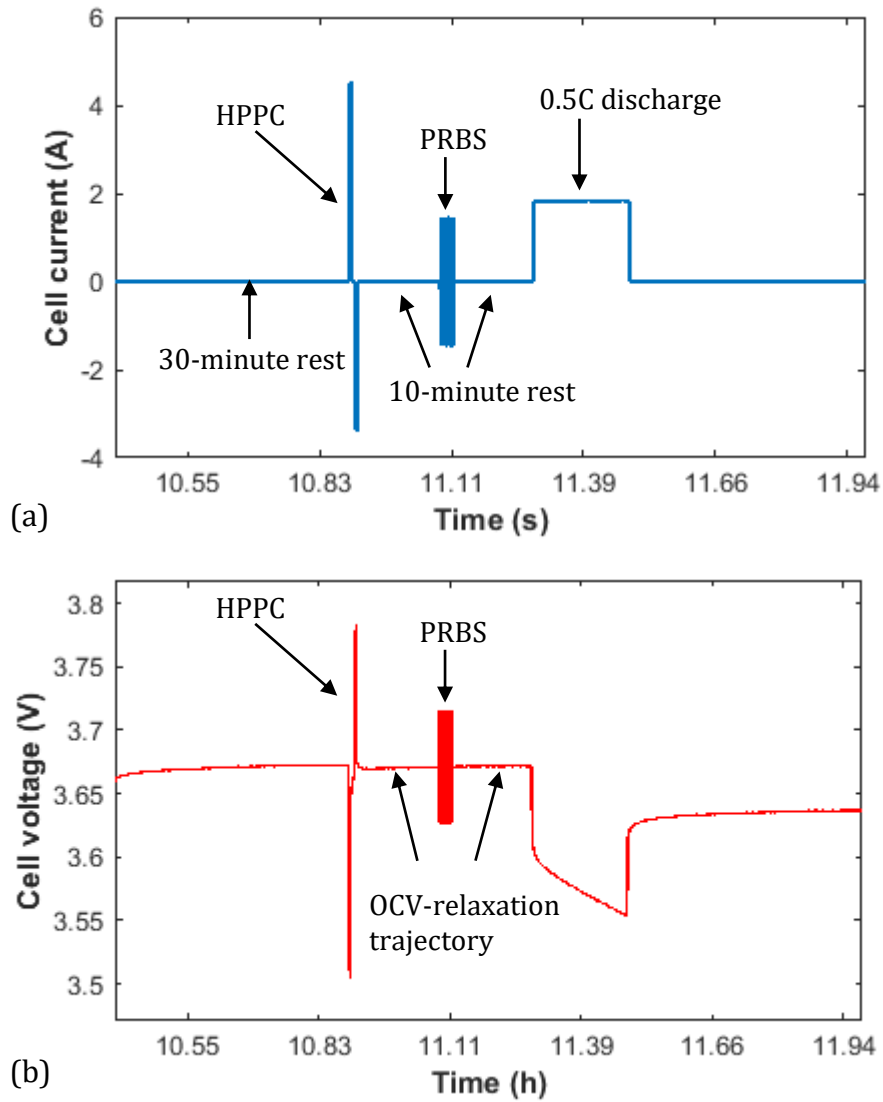
Fig. 6.14 Excerpt of the modified HPPC test profile, (a) current and (b) voltage

A similar behaviour is observable for the LFP cell, as demonstrated by Table 6.4. This finding validates two points; 1) the chosen current amplitude of ±0.4C used for PRBS excitation of the NMC and LFP cells is sufficiently large, without causing an overall change in the cells' dynamics, and, 2) the cells under test can be considered as a linear time-invariant (LTI) system over the period of PRBS excitation, which implies that the cells' impedances will be correctly estimated.
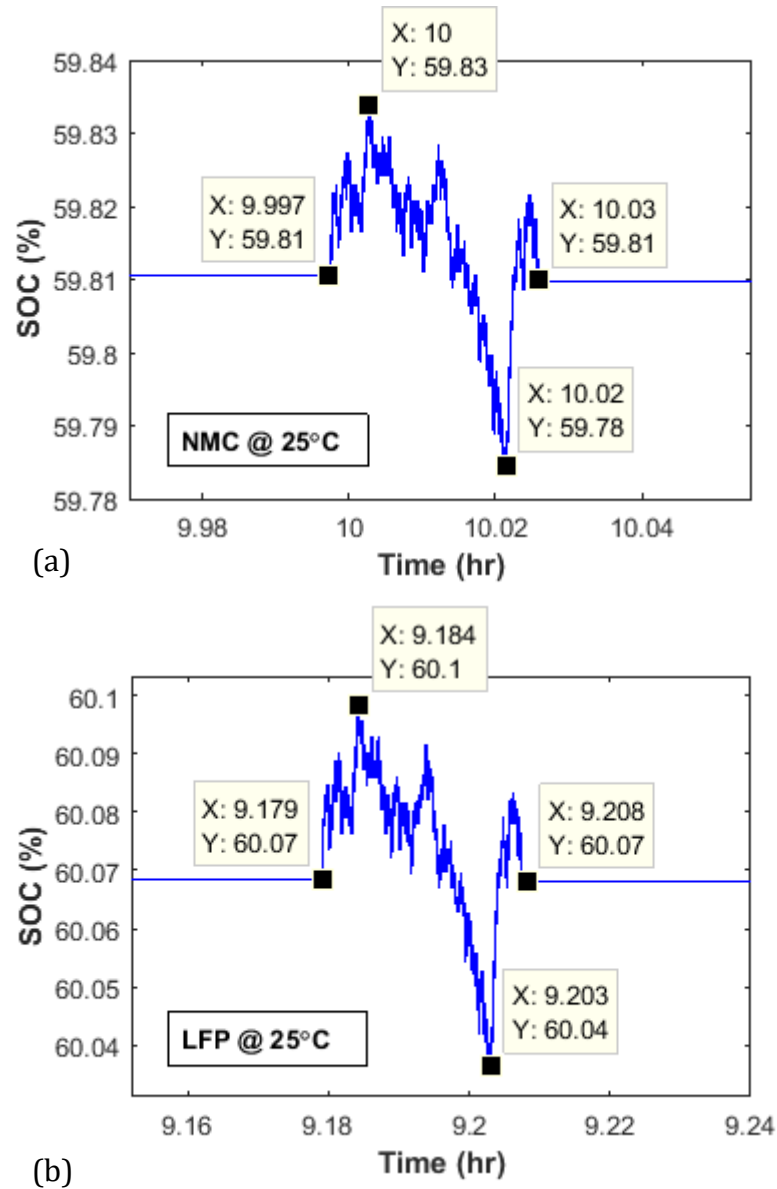
Fig. 6.15 (a) NMC and (b) LFP cell SOC deviation when applied with ±0.4C pulses, over one complete 10-bit 10 Hz PRBS sequence

Second, the ArtHiUFL dynamic test profile of section 2.3.2.8 has been used to provide a realistic operating condition for the validation of the proposed hybrid battery parameter identification technique and its application to battery SOP estimation in real time. At time-step $k = 0$, the parameters vector $\boldsymbol{\theta}_k$ in the weight EKF (see Table 4.2 for the state and weight EKF equations) is initialised with the PRBS-obtained parameters at SOC = 80%. Moreover, the state EKF is incorrectly initialised at SOC = 20%, whilst true SOC = 80%. This is to demonstrate the SOC convergence capability of the states EKF, even under erroneous initial conditions.
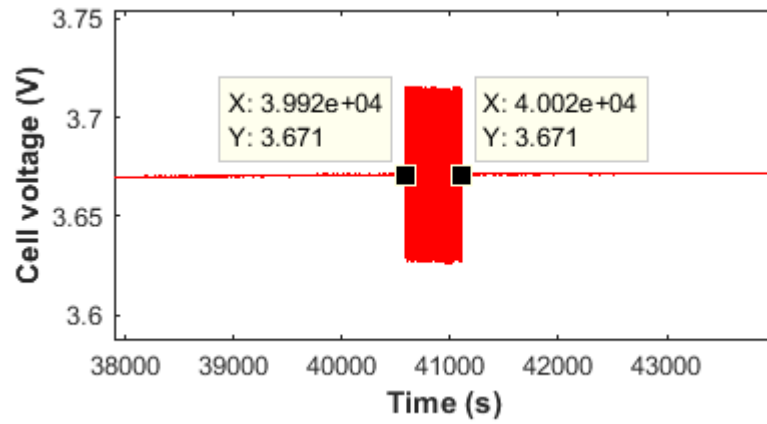
Fig. 6.16 Trajectory of OCV relaxation for the NMC cell, showing a balanced PRBS

Table 6.4 Cell OCV measurements taken for the NMC and LFP cells before and after PRBS injection

SOC	Cell OCV (V)			
	NMC		LFP	
	Before PRBS	After PRBS	Before PRBS	After PRBS
0.1	3.455	3.455	3.124	3.124
0.2	3.536	3.536	3.218	3.217
0.3	3.598	3.598	3.259	3.259
0.4	3.636	3.636	3.288	3.288
0.5	3.671	3.671	3.296	3.296
0.6	3.740	3.740	3.297	3.297
0.7	3.839	3.839	3.302	3.302
0.8	3.937	3.937	3.331	3.331
0.9	4.047	4.047	3.335	3.334

Fig. 6.17 and Fig. 6.18 present the magnitudes of the complex impedances obtained for the NMC and LFP test cells using, the EIS technique and the proposed PRBS excitation method over the selected frequency band of 5 mHz to 5 Hz. Generally, a good agreement between the EIS and PRBS results can be observed at 5°C, 25°C and 45°C ambient temperatures.
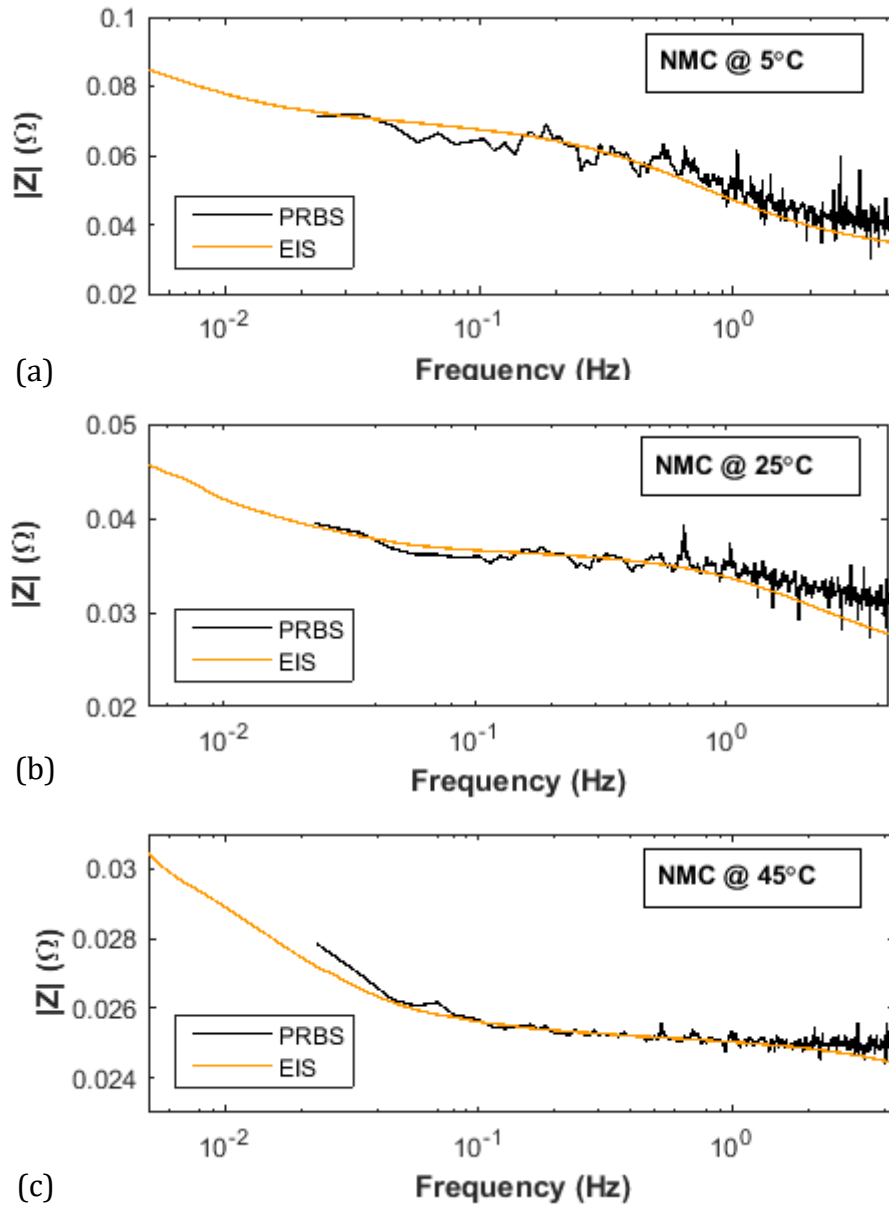
Fig. 6.17 NMC Cell impedance magnitudes obtained at 80% SOC and at (a) 5°C, (b) 25°C and (c) 45°C, using the EIS and proposed PRBS identification method

At low frequency, the two methods pose excellent agreement for both variations of lithium-ion cells. However, towards the high end of the spectrum, the cell impedances obtained using the PRBS technique become more prone to measurement noise. This is due to the hardware low-pass filtering of the voltage and current signals acquired by the MACCOR battery tester, which can result in out-of-phase measurements. Nevertheless, the cell impedances obtained from the PRBS technique can be safely applied to the dual-EKF estimator for robust initialisation.
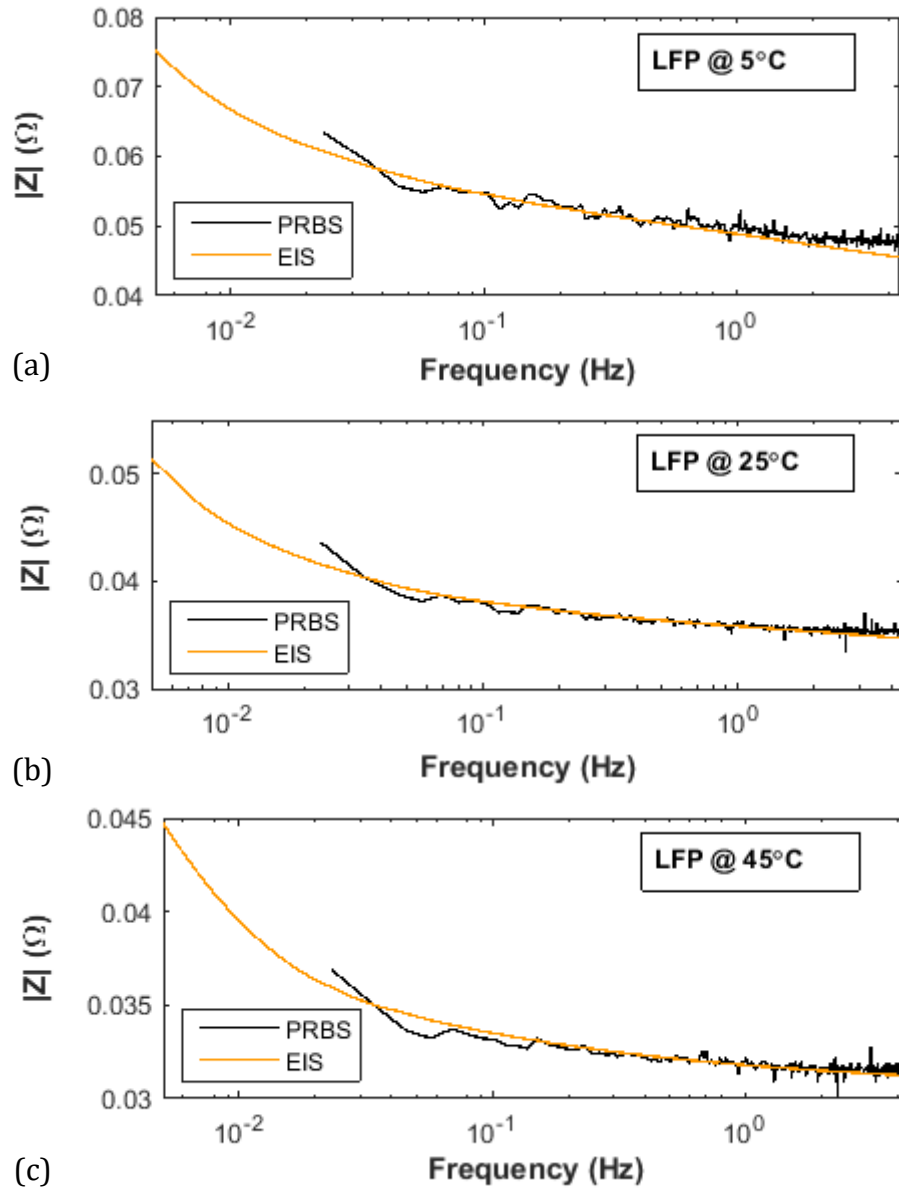
Fig. 6.18 LFP Cell impedance magnitudes obtained at 80% SOC and at (a) 5°C, (b) 25°C and (c) 45°C, using the EIS and proposed PRBS identification method

Using the nonlinear least-squares method described in Chapter 2, the parameters of the 2-*RC* model structure are extracted from the EIS and PRBS complex impedances. After correct initialisation of the weight EKF using the PRBS-attained battery parameters at SOC = 80%, the dual-EKF algorithm is then implemented recursively to effectively capture and adapt to those SOC-induced variations in the constituent *RC* elements.

Fig. 6.19 and Fig. 6.20 present the 2-*RC* model parameters identified as a function of SOC using the EIS, PRBS and the PRBS-initialised dual-EKF estimator. It should be noted that the SOC state has been allowed to fully converge (i.e. enter and stay within ±5% error band), before the first set of estimated parameters were used for absolute error calculations with respect to the EIS measurements; thus, the results for the hybrid dual-EKF estimator are displayed over the SOC range of 70% to 20% instead of 80% to 20%. The performance of each technique is quantified by calculating the mean-absolute-error (MAE) between the PRBS- and EKF-identified model parameters with those obtained from the accurate sine-swept EIS method.

$$\text{MAE (\%)} = \left(\frac{1}{d} \sum_{i=1}^{d} \frac{|\hat{\rho}_i - \rho_i|}{\rho_i} \right) \times 100 \qquad (6.16)$$

where $\hat{\rho}_i$ is the estimated parameter (i.e. PRBS- or EKF-attained), ρ_i is the EIS-attained parameter and d is the number of SOC steps at which the parameters are identified. Table 6.5 and Table 6.6 provide the resulting MAE for the NMC and LFP cells respectively. It is evident that the low-cost PRBS identification technique is capable of producing a fairly accurate set of model parameters for both variations of lithium-ion cells studied in this thesis. By correctly initialising the weight filter in the dual-EKF algorithm with the *RC* parameters obtained at SOC = 80% using PRBS, the error between the estimated and EIS-attained parameters are further reduced; this is a significant contribution related to the proposed hybrid battery identification technique.
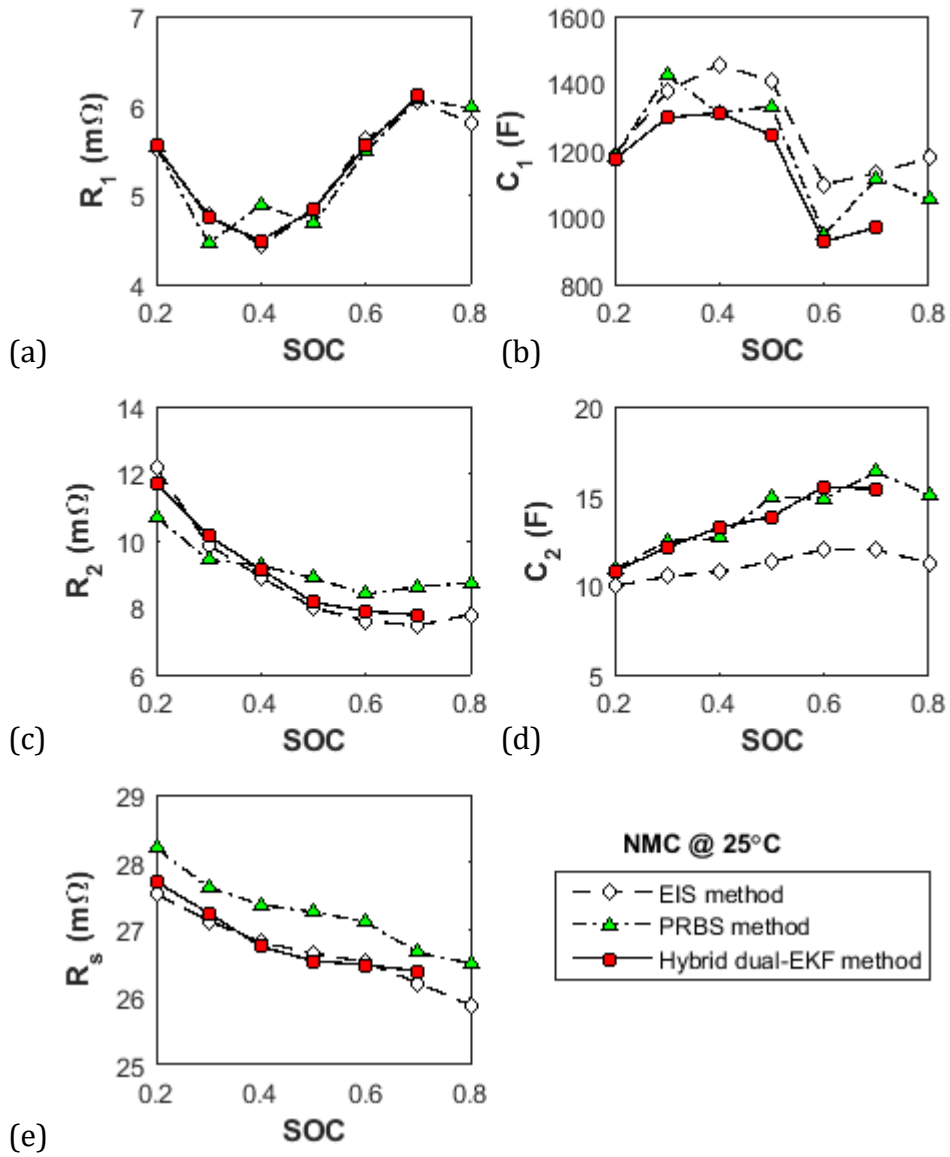
Fig. 6.19 Comparison of 2-*RC* model parameters identified using EIS, PRBS and the proposed hybrid dual-EKF method for the NMC cell at 25°C

Table 6.5 MAE assessment of the proposed PRBS and hybrid dual-EKF identification methods, when compared with the EIS results for the NMC cell

NMC	MAE (%)				
	R_s	R_1	C_1	R_2	C_2
PRBS	2.14	0.142	5.36	3.61	24.93
Hybrid dual-EKF	0.29	0.123	8.26	1.32	18.45
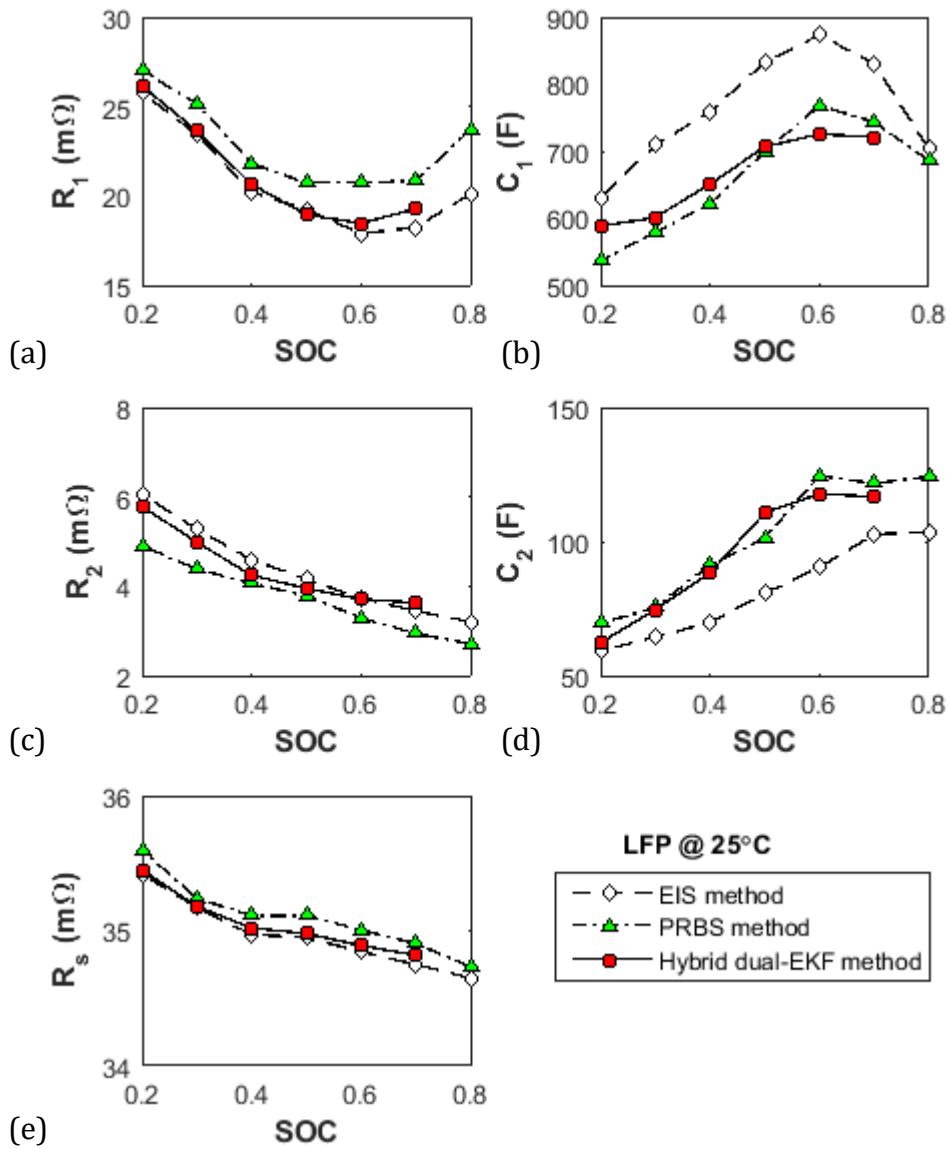
Fig. 6.20 Comparison of 2-*RC* model parameters identified using EIS, PRBS and the proposed hybrid dual-EKF method for the LFP cell at 25°C

Table 6.6 MAE assessment of the proposed PRBS and hybrid dual-EKF identification methods, when compared with the EIS results for the LFP cell

LFP	MAE (%)				
	R_s	R_1	C_1	R_2	C_2
PRBS	0.387	10.42	13.20	14.36	24.03
Hybrid dual-EKF	0.129	4.09	12.35	4.76	21.68

In Chapter 6, it was shown that under steady-state conditions, only the resistive-element parameters of the 2-RC battery model (i.e. R_s, R_1 and R_2) are required in order to produce an accurate SOP estimate. Therefore, by PRBS extraction of the aforementioned model parameters, in addition to correct initialisation of the dual-EKF estimator, it is also possible to achieve a *priori* knowledge of the battery's power capability at the current time, before sourcing/sinking a particular load profile. Thus, to analyse the performance of the PRBS battery identification technique for battery SOP estimation, the resistive-element parameters identified over the SOC range of 10% to 90%, in 10% steps, are applied to equations (6.8) and (6.9) for the test cells' discharge and charge SOP levels, respectively. Moreover, the standard HPPC method (refer to Chapter 2, section 2.3.2.4 for more details) is used here as a reference framework for the verification of the estimated cell power capabilities.

The results obtained for the NMC and LFP cells at 5°C, 25°C and 45°C are presented in Fig. 6.21 and Fig. 6.22, respectively. For all the three temperatures, there exists a good agreement between the EIS-, PRBS- and HPP-estimated battery powers for both charge and discharge. Additionally, a drop in both cells' power capabilities with temperature can be observed as expected. This can be attributed to the fact that, at low temperatures, the cell's impedance grows due to the solidification of the active materials, reducing the charge-acceptance and, thus, the power capability of the cell [10]. An opposite effect is true at high temperatures, where the cell's impedance drops, resulting in a higher source/sink power capability.

When comparing the performance of an SOP estimator against the standard HPPC, one should note that the estimated power extracted from the HPPC data is mainly dependent on the duration of the applied current pulse and the initial battery condition. In other words, if the battery is not well-rested or is applied with a discharge pulse for a longer duration than the HPPC's (i.e. 18 seconds), the voltage drop at the end of the pulse will be higher, resulting in a decrease in the estimated power capability. On the other hand, as discussed in Chapter 6, the power definitions given by (6.8) and (6.9) reflect on the battery's steady-state power capabilities. However, comparing two separate approaches of estimation for the same quantity is a respected way of checking the validity of the proposed method.
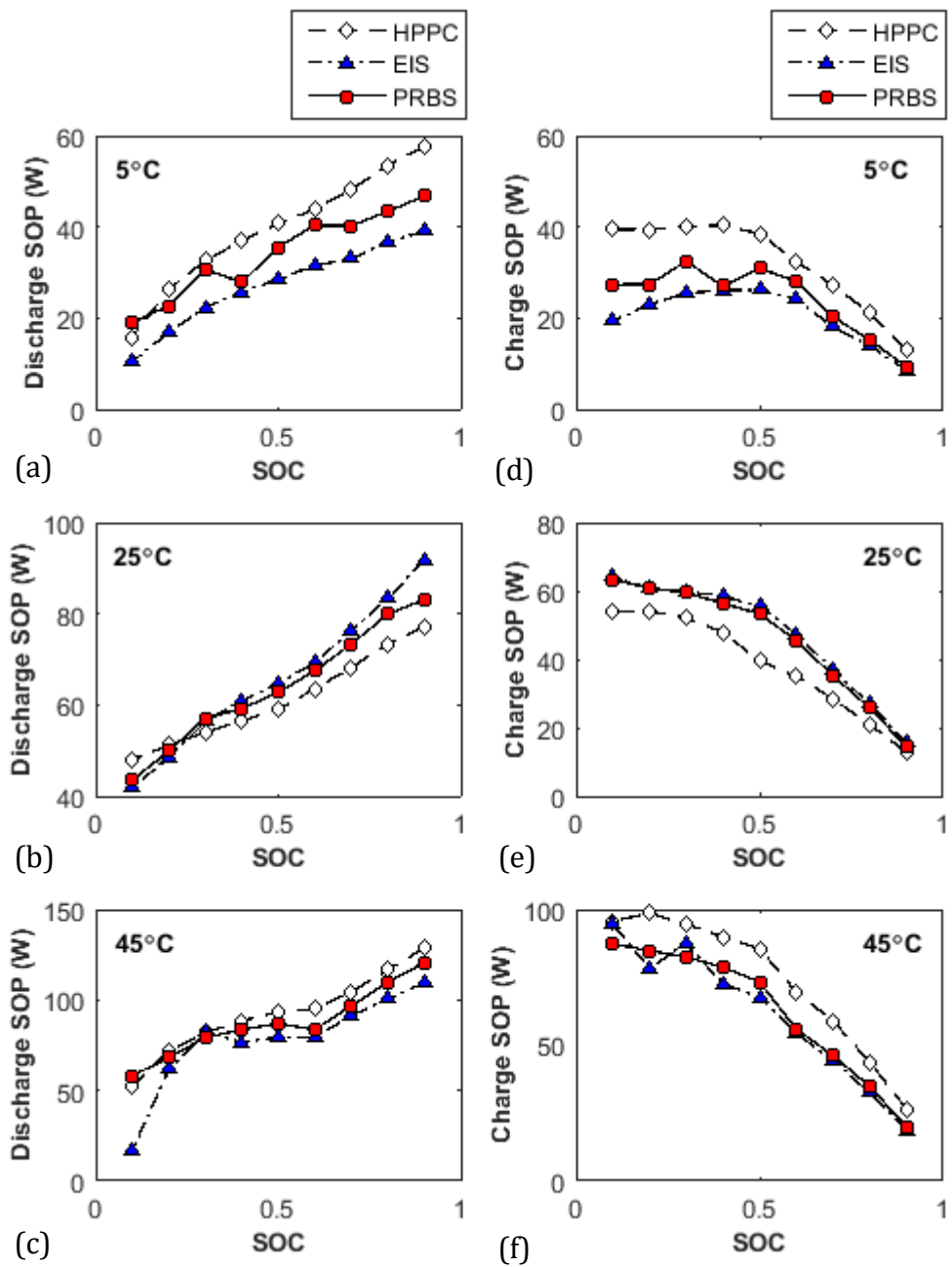
Fig. 6.21 Comparison of PRBS- and EIS-based SOP estimates with the standard HPPC results for the NMC cell, obtained over the SOC range of 10% to 90% at 5°C, 25°C and 45°C
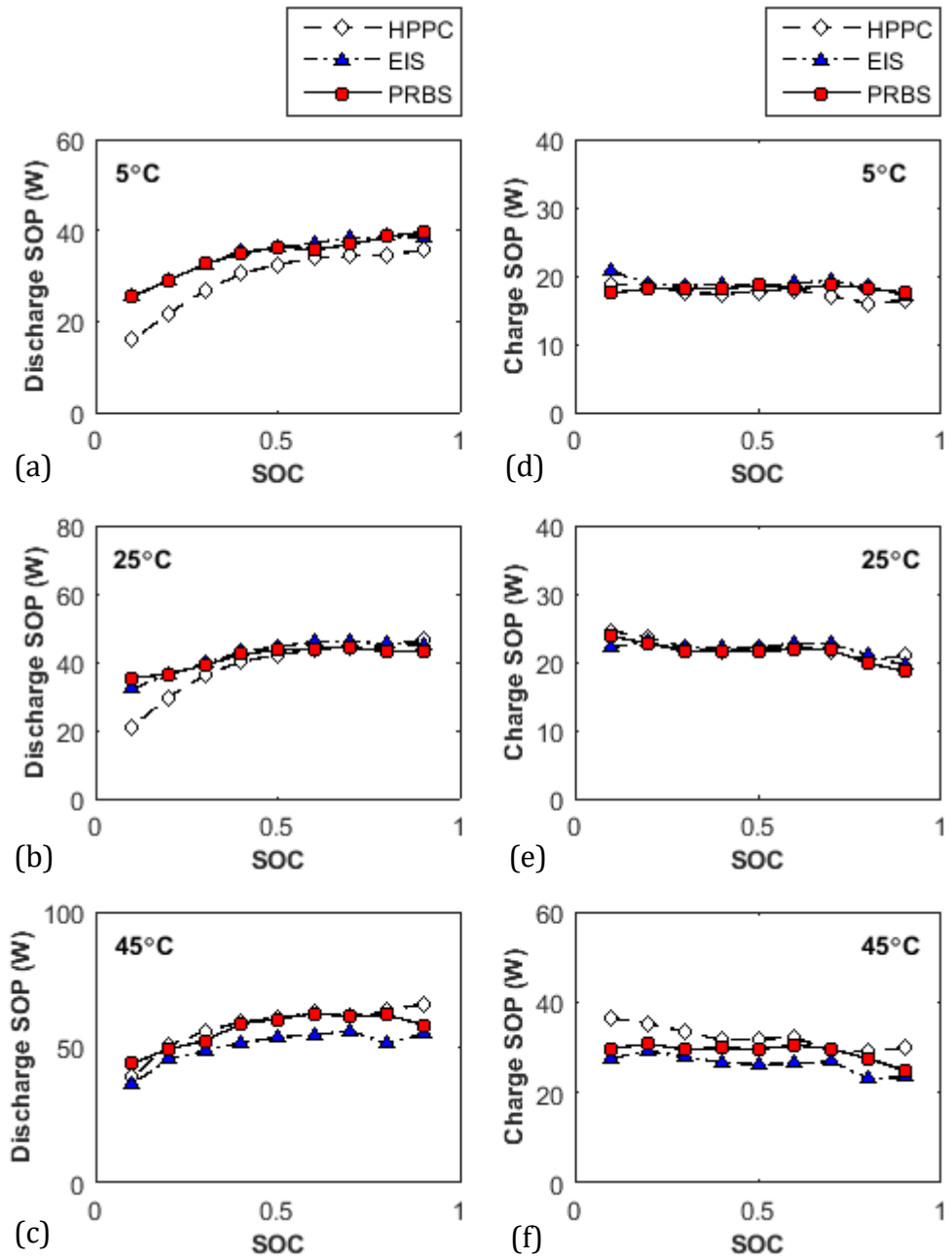
Fig. 6.22 Comparison of PRBS- and EIS-based SOP estimates with the standard HPPC results for the LFP cell, obtained over the SOC range of 10% to 90% at 5°C, 25°C and 45°C
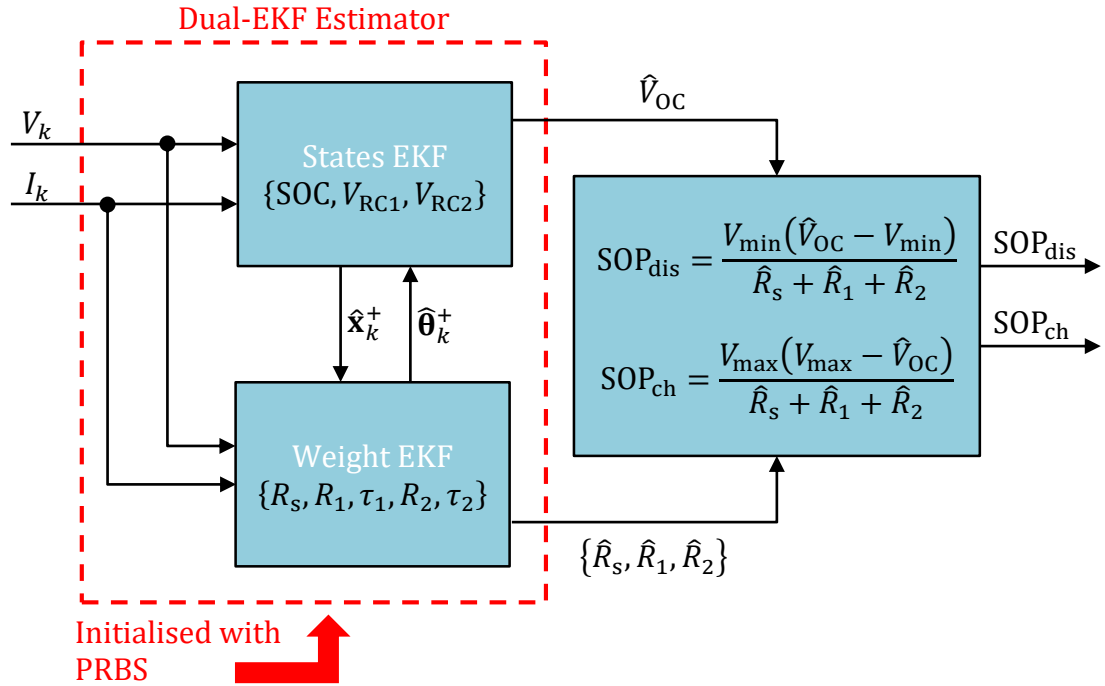
Fig. 6.23 Block diagram illustrating the structure of the online EKF-based battery SOP estimator

In general, the accuracy of an online SOP estimate obtained using equations (6.8) and (6.9) depends on the quality of $\hat{R}_s$, $\hat{R}_1$, $\hat{R}_2$ and $\hat{V}_{OC}$ used in the battery model. In Chapter 6, section 6.2.3, it was shown that, if initialised with correct battery model parameters at time-step $k = 0$, the dual-EKF estimator can robustly track any slowly time-varying deviations in the identified model parameters caused by the battery's operating conditions.

In this thesis, an EKF-based battery SOP estimator is developed for an improved battery power characterisation, whose structure is illustrated in Fig. 6.23. The parameter estimates $\hat{R}_s$, $\hat{R}_1$ and $\hat{R}_2$ are provided by the dual-EKF at each time step k. Note that for online SOP estimation, $\hat{V}_{OC}$ is predicted based on the EKF-estimated SOC and the eighth-order OCV-SOC polynomial function derived in Chapter 4, section 4.4.1. On the other hand, for the HPPC method, $\hat{V}_{OC}$ is derived from the zero-current rested cell voltages prior to HPPC pulse injection. Finally, the performance of the proposed EKF-based SOP estimator is verified on the ArtHiUFL dynamic test profile of section 2.3.2.8, conducted at 25°C and over the SOC range of 80% to 20%.
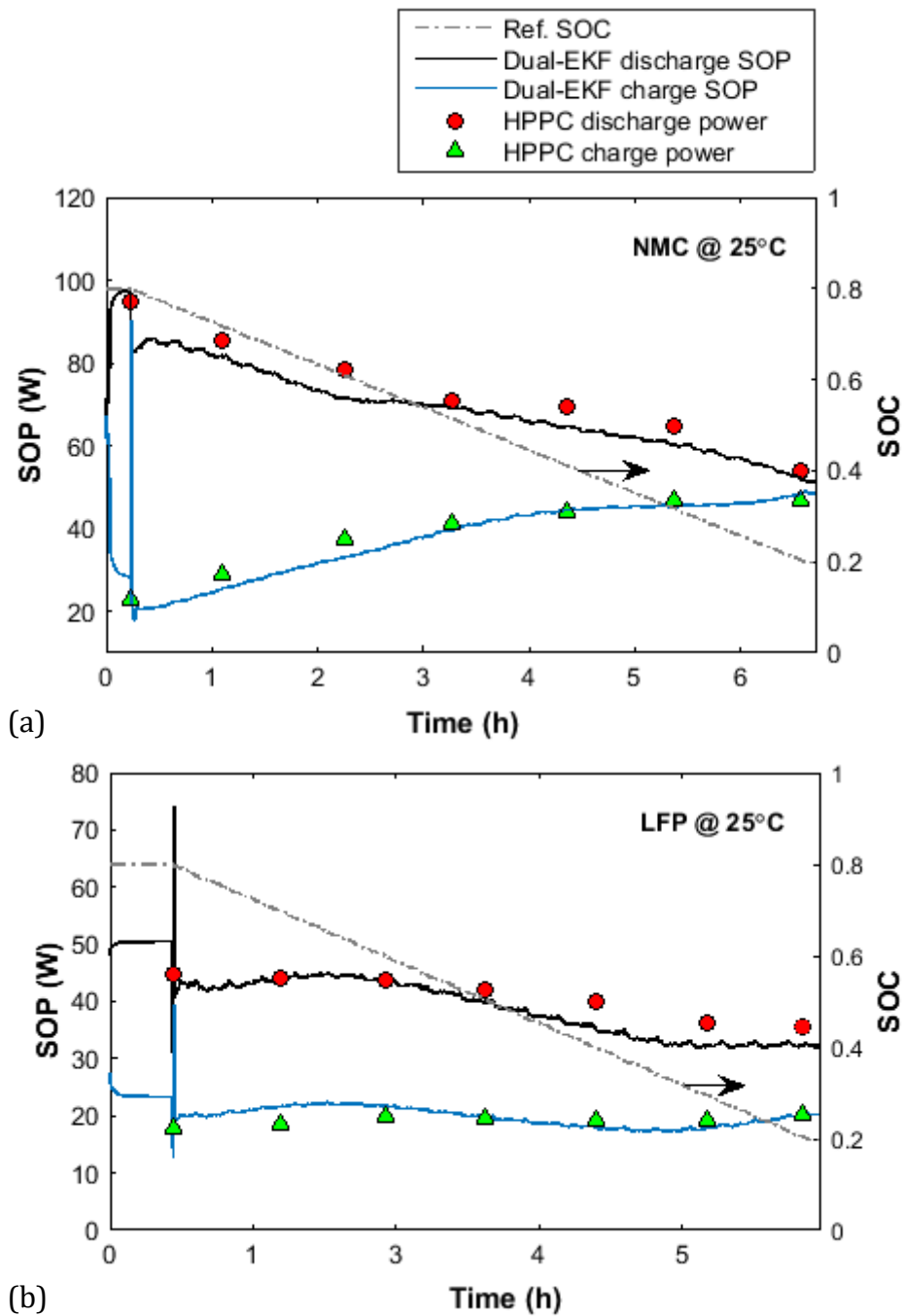
Fig. 6.24 SOP estimation results for (a) NMC and (b) LFP cells, comparing the performance of the online EKF-based method and the standard HPPC method

Fig. 6.24 compares the online SOP estimates obtained for the NMC and LFP cells using the PRBS-initialised dual-EKF estimator and the HPPC method. It can be seen that, as SOC moves down towards 20%, the EKF-based discharge SOP for both cells shows a decreasing trend, while the charge SOP estimate poses the opposite trend, indicating a higher sink power capability at low SOC levels. This behaviour is verified

against the standard HPPC results, where a similar trend in the predicted charge/discharge powers can be observed. For example, at SOC = 70%, the NMC (LFP) cell's EKF-estimated discharge and charge power is 82 W (44 W) and 25 W (21 W), whilst for the HPP method, the cell's power is predicted at 85 W (44 W) and 29 W (18 W) for discharge and charge respectively. Similarly, at the lower end of SOC range, the EFK-estimated NMC (LFP) cell power is 52 W (32 W) and 49 W (20 W), whilst the HPP predicted power levels are 54 W (30 W) and 47 W (20 W) for discharge and charge respectively. Despite the fact that HPPC and the proposed battery power SOP estimation techniques differ in implementation, a good agreement between the two methods can be observed, which adds further confidence to the proposed hybrid battery identification technique.

6.5 Chapter Conclusions

It was discussed that, in order to realise a proper identification of the battery parameters using the dual-EKF estimator, the weight EKF needs to be initialised with a sufficient *a priori* knowledge of the unknown model parameters. Of course in practice, such information might not be available to the BMS or the EKF's input/output signal may not be persistently exciting at all times for the convergence to occur; thus a hybrid battery identification technique has been proposed in this Chapter. The technique consisted of a carefully designed PRBS excitation signal for the characterisation of the battery's impedance, given an open-circuit rest period of at least 30 minutes is allowed. The parameters for a 2-*RC* battery model were then extracted using a nonlinear least-squares approach and used for the correct initialisation of the weight EKF in the dual-EKF algorithm. Thereafter, the dual-EKF algorithm was implemented recursively to adapt the model parameters with respect to those disturbances caused by varying operating conditions (e.g. SOC). The proposed technique was then applied to battery SOP estimation for an EV-based dynamic load profile. The performance capability of the proposed EKF-based battery SOP estimator has been experimentally verified against the well-known HPPC method; the results showed a good agreement, giving confidence to the proposed hybrid battery identification technique.

Chapter **7**

On-Chip Monitoring of Critical Battery States Through a Decentralised EKF Framework

In Chapter 6, the importance of an accurate battery parameter identification technique for correct characterisation of battery available power, or SOP, has been considered. Based on the steady-state SOP definitions given in that Chapter, it was seen that, as well as a true set of battery resistive-element parameters, an estimate for the battery's OCV in real time is also required, making SOP a SOC-dependent metric. Thus far in this thesis, the dual-EKF algorithm has been used in conjunction with a pre-determined OCV-SOC relationship to provide an online estimate of SOC for both NMC and LFP variants of lithium-ion battery chemistry. However, for the LFP batteries, the OCV curve obtained over the battery's linear operating voltage range is fairly flat, which means that even the smallest error in the OCV estimate can lead to a divergence in battery's SOC, and thus, SOP. As a remedy, this Chapter proposes a decentralised EKF framework for adaptive estimation of SOC for those lithium-ion batteries which suffer from a flat OCV-SOC relationship. In addition, a dynamic SOH estimation technique based on the battery's SOC and the transferred coulombic charge is proposed herein that is suitable for real-time applications. Finally, the BMS algorithms developed throughout this thesis are all brought together and implemented on a low-cost ARM-based micro-processor unit, to give realisation to an online battery states monitoring system with the lowest number of components possible.

7.1 Introduction

Thus far, in this thesis, the importance of an accurate dynamic battery model, such as the 2-*RC* equivalent-circuit model, in proper characterisation of a battery device for *in situ* applications has been discussed. Moreover, it has been shown that for a reliable SOP estimate, it is necessary to account for the time-variability of the battery impedance parameters while the battery is in operation. This lead to the development of the hybrid battery identification technique proposed in Chapter 6. However, in order to fulfil the ultimate objective of this thesis, that is, the development of an adaptive battery monitoring system, an accurate estimate of battery states other than SOP, such as SOH and SOC, is required.

In Chapter 3, a cycle-based SOH estimation technique has been developed, suitable for μP implementation. Despite the satisfactory performance of the online SOH estimator, the proposed technique required the battery to be charged and discharged between 20% to 80% SOC, covering the entire linear voltage range in order to be able to establish a *Q-V* relationship, and, thus the battery's SOH. This condition might not be met under certain dynamic applications (e.g. EV/HEVs) where the consumer's psychological attitude towards battery charging and usage is unpredictable.

Therefore, in this Chapter, at first, a dynamic SOH estimation technique based on SOC and coulomb-counting is developed. Thereafter, a decentralised adaptive EKF framework is proposed for the enhancement of the OCV-based SOC estimate produced by the dual-EKF (DEKF) estimator in Chapter 4. The proposed technique benefits from real-time assessment of the filter noise statistical parameters, in an effort to reduce those modelling uncertainties that arise as a result of poorly modelled OCV-SOC relationship. This attribution is of special interest to those batteries with a fairly flat OCV curves, especially the LFP power cells, where even a small error in the model-based OCV estimate can result in intolerable SOC inaccuracies.

At last, this Chapter reports on the μP implementation of the proposed EKF-based battery states monitoring algorithm in this thesis. The proposed system features an

NXP μP unit, which is utilised as a standalone platform for the decentralised adaptive EKF algorithm to perform an online SOC, SOP, and SOH estimation. Finally, the experimental results obtained using the high-precision MACCOR battery tester and processed offline on PC are used to verify the convergence and tracking performance of the developed battery states monitoring system.

7.2 A Dynamic SOH Estimation Method

As mentioned in Chapter 2, section 2.2.5, there are two distinct definitions for SOH, relating it to either a power or energy fade. The source/sink power capability of a battery largely depends on its internal resistance. As the resistance grows with ageing, the battery's instantaneous available power fades away. Moreover, as the battery ages, it loses some of its ampere-hour capacity, leading to an energy fade.

Thus, to establish a comprehensive battery state monitoring system, in this thesis, both definitions of SOH as given by (7.1) and (7.2) are considered.

$$\text{SOH}_{\text{pwr}} = 1 - \left(\frac{R_{\text{now}}^{\text{s}} - R_0^{\text{s}}}{R_0^{\text{s}}} \right) \times 100\% \tag{7.1}$$

$$\text{SOH}_{\text{enr}} = \frac{C_{\text{now}}^{\text{Ah}}}{C_0^{\text{Ah}}} \times 100\% \tag{7.2}$$

where SOH_{pwr} is the power-based definition, relating the battery's current series resistance $R_{\text{now}}^{\text{s}}$ to that of a reference value R_0^{s}, and SOH_{enr} is the energy-based definition, which is the ratio of the battery's current capacity $C_{\text{now}}^{\text{Ah}}$ in ampere-hour to that of a reference value C_0^{Ah}. It should be noted that, equation (7.1) is only valid if $R_{\text{now}}^{\text{s}} \leq 2R_0^{\text{s}}$. The reference quantities R_0^{s} and C_0^{Ah} can either be determined experimentally at the beginning of the battery's life at a reasonable temperature, or they can be exported from the manufacture's datasheet. In this case, both have been determined experimentally at 25 °C when the cells first arrived at the lab, using the test setup described in Chapter 2, section 2.3.1.

In order to predict $C_{\text{now}}^{\text{Ah}}$ without performing a full charge/discharge cycle, a new method is proposed. During a charge/discharge cycle, the quantity of coulombic charge in the battery is modified according to (7.3).

$$Q_{\text{mod}} = Q_\alpha - Q_\beta = Q_\alpha - \sum_{k=\alpha}^{\beta} I_k \cdot \Delta t \tag{7.3}$$

where Q_α is the initial charge at discrete time-step $k = \alpha$; Q_β is the final charge value at $k = \beta$; and Δt is the sampling period in seconds. For intervals of short charge/discharge durations (i.e. minutes to hours), Q_β can be calculated using the integral of the current-sensor measurements. This is also referred to as coulomb counting. During the charge modification interval, the SOC is also modified as,

$$\text{SOC}_{\text{mod}} = \text{SOC}_\alpha - \text{SOC}_\beta = \frac{Q_{\text{mod}}}{Q_{\text{nom}} = C_{\text{now}}^{\text{Ah}} \times 3600}. \tag{7.4}$$

Now, considering the definition of SOC given in equation (7.4), and assuming an accurate estimate for SOC_{mod} is available during the charge modification period (i.e. $\alpha \leq t \leq \beta$) via an online estimator, the battery's ampere-hour capacity, $\hat{C}_{\text{now}}^{\text{Ah}}$, can be predicted as,

$$\hat{C}_{\text{now}}^{\text{Ah}} = \frac{Q_{\text{mod}}}{3600 \times \text{SOC}_{\text{mod}}}. \tag{7.5}$$

7.3 Enhanced Real-Time SOC Estimation

Whilst many real-time SOC estimation techniques for other chemistries of the lithium-ion battery family have been presented (e.g. [88], [97], [250], [254], [268]), those for the LFP variation are less frequently reported. The LFP cells are regarded as the preferred choice of battery chemistry for many power applications [32]. Difficulty arises in relating the SOC to the OCV curves obtained for these cells.

As discussed previously in this thesis, the OCV-SOC relationship for most battery chemistries often provides a good estimate of SOC. However, for the LFP variation of the lithium-ion cell chemistry, the OCV curve is fairly flat over the linear SOC range. The OCV curve as a function of SOC at different temperatures for a typical LFP cell is shown in Fig. 7.1. Note that within the linear SOC range of 20-80%, the OCV curves obtained are fairly flat, even at low operating temperatures where nonlinearities are usually most apparent. This implies that even a small error in the model-based OCV obtained within this region can result in a large deviation from the actual SOC value.
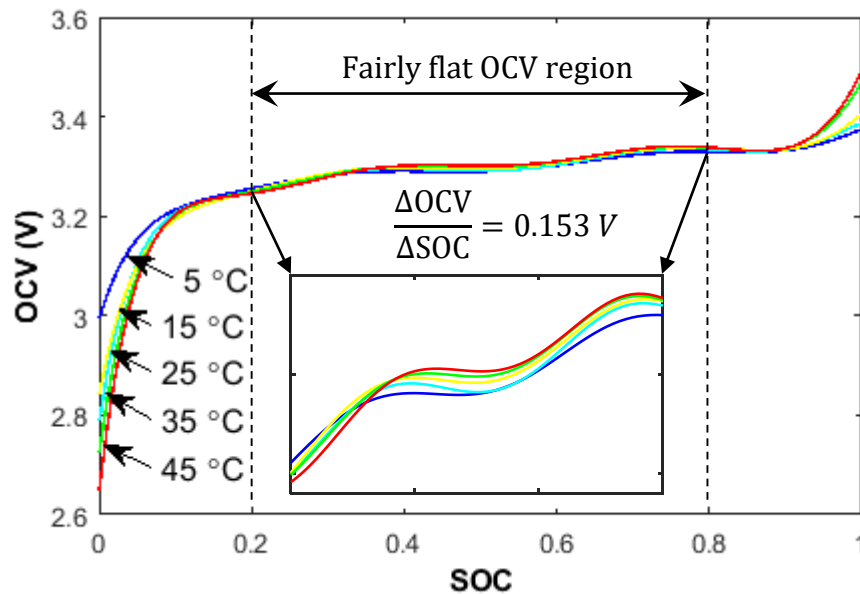
Fig. 7.1 The OCV curves measured as a function of SOC and temperature for an LFP cell, showing the fairly flat OCV region between 20% to 80% SOC

Therefore, as a remedy, this Chapter proposes a decentralised framework for the adaptive EKF estimation of SOC for both LFP and NMC cells, with real-time process and measurement covariance assessment. Essentially, the adaptive EKF estimator is employed to treat those OCV-induced modelling uncertainties that are introduced into the SOC estimate, caused by the cell's flat OCV-SOC relationship. Consequently, problems such as divergence and large estimation errors that occur around the linear SOC range of LFP cells can be remedied. The proposed technique will also be

verified on an NMC cell to demonstrate its performance on those lithium-ion cell chemistries whose OCV curves are not as severely flat as LFP cells.

7.3.1 Dual-EKF Response to Flat OCV curves

In order to demonstrate the effect of a flat OCV curve on the SOC estimate obtained using the standard DEKF, the algorithm was run on the dataset gathered for an LFP cell, using the self-designed pulsed-current test profile described in Chapter 2, section 2.3.2.5. For details on recursive DEKF estimation of battery SOC, the reader is referred to Chapter 4, section 4.5.
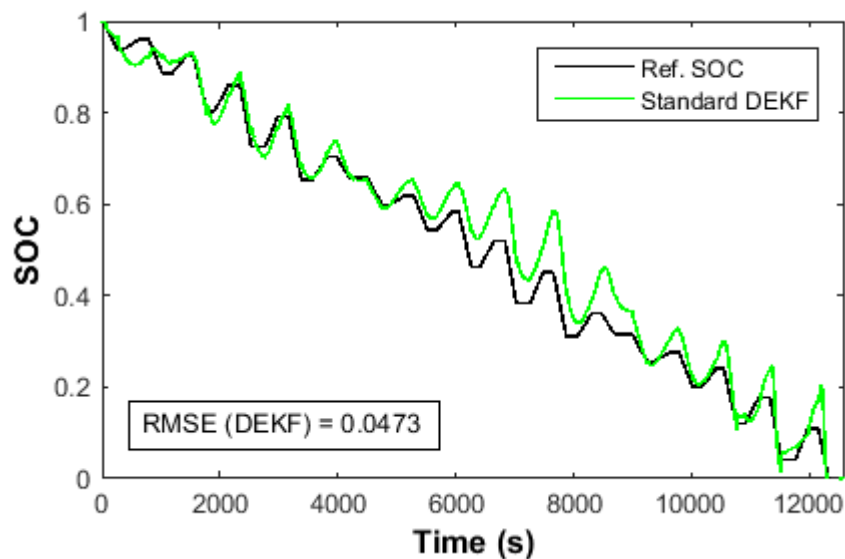
Fig. 7.2 DEKF estimation of SOC for an LFP cell, showing the impact of a flat OCV curve

Fig. 7.2 compares the SOC estimated using the standard DEKF estimator with that measured by the coulomb-counting method (denoted as Ref. SOC). Despite the reasonable RMSE of less than 5% obtained over the SOC range of 0-100%, at ~60% SOC, the DEKF-based SOC estimate starts to drift away from the reference SOC (black line), resulting in an estimation error of up to 13 percentage point. This error is largely caused by the modelling uncertainties introduced into the filter's output equation, as a result of the inherently flat OCV-SOC relationships observed for LFP power cells.

218

7.3.2 A Decentralised Adaptive EKF Framework

In order to account for the flatness of the OCV-SOC curve for LFP cells, as discussed previously, and to produce an accurate OCV estimate for the SOP calculations using the steady-state definitions given by equations (6.8) and (6.9), a decentralised EKF framework is proposed.
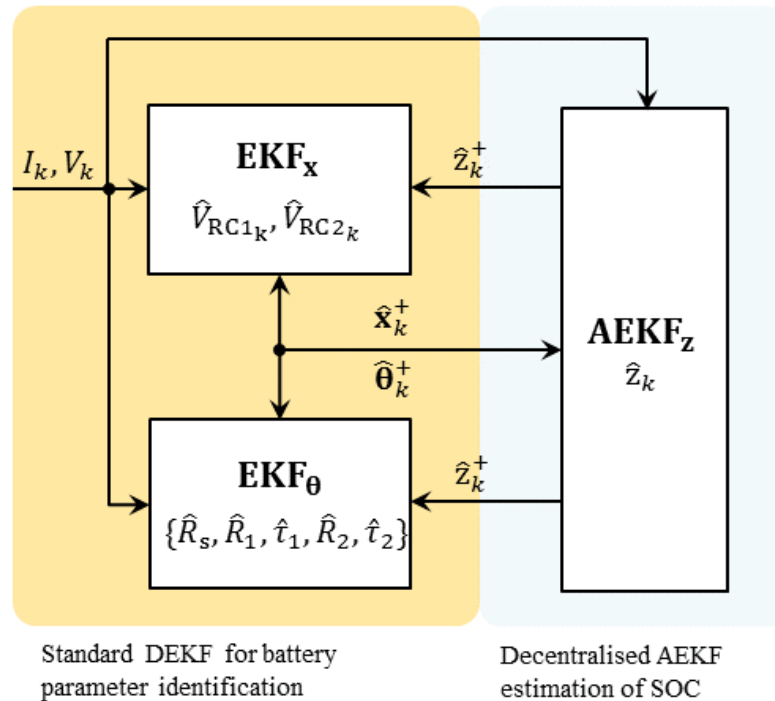
Fig. 7.3 Block diagram illustrating the structure of the proposed decentralised-AEKF framework for enhanced SOC estimation of LFP power cells

As illustrated in Fig. 7.3, the proposed technique is comprised of two ordinary EKFs implemented in a dual/parallel formation (refer to Chapter 4, section 4.5 for more details on dual-EKF algorithm) to estimate the 2-RC battery model parameters (i.e. R_s, R_1, τ_1, R_2 and τ_2) and states (i.e. V_{RC1} and V_{RC2}). Thereafter, assuming a zero correlation exists between the process and measurement noise covariance, an additional EKF is designed to decentralise the SOC estimation from the standard dual-EKF algorithm's states filter. Thereafter, the process and measurement noise statistics for the decentralised SOC filter are predicted in real time, resulting in an adaptive EKF (AEKF) algorithm for the enhancement of the SOC estimate, $\hat{z}_k$, obtained for LFP power cells.

The update procedure of the 2-*RC* model states and parameters by $\mathrm{EKF_x}$ and $\mathrm{EKF_\theta}$ estimators in Fig. 7.3 is realised through the standard DEKF equations given in Table 4.2 of Chapter 4. Moreover, assuming that the cell voltage and current are the only measurable quantities available at time step k, the state-space equations for the decentralised AEKF estimator can be derived.

$$
\begin{aligned}
\mathrm{z}_k &= f(\mathrm{z}_{k-1}, \mathrm{u}_k) + \mathrm{w}_k^{\mathrm{z}} \\
\mathrm{y}_k &= h(\mathrm{z}_k, \mathrm{u}_k) + \mathrm{v}_k^{\mathrm{z}} \\
\mathrm{w}_k^{\mathrm{z}} &\sim N(0, \mathrm{Q}_k^{\mathrm{z}}) \\
\mathrm{v}_k^{\mathrm{z}} &\sim N(0, \mathrm{R}_k^{\mathrm{z}})
\end{aligned}
\tag{7.6}
$$

where z_k is the SOC estimate and y_k is the model-based terminal voltage estimate at time-step k; $f(\mathrm{z}_{k-1}, \mathrm{u}_k) = \mathrm{z}_{k-1} - (\eta \Delta t / Q_{\mathrm{nom}}) \cdot I_k$ is the state transition model; $h(\mathrm{z}_k, \mathrm{u}_k) = V_{\mathrm{OC}}(\mathrm{z}_k) - V_{\mathrm{RC1}_k} - V_{\mathrm{RC2}_k} - I_k R_{\mathrm{s}}$ is the nonlinear observation model; and, $\mathrm{w}_k^{\mathrm{z}}$ and $\mathrm{v}_k^{\mathrm{z}}$ are the filter's process and measurement Gaussian noises of covariance $\mathrm{Q}_k^{\mathrm{z}}$ and $\mathrm{R}_k^{\mathrm{z}}$, respectively.

Similar to the DEKF algorithm in Chapter 4, the SOC AEKF proposed here also performs three steps to compute an estimate for the battery's SOC.

A) Initialisation.

At time-step $k = 0$, the SOC state and the associated error covariance matrix are set to their best-guess values as per (7.7).

$$
\hat{\mathrm{z}}_0^+ = E[\mathrm{z}_0], \qquad \mathrm{P}_{\hat{\mathrm{z}},0}^+ = E[(\mathrm{z} - \hat{\mathrm{z}}_0^+)(\mathrm{z} - \hat{\mathrm{z}}_0^+)^T]
\tag{7.7}
$$

B) Time-update equations.

At this step, the filter updates the *a priori* SOC state $\hat{\mathrm{z}}_k^-$ and the corresponding error covariance $\mathrm{P}_{\hat{\mathrm{z}},k}^-$. The subsequent time-update equation for the adaptive SOC filter becomes,

$$\hat{z}_k^- = \hat{z}_{k-1}^+ - \left[\frac{\eta \Delta t}{Q_{\text{cell}}}\right] \cdot I_k$$

$$P_{\tilde{z},k}^- = F_{k-1} P_{\tilde{z},k-1}^+ F_{k-1}^T + Q_k^z$$

(7.8)

where $Q_{\text{cell}} = C_0^{\text{Ah}} \times 3600$ is the cell's coulombic capacity; η is the cell's coulombic efficiency and is assumed to be unity; $\Delta t = 100$ ms is the sampling period; $\hat{z}_{k-1}^+$ is *a posteriori* estimate of the SOC state at time-step $k-1$, $F_{k-1} = \partial \hat{z}_k^- / \partial \hat{z}_{k-1}^+ = 1$; and Q_k^z is the process noise covariance for the SOC filter to be estimated adaptively.

C) Measurement-update equations

After a voltage and current measurement has been taken at time step k, the AEKF estimator takes this into consideration in order to compute the Kalman gain L_k^z and to update the SOC state $\hat{z}_k^+$ and its corresponding error covariance as $P_{\tilde{z},k}^+$.

$$L_k^z = P_{\tilde{z},k}^- (H_k^z)^T \left[H_k^z P_{\tilde{z},k}^- (H_k^z)^T + R_k^z \right]^{-1}$$

$$\hat{z}_k^+ = \hat{z}_k^- + L_k^z [y_k - h(\hat{z}_k^-, u_k)]$$

$$P_{\tilde{z},k}^+ = (I - L_k^z H_k^z) P_{\tilde{z},k}^- (I - L_k^z H_k^z)^T + L_k^z R_k^z (L_k^z)^T$$

(7.9)

where $H_k^z = \partial h(\hat{z}_k^-, u_k)/\partial \hat{z}_k^- = \partial V_{\text{OC}}(\hat{z}_k^-)/\partial \hat{z}_k^-$ is the linearised observation model that maps the time-updated SOC state into the observed space. Note that, due to the scalar property of the state vector for the AEKF-based SOC estimator given by (7.8) and (6.4), the computational power and/or memory required of the μP unit for calculating the Kalman gain L_k^z of the decentralised SOC filter is comparatively lower than calculating the Kalman gain for an adaptive DEKF algorithm with SOC as one of its estimable states. This is owed to the fact that for the latter case, the inverse of a 3-by-3 matrix would be required to compute the Kalman gain, $\mathbf{L}_k^x$, for the DEKF estimator as per (4.23), whereas for the proposed decentralised SOC filter, this inverse operation only applies to a 1-by-1 matrix.

Finally, in order to account for those modelling errors associated with the flatness of the OCV curves for LFP power cells, the process and measurement noise

covariance Q_k^z and R_k^z, respectively, are predicted online, using an index weighted method as explored in [254]. Accordingly, Q_k^z and R_k^z can be recursively updated for the decentralised SOC EKF as,

$$Q_k^z = (1 - \delta_{k-1})Q_{k-1}^z + \delta_{k-1}\left(\sum_{i=0}^{N_s-1} \left[L_i^z \tilde{y}_i \tilde{y}_i^T (L_i^z)^T + P_{\tilde{z},i}^+ - P_{\tilde{z},i}^-\right]\right)$$

$$R_k^z = (1 - \delta_{k-1})R_{k-1}^z + \delta_{k-1}\left(\sum_{i=0}^{N_s-1} \left[\tilde{y}_i \tilde{y}_i^T - P_{\tilde{z},i}^-\right]\right)$$

(7.10)

where $N_s = 30$ is the observation sample size; $\delta_{k-1} = (1-\lambda)/(1-\lambda^k)$ is a weighting factor and $\lambda = 0.95$ is the forgetting factor; and $\tilde{y}_i = y_i - h(\hat{z}_i^-, u_i)$ is the measurement innovation. In order to ensure all the error covariance matrices are non-singular, Q_k^z and R_k^z must be positive-semidefinite and positive-definite respectively. Thus, to meet these conditions, a conservative approach is undertaken here, where the diagonal elements of Q_k^z and R_k^z are forced to their absolute values at every iteration.
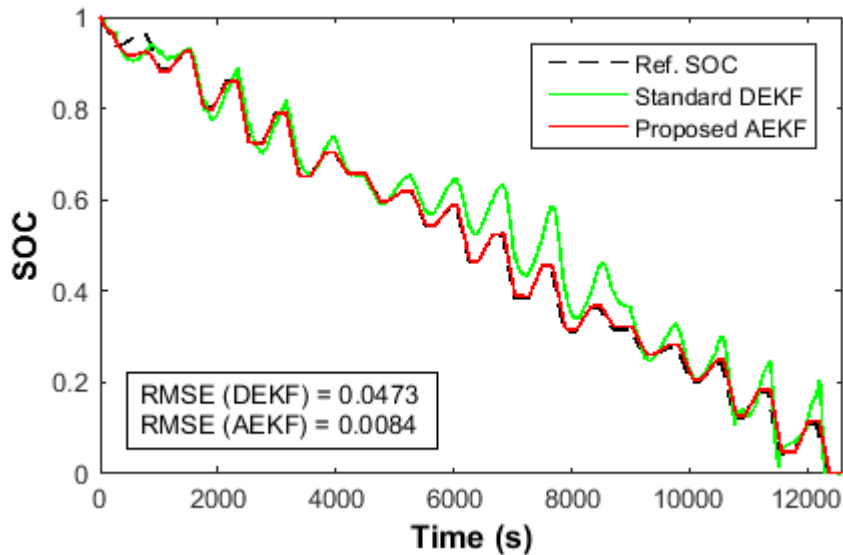
Fig. 7.4 Enhanced AEKF estimation of SOC for an LFP cell

Fig. 7.4 compares the resulting SOC estimates obtained for the same LFP cell as shown in Fig. 7.2. For analysis purposes, the self-designed pulsed-current profile, as derived in Chapter 2, section 2.3.2.5 has been used herein. It is evident that the proposed decentralised AEKF method has resulted in a much better SOC tracking performance than the standard DEKF method. To further verify the performance of the AEKF SOC estimator, the initial SOC state has been intentionally set to two erroneous conditions of 80% and 40%, while the actual SOC was at 100%. Fig. 7.5 demonstrates the excellent convergence of the proposed SOC estimator, in spite of the large offset error present at the initialisation step.
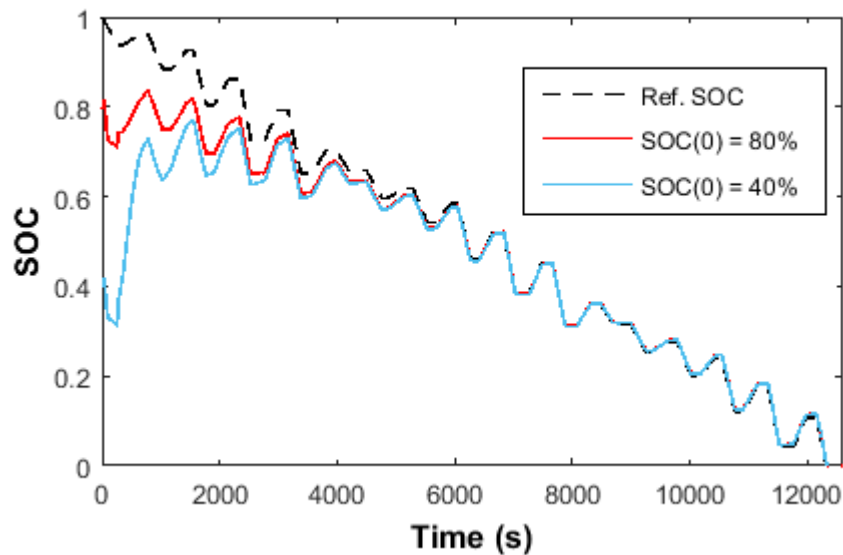
Fig. 7.5 AKEF SOC estimation performance with respect to erroneous initial conditions

7.4 Battery Monitoring System Development

In order to realise an embedded battery states monitoring system, the online DEKF battery parameters identification method explored in Chapter 4, together with the decentralised AEKF SOC estimation method proposed in this Chapter, are converted into a C++ script, suitable for deployment on the ARM-based μP unit of interest here. For the verification tests, the MACCOR battery tester is used as the experimental rig to control the cell charge/discharge current, whilst the developed battery monitoring system is connected to the cell terminals.

7.4.1 Reduced-Order OCV-SOC Polynomial
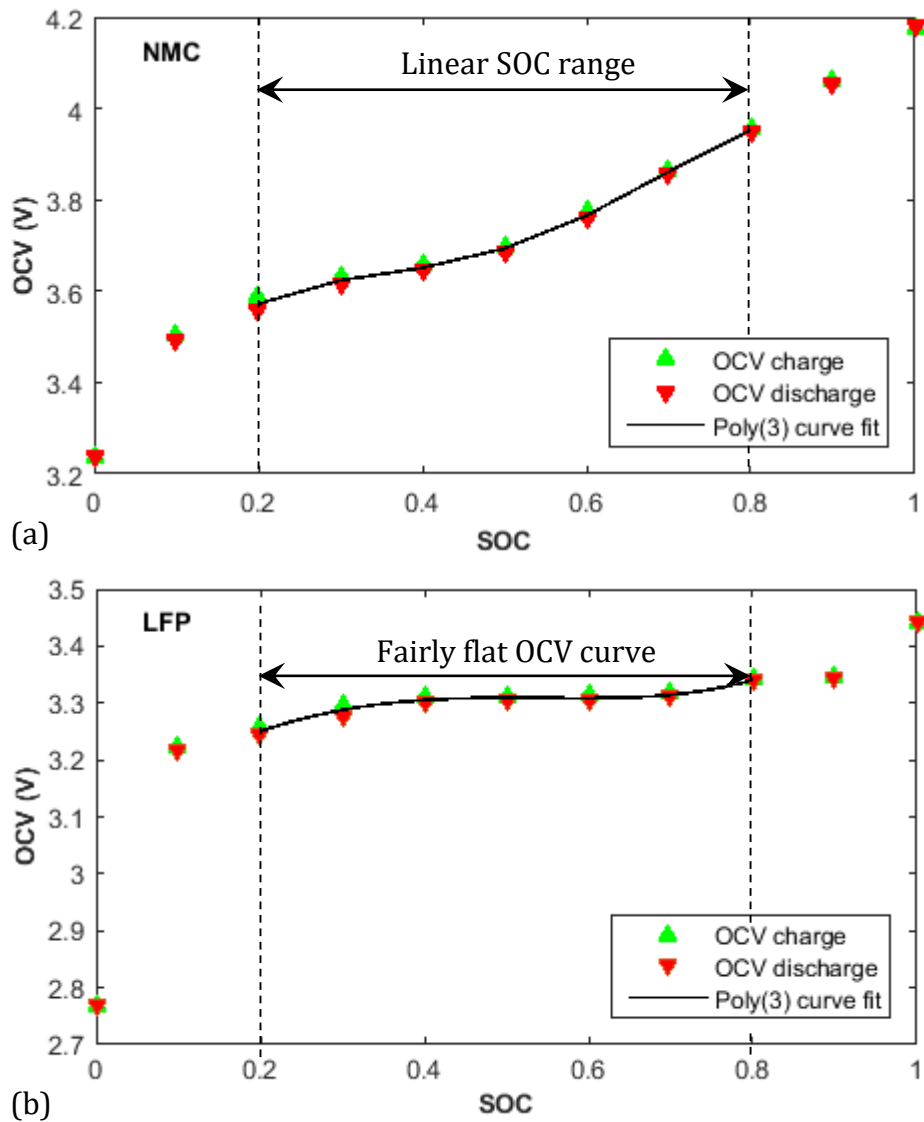
Fig. 7.6 OCV-SOC relationship for (a) NMC and (b) LFP lithium-ion cells, showing adequacy of a third-order polynomial fit over the linear SOC range

In order to estimate SOC using the proposed decentralised AEKF method to estimate SOC in real time, a mathematical relationship between the battery's OCV and SOC is required. In Chapter 4, section 4.4.1, the OCV-SOC relationship over the entire SOC range was modelled using an eighth-order polynomial function. However, in Fig. 7.6, it can be seen that over an operational SOC range of 20-80%, for both LFP and NMC cell types, the OCV-SOC relationship can be described using a third-order

polynomial, without loss of accuracy. In terms of memory usage, the reduced-order OCV function offers a better performance, when implemented on a low-cost μP unit.

$$V_{\text{OC}}(\text{SOC}) = p_3 \times \text{SOC}^3 + p_2 \times \text{SOC}^2 + p_1 \times \text{SOC} + p_0 \qquad (7.11)$$

where coefficients $p_{0 \to 3}$ are experimentally determined. As reported in [91] and [269], the variation of the OCV coefficients with ageing and temperature is negligible. Thus, the OCV coefficients established at one practical temperature (e.g. at 25°C) can be stored on the μP's flash memory for real-time SOC estimation.

7.4.2 Hardware Configuration
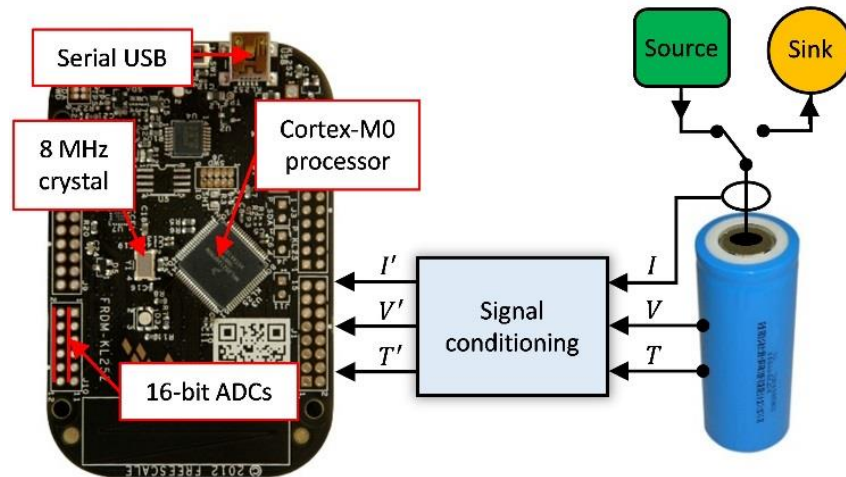
Fig. 7.7 Hardware configuration for embedded battery monitoring system

As depicted in Fig. 7.7, the developed battery monitoring system is comprised of an ARM Cortex-M0 processor, namely NXP KL25z128, with six embedded 16-bit analogue-to-digital-converters (ADCs). Battery current is measured using a bidirectional Hall-effect sensor, namely Allegro ACS712-20A, as depicted in Fig. 7.8.
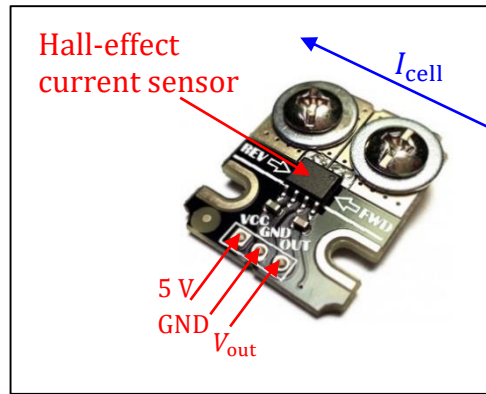
Fig. 7.8 Photograph of the 20 A Hall-effect current sensor

The current sensor generates a proportional 0-5 V analogue voltage cantered at 2.5 V, for current flows in both directions. The battery surface temperature is measured using a 10 kΩ thermistor, which is calibrated using a three-point method and the Steinhart-Hart equation [270]. The data acquisition is performed at 10 Hz. Prior to digital conversion of the analogue voltage and current signals, they are conditioned accordingly; this involves an intermediate amplification stage that ensures the input signals are within the μP's operating voltage range of 0-3.3 V; and a low-pass filter stage (f_{corner} = 1 kHz) is added to remove any high-frequency noise contents from the digital circuitry on-board the μP unit.

7.4.3 Software Configuration

The process flow-chart for the developed battery monitoring system is illustrated in Fig. 7.9. It starts by initialising the DEKF battery impedance parameters estimator and the decentralised AEKF SOC estimator, using the PRBS identification method developed in Chapter 6.

Thereafter, battery terminal data (i.e. voltage, current) are acquired and fed into the DEKF and the AEKF estimators every Δt seconds. Upon the completion of DEKF and AEKF measurement-update at time-step k, SOC, OCV and RC model parameters are estimated. Then, the updated estimates are applied to equations (7.12)-(7.14) to obtain an online estimate for the cell's SOP and SOF, respectively.
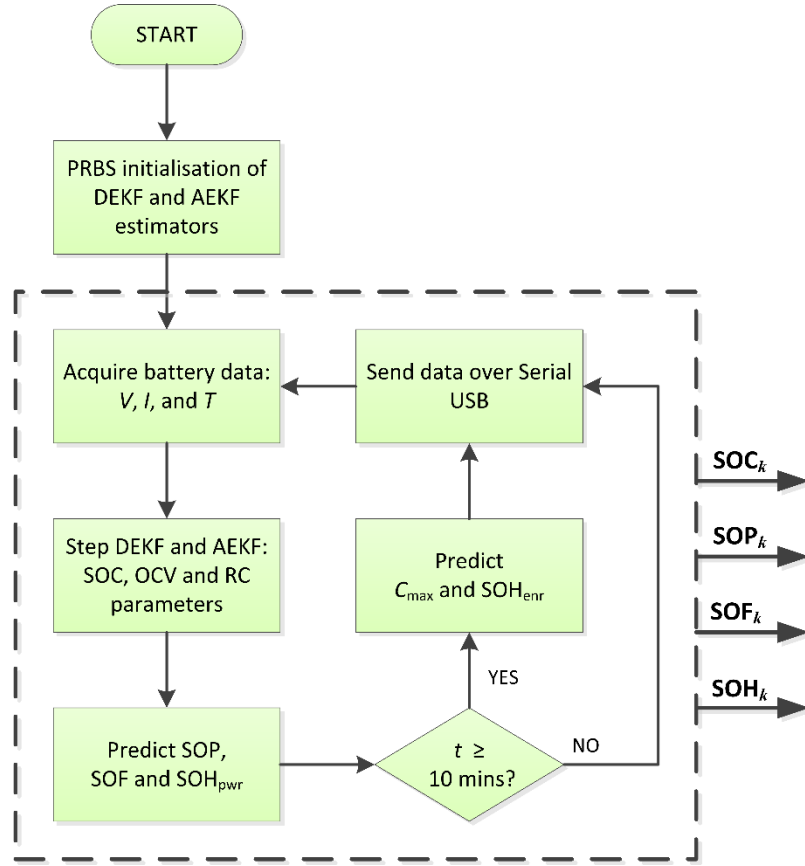
Fig. 7.9 Flow chart showing the software structure of the real-time battery states monitoring system

$$P_k^{\text{dis}} = \frac{V_{\min}\left(\widehat{V}_{\text{OC},k} - V_{\min}\right)}{\widehat{R}_{\text{s}} + \widehat{R}_1 + \widehat{R}_2} \tag{7.12}$$

$$P_k^{\text{ch}} = \frac{V_{\max}\left(V_{\max} - \widehat{V}_{\text{OC},k}\right)}{\widehat{R}_{\text{s}} + \widehat{R}_1 + \widehat{R}_2} \tag{7.13}$$

where $V_{\min}$ and $V_{\max}$ are the minimum and maximum battery threshold voltages, as specified in Table 2.5, for a safe operation of the LFP and NMC test cells. $\widehat{R}_{\text{s}}$, $\widehat{R}_1$ and $\widehat{R}_2$ are the estimates of the resistive-element RC model parameters, and $\widehat{V}_{\text{OC}}$ is an estimate of the battery's OCV at time-step k. Consequently, using (7.12) and (7.13), a power-based definition for the battery's functionality or, SOF, is developed.

227

$$SOF = \begin{cases} 1, & \text{for } P_k^{ch} \geq P_{req}^{ch} \text{ and } P_k^{dis} \geq P_{req}^{dis} \\ 0, & \text{for } P_k^{ch} < P_{req}^{ch} \text{ and } P_k^{dis} < P_{req}^{dis} \end{cases} \qquad (7.14)$$

where $P_{req}^{ch} = I_{req}^{ch} \times V_{max}$ and $P_{req}^{dis} = I_{req}^{dis} \times V_{min}$ are, respectively, the quantities of required charge or discharge power, in order to fulfil a particular task. To verify the quality of the charge and discharge SOP estimates given by (7.12) and (7.13), respectively, a similar approach to Chapter 6 is taken, where the HPPC method [198] is adopted as a means of reference framework.

Since cell capacity C_{now}^{Ah} is a very slow time-varying parameter, it is predicted every 10 minutes. The capacity estimate is then applied to equation (7.2) in order to predict the cell's energy-based SOH (i.e. SOH_{enr}) at the current time step.

7.4.4 μP Programming
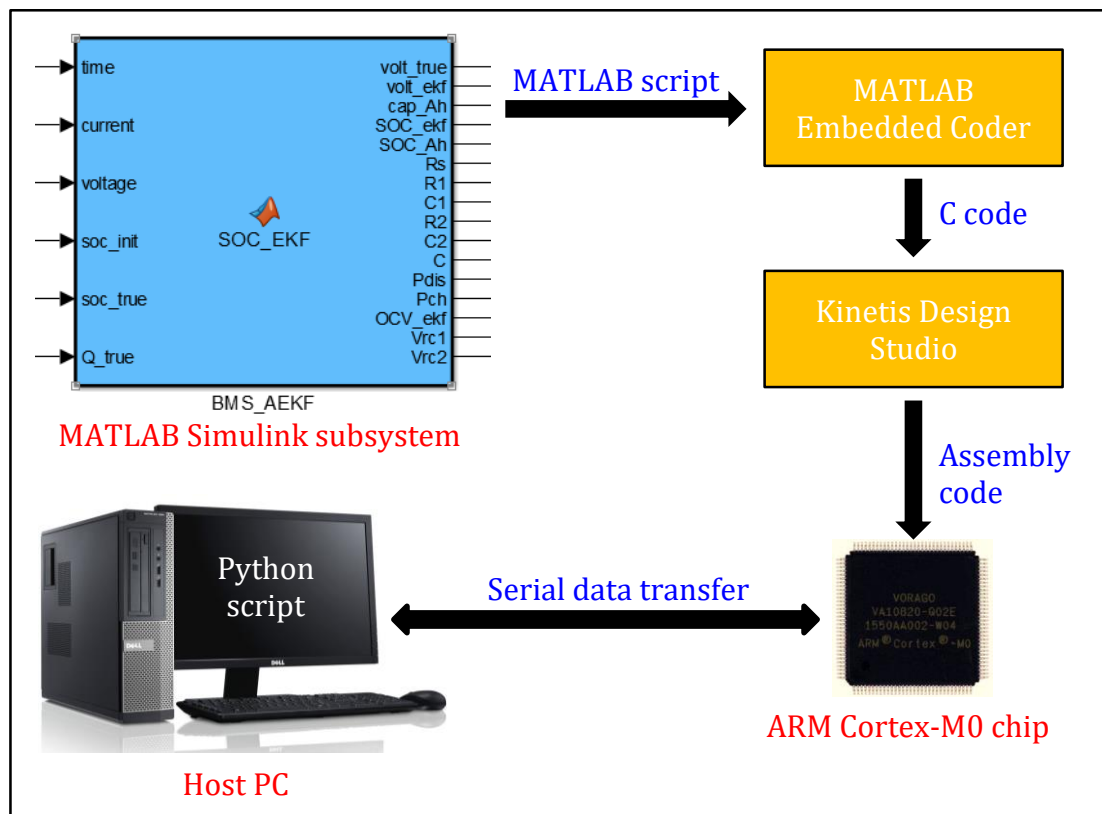
Fig. 7.10 Evolution of software code for μP programming

The developed algorithm is initially simulated using a MATLAB Simulink function block, as show in Fig. 7.10. Thereafter, the MATLAB Embedded Coder wizard is used to convert the MATLAB script into a C code, for deployment on the μP unit. The software used for transferring the C code onto the NXP μP unit was the Kinetis Design Studio. This software allows for the deployment of the generated BMS code onto the ARM Cortex-M0 processor. A script written in Python enabled to establish a serial communication between the μP unit and the host PC, for data storage and visual interface.

7.5 Experimental Results

In order to verify the performance of the battery monitoring system developed in this Chapter, the LFP and NMC test cells are applied with a dynamic EV-based Artemis drive cycle, using the multi-channel MACCOR battery tester. The resulting test profile, as presented in Fig. 7.11 is similar to that reported in Chapter 6.
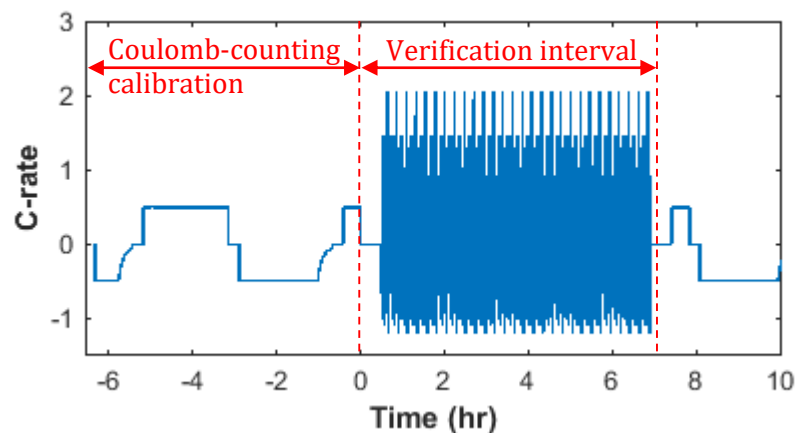
Fig. 7.11 Experimental C-rate profile employed for the verification of the developed battery states monitoring system on LFP and NMC cells

The test profile is comprised of a full charge and discharge cycle to measure the test cells' actual capacities and to calibrate the coulomb-counter used for the reference SOC (Ref. SOC) calculation. Then, using a 0.5 C discharge current, the cells are discharged from 100% to 80% SOC, which is a typical starting SOC level in applications with regenerative currents (e.g. in EVs). Once discharged to 80% SOC, a 30-minute rest period is allowed for the cells to reach a steady-state condition.

Thereafter, each test cell is applied with approximately 28 repetitions of the Artemis-based c-rate profile derived in Chapter 6, in order to dynamically discharge the cells from 80% to 20% SOC.

Fig. 7.12(a) and (b) present the cell terminal voltages measured using the MACCOR system, the EKF-estimated voltages using the developed μP-based platform, and the predicted OCVs for the NMC and LFP test cells, respectively. A zoomed-in view of the filter's performance over a single cycle is presented in Fig. 7.13. Table 7.1 provides the voltage estimation error results for the two test cells. In both cases, a satisfactory absolute error performance has been accomplished by the proposed AEKF estimator ran on the NXP μP unit.

(a)

(b)
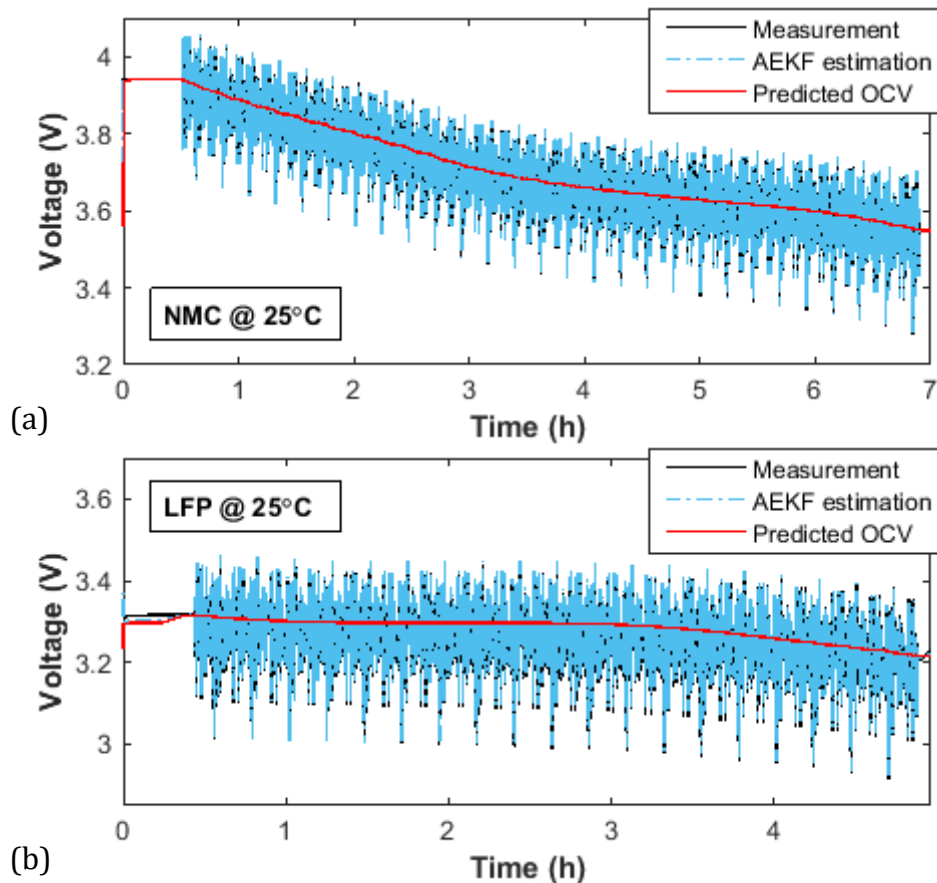
Fig. 7.12 Comparison of measured and AEKF-estimated terminal voltage and predicted OCV for the (a) NMC and (b) LFP test cells
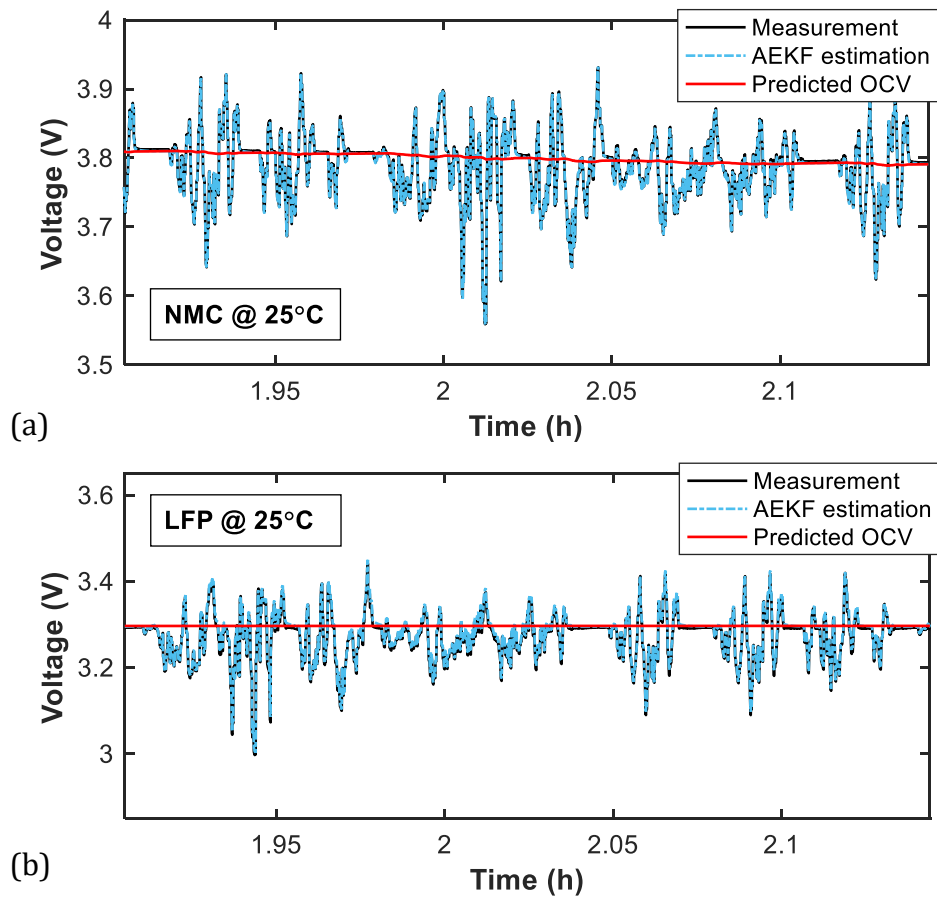
Fig. 7.13 Zoomed-in views of measured and AEKF-estimated terminal voltages for (a) NMC and (b) LFP test cells

Table 7.1 AEKF cell terminal voltage estimation performance

Cell	Max absolute error (mV)	Mean absolute error (mV)
NMC	20.9	1.3
LFP	19.2	5.2

Fig. 7.14 displays the EKF-identified resistive-element RC model parameters R_s, R_1 and R_2 and their variations with respect to SOC for both NMC and LFP cells. Generally, as SOC decreases, the over-potential gradient between the positive and negative electrodes grows.
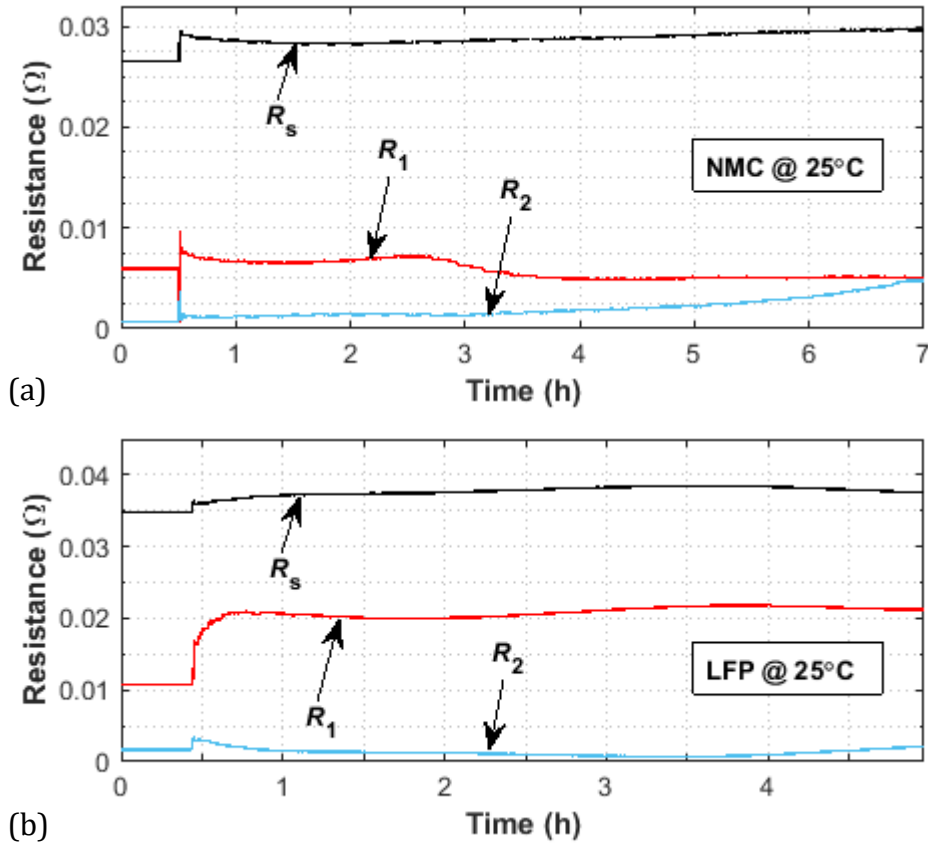
Fig. 7.14 EKF-identified resistive-element RC model parameters $\boldsymbol{R_s}$, $\boldsymbol{R_1}$ and $\boldsymbol{R_2}$ for (a) NMC and (b) LFP test cells

This explains the increasing trend of R_s as observed in Fig. 7.14(a) and (b). During the first 30 minutes, whilst the cells are in open-circuit mode, the EKF produces unrealistic estimates. This is due to the lack of persistence of excitation of the input signal. However, as soon as the load is engaged (i.e. at $t = 1800$ seconds), the algorithm starts to converge towards the 'true' estimates. It should be noted that the EKF responsible for cell parameters estimation has been initialised with the PRBS-attained RC parameters identified at SOC = 80%. For details on PRBS battery identification, the reader is referred to Chapter 6.

To verify the convergence of the proposed SOC estimator, the initial SOC for both cells has been intentionally set to an incorrect value of 20%, whilst the true SOC was 79.57% for the NMC cell and 80% for the LFP cell. Fig. 7.15 presents the estimation results for the NMC cell, whereas Table 7.2 provides the obtained error performance. As observed, the SOC given by the coulomb-counting method

gradually drifts away from the true 'Ref. SOC'. This is due to the accumulation of sensor noise during the test period. As a result, the final SOC reported by the coulomb-counting method is measured at 14%, whilst the actual SOC is at 19.47%. On the other hand, despite the noisy current measurements provided by the low-cost Hall-effect sensor (see Fig. 7.8) and the incorrect initialisation of the SOC state, the proposed AEKF estimator is capable of realising an excellent tracking of the cell's SOC. This is a significant achievement over the conventional coulomb-counting method for SOC determination in dynamic applications.

The performance of the decentralised AEKF estimator for the OCV-based SOC estimation of LFP cells is demonstrated in Fig. 7.16. Similar to the NMC case, the SOC state for the LFP filter was incorrectly initialised at 20%, whilst the true SOC was experimentally determined to be at 80%. From Fig. 7.16, it is observable that the standard DEKF algorithm fails to keep a track of the true SOC within the region of 70% to 30% SOC. Nevertheless, by updating the filter process and measurement noise statistics, the AEKF has been able to adapt to those OCV-based modelling uncertainties. This has resulted in a significant improvement in the SOC estimated online for this particular lithium-ion power cell which suffers from an inherently flat OCV curve within its linear operating voltage range (i.e. ~20-80% SOC).
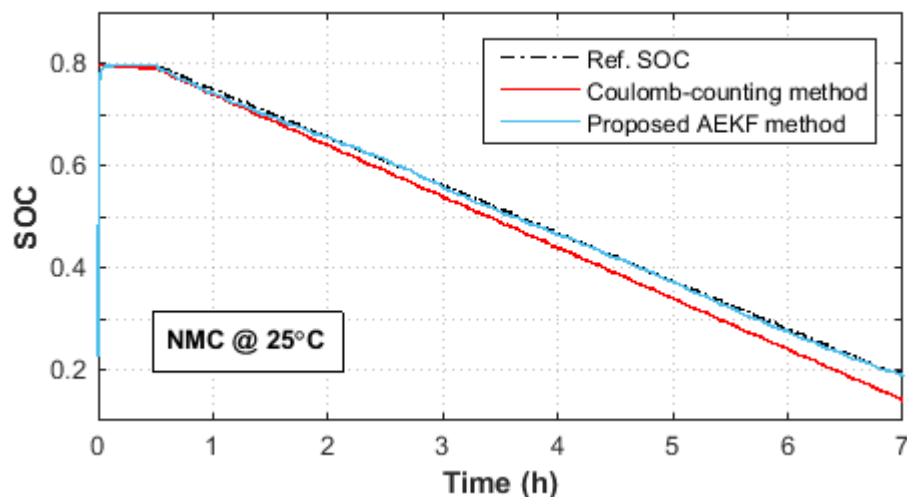
Fig. 7.15 SOC obtained for the NMC cell using the coulomb-counting and the proposed AEKF method, showing the effect of current-sensor error accumulation

Table 7.2 SOC estimation error performance for the NMC cell

Method	Max absolute error	Mean absolute error
Coulomb-counting	0.0606	0.0269
AEKF estimator	0.0111	0.0039
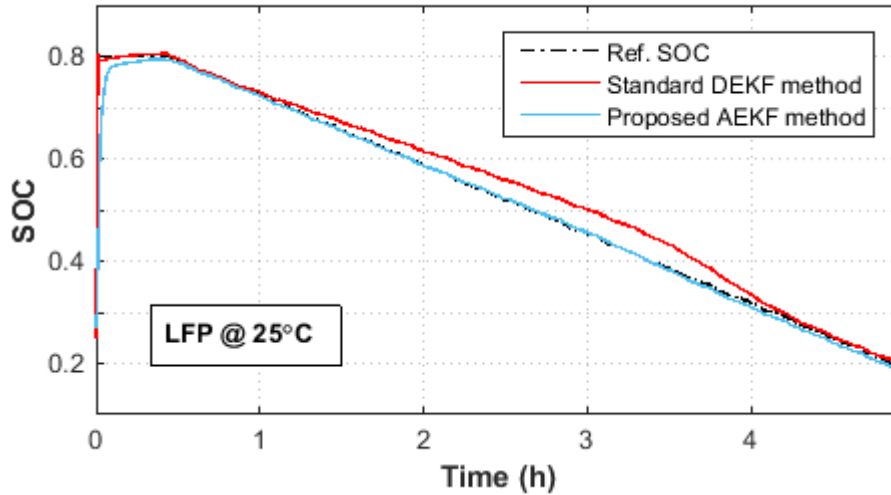
Fig. 7.16 SOC estimation results for the LFP cell, comparing the performance of the proposed AEKF method with that of the standard DEKF method

Table 7.3 SOC estimation error performance for the LFP cell

Method	Max absolute error	Mean absolute error
Standard DEKF	0.0499	0.0224
Proposed AEKF	0.0099	0.0036

In order to quantify and compare the performance of the two SOC estimation methods, a statistical analysis of SOC error has been conducted and the results are listed in Table 7.3. The errors were calculated after both filters had converged and entered an error bound of ±0.5% SOC for the first time, with respect to 'Ref. SOC' in Fig. 7.16. Respectively, the DEKF estimator has resulted in a maximum absolute SOC error of around 5%, where that calculated for the AEKF method is only 1%. Furthermore, over the SOC range of 20-80%, the AEKF method produced a SOC

estimate with a mean absolute error of less than 0.5%. Compared to the 2% mean error obtained using the standard DEKF method, this is a significant improvement of the OCV-based SOC estimation for the LFP cells.

Similar to Chapter 6, here, the HPPC method has been employed as a reference framework for the validation of the charge and discharge power estimates obtained online using the μP-based platform. Fig. 7.17 presents the cell power estimation results obtained for both the NMC and LFP cells, using the steady-state SOP definitions given by (7.12) and (7.13). For both lithium-ion cell types, the power values estimated online using the PRBS-initialised DEKF algorithm, together with the improved OCV estimates produced by the proposed decentralised AKEF method demonstrate an excellent agreement with the HPPC predictions obtained over the same SOC range. This further validates the performance of the developed battery states monitoring system for online SOP estimation of both NMC and LFP cells.

In order to estimate the test cells' current SOH levels using the definitions given in (7.1) and (7.2), the initial cell capacity and series-resistance values have been experimentally determined as $C_0^{Ah} = 3.718$ Ah and $R_0^s = 0.028\ \Omega$ for the NMC cell, and, $C_0^{Ah} = 3.037$ Ah and $R_0^s = 0.031\ \Omega$ for the LFP cell. It should be noted that the initial cell capacity was measured using the static capacity test procedure described in Chapter 2, section 2.3.2.1, whereas, the initial cell resistance was determined using the EIS method outlined in Chapter 2, section 2.3.2.2. Subsequently, using the accurately estimated SOC using the decentralised AEKF method, and the transferred coulombic charge measured using the low-cost Hall-effect current sensor during 10-minute window intervals, the capacities for both cells are predicted according to equations (7.3)-(7.5).
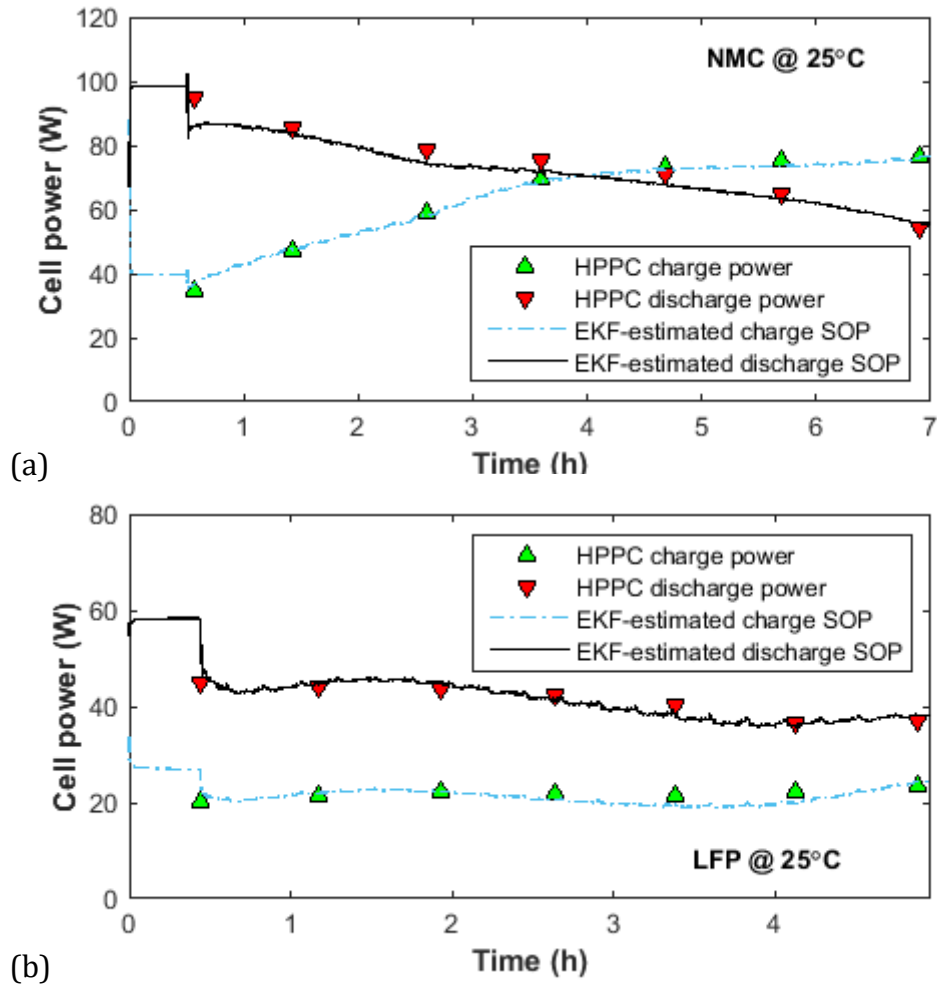
Fig. 7.17 SOP estimation results gathered online for (a) NMC and (b) LFP test cells

Fig. 7.18 presents the online capacity prediction results obtained using the μP-based platform for both NMC and LFP test cells. Note that, since cell capacity is a very slowly time-varying parameter, the algorithm takes around 90 minutes to converge to within ±5% of the actual Ah capacity for both cell types. Thus, by taking the arithmetic mean of the capacity estimates obtained after 90 minutes of operation, the capacity of the NMC cell has been estimated at $C_{now}^{Ah} = 3.627$ Ah, whereas the actual cell capacity after a full charge/discharge cycle has been determined to be at 3.642 Ah. Similarly, for the LFP cell, the ampere-hour capacity has been estimated at $C_{now}^{Ah} = 2.371$ Ah, while the actual capacity has been experimentally determined to be at 2.391 Ah.

In addition to the capacity estimates, the series resistances identified by the DEKF algorithm for both NMC and LFP cells, as presented in Fig. 7.14(a) and (b) respectively, are used to produce a power-based SOH estimate. Subsequently, by taking the arithmetic mean of the series-resistance values, R^s_{now} is determined to be at 0.029 Ω for the NMC cell and 0.038 Ω for the LFP cell.

(a)

(b)
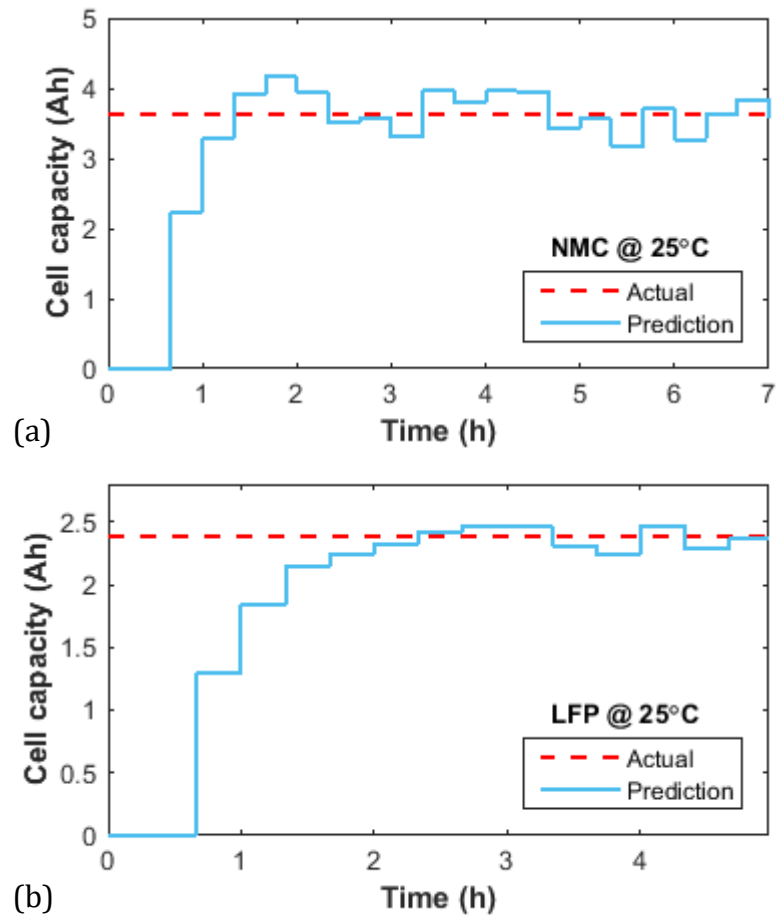
Fig. 7.18 Online capacity prediction results for SOH estimation, obtained for (a) NMC and (b) LFP test cells

Finally, by using the energy- and power-based SOH definitions given by (7.1) and (7.2), respectively, the cells' current SOH levels can be predicted. The results for both NMC and LFP test cells are presented in Table 7.4. In both cases, the predicted energy- and power-based SOH metrics very closely match the actual SOH levels calculated using the cell capacities obtained from a static capacity test. This gives further confidence to the performance capabilities of the developed low-cost battery states monitoring system for NMC and LFP variants of lithium-ion cell chemistry.

Table 7.4 SOH estimation results for the NMC and LFP test cells

Cell	Actual SOH (%)	Predicted SOH_{enr} (%)	Predicted SOH_{pwr} (%)
NMC	97.94%	97.55%	96.43%
LFP	78.72%	78.07%	77.42%

7.6 Chapter Conclusions

This Chapter reported on the development of a low-cost μP-based battery states monitoring system. The developed system consisted of an ARM Cortex-M0 processor with embedded ADCs for data acquisition and processing. The battery states of interest in this Chapter included SOC, SOP and SOH, for which two definitions were given; SOH_{enr}, which related to the energy storage capacity of the cell, and, SOH_{pwr}, which related to a fade in the battery's power capabilities. Subsequently, a technique for online prediction of battery capacity for SOH_{enr} characterisation has been proposed. the proposed technique required an accurate estimate of the battery's SOC in real time. As a result, a decentralised AEKF method for the adaptive estimation of SOC has been proposed in this Chapter. The adaptive technique is mainly beneficial to the LFP cells, whose OCV response is fairly flat within their linear operating voltage range, whereby separating the SOC state from the ordinary DEKF estimator and designing a third EKF for SOC estimation with real-time process and measurement noise covariance (i.e. Q^z and R^z), those OCV-induced modelling uncertainties can be accounted for, yielding an enhanced SOC estimate for the LFP power cells. Finally, the developed system has been experimentally verified on an NMC and LFP cell. Despite the large current sensor-drift and incorrect initialisation of the SOC state, the decentralised EKF-based estimator has posed excellent SOC, SOP and SOH tracking capabilities. This attribution is of particular interest to those applications which necessitate for an accurate knowledge of the battery's states to be available for the proper execution of various battery energy and power management strategies. Further, to prolong the battery's lifetime, the proposed system can also be utilised as a low-cost platform to perform the necessary control actions required for a safe battery operation.

Chapter 8

Conclusions and Future Work

This Chapter provides a summary of the work carried out in this thesis, discussing the role of each chapter in achieving the main objective of the thesis and the contributions made to the body of knowledge as a whole. An overall conclusion is then drawn and the scope for the future work which expand on this thesis is also set out.

8.1 Summary

The main objective of this thesis was to develop and optimise an online monitoring system for lithium-ion batteries which could adapt to changes imposed by varying operating conditions.

As set out in Chapter 1, the motivation for the work carried out in this thesis is to increase the future uptake of lithium-ion battery energy storage devices in safety-critical applications, such as in electric/hybrid-electric vehicles (EV/HEVs), unmanned aerial vehicles (UAVs) and the rapidly evolving smart grid. The battery management system BMS and its incorporated estimation algorithms is identified as one the main areas of research for improving the future adoption of these delicate energy storage devices in a wider range of power applications. Hence, this thesis puts its focus on developing a novel battery states monitoring system, whereby optimising the embedded BMS algorithms, not only the safety aspect of the battery

system will be improved through close monitoring of the battery's electrical and thermal performance, but also a better utilisation of the battery in terms of power and energy delivery can be realised.

Subsequently, to complete a coherent piece of research, the *state-of-the-art* of battery energy storage systems, including a comparative study of different battery chemistries and the employed BMS structures, as presented in literature, is reviewed in Chapter 2. At first, to familiarise the reader with the common battery terminologies used in literature, a list of those terms relevant to this thesis are provided. Then, the basic electrochemistry of battery energy storage devices is explained. Various battery technologies and their applications are discussed. Thereafter, to provide the reader with appreciation for the attributions of each chapter, a comprehensive review of the battery states of interest to a BMS, such as state-of-charge (SOC), state-of-health (SOH), state-of-power (SOP) and state-of-function (SOF) is undertaken. Various methods for direct and model-based characterisation of battery impedance parameters and the aforementioned states are discussed. Finally, the setup and procedures for experimental control and verification of the proposed battery estimation techniques in this thesis is explained.

Chapter 3 discusses the importance of SOH estimation in battery-powered applications. Subsequently, a bespoke bidirectional microprocessor-based battery power cycler, for the purpose of cycle-based SOH characterisation, is developed. Also in this Chapter, a method for the online estimation of SOH for the lithium-ion iron phosphate (LFP) cells is proposed, which is implemented on an AVR microprocessor (μP) unit. In addition, an empirical model for battery remaining-useful-life (RUL) prediction is developed, whose coefficients are calculated based on the first 3-4% of SOH degradation.

For online estimation and monitoring of various battery states (e.g. SOC), appropriate battery models must be employed. To this end, an experimental study on most commonly used battery models in both motive and stationary battery storage applications is undertaken in Chapter 4. Ten battery model structures including, the combined model, Rint model, two different hysteresis models,

Randles model, a modified Randles model, and two resistor-capacitor (*RC*) network models with and without hysteresis included are studied. The performance of each model structure is examined under various operating conditions, with respect to terminal voltage, SOC and SOP estimation accuracy. The results obtained in this Chapter suggest that an *RC* network model structure can provide the highest level of accuracy for the purpose of online battery states monitoring, when compared to other electrical equivalent-circuit battery models.

To identify the minimum order number for the chosen *RC* network battery model, a frequency-domain analysis on the complex impedance data gathered for a nickel manganese cobalt oxide (NMC) and LFP cell is conducted in Chapter 5. The results show that a 2-*RC* model structure, with two dynamic states and five identifiable parameters is an optimum choice in terms of both modelling accuracy and complexity. Then, a sensitivity analysis on the selected 2-*RC* model structure is carried out with respect to parameterisation error, in an effort to gain a better understanding of the impact of erroneous or static model parameters on the quality of the model-based battery state estimates such as SOC and SOP. The results for the sensitivity analysis conducted in this Chapter imply that for accurate model-based SOP estimates, model parameters need to be identified in real time, in parallel to the battery's SOC. This is to ensure that any changes in the battery parameters caused by varying operating conditions (e.g. ambient temperature) are accounted for.

In Chapter 6, a novel hybrid battery identification technique is proposed to identify the parameters of the selected 2-*RC* network battery model, in an adaptive deterministic fashion. The proposed technique is comprised of a carefully designed pseudorandom binary sequences (PRBS), which is used to properly excite the battery under test over a prescribed frequency band. The 2-*RC* battery model parameters are then extracted form from the measured complex impedance data using a nonlinear least-squares method. The identified parameters are then used to correctly and deterministically initialise a Dual Extended Kalman Filter (DEKF) algorithm, in an effort to capture any variations imposed on the battery under real-time operation, due to SOC modification and/or varying operating conditions such as the ambient temperature. The proposed hybrid battery identification technique

is then applied to online SOP estimation for both NMC and LFP test cells used in this thesis. The standard hybrid-pulse-power-characterisation (HPPC) test is used as a reference framework for the verification of the online battery SOP estimation technique.

The battery's open-circuit voltage (OCV) forms the basis for many real-time battery SOC estimation algorithms. For most battery chemistries, a pre-determined OCV-SOC relationship can be employed to provide a good estimate of the battery's SOC. However, for the LFP cell chemistry, the OCV curve obtained over the battery's linear operating voltage range is fairly flat, which makes it difficult to realise an accurate SOC estimate for this particular lithium-ion cell variant. Thus, as result, a decentralised EKF framework is put forward in Chapter 7 to adaptively estimate SOC by predicting the filter's process and measurement noise covariance in real time. in addition, a dynamic battery SOH estimation technique is also proposed in this Chapter, which is computationally light and unlike the method developed in Chapter 3, the SOH obtained using this method is directly related to the battery's ampere-hour capacity fade. Finally, the battery SOC, SOH and SOP estimation techniques developed throughout this thesis are all brought together and implemented on an ARM Cotex-M0 μP unit, to give realisation to a low-cost adaptive battery states monitoring system.

8.2 Thesis Conclusions

This thesis aimed to develop an adaptive battery monitoring system to increase the future uptake of battery energy storage devices for safety-critical applications (e.g. EV/HEVs and UAVs), and also to make lithium-ion batteries a safer and more appealing choice for a wider range of battery-powered applications. As a result, a range of online techniques for adaptive estimation of battery states, such as SOC, SOP and SOH were developed to improve upon the *state-of-the-art* of BMS algorithms presented in literature and to achieve the aforementioned objectives. This thesis contributed to the body of knowledge through the advancement of the standard dual-EKF method, which is commonly used in modern BMS algorithms for online battery impedance parameters and SOC estimation. Subsequently, a hybrid battery parameters identification technique based on the PRBS-initialisation of the

dual-EKF estimator was developed. In addition, a decentralised adaptive EKF framework was proposed for the enhancement of SOC estimation for those battery chemistries (e.g. LFP) whose OCV-SOC relationships are inherently flat. Although the techniques developed in this thesis were only tested on two cylindrical variants of lithium-ion battery chemistry (i.e. NMC and LFP), the governing equations are generic and non-specific to any particular battery chemistry. Therefore, with a few minor modifications to certain chemistry-specific model parameters, such as the coefficients of the OCV-SOC polynomial function, the techniques presented herein can be applied to other battery designs/chemistries.

Collectively, the proposed techniques in this thesis will allow for a better utilisation of lithium-ion batteries by continuously monitoring their health and the power capabilities, without the need for laborious and time-consuming characterisation tests which are non-ideal in a practical sense. Ultimately, the future uptake of lithium-ion batteries in applications where battery and consumer safety are of main priority can be improved. This is facilitated by the enhanced estimation of SOC and battery impedance parameters, which are vital to correct characterisation of available battery power, or SOP, in real time. In situations where the battery is likely to experience an over-charge or discharge condition due to lack of knowledge of the internal battery parameters, the proposed techniques in this thesis will allow the BMS to take a more rational control decision, preventing the battery from an internal permanent damage, whilst delivering its maximum power; thus, improving the battery's overall performance and possibly its service lifetime in the long run.

8.3 Scope for Future Work

Although a conclusive body of work has been presented herein and benefits offered over the state of the art, there are areas which this thesis can expand on. Moreover, the techniques presented in this thesis can be employed to answer some of the research questions raised in other electrical energy storage problems, especially in the rapidly-evolving smart grid and vehicle-to-grid (V2G) technologies [271]. The list below summarises the scope for future work which can lead on from this thesis.

- Application of the developed battery states monitoring system to series and/or parallel connected cells in the form of a large battery pack;
- Application of the hybrid system identification technique to other electrochemical energy storage devices, e.g. supercapacitors;
- Application of the proposed adaptive system identification technique to sensor-less estimation of constituent cells in large-scale grid-tie battery energy storage systems
- Application of the developed battery impedance identification technique to sensor-less thermal characterisation of large-scale battery energy storage systems;
- Feasibility of a smart cell architecture for distributed energy/power management of large-scale battery energy storage systems using the developed on-chip battery monitoring system

REFERENCES

[1]   Wikipedia, "Boeing 787 Dreamliner battery problems." [Online]. Available: https://en.wikipedia.org/wiki/Boeing_787_Dreamliner_battery_problems. [Accessed: 10-Apr-2017].

[2]   L. Lu, X. Han, J. Li, J. Hua, and M. Ouyang, "A review on the key issues for lithium-ion battery management in electric vehicles," *J. Power Sources*, vol. 226, pp. 272–288, 2013.

[3]   C. C. Chan, "The state of the art of electric, hybrid, and fuel cell vehicles," *Proc. IEEE*, vol. 95, no. 4, pp. 704–718, 2007.

[4]   A. S. Gohardani, G. Doulgeris, and R. Singh, "Challenges of future aircraft propulsion: A review of distributed propulsion technology and its potential application for the all electric commercial aircraft," *Prog. Aerosp. Sci.*, vol. 47, no. 5, pp. 369–391, 2011.

[5]   D. Linden and T. B. Reddy, *Linden's Handbook of Batteries*, Fourth. New York: McGraw-Hill Education, 2010.

[6]   T. F. Barak M, Dickinson T, Falk U, Sudworth HR, *Electrochemical Power Sources: Primary & Secondary Batteries*, IEEE Energ. Exeter: A. Wheaton & Co, 1980.

[7]   S. W. Swogger, P. Everill, D. P. Dubey, and N. Sugumaran, "Discrete carbon nanotubes increase lead acid battery charge acceptance and performance," *J. Power Sources*, vol. 261, pp. 55–63, 2014.

[8]   P. T. Moseley, R. F. Nelson, and A. F. Hollenkamp, "The role of carbon in valve-regulated lead--acid battery technology," *J. Power Sources*, vol. 157, no. 1, pp. 3–10, 2006.

[9]   M. Saravanan, M. Ganesan, and S. Ambalavanan, "An in situ generated carbon as integrated conductive additive for hierarchical negative plate of lead-acid battery," *J. Power Sources*, vol. 251, pp. 20–29, 2014.

[10]   R. T. B. Linden David, *Handbook of Batteries*, Third. McGraw-Hill, 2000.

[11]   R. A. K. Bockris John O'M, *Modern Electrochemistry 2B*. New York, NY: Springer, 2000.

[12]   F. L. R. Bard Allen J, *Electrochemical Methods: Fundamentals and Applications*, Second. John Wiley & Sons, Inc., 1980.

[13] G. Ning, R. E. White, and B. N. Popov, "A generalized cycle life model of rechargeable Li-ion batteries," *Electrochim. Acta*, vol. 51, no. 10, pp. 2012–2022, Feb. 2006.

[14] P. T. Moseley, J. Garche, and C. D. Parker, *Valve-regulated lead-acid batteries*. Elsevier, 2004.

[15] J. F. Cole, "Battery energy-storage systems — an emerging market for lead/acid batteries," *J. Power Sources*, vol. 53, no. 2, pp. 239–243, Feb. 1995.

[16] D. H. Doughty, P. C. Butler, A. A. Akhil, N. H. Clark, and J. D. Boyes, "Batteries for large-scale stationary electrical energy storage," *Electrochem. Soc. Interface*, vol. 19, no. 3, pp. 49–53, 2010.

[17] J. Bishop, A. Nedungadi, G. Ostrowski, B. Surampudi, P. Armiroli, and E. Taspinar, "An engine start/stop system for improved fuel economy," 2007.

[18] H. Chen, T. N. Cong, W. Yang, C. Tan, Y. Li, and Y. Ding, "Progress in electrical energy storage system: A critical review," *Prog. Nat. Sci.*, vol. 19, no. 3, pp. 291–312, 2009.

[19] A. Shukla, "Nickel-based rechargeable batteries," *J. Power Sources*, vol. 100, no. 1–2, pp. 125–148, Nov. 2001.

[20] M. A. Fetcenko *et al.*, "Recent advances in NiMH battery technology," *J. Power Sources*, vol. 165, no. 2, pp. 544–551, 2007.

[21] A. Poullikkas, "A comparative overview of large-scale battery systems for electricity storage," *Renew. Sustain. Energy Rev.*, vol. 27, pp. 778–788, 2013.

[22] R. J. Bones, D. A. Teagle, S. D. Brooker, and F. L. Cullen, "Development of a Ni, NiCl2 positive electrode for a liquid sodium (ZEBRA) battery cell," *J. Electrochem. Soc.*, vol. 136, no. 5, pp. 1274–1277, 1989.

[23] M. Kamibayashi and K. Tanaka, "Recent sodium sulfur battery applications," in *Transmission and Distribution Conference and Exposition, 2001 IEEE/PES*, 2001, vol. 2, pp. 1169–1173 vol.2.

[24] F. Beck and P. Rüetschi, "Rechargeable batteries with aqueous electrolytes," *Electrochim. Acta*, vol. 45, no. 15, pp. 2467–2482, 2000.

[25] C. J. Rydh and B. Svärd, "Impact on global metal flows arising from the use of portable rechargeable batteries," *Sci. Total Environ.*, vol. 302, no. 1, pp. 167–184, 2003.

[26] J. Baker, "New technology and possible advances in energy storage," *Energy*

Policy, vol. 36, no. 12, pp. 4368–4373, 2008.

[27]   A. Parasuraman, T. M. Lim, C. Menictas, and M. Skyllas-Kazacos, "Review of material research and development for vanadium redox flow battery applications," *Electrochim. Acta*, vol. 101, pp. 27–40, 2013.

[28]   S. J. Dillon and K. Sun, "Microstructural design considerations for Li-ion battery systems," *Curr. Opin. Solid State Mater. Sci.*, vol. 16, no. 4, pp. 153–162, Aug. 2012.

[29]   H. Rahimi-Eichi, U. Ojha, F. Baronti, and M. Y. Chow, "Battery Management System: An Overview of Its Application in the Smart Grid and Electric Vehicles," *IEEE Ind. Electron. Mag.*, vol. 7, no. 2, pp. 4–16, Jun. 2013.

[30]   N. Omar *et al.*, "Assessment of performance of lithium iron phosphate oxide, nickel manganese cobalt oxide and nickel cobalt aluminum oxide based cells for using in plug-in battery electric vehicle applications," in *2011 IEEE Vehicle Power and Propulsion Conference*, 2011, pp. 1–7.

[31]   A. J. Cavallo, "Energy storage technologies for utility scale intermittent renewable energy systems," *J. Sol. energy Eng.*, vol. 123, no. 4, pp. 387–389, 2001.

[32]   A. Väyrynen and J. Salminen, "Lithium ion battery production," *J. Chem. Thermodyn.*, vol. 46, no. 0, pp. 80–85, 2012.

[33]   T. Dong, X. Wei, and H. Dai, "Research on high-precision data acquisition and SOC calibration method for power battery," in *2008 IEEE Vehicle Power and Propulsion Conference*, 2008, pp. 1–5.

[34]   Y. Xiao, "Model-Based Virtual Thermal Sensors for Lithium-Ion Battery in EV Applications," *IEEE Trans. Ind. Electron.*, vol. 62, no. 5, pp. 3112–3122, May 2015.

[35]   Y. Wang, Z. Han, and J. Shi, "One cell Lithium-ion battery protection IC," in *2014 9th IEEE Conference on Industrial Electronics and Applications*, 2014, pp. 1427–1432.

[36]   J.-H. Lee and J. Sung, "Design of battery protection circuit," in *Intelligent Signal Processing and Communication Systems, 2004. ISPACS 2004. Proceedings of 2004 International Symposium on*, 2004, pp. 784–786.

[37]   Z. Ye, X. Wu, Y. Sun, and J. Lu, "A Universal Protection Controller for Li-ion Battery Charger," in *2010 Asia-Pacific Power and Energy Engineering Conference*, 2010, pp. 1–4.

[38] I. Aizpuru, U. Iraola, J. M. Canales, M. Echeverria, and I. Gil, "Passive balancing design for Li-ion battery packs based on single cell experimental tests for a CCCV charging mode," in *Clean Electrical Power (ICCEP), 2013 International Conference on*, 2013, pp. 93–98.

[39] K. Vitols, "Design of an embedded battery management system with passive balancing," in *Education and Research Conference (EDERC), 2014 6th European Embedded Design in*, 2014, pp. 142–146.

[40] M. Y. Kim, C. H. Kim, J. H. Kim, and G. W. Moon, "A Chain Structure of Switched Capacitor for Improved Cell Balancing Speed of Lithium-Ion Batteries," *IEEE Trans. Ind. Electron.*, vol. 61, no. 8, pp. 3989–3999, Aug. 2014.

[41] T. Morstyn, M. Momayyezan, B. Hredzak, and V. Agelidis, "Distributed Control for State of Charge Balancing Between the Modules of a Reconfigurable Battery Energy Storage System," *IEEE Trans. Power Electron.*, vol. PP, no. 99, p. 1, 2016.

[42] W. Huang and J. A. A. Qahouq, "Energy Sharing Control Scheme for State-of-Charge Balancing of Distributed Battery Energy Storage System," *IEEE Trans. Ind. Electron.*, vol. 62, no. 5, pp. 2764–2776, May 2015.

[43] Z. Rao and S. Wang, "A review of power battery thermal energy management," *Renew. Sustain. Energy Rev.*, vol. 15, no. 9, pp. 4554–4571, 2011.

[44] X. M. Xu and R. He, "Research on the heat dissipation performance of battery pack based on forced air cooling," *J. Power Sources*, vol. 240, pp. 33–41, 2013.

[45] M. R. Giuliano, A. K. Prasad, and S. G. Advani, "Experimental study of an air-cooled thermal management system for high capacity lithium--titanate batteries," *J. Power Sources*, vol. 216, pp. 345–352, 2012.

[46] L. Fan, J. M. Khodadadi, and A. A. Pesaran, "A parametric study on thermal management of an air-cooled lithium-ion battery module for plug-in hybrid electric vehicles," *J. Power Sources*, vol. 238, pp. 301–312, 2013.

[47] A. A. Pesaran, S. Burch, and M. Keyser, "An approach for designing thermal management systems for electric and hybrid vehicle battery packs," *Proc. 4th Veh. Therm. Manag. Syst.*, pp. 24–27, 1999.

[48] S. C. Kim, J. P. Won, Y. S. Park, T. W. Lim, and M. S. Kim, "Performance evaluation of a stack cooling system using CO 2 air conditioner in fuel cell vehicles," *Int. J. Refrig.*, vol. 32, no. 1, pp. 70–77, 2009.

[49] C.-V. Hémery, F. Pra, J.-F. Robin, and P. Marty, "Experimental performances of a battery thermal management system using a phase change material," *J.*

Power Sources, vol. 270, pp. 349–358, 2014.

[50] S.-G. Jeong, O. Chung, S. Yu, S. Kim, and S. Kim, "Improvement of the thermal properties of Bio-based PCM using exfoliated graphite nanoplatelets," *Sol. Energy Mater. Sol. Cells*, vol. 117, pp. 87–92, 2013.

[51] Z. G. Qu, W. Q. Li, and W. Q. Tao, "Numerical model of the passive thermal management system for high-power lithium ion battery by using porous metal foam saturated with phase change material," *Int. J. Hydrogen Energy*, vol. 39, no. 8, pp. 3904–3913, 2014.

[52] C. Alaoui, "Solid-State Thermal Management for Lithium-Ion EV Batteries," *IEEE Trans. Veh. Technol.*, vol. 62, no. 1, pp. 98–107, Jan. 2013.

[53] R. Zhao, S. Zhang, J. Gu, J. Liu, S. Carkner, and E. Lanoue, "An experimental study of lithium ion battery thermal management using flexible hydrogel films," *J. Power Sources*, vol. 255, pp. 29–36, 2014.

[54] H. Zhou, T. Bhattacharya, D. Tran, T. S. T. Siew, and A. M. Khambadkone, "Composite Energy Storage System Involving Battery and Ultracapacitor With Dynamic Energy Management in Microgrid Applications," *IEEE Trans. Power Electron.*, vol. 26, no. 3, pp. 923–930, Mar. 2011.

[55] M. E. Glavin, P. K. W. Chan, S. Armstrong, and W. G. Hurley, "A stand-alone photovoltaic supercapacitor battery hybrid energy storage system," in *Power Electronics and Motion Control Conference, 2008. EPE-PEMC 2008. 13th*, 2008, pp. 1688–1695.

[56] Z. Guoju, T. Xisheng, and Q. Zhiping, "Research on battery supercapacitor hybrid storage and its application in microgrid," in *Power and Energy Engineering Conference (APPEEC), 2010 Asia-Pacific*, 2010, pp. 1–4.

[57] M. Koot, J. T. B. A. Kessels, B. de Jager, W. P. M. H. Heemels, P. P. J. van den Bosch, and M. Steinbuch, "Energy management strategies for vehicular electric power systems," *IEEE Trans. Veh. Technol.*, vol. 54, no. 3, pp. 771–782, May 2005.

[58] A. Urtasun, E. L. Barrios, P. Sanchis, and L. Marroyo, "Frequency-Based Energy-Management Strategy for Stand-Alone Systems With Distributed Battery Storage," *IEEE Trans. Power Electron.*, vol. 30, no. 9, pp. 4794–4808, Sep. 2015.

[59] R. J. Wai, S. J. Jhung, J. J. Liaw, and Y. R. Chang, "Intelligent Optimal Energy Management System for Hybrid Power Sources Including Fuel Cell and Battery," *IEEE Trans. Power Electron.*, vol. 28, no. 7, pp. 3231–3244, Jul. 2013.

[60] P. Thounthong, S. Raël, and B. Davat, "Energy management of fuel cell/battery/supercapacitor hybrid power source for vehicle applications," *J. Power Sources*, vol. 193, no. 1, pp. 376–385, 2009.

[61] C. Fleischer, W. Waag, H.-M. Heyn, and D. U. Sauer, "On-line adaptive battery impedance parameter and state estimation considering physical principles in reduced order equivalent circuit battery models: Part 1. Requirements, critical review of methods and modeling," *J. Power Sources*, vol. 260, pp. 276–291, 2014.

[62] J. H. Aylor, A. Thieme, and B. W. Johnso, "A battery state-of-charge indicator for electric wheelchairs," *IEEE Trans. Ind. Electron.*, vol. 39, no. 5, pp. 398–409, Oct. 1992.

[63] Y. Yang, J. Liu, and C. Tsai, "Improved estimation of residual capacity of batteries for electric vehicles," *J. Chinese Inst. Eng.*, vol. 31, no. 2, pp. 313–322, 2008.

[64] W. Waag and D. U. Sauer, "Adaptive estimation of the electromotive force of the lithium-ion battery after current interruption for an accurate state-of-charge and capacity determination," *Appl. Energy*, vol. 111, pp. 416–427, 2013.

[65] V. Pop, H. J. Bergveld, D. Danilov, P. P. L. Regtien, and P. H. L. Notten, *Battery management systems: Accurate state-of-charge indication for battery-powered applications*, vol. 9. Springer Science & Business Media, 2008.

[66] V. Coroban, I. Boldea, and F. Blaabjerg, "A novel on-line state-of-charge estimation algorithm for valve regulated lead-acid batteries used in hybrid electric vehicles," in *Electrical Machines and Power Electronics, 2007. ACEMP '07. International Aegean Conference on*, 2007, pp. 39–46.

[67] H. J. Bergveld, V. Pop, and P. H. L. Notten, "Method of estimating the State-of-Charge and of the use time left of a rechageable battery, and apparatus for executing such a method." Google Patents, 2005.

[68] H. Blanke *et al.*, "Impedance measurements on lead–acid batteries for state-of-charge, state-of-health and cranking capability prognosis in electric and hybrid electric vehicles," *J. Power Sources*, vol. 144, no. 2, pp. 418–425, 2005.

[69] A. Zenati, P. Desprez, H. Razik, and S. Rael, "Impedance measurements combined with the fuzzy logic methodology to assess the SOC and SOH of lithium-ion cells," in *2010 IEEE Vehicle Power and Propulsion Conference*, 2010, pp. 1–6.

[70] A. H. Ranjbar, A. Banaei, A. Khoobroo, and B. Fahimi, "Online Estimation of

State of Charge in Li-Ion Batteries Using Impulse Response Concept," *Smart Grid, IEEE Trans.*, vol. 3, no. 1, pp. 360–367, Mar. 2012.

[71]   S. Rodrigues, N. Munichandraiah, and A. K. Shukla, "A review of state-of-charge indication of batteries by means of a.c. impedance measurements," *J. Power Sources*, vol. 87, no. 1, pp. 12–20, 2000.

[72]   J. Xu, C. C. Mi, B. Cao, and J. Cao, "A new method to estimate the state of charge of lithium-ion batteries based on the battery impedance model," *J. Power Sources*, vol. 233, pp. 277–284, 2013.

[73]   W. Waag, S. Käbitz, and D. U. Sauer, "Experimental investigation of the lithium-ion battery impedance characteristic at various conditions and aging states and its influence on the application," *Appl. Energy*, vol. 102, pp. 885–897, 2013.

[74]   S. Nejad, D. T. Gladwin, and D. A. Stone, "Sensitivity of lumped parameter battery models to constituent parallel-RC element parameterisation error," in *Industrial Electronics Society, IECON 2014 - 40th Annual Conference of the IEEE*, 2014, pp. 5660–5665.

[75]   M. Coleman, C. K. Lee, C. Zhu, and W. G. Hurley, "State-of-Charge Determination From EMF Voltage Estimation: Using Impedance, Terminal Voltage, and Current for Lead-Acid and Lithium-Ion Batteries," *Ind. Electron. IEEE Trans.*, vol. 54, no. 5, pp. 2550–2557, Oct. 2007.

[76]   H. He, R. Xiong, and J. Fan, "Evaluation of Lithium-Ion Battery Equivalent Circuit Models for State of Charge Estimation by an Experimental Approach," *Energies*, vol. 4, no. 12, pp. 582–598, Mar. 2011.

[77]   F. Baronti *et al.*, "State-of-charge estimation enhancing of lithium batteries through a temperature-dependent cell model," in *Applied Electronics (AE), 2011 International Conference on*, 2011, pp. 1–5.

[78]   R. Xiong, H. He, F. Sun, X. Liu, and Z. Liu, "Model-based state of charge and peak power capability joint estimation of lithium-ion battery in plug-in hybrid electric vehicles," *J. Power Sources*, vol. 229, pp. 159–169, 2013.

[79]   J. Li, J. Klee Barillas, C. Guenther, and M. A. Danzer, "A comparative study of state of charge estimation algorithms for LiFePO4 batteries used in electric vehicles," *J. Power Sources*, vol. 230, pp. 244–250, 2013.

[80]   M. Gholizadeh and F. R. Salmasi, "Estimation of state of charge, unknown nonlinearities, and state of health of a lithium-ion battery based on a comprehensive unobservable model," *IEEE Trans. Ind. Electron.*, vol. 61, no. 3, pp. 1335–1344, 2014.

[81] H. Chaoui, N. Golbon, I. Hmouz, R. Souissi, and S. Tahar, "Lyapunov-Based Adaptive State of Charge and State of Health Estimation for Lithium-Ion Batteries," *IEEE Trans. Ind. Electron.*, vol. 62, no. 3, pp. 1610–1618, Mar. 2015.

[82] Y. Wang, H. Fang, Z. Sahinoglu, T. Wada, and S. Hara, "Adaptive Estimation of the State of Charge for Lithium-Ion Batteries: Nonlinear Geometric Observer Approach," *IEEE Trans. Control Syst. Technol.*, vol. 23, no. 3, pp. 948–962, May 2015.

[83] S. Dey, B. Ayalew, and P. Pisu, "Nonlinear Robust Observers for State-of-Charge Estimation of Lithium-Ion Cells Based on a Reduced Electrochemical Model," *IEEE Trans. Control Syst. Technol.*, vol. 23, no. 5, pp. 1935–1942, Sep. 2015.

[84] C. Zhang, L. Y. Wang, X. Li, W. Chen, G. G. Yin, and J. Jiang, "Robust and Adaptive Estimation of State of Charge for Lithium-Ion Batteries," *IEEE Trans. Ind. Electron.*, vol. 62, no. 8, pp. 4948–4957, Aug. 2015.

[85] D. Kim, K. Koo, J. J. Jeong, T. Goh, and S. W. Kim, "Second-Order Discrete-Time Sliding Mode Observer for State of Charge Determination Based on a Dynamic Resistance Li-Ion Battery Model," *Energies*, vol. 6, no. 10, p. 5538, 2013.

[86] L. Liu, L. Y. Wang, Z. Chen, C. Wang, F. Lin, and H. Wang, "Integrated System Identification and State-of-Charge Estimation of Battery Systems," *IEEE Trans. Energy Convers.*, vol. 28, no. 1, pp. 12–23, Mar. 2013.

[87] X. Chen, W. Shen, Z. Cao, and A. Kapoor, "A novel approach for state of charge estimation based on adaptive switching gain sliding mode observer in electric vehicles," *J. Power Sources*, vol. 246, pp. 667–678, 2014.

[88] H. Rahimi-Eichi, F. Baronti, and M.-Y. Chow, "Online Adaptive Parameter Identification and State-of-Charge Coestimation for Lithium-Polymer Battery Cells," *Ind. Electron. IEEE Trans.*, vol. 61, no. 4, pp. 2053–2061, Apr. 2014.

[89] M. Verbrugge and E. Tate, "Adaptive state of charge algorithm for nickel metal hydride batteries including hysteresis phenomena," *J. Power Sources*, vol. 126, no. 1–2, pp. 236–249, Feb. 2004.

[90] F. Auger, M. Hilairet, J. M. Guerrero, E. Monmasson, T. Orlowska-Kowalska, and S. Katsura, "Industrial Applications of the Kalman Filter: A Review," *Ind. Electron. IEEE Trans.*, vol. 60, no. 12, pp. 5458–5471, Dec. 2013.

[91] A. El Mejdoubi, A. Oukaour, H. Chaoui, H. Gualous, J. Sabor, and Y. Slamani, "State-of-Charge and State-of-Health Lithium-Ion Batteries' Diagnosis According to Surface Temperature Variation," *IEEE Trans. Ind. Electron.*, vol. 63, no. 4, pp. 2391–2402, Apr. 2016.

[92] C. R. Gould, C. M. Bingham, D. A. Stone, and P. Bentley, "New battery model and state-of-health determination through subspace parameter estimation and state-observer techniques," *IEEE Trans. Veh. Technol.*, vol. 58, no. 8, pp. 3905–3916, Oct. 2009.

[93] Z. Chen, Y. Fu, and C. C. Mi, "State of Charge Estimation of Lithium-Ion Batteries in Electric Drive Vehicles Using Extended Kalman Filtering," *IEEE Trans. Veh. Technol.*, vol. 62, no. 3, pp. 1020–1030, Mar. 2013.

[94] J. Kim, S. Lee, and B. H. Cho, "Complementary Cooperation Algorithm Based on DEKF Combined With Pattern Recognition for SOC/Capacity Estimation and SOH Prediction," *Power Electron. IEEE Trans.*, vol. 27, no. 1, pp. 436–451, Jan. 2012.

[95] C. Hu, B. D. Youn, and J. Chung, "A multiscale framework with extended Kalman filter for lithium-ion battery SOC and capacity estimation," *Appl. Energy*, vol. 92, pp. 694–704, Apr. 2012.

[96] B. S. Bhangu, P. Bentley, D. A. Stone, and C. M. Bingham, "Observer techniques for estimating the state-of-charge and state-of-health of VRLABs for hybrid electric vehicles," in *Vehicle Power and Propulsion, 2005 IEEE Conference*, 2005, p. 10 pp.-pp.

[97] J. Kim and B.-H. Cho, "State-of-Charge Estimation and State-of-Health Prediction of a Li-Ion Degraded Battery Based on an EKF Combined With a Per-Unit System," *Veh. Technol. IEEE Trans.*, vol. 60, no. 9, pp. 4249–4260, Nov. 2011.

[98] S. Yuan, H. Wu, and C. Yin, "State of Charge Estimation Using the Extended Kalman Filter for Battery Management Systems Based on the ARX Battery Model," *Energies*, vol. 6, no. 1, p. 444, 2013.

[99] X. Hu, S. Li, H. Peng, and F. Sun, "Robustness analysis of State-of-Charge estimation methods for two types of Li-ion batteries," *J. Power Sources*, vol. 217, pp. 209–219, 2012.

[100] R. Xiong, F. Sun, Z. Chen, and H. He, "A data-driven multi-scale extended Kalman filtering based parameter and state estimation approach of lithium-ion olymer battery in electric vehicles," *Appl. Energy*, vol. 113, pp. 463–476, 2014.

[101] H. Aung, K. S. Low, and S. T. Goh, "State-of-Charge Estimation of Lithium-Ion Battery Using Square Root Spherical Unscented Kalman Filter (Sqrt-UKFST) in Nanosatellite," *IEEE Trans. Power Electron.*, vol. 30, no. 9, pp. 4774–4783, Sep. 2015.

[102] J. Meng, G. Luo, and F. Gao, "Lithium Polymer Battery State-of-Charge Estimation Based on Adaptive Unscented Kalman Filter and Support Vector Machine," *IEEE Trans. Power Electron.*, vol. 31, no. 3, pp. 2226–2238, Mar. 2016.

[103] G. L. Plett, "Sigma-point Kalman filtering for battery management systems of LiPB-based HEV battery packs," *J. Power Sources*, vol. 161, no. 2, pp. 1369–1384, Oct. 2006.

[104] Z. He, M. Gao, C. Wang, L. Wang, and Y. Liu, "Adaptive State of Charge Estimation for Li-Ion Batteries Based on an Unscented Kalman Filter with an Enhanced Battery Model," *Energies*, vol. 6, no. 8, p. 4134, 2013.

[105] Y. Xing, W. He, M. Pecht, and K. L. Tsui, "State of charge estimation of lithium-ion batteries using the open-circuit voltage at various ambient temperatures," *Appl. Energy*, vol. 113, pp. 106–115, 2014.

[106] G. L. Plett, "Sigma-point Kalman filtering for battery management systems of LiPB-based HEV battery packs. Part 1: Introduction and state estimation," *J. Power Sources*, vol. 161, no. 2, pp. 1356–1368, 2006.

[107] Liye Wang, Lifang Wang, Chenglin Liao, and Jun Liu, "Sigma-point Kalman filter application on estimating battery SOC," in *2009 IEEE Vehicle Power and Propulsion Conference*, 2009, pp. 1592–1595.

[108] R. Xiong, H. He, F. Sun, and K. Zhao, "Evaluation on State of Charge Estimation of Batteries With Adaptive Extended Kalman Filter by Experiment Approach," *IEEE Trans. Veh. Technol.*, vol. 62, no. 1, pp. 108–117, Jan. 2013.

[109] S. Sepasi, R. Ghorbani, and B. Y. Liaw, "A novel on-board state-of-charge estimation method for aged Li-ion batteries based on model adaptive extended Kalman filter," *J. Power Sources*, vol. 245, pp. 337–344, 2014.

[110] J. Han, D. Kim, and M. Sunwoo, "State-of-charge estimation of lead-acid batteries using an adaptive extended Kalman filter," *J. Power Sources*, vol. 188, no. 2, pp. 606–612, 2009.

[111] H. He, R. Xiong, and H. Guo, "Online estimation of model parameters and state-of-charge of LiFePO4 batteries in electric vehicles," *Appl. Energy*, vol. 89, no. 1, pp. 413–420, 2012.

[112] R. Xiong, F. Sun, X. Gong, and H. He, "Adaptive state of charge estimator for lithium-ion cells series battery pack in electric vehicles," *J. Power Sources*, vol. 242, pp. 699–713, 2013.

[113] R. Xiong, X. Gong, C. C. Mi, and F. Sun, "A robust state-of-charge estimator for

multiple types of lithium-ion batteries using adaptive extended Kalman filter,"
J. Power Sources, vol. 243, pp. 805–816, 2013.

[114] R. Xiong, F. Sun, X. Gong, and C. Gao, "A data-driven based adaptive state of charge estimator of lithium-ion polymer battery used in electric vehicles," *Appl. Energy*, vol. 113, pp. 1421–1433, 2014.

[115] F. Sun, X. Hu, Y. Zou, and S. Li, "Adaptive unscented Kalman filtering for state of charge estimation of a lithium-ion battery for electric vehicles," *Energy*, vol. 36, no. 5, pp. 3531–3540, 2011.

[116] M. E. Orchard, P. Hevia-Koch, B. Zhang, and L. Tang, "Risk Measures for Particle-Filtering-Based State-of-Charge Prognosis in Lithium-Ion Batteries," *IEEE Trans. Ind. Electron.*, vol. 60, no. 11, pp. 5260–5269, Nov. 2013.

[117] S. Schwunk, N. Armbruster, S. Straub, J. Kehl, and M. Vetter, "Particle filter for state of charge and state of health estimation for lithium–iron phosphate batteries," *J. Power Sources*, vol. 239, pp. 705–710, 2013.

[118] Y. He, X. Liu, C. Zhang, and Z. Chen, "A new model for State-of-Charge (SOC) estimation for high-power Li-ion batteries," *Appl. Energy*, vol. 101, pp. 808–814, 2013.

[119] L. Zhong, C. Zhang, Y. He, and Z. Chen, "A method for the estimation of the battery pack state of charge based on in-pack cells uniformity analysis," *Appl. Energy*, vol. 113, pp. 558–564, 2014.

[120] X. Chen, W. Shen, M. Dai, Z. Cao, J. Jin, and A. Kapoor, "Robust Adaptive Sliding-Mode Observer Using RBF Neural Network for Lithium-Ion Battery State of Charge Estimation in Electric Vehicles," *IEEE Trans. Veh. Technol.*, vol. 65, no. 4, pp. 1936–1947, Apr. 2016.

[121] M. Landi and G. Gross, "Measurement Techniques for Online Battery State of Health Estimation in Vehicle-to-Grid Applications," *IEEE Trans. Instrum. Meas.*, vol. 63, no. 5, pp. 1224–1234, May 2014.

[122] Y. S. Lee, W. Y. Wang, and T. Y. Kuo, "Soft Computing for Battery State-of-Charge (BSOC) Estimation in Battery String Systems," *IEEE Trans. Ind. Electron.*, vol. 55, no. 1, pp. 229–239, Jan. 2008.

[123] W. X. Shen, K. T. Chau, C. C. Chan, and E. W. C. Lo, "Neural network-based residual capacity indicator for nickel-metal hydride batteries in electric vehicles," *IEEE Trans. Veh. Technol.*, vol. 54, no. 5, pp. 1705–1712, Sep. 2005.

[124] W.-Y. Chang, "Estimation of the state of charge for a LFP battery using a hybrid method that combines a RBF neural network, an OLS algorithm and AGA," *Int.*

J. Electr. Power Energy Syst., vol. 53, pp. 603–611, 2013.

[125] C. Hametner and S. Jakubek, "State of charge estimation for Lithium Ion cells: Design of experiments, nonlinear identification and fuzzy observer design," *J. Power Sources*, vol. 238, pp. 413–421, 2013.

[126] A. Zenati, P. Desprez, and H. Razik, "Estimation of the SOC and the SOH of li-ion batteries, by combining impedance measurements with the fuzzy logic inference," in *IECON 2010 - 36th Annual Conference on IEEE Industrial Electronics Society*, 2010, pp. 1773–1778.

[127] A. J. Salkind, C. Fennie, P. Singh, T. Atwater, and D. E. Reisner, "Determination of state-of-charge and state-of-health of batteries by fuzzy logic methodology," *J. Power Sources*, vol. 80, no. 1, pp. 293–300, 1999.

[128] T. Kim *et al.*, "Model-based condition monitoring for lithium-ion batteries," *J. Power Sources*, vol. 295, pp. 16–27, 2015.

[129] J. C. Á. Antón, P. J. G. Nieto, C. B. Viejo, and J. A. V. Vilán, "Support Vector Machines Used to Estimate the Battery State of Charge," *IEEE Trans. Power Electron.*, vol. 28, no. 12, pp. 5919–5926, Dec. 2013.

[130] B. Pattipati, C. Sankavaram, and K. Pattipati, "System Identification and Estimation Framework for Pivotal Automotive Battery Management System Characteristics," *IEEE Trans. Syst. Man, Cybern. Part C (Applications Rev.*, vol. 41, no. 6, pp. 869–884, Nov. 2011.

[131] T. Hansen and C.-J. Wang, "Support vector based battery state of charge estimator," *J. Power Sources*, vol. 141, no. 2, pp. 351–358, 2005.

[132] W. Junping, C. Quanshi, and C. Binggang, "Support vector machine based battery model for electric vehicles," *Energy Convers. Manag.*, vol. 47, no. 7, pp. 858–864, 2006.

[133] M. Charkhgard and M. Farrokhi, "State-of-Charge Estimation for Lithium-Ion Batteries Using Neural Networks and EKF," *Ind. Electron. IEEE Trans.*, vol. 57, no. 12, pp. 4178–4187, Dec. 2010.

[134] P. H. Michel and V. Heiries, "An Adaptive Sigma Point Kalman Filter Hybridized by Support Vector Machine Algorithm for Battery SoC and SoH Estimation," in *2015 IEEE 81st Vehicular Technology Conference (VTC Spring)*, 2015, pp. 1–7.

[135] M. Shahriari and M. Farrokhi, "Online State-of-Health Estimation of VRLA Batteries Using State of Charge," *IEEE Trans. Ind. Electron.*, vol. 60, no. 1, pp. 191–202, Jan. 2013.

[136] Y. Zheng, L. Lu, X. Han, J. Li, and M. Ouyang, "LiFePO4 battery pack capacity estimation for electric vehicles based on charging cell voltage curve transformation," *J. Power Sources*, vol. 226, pp. 33–41, 2013.

[137] C. Weng, Y. Cui, J. Sun, and H. Peng, "On-board state of health monitoring of lithium-ion batteries using incremental capacity analysis with support vector regression," *J. Power Sources*, vol. 235, pp. 36–44, 2013.

[138] I. Bloom, L. K. Walker, J. K. Basco, D. P. Abraham, J. P. Christophersen, and C. D. Ho, "Differential voltage analyses of high-power lithium-ion cells. 4. Cells containing NMC," *J. Power Sources*, vol. 195, no. 3, pp. 877–882, 2010.

[139] M. Einhorn, F. V Conte, C. Kral, and J. Fleig, "A Method for Online Capacity Estimation of Lithium Ion Battery Cells Using the State of Charge and the Transferred Charge," *Ind. Appl. IEEE Trans.*, vol. 48, no. 2, pp. 736–741, Mar. 2012.

[140] S. Lee, J. Kim, J. Lee, and B. H. Cho, "State-of-charge and capacity estimation of lithium-ion battery using a new open-circuit voltage versus state-of-charge," *J. Power Sources*, vol. 185, no. 2, pp. 1367–1373, Dec. 2008.

[141] J. T. B. A. Kessels, B. Rosca, H. J. Bergveld, and P. P. J. van den Bosch, "On-line battery identification for electric driving range prediction," in *2011 IEEE Vehicle Power and Propulsion Conference*, 2011, pp. 1–6.

[142] M. A. Roscher, J. Assfalg, and O. S. Bohlen, "Detection of Utilizable Capacity Deterioration in Battery Systems," *Veh. Technol. IEEE Trans.*, vol. 60, no. 1, pp. 98–103, Jan. 2011.

[143] B. S. Bhangu, P. Bentley, D. A. Stone, and C. M. Bingham, "Nonlinear observers for predicting state-of-charge and state-of-health of lead-acid batteries for hybrid-electric vehicles," *IEEE Trans. Veh. Technol.*, vol. 54, no. 3, pp. 783–794, May 2005.

[144] G. L. Plett, "Recursive approximate weighted total least squares estimation of battery cell total capacity," *J. Power Sources*, vol. 196, no. 4, pp. 2319–2331, 2011.

[145] X. Hu, F. Sun, Y. Zou, and H. Peng, "Online estimation of an electric vehicle Lithium-Ion battery using recursive least squares with forgetting," in *Proceedings of the 2011 American Control Conference*, 2011, pp. 935–940.

[146] G. L. Plett, "Extended Kalman filtering for battery management systems of LiPB-based HEV battery packs: Part 3. State and parameter estimation," *J. Power Sources*, vol. 134, no. 2, pp. 277–292, 2004.

[147] S. Sepasi, R. Ghorbani, and B. Y. Liaw, "Inline state of health estimation of lithium-ion batteries using state of charge calculation," *J. Power Sources*, vol. 299, pp. 246–254, 2015.

[148] A. Jossen, "Fundamentals of battery dynamics," *J. Power Sources*, vol. 154, no. 2, pp. 530–538, Mar. 2006.

[149] P. Verma, P. Maire, and P. Novák, "A review of the features and analyses of the solid electrolyte interphase in Li-ion batteries," *Electrochim. Acta*, vol. 55, no. 22, pp. 6332–6341, Sep. 2010.

[150] E. Din, C. Schaef, K. Moffat, and J. T. Stauth, "Online spectroscopic diagnostics implemented in an efficient battery management system," in *2015 IEEE 16th Workshop on Control and Modeling for Power Electronics (COMPEL)*, 2015, pp. 1–7.

[151] V. T. Doan, V. B. Vu, H. N. Vu, D. H. Tran, and W. Choi, "Intelligent charger with online battery diagnosis function," in *2015 9th International Conference on Power Electronics and ECCE Asia (ICPE-ECCE Asia)*, 2015, pp. 1644–1649.

[152] A. Densmore and M. Hanif, "Determining battery SoC using Electrochemical Impedance Spectroscopy and the Extreme Learning Machine," in *Future Energy Electronics Conference (IFEEC), 2015 IEEE 2nd International*, 2015, pp. 1–7.

[153] W. Huang and J. A. Qahouq, "An Online Battery Impedance Measurement Method Using DC-DC Power Converter Control," *Ind. Electron. IEEE Trans.*, vol. 61, no. 11, pp. 5987–5995, Nov. 2014.

[154] J. A. A. Qahouq, "Online battery impedance spectrum measurement method," in *2016 IEEE Applied Power Electronics Conference and Exposition (APEC)*, 2016, pp. 3611–3615.

[155] K. Zou, S. Nawrocki, R. Wang, and J. Wang, "High current battery impedance testing for power electronics circuit design," in *2009 IEEE Vehicle Power and Propulsion Conference*, 2009, pp. 531–535.

[156] M. Green and J. B. Moore, "Persistence of Excitation in Linear Systems," in *American Control Conference, 1985*, 1985, pp. 412–417.

[157] J. Schorsch, H. Garnier, M. Gilson, and P. C. Young, "Instrumental variable methods for identifying partial differential equation models," *Int. J. Control*, vol. 86, no. 12, pp. 2325–2335, 2013.

[158] H. E. Perez and S. J. Moura, "Sensitivity-based interval PDE observer for battery SOC estimation," in *2015 American Control Conference (ACC)*, 2015, pp.

323–328.

[159] S. J. Moura, M. Krstic, and N. A. Chaturvedi, "Adaptive PDE observer for battery SOC/SOH estimation," in *ASME 2012 5th Annual Dynamic Systems and Control Conference joint with the JSME 2012 11th Motion and Vibration Conference*, 2012, pp. 101–110.

[160] S. J. Moura, N. A. Chaturvedi, and M. Krstić, "Adaptive partial differential equation observer for battery state-of-charge/state-of-health estimation via an electrochemical model," *J. Dyn. Syst. Meas. Control*, vol. 136, no. 1, p. 11015, 2014.

[161] G. K. Prasad and C. D. Rahn, "Model based identification of aging parameters in lithium ion batteries," *J. Power Sources*, vol. 232, pp. 79–85, 2013.

[162] M. F. Samadi, S. M. M. Alavi, and M. Saif, "Online state and parameter estimation of the Li-ion battery in a Bayesian framework," in *2013 American Control Conference*, 2013, pp. 4693–4698.

[163] G. Plett, "Dual and joint EKF for simultaneous SOC and SOH estimation," in *Proceedings of the 21st Electric Vehicle Symposium (EVS21), Monaco*, 2005, pp. 1–12.

[164] Z. He, Y. Liu, M. Gao, and C. Wang, "A joint model and SOC estimation method for lithium battery based on the sigma point KF," in *2012 IEEE Transportation Electrification Conference and Expo (ITEC)*, 2012, pp. 1–5.

[165] J. Remmlinger, M. Buchholz, T. Soczka-Guth, and K. Dietmayer, "On-board state-of-health monitoring of lithium-ion batteries using linear parameter-varying models," *J. Power Sources*, pp. 1–7, Nov. 2012.

[166] S. Nejad, D. T. Gladwin, and D. A. Stone, "Enhanced state-of-charge estimation for lithium-ion iron phosphate cells with flat open-circuit voltage curves," in *Industrial Electronics Society, IECON 2015 - 41st Annual Conference of the IEEE*, 2015, pp. 3187–3192.

[167] H. He, X. Zhang, R. Xiong, Y. Xu, and H. Guo, "Online model-based estimation of state-of-charge and open-circuit voltage of lithium-ion batteries in electric vehicles," *Energy*, vol. 39, no. 1, pp. 310–318, 2012.

[168] H. Rahimi-eichi, S. Member, and M. Chow, "Adaptive Parameter Identification and State-of-Charge Estimation of Lithium- Ion Batteries Adaptive Parameter Identification and State-of-Charge Estimation of Lithium-Ion Batteries," 2012.

[169] T. Kim and W. Qiao, "A Hybrid Battery Model Capable of Capturing Dynamic Circuit Characteristics and Nonlinear Capacity Effects," *Energy Conversion,*

IEEE Trans., vol. 26, no. 4, pp. 1172–1180, Dec. 2011.

[170] M. T. Zareifard and A. V Savkin, "Model predictive control for wind power generation smoothing with controlled battery storage based on a nonlinear battery mathematical model," in *Control Conference (ASCC), 2015 10th Asian*, 2015, pp. 1–6.

[171] L. W. Juang, P. J. Kollmeyer, T. M. Jahns, and R. D. Lorenz, "Improved Nonlinear Model for Electrode Voltage-Current Relationship for More Consistent Online Battery System Identification," *IEEE Trans. Ind. Appl.*, vol. 49, no. 3, pp. 1480–1488, May 2013.

[172] S. Yuan, H. Wu, X. Zhang, and C. Yin, "Online Estimation of Electrochemical Impedance Spectra for Lithium-Ion Batteries via Discrete Fractional Order Model," in *Vehicle Power and Propulsion Conference (VPPC), 2013 IEEE*, 2013, pp. 1–6.

[173] J. M. Francisco *et al.*, "Lithium-ion battery state of charge estimation using a fractional battery model," in *Fractional Differentiation and Its Applications (ICFDA), 2014 International Conference on*, 2014, pp. 1–6.

[174] J. Sabatier, M. Merveillaut, J. M. Francisco, F. Guillemard, and D. Porcelatto, "Fractional models for lithium-ion batteries," in *Control Conference (ECC), 2013 European*, 2013, pp. 3458–3463.

[175] T. Takamatsu and H. Ohmori, "State and parameter estimation of lithium-ion battery by Kreisselmeier-type adaptive observer for fractional calculus system," in *Society of Instrument and Control Engineers of Japan (SICE), 2015 54th Annual Conference of the*, 2015, pp. 86–90.

[176] I.-S. Kim, "The novel state of charge estimation method for lithium battery using sliding mode observer," *J. Power Sources*, vol. 163, no. 1, pp. 584–590, 2006.

[177] I. Kim, "A technique for estimating the state of health of lithium batteries through a dual-sliding-mode observer," *IEEE Trans. Power Electron.*, vol. 25, no. 4, pp. 1013–1022, Apr. 2010.

[178] L. Xue, J. Jiuchun, Z. Caiping, Z. Weige, and S. Bingxiang, "Effects analysis of model parameters uncertainties on battery SOC estimation using H-infinity observer," in *2014 IEEE 23rd International Symposium on Industrial Electronics (ISIE)*, 2014, pp. 1647–1653.

[179] E. Krüger, Q. T. Tran, and K. Mamadou, "Normalized least mean squares observer for battery parameter estimation," in *PowerTech, 2015 IEEE Eindhoven*, 2015, pp. 1–6.

[180] P. Kumar and P. Bauer, "Parameter extraction of battery models using multiobjective optimization genetic algorithms," in *Power Electronics and Motion Control Conference (EPE/PEMC), 2010 14th International*, 2010, pp. T9-106-T9-110.

[181] X. Hu, S. Li, and H. Peng, "A comparative study of equivalent circuit models for Li-ion batteries," *J. Power Sources*, vol. 198, pp. 359–367, Jan. 2012.

[182] M. Shahriari and M. Farrokhi, "State of health estimation of VRLA batteries using fuzzy logic," in *2010 18th Iranian Conference on Electrical Engineering*, 2010, pp. 629–634.

[183] P. Singh and D. Reisner, "Fuzzy logic-based state-of-health determination of lead acid batteries," in *Telecommunications Energy Conference, 2002. INTELEC. 24th Annual International*, 2002, pp. 583–590.

[184] P. Singh, S. Kaneria, J. Broadhead, X. Wang, and J. Burdick, "Fuzzy logic estimation of SOH of 125Ah VRLA batteries," *2004 10th Int. Work. Comput. Electron. (IEEE Cat. No.04EX915)*, pp. 524–531, 2002.

[185] A. Eddahech, O. Briat, N. Bertrand, J.-Y. Delétage, and J.-M. Vinassa, "Behavior and state-of-health monitoring of Li-ion batteries using impedance spectroscopy and recurrent neural networks," *Int. J. Electr. Power Energy Syst.*, vol. 42, no. 1, pp. 487–494, 2012.

[186] D. Andre, A. Nuhic, T. Soczka-Guth, and D. U. Sauer, "Comparative study of a structured neural network and an extended Kalman filter for state of health determination of lithium-ion batteries in hybrid electricvehicles," *Eng. Appl. Artif. Intell.*, vol. 26, no. 3, pp. 951–961, 2013.

[187] J. Liu, W. Wang, and F. Ma, "A regularized auxiliary particle filtering approach for system state estimation and battery life prediction," *Smart Mater. Struct.*, vol. 20, no. 7, p. 75021, 2011.

[188] B. Saha, K. Goebel, S. Poll, and J. Christophersen, "Prognostics Methods for Battery Health Monitoring Using a Bayesian Framework," *IEEE Trans. Instrum. Meas.*, vol. 58, no. 2, pp. 291–296, Feb. 2009.

[189] Q. Miao, L. Xie, H. Cui, W. Liang, and M. Pecht, "Remaining useful life prediction of lithium-ion battery with unscented particle filter technique," *Microelectron. Reliab.*, vol. 53, no. 6, pp. 805–810, 2013.

[190] D. Wang, Q. Miao, and M. Pecht, "Prognostics of lithium-ion batteries based on relevance vectors and a conditional three-parameter capacity degradation model," *J. Power Sources*, vol. 239, pp. 253–264, 2013.

[191] W. He, N. Williard, M. Osterman, and M. Pecht, "Prognostics of lithium-ion batteries based on Dempster–Shafer theory and the Bayesian Monte Carlo method," *J. Power Sources*, vol. 196, no. 23, pp. 10314–10321, 2011.

[192] Y. Chen, Q. Miao, B. Zheng, S. Wu, and M. Pecht, "Quantitative Analysis of Lithium-Ion Battery Capacity Prediction via Adaptive Bathtub-Shaped Function," *Energies*, vol. 6, no. 6, p. 3082, 2013.

[193] A. Widodo, M.-C. Shim, W. Caesarendra, and B.-S. Yang, "Intelligent prognostics for battery health monitoring based on sample entropy," *Expert Syst. Appl.*, vol. 38, no. 9, pp. 11763–11769, 2011.

[194] G. Plett, "High-performance battery-pack power estimation using a dynamic cell model," *Veh. Technol. IEEE Trans.*, vol. 53, no. 5, pp. 1586–1593, 2004.

[195] J. Do Yang and others, "Method of estimating maximum output of battery for hybrid electric vehicle," 2009.

[196] H. L. Martin and R. E. Goodson, "Monitoring apparatus and method for battery power supply." Google Patents, 1983.

[197] D. Reni and M. F. Culbert, "Battery charge state determination," 1994.

[198] U.S. Department of Energy, "PNGV Battery Test Manual," 2001.

[199] J. P. Christophersen *et al.*, "Advanced technology development program for lithium-ion batteries: gen 2 performance evaluation final report," *Idaho Natl. Lab.*, 2006.

[200] G. Hunt and others, "USABC electric vehicle battery test procedures manual," *Washington, DC, USA United States Dep. Energy*, 1996.

[201] R. Xiong, H. He, F. Sun, and K. Zhao, "Online Estimation of Peak Power Capability of Li-Ion Batteries in Electric Vehicles by a Hardware-in-Loop Approach," *Energies*, vol. 5, no. 5, p. 1455, 2012.

[202] R. D. Anderson, Y. Zhao, X. Wang, X. G. Yang, and Y. Li, "Real time battery power capability estimation," in *2012 American Control Conference (ACC)*, 2012, pp. 592–597.

[203] L. W. Juang, P. J. Kollmeyer, T. M. Jahns, and R. D. Lorenz, "Implementation of online battery state-of-power and state-of-function estimation in electric vehicle applications," in *Energy Conversion Congress and Exposition (ECCE), 2012 IEEE*, 2012, pp. 1819–1826.

[204] F. Sun, R. Xiong, H. He, W. Li, and J. E. E. Aussems, "Model-based dynamic multi-

parameter method for peak power estimation of lithium–ion batteries," *Appl. Energy*, vol. 96, pp. 378–386, 2012.

[205] W. Waag, C. Fleischer, and D. U. Sauer, "Adaptive on-line prediction of the available power of lithium-ion batteries," *J. Power Sources*, vol. 242, pp. 548–559, 2013.

[206] S. Wang, M. Verbrugge, J. S. Wang, and P. Liu, "Power prediction from a battery state estimator that incorporates diffusion resistance," *J. Power Sources*, vol. 214, pp. 399–406, 2012.

[207] M. Ehsani, Y. Gao, and A. Emadi, *Modern electric, hybrid electric, and fuel cell vehicles: fundamentals, theory, and design*. CRC press, 2009.

[208] "Cell, Module, And Pack For EV Applications | Automotive Energy Supply Corporation." [Online]. Available: http://www.eco-aesc-lb.com/en/product/liion_ev/. [Accessed: 23-Jun-2016].

[209] "Cell, Module, And Pack For EV Applications | Automotive Energy Supply Corporation." .

[210] T. Barlow, S. Latham, I. Mccrae, and P. Boulter, "A reference book of driving cycles for use in the measurement of road vehicle emissions," 2009.

[211] N. Watrin, B. Blunier, and A. Miraoui, "Review of adaptive systems for lithium batteries state-of-charge and state-of-health estimation," *IEEE Transp. Electrif. Conf. Expo*, no. 3, pp. 1–6, Jun. 2012.

[212] J. Zhang and J. Lee, "A review on prognostics and health monitoring of Li-ion battery," *J. Power Sources*, vol. 196, no. 15, pp. 6007–6014, Aug. 2011.

[213] K. S. Ng, C.-S. Moo, Y.-P. Chen, and Y.-C. Hsieh, "Enhanced coulomb counting method for estimating state-of-charge and state-of-health of lithium-ion batteries," *Appl. Energy*, vol. 86, no. 9, pp. 1506–1511, Sep. 2009.

[214] M. Micea and L. Ungurean, "Online state-of-health assessment for battery management systems," *IEEE Trans. Instrum. Meas.*, vol. 60, no. 6, pp. 1997–2006, 2011.

[215] S. Nejad, D. T. Gladwin, and D. A. Stone, "A microcontroller-based state-of-health estimator for lithium-ion batteries," in *Power Electronics, Machines and Drives (PEMD 2014), 7th IET International Conference on*, 2014, pp. 1–6.

[216] A. J. Fairweather, M. P. Foster, and D. A. Stone, "Modelling of VRLA batteries over operational temperature range using pseudo random binary sequences," *J. Power Sources*, vol. 207, pp. 56–59, Jun. 2012.

[217] "NASA Battery Dataset." [Online]. Available: http://ti.arc.nasa.gov/tech/dash/pcoe/prognostic-data-repository/. [Accessed: 20-Dec-2013].

[218] W. H. Press, *Numerical recipes 3rd edition: The art of scientific computing*. Cambridge university press, 2007.

[219] S. Tang, C. Yu, X. Wang, X. Guo, and X. Si, "Remaining useful life prediction of lithium-ion batteries based on the wiener process with measurement error," *Energies*, vol. 7, no. 2, pp. 520–547, 2014.

[220] T. Huria, G. Ludovici, and G. Lutzemberger, "State of charge estimation of high power lithium iron phosphate cells," *J. Power Sources*, vol. 249, no. 0, pp. 92–102, 2014.

[221] S. Jung, "Mathematical model of lithium-ion batteries with blended-electrode system," *J. Power Sources*, vol. 264, no. 0, pp. 184–194, 2014.

[222] A. Khandelwal *et al.*, "Generalized moving boundary model for charge–discharge of LiFePO4/C cells," *J. Power Sources*, vol. 248, no. 0, pp. 101–114, 2014.

[223] N. A. Chaturvedi and R. Klein, "Modeling , estimation , and control challenges for lithium-ion batteries," pp. 1997–2002, 2010.

[224] K. Smith, "Electrochemical control of lithium-ion batteries," *Control Syst. IEEE*, no. April, pp. 18–25, 2010.

[225] J. Marcicki, A. T. Conlisk, and G. Rizzoni, "A lithium-ion battery model including electrical double layer effects," *J. Power Sources*, vol. 251, no. 0, pp. 157–169, 2014.

[226] G. K. Prasad and C. D. Rahn, "Reduced Order Impedance Models of Lithium Ion Batteries," *J. Dyn. Syst. Meas. Control*, vol. 136, no. 4, p. 41012, Apr. 2014.

[227] J. L. Lee, L. L. Aldrich, K. D. Stetzel, and G. L. Plett, "Extended operating range for reduced-order model of lithium-ion cells," *J. Power Sources*, vol. 255, no. 0, pp. 85–100, 2014.

[228] C. Speltino, D. Di Domenico, G. Fiengo, and a. Stefanopoulou, "Comparison of reduced order lithium-ion battery models for control applications," *Proc. 48h IEEE Conf. Decis. Control held jointly with 2009 28th Chinese Control Conf.*, pp. 3276–3281, Dec. 2009.

[229] C. M. Shepherd, "Design of Primary and Secondary Cells II. An Equation Describing Battery Discharge," *J. Electrochem. Soc.*, vol. 112, pp. 657–664,

1965.

[230] S. Li and B. Ke, "Study of battery modeling using mathematical and circuit oriented approaches," in *IEEE Power and Energy Society General Meeting*, 2011, pp. 1–8.

[231] O. Tremblay, M. Ieee, L. Dessaint, S. M. Ieee, and A. Dekkiche, "A Generic Battery Model for the Dynamic Simulation of Hybrid Electric Vehicles," no. V, pp. 284–289, 2007.

[232] H. Rahimi-Eichi, F. Baronti, and M.-Y. Chow, "Modeling and online parameter identification of Li-Polymer battery cells for SOC estimation," in *Industrial Electronics (ISIE), 2012 IEEE International Symposium on*, 2012, pp. 1336–1341.

[233] J. Unger, C. Hametner, S. Jakubek, and M. Quasthoff, "A novel methodology for non-linear system identification of battery cells used in non-road hybrid electric vehicles," *J. Power Sources*, vol. 269, no. 0, pp. 883–897, 2014.

[234] G. L. Plett, "Extended Kalman filtering for battery management systems of LiPB-based HEV battery packs: Part 1. Background," *J. Power Sources*, vol. 134, no. 1, pp. 252–261, 2004.

[235] G. L. Plett, "Extended Kalman filtering for battery management systems of LiPB-based HEV battery packs Part 2. Modeling and identification," *J. Power Sources*, vol. 134, no. 2, pp. 262–276, Aug. 2004.

[236] M. A. Roscher and D. U. Sauer, "Dynamic electric behavior and open-circuit-voltage modeling of LiFePO4-based lithium ion secondary batteries," *J. Power Sources*, vol. 196, no. 1, pp. 331–336, 2011.

[237] R. R. Richardson and D. A. Howey, "Sensorless Battery Internal Temperature Estimation Using a Kalman Filter With Impedance Measurement," *IEEE Trans. Sustain. Energy*, vol. 6, no. 4, pp. 1190–1199, Oct. 2015.

[238] Y.-H. Chiang, W.-Y. Sean, and J.-C. Ke, "Online estimation of internal resistance and open-circuit voltage of lithium-ion batteries in electric vehicles," *J. Power Sources*, vol. 196, no. 8, pp. 3921–3932, 2011.

[239] J. Kim and B. Cho, "State-of-charge estimation and state-of-health prediction of a Li-ion degraded battery based on an EKF combined with a per-unit system," *Veh. Technol. IEEE Trans.*, vol. 60, no. 9, pp. 4249–4260, 2011.

[240] M. Sitterly, L. Y. Wang, G. G. Yin, and C. Wang, "Enhanced Identification of Battery Models for Real-Time Battery Management," *Sustain. Energy, IEEE Trans.*, vol. 2, no. 3, pp. 300–308, Jul. 2011.

[241] D. Andre, M. Meiler, K. Steiner, H. Walz, T. Soczka-Guth, and D. U. Sauer, "Characterization of high-power lithium-ion batteries by electrochemical impedance spectroscopy. II: Modelling," *J. Power Sources*, vol. 196, no. 12, pp. 5349–5356, 2011.

[242] L. E. Unnewehr and S. A. Nasar, "Electric Vehicle Technology," New York: John Wiley & Sons, Inc., 1982, pp. 81–91.

[243] V. H. Johnson, "Battery performance models in {ADVISOR}," *J. Power Sources*, vol. 110, no. 2, pp. 321–329, 2002.

[244] M. S. R. Khatib, A.L. Dalverny and M. L. D. M. Gaberscek, "Origin of the Voltage Hysteresis in the CoP Conversion Material for Li-Ion Batteries," *J. Phys. Chem.*, vol. 117, no. 2, pp. 837–849, 2013.

[245] A. A.-H. Hussein, N. Kutkut, and I. Batarseh, "A hysteresis model for a Lithium battery cell with improved transient response," *2011 Twenty-Sixth Annu. IEEE Appl. Power Electron. Conf. Expo.*, pp. 1790–1794, Mar. 2011.

[246] C. Gould, J. Wang, D. Stone, and M. Foster, "EV/HEV Li-ion battery modelling and state-of-function determination," *Int. Symp. Power Electron. Power Electron. Electr. Drives, Autom. Motion*, pp. 353–358, Jun. 2012.

[247] F. Sun, R. Xiong, and H. He, "Estimation of state-of-charge and state-of-power capability of lithium-ion battery considering varying health conditions," *J. Power Sources*, vol. 259, pp. 166–176, Aug. 2014.

[248] M. A. Roscher, O. S. Bohlen, and D. U. Sauer, "Reliable State Estimation of Multicell Lithium-Ion Battery Systems," *Energy Conversion, IEEE Trans.*, vol. 26, no. 3, pp. 737–743, Sep. 2011.

[249] J. Remmlinger, M. Buchholz, M. Meiler, P. Bernreuter, and K. Dietmayer, "State-of-health monitoring of lithium-ion batteries in electric vehicles by on-board internal resistance estimation," *J. Power Sources*, vol. 196, no. 12, pp. 5357–5363, Jun. 2011.

[250] M. Ouyang, G. Liu, L. Lu, J. Li, and X. Han, "Enhancing the estimation accuracy in low state-of-charge area: A novel onboard battery model through surface state of charge determination," *J. Power Sources*, vol. 270, no. 0, pp. 221–237, 2014.

[251] C. Y. Chun *et al.*, "Current sensor-less state-of-charge estimation algorithm for lithium-ion batteries utilizing filtered terminal voltage," *J. Power Sources*, vol. 273, pp. 255–263, Jan. 2015.

[252] S. Wang, M. Verbrugge, J. S. Wang, and P. Liu, "Multi-parameter battery state

estimator based on the adaptive and direct solution of the governing differential equations," *J. Power Sources*, vol. 196, no. 20, pp. 8735–8741, Oct. 2011.

[253] J. Du, Z. Liu, and Y. Wang, "State of charge estimation for Li-ion battery based on model from extreme learning machine," *Control Eng. Pract.*, vol. 26, pp. 11–19, 2014.

[254] H. He, R. Xiong, X. Zhang, F. Sun, and J. Fan, "State-of-Charge Estimation of the Lithium-Ion Battery Using an Adaptive Extended Kalman Filter Based on an Improved Thevenin Model," *Veh. Technol. IEEE Trans.*, vol. 60, no. 4, pp. 1461–1469, May 2011.

[255] R. G. Brown and P. Y. C. Hwang, *Introduction to Random Signals and Applied Kalman Filtering*, Third. New York, NY: John Wiley & Sons, Inc., 1997.

[256] V. A. Bavdekar, A. P. Deshpande, and S. C. Patwardhan, "Identification of process and measurement noise covariance for state and parameter estimation using extended Kalman filter," *J. Process Control*, vol. 21, no. 4, pp. 585–601, 2011.

[257] Y. Ji, Y. Zhang, and C.-Y. Wang, "Li-ion cell operation at low temperatures," *J. Electrochem. Soc.*, vol. 160, no. 4, pp. A636--A649, 2013.

[258] V. V Chalam, *Adaptive Control Systems: Techniques and Applications*. New York: Marcel Dekker, Inc., 1987.

[259] D. Andre, M. Meiler, K. Steiner, C. Wimmer, T. Soczka-Guth, and D. U. Sauer, "Characterization of high-power lithium-ion batteries by electrochemical impedance spectroscopy. I. Experimental investigation," *J. Power Sources*, vol. 196, no. 12, pp. 5334–5341, 2011.

[260] D. W. Marquardt, "An Algorithm for Least-Squares Estimation of Nonlinear Parameters," *J. Soc. Ind. Appl. Math.*, vol. 11, no. 2, pp. 431–441, 1963.

[261] D. M. Hamby, "A review of techniques for parameter sensitivity analysis of environmental models," *Environ. Monit. Assess.*, vol. 32, no. 2, pp. 135–154, 1994.

[262] Y. Jiang, W. W. Hager, and J. Li, "The geometric mean decomposition," *Linear Algebra Appl.*, vol. 396, no. 1–3, pp. 373–384, 2005.

[263] J. N. Davidson, D. A. Stone, M. P. Foster, and D. T. Gladwin, "Improved Bandwidth and Noise Resilience in Thermal Impedance Spectroscopy by Mixing PRBS Signals," *IEEE Trans. Power Electron.*, vol. 29, no. 9, pp. 4817–4828, 2014.

[264] A. K. Tangirala, *Principles of System Identification: Theory and Practice*. CRC Press, 2014.

[265] W. D. T. Davies, "System identification for self-adaptive control," London, UK: Wiley-interscience, 1970, pp. 44–88.

[266] R. L. T. Hampton, "A hybrid analog-digital pseudo-random noise generator," in *Proceedings of the April 21-23, 1964, spring joint computer conference*, 1964, pp. 287–301.

[267] P. E. Wellstead, "Non-parametric methods of system identification," *Automatica*, vol. 17, no. 1, pp. 55–69, 1981.

[268] C. R. Gould, C. M. Bingham, D. A. Stone, and P. Bentley, "Novel battery model of an all-electric personal rapid transit vehicle to determine state-of-health through subspace parameter estimation and a Kalman Estimator," *2008 Int. Symp. Power Electron. Electr. Drives, Autom. Motion*, pp. 1217–1222, Jun. 2008.

[269] S. Nejad, D. T. Gladwin, and D. A. Stone, "A systematic review of lumped-parameter equivalent circuit models for real-time estimation of lithium-ion battery states," *J. Power Sources*, vol. 316, pp. 183–196, 2016.

[270] J. S. Steinhart and S. R. Hart, "Calibration curves for thermistors," in *Deep Sea Research and Oceanographic Abstracts*, 1968, vol. 15, no. 4, pp. 497–503.

[271] Y. Ma, T. Houghton, A. Cruden, D. Infield, and S. Member, "Modeling the Benefits of Vehicle-to-Grid Technology to a Power System," vol. 27, no. 2, pp. 1012–1020, 2012.